

Copyright Undertaking

This thesis is protected by copyright, with all rights reserved.

By reading and using the thesis, the reader understands and agrees to the following terms:

- 1. The reader will abide by the rules and legal ordinances governing copyright regarding the use of the thesis.
- 2. The reader will use the thesis for the purpose of research or private study only and not for distribution or further reproduction or any other purpose.
- 3. The reader agrees to indemnify and hold the University harmless from and against any loss, damage, cost, liability or expenses arising from copyright infringement or unauthorized usage.

IMPORTANT

If you have reasons to believe that any materials in this thesis are deemed not suitable to be distributed in this form, or a copyright owner having difficulty with the material being included in our database, please contact lbsys@polyu.edu.hk providing details. The Library will look into your claim and consider taking remedial action upon receipt of the written requests.

THEORETICAL AND EXPERIMENTAL INVESTIGATIONS ON CEMENTED SOIL AT SMALL AND LARGE STRAINS

JIAO KANGFU

PhD

The Hong Kong Polytechnic University

The Hong Kong Polytechnic University

Department of Civil and Environmental Engineering

Theoretical and experimental investigations on cemented soil at small and large strains

JIAO KANGFU

A thesis submitted in partial fulfillment of the requirements for the degree of Doctor of Philosophy

Certificate of originality

I hereby declare that this thesis is my own work and that, to the best of my knowledge and

belief, it reproduces no material previously published or written, nor material that has been

accepted for the award of any other degree of diploma, except where due acknowledgement

has been made in the text.

Signature:

Name: JIAO Kangfu

I

Abstract

The deep cement mixing (DCM) method has garnered increasing attention in recent years due to its environmental benefits and high efficiency. The strain of DCM columns under working conditions at the serviceability limit state is typically within the small strain range. Therefore, understanding the behaviour of cemented soil at small strains is crucial for predicting foundation displacement and evaluating performance under working conditions. Many experimental and theoretical studies of cemented soil have been carried out, but they mainly focused on large-strain behaviour, such as strength and post-peak strain softening. These studies also have some major limitations. First of all, some constitutive models for cemented soil exist, mostly within the classical elastoplastic framework, focusing on strainsoftening. However, these models fail to capture the nonlinearity of cemented soil behaviour at small strains, such as the non-linear stiffness. Secondly, the impacts of curing temperature (T_c) and stress (S_c) on the behaviour of cemented soil over a wide strain range remain unclear. According to the field data, the temperature inside DCM columns can reach 40°C, and the effective confining pressure ranges from 0 to approximately 200-300 kPa. Ignoring the distinctions between laboratory and field curing conditions may result in inaccurate parameters and improper designs.

The principal objective of this study is to investigate the impact of curing conditions on the properties of cemented marine clay and improve the theoretical modelling of cemented soils from small to large strains. More specifically, it aims to (i) investigate the strength and small strain stiffness of cemented soil cured under various temperatures and stresses, reflecting field conditions; (ii) develop a constitutive model incorporating the small strain behaviour and strain-softening of cemented soil; (iii) develop a numerical code based on the proposed theoretical model; and (iv) conduct a parametric study of DCM-stabilised foundation using the proposed advanced constitutive model to improve design methods in current engineering practice.

To achieve these objectives, a new temperature and stress-controlled curing apparatus was developed to prepare cemented marine clay at three temperature levels (20, 30, and 40°C) and three stress levels (0, 150, and 300 kPa). The specimens underwent unconfined compression (UC) tests, undrained triaxial tests, Brazilian splitting tests, and direct tension tests after 28 days of curing, with local strain to measure small strain stiffness. Additionally, microstructural analysis was employed to interpret experimental results. Test results reveal that increases in T_c and S_c can enhance strength and stiffness, decrease the elastic threshold strain, and increase the

rate of stiffness degradation within the small strain range. These findings are attributed to the fact that higher T_c can accelerate the cement hydration reaction, enhance the pozzolanic reaction, which generates stronger cementation products between soil particles, and refine the pore structure. While S_c has minimal impact on cement hydration, it enhances density and contact area between soil particles, leading to more effective cementitious bonding. The findings suggest that considering the effects of T_c and S_c can lead to more cost-effective designs.

A new constitutive model (denoted as the full version model in this thesis) for cemented soils suitable for both small and large strains was developed. To enhance the modelling of nonlinear stiffness at small strains and strain-softening at large strains, some new formulations were proposed, including (i) the elastic shear modulus over a wide range of stress conditions and (ii) the non-linear degradation of bonding strength (p_b) with damage strain (ε_d) in the p_b - ε_d plane. Furthermore, the new constitutive models were implemented in finite element software (FEM) in a modular approach. The full version model consists of a simplified version (denoted as the basic version model in this thesis) with two additional modules. The full version and basic version models allow users to select the appropriate model based on test data and engineering requirements.

The performance and advantages of the proposed model are highlighted by simulating different boundary value problems using the full version model, the basic version model, and the Mohr-Coulomb (MC) model. Both the full version and basic version models can simulate small strain modulus degradation and strain-softening behaviour well. The full version model simulates the dilatancy behaviour well, while the basic version model shows some limitations in simulating the dilation behaviour. However, the MC model is inadequate in simulating the strain-softening and the degradation of the small strain modulus of cemented soils. Through parameter analysis, the study compares the bearing capacity and settlement calculations of DCM-stabilised foundations using the advanced model with those based on current design guidelines. The results show that the linear calculation methods commonly used in current standards result in considerable inaccuracies in settlement predictions as the safety factor varies. Specifically, overestimates settlement by approximately 50% when the safety factor is 2.0 and progressively underestimates settlement by 30% when the safety factor is 1.0.

Publications arising from the Thesis

Journal papers:

- Jiao, K. F., & Zhou, C. (2024). A bounding surface model for cemented soil at small and large strains. Journal of Geotechnical and Geoenvironmental Engineering, 150(2), 04023136.
- Jiao, K. F., Zhou, C., Chen, W. B., & Ruan, Z. J. (2025). Effects of Curing Temperature and Stress on Small-Strain Stiffness of Cemented Marine Clay. Journal of Geotechnical and Geoenvironmental Engineering, 151(6), 04025033.
- Jiao, K. F., & Zhou, C. (2025) Effects of curing temperature and stress on the shear and tensile behaviour of binder stabilised marine clay. Engineering Geology, under review.
- Jiao, K. F., Zhou, C., Lee, S. W., & Cheang, W. W. (2025) A simple model for binder-stabilised soils considering nonlinear stiffness characteristics and strain softening. Computers and Geotechnics, under review.
- Jiao, K. F., Zhou, C. Applicability of advanced constitutive models in the design and analysis of DCM-stabilized ground. under preparation.

Conference paper:

Jiao, K. F. and Zhou, C. (2023). Effects of Curing Temperature and Stress on the Mechanical Behaviour of Cemented Hong Kong Marine Clay. Proceedings of The HKIE Geotechnical Division 43rd Annual Seminar.

Acknowledgements

My nearly four-year PhD journey, filled with exciting experiences and challenges, is coming to an end. I would like to take this opportunity to thank everyone who has supported me along the way sincerely. I would like to express my deepest gratitude to my supervisor, Professor Chao Zhou, for his profound knowledge, rigorous academic standards, and exemplary character. His remarkable achievements in academia, noble personality, and selfless dedication have deeply inspired me. Throughout nearly four years of study, Professor Zhou has provided me with invaluable guidance and support, not only in my academic pursuits but also in my personal development and future planning. I would also like to thank my co-supervisor, Prof. Jianhua Yin, for providing the advanced testing devices in our soil lab, which were crucial for my research. My appreciation also extends to Prof. Limin Zhang and Prof. Yilin Yao for their valuable time examining my thesis as the external examiners. I am also deeply thankful to Prof. Alessandro STOCCHINO of CEE, who chaired my oral examination, for his distinguished guidance and support.

I extend my heartfelt thanks to Dr. Wenbo Chen, Dr. Zejian Chen, and Dr. Dingbao Song for their encouragement, guidance, and support, which helped me overcome challenges during my PhD studies. I am also sincerely grateful to Mr. Kit, the technician in the soil mechanics laboratory, and Mr. David from the Civil Engineering workshop for their assistance in designing and modifying various equipment.

I am immensely grateful to my friends for accompanying me through nearly four years of a vibrant and fulfilling life in Hong Kong. Special thanks to my fellow, especially Guo Chang, who selflessly helped me when I started my experiments and introduced me to basketball and swimming, adding joy to my otherwise singular PhD journey. Thanks to Dai Baolin for the late-night academic discussions and to Zhan Zhiqi for the valuable advice on research and life. Thanks to Weifeng Huang for assisting me in experiments, and to James Ruan for his support in life and engineering knowledge, and for staying up late with me to work on academic projects. I am grateful to Zhang Qi from HKUST for his selfless advice and guidance when I needed it most. Thanks to Yu Chenghao for his companionship and Guyang Lin for inspiring me to become more confident and brave, as well as for the nights we spent together in our shared dormitory, staying up late and having barbecued skewers.

Finally, I am deeply thankful to my parents and sister for their unconditional support throughout my academic journey, which has motivated me to persevere. Most importantly, I am grateful to my wife, Wenjuan, for her patient waiting, companionship, and selfless dedication to our family.

Table of Contents

Certificate of originality	I
Abstract	II
Publications arising from the Thesis	IV
Acknowledgements	V
Table of Contents	VII
List of figures	XII
CHAPTER 1 Introduction	1
1.1 Research background	1
1.2 Research objectives and strategy	4
1.3 Thesis organization	5
CHAPTER 2 Literature review	7
2.1 Mechanism of cementation effects and the microstructure of cemented soil	7
2.1.1 Mechanism of soil stabilisation using cement	7
2.1.2 Micro-structure of cemented soil	8
2.2 Mechanical behaviour of cemented soil	12
2.2.1 Strength	12
2.2.2 Strain-softening behaviour	17
2.2.3 Stiffness	18
2.3 Constitutive modelling for cemented soil	25
2.3.1 Models based on the classical elastoplasticity framework	25
2.3.2 Models based on the advanced constitutive model theory	26
2.4 Numerical simulation and design method of DCM	29
2.4.1 Constitutive models used for DCM in numerical simulation	29
2.4.2 Numerical simulation of DCM-stabilised foundation	30
2.4.3 Design method of DCM-stabilised foundation	31
2.5 Summary	32
CHAPTER 3 Test material, programme and methods	34
3.1 Test material and specimen preparation	34
3.1.1 Test material	34
3.1.2 Specimen preparation	35

3.1.3 A new temperature and stress-controlled curing apparatus	36
3.2 Test programme	37
3.3 Test procedures and apparatuses	38
3.3.1 Unconfined compression tests	38
3.3.2 Consolidated undrained triaxial shear tests	39
3.3.3 Brazilian test	40
3.3.4 Direct tensile test	41
3.3.5 Microstructural analysis	42
CHAPTER 4 Effects of curing condition on stiffness and strength	44
4.1 Curing condition effects on the microstructure of cemented soil	44
4.1.1 Comparison of SEM results between uncemented and cemented clay	44
4.1.2 Effects of curing temperature	45
4.1.3 Effects of curing stress	48
4.2 Interpretations of unconfined compression test and microstructure test results	50
4.2.1 Effects of cement content on the unconfined compression test behaviour	50
4.2.2 Effects of curing temperature on the unconfined compression test behaviour	51
4.2.3 Effects of curing stress on the unconfined compression test behaviour	54
4.3 Interpretations of undrained triaxial shear test results	56
4.3.1 Effects of cement content on the undrained triaxial shear behaviour	56
4.3.2 Effects of curing temperatures on the undrained triaxial shear behaviour	59
4.3.3 Effects of curing stress on the undrained triaxial shear behaviour	61
4.4 Interpretations of tensile test results	63
4.5 Correlation between stiffness and strength	64
4.5.1 Correlation between UCS and E50	64
4.5.2 Correlation between UCS and tensile strength	67
4.6 Summary	68
CHAPTER 5 A bounding surface model for cemented soil at small and large strains	70
5.1 Mathematical formulations	70
5.1.1 Elastoplasticity	70
5.1.2 Bounding and yield surfaces	71
5.1.3 Cementation hand strength	73

	5.1.4 Elastic moduli	74
	5.1.5 Critical state and state parameter	75
	5.1.6 State-dependent dilatancy	76
	5.1.7 Hardening law and condition of consistency	77
	5.1.8 Tension cut-off	78
	5.2 Multiaxial Generalization	78
	5.3 Calibration of model parameters	81
	5.4 Model validation using test data in the literature	82
	5.4.1 Elastic shear modulus	82
	5.4.2 Stress-strain relation and dilatancy during drained shearing	83
	5.4.3 Stress-strain relation and effective stress path during undrained shearing	86
	5.4.4 Stiffness at very small strains and small strains	88
	5.4.5 Mechanical behaviour of cemented soil from small to large strains	89
	5.4.6 Stress-strain behaviour during the loading and reloading process	91
	5.5 Model validation using test data from the current study	92
	5.6 Summary	96
CF	HAPTER 6 Model implementation in a modular approach and comparisons among differen	nt models
•••		97
	6.1 Implementation of the newly proposed model in a modular approach	97
	6.2 Basic version of the proposed model	98
	6.2.1 Elastoplasticity	98
	6.2.2 Bounding and yield surfaces	99
	6.2.3 Cementation bond strength and its degradation	99
	6.2.4 Critical state	100
	6.2.5 Determination of dilatancy	100
	6.2.6 Determination of loading index	101
	6.2.7 Tension cut-off	101
	6.3 The calibration of the seven model parameters is described as follows:	101
	6.4 Optional modules	102
	6.5 Comparison of different models	103
	6.5.1 Simulating drained triaxial shear tests	103

6.5.2 Simulating undrained triaxial shear tests	107
6.5.3 Simulating centrifuge tests of DCM-support excavation	109
6.5.4 Simulating physical model tests of DCM-supported rigid footing	115
6.5.5 Simulating a field test of DCM-supported embankment	121
6.6 Summary	125
CHAPTER 7 Parametric study of DCM-stabilised foundation	126
7.1 Analytical formulations for designing DCM-stabilised foundation	126
7.2 Comparisons between the results computed using advanced numerical model and simple	ole
design formulations	128
7.2.1 The influence of pile length and replacement ratio	128
7.2.2 Influence of soft soil Parameters	131
7.3 Sensitivity analysis based on the advanced numerical model	134
7.3.1 Influence of model parameters for elasticity	134
7.3.2 Influence of model parameters for critical state	136
7.3.3 Influence of model parameters for flow rule and hardening law	138
7.3.4 Influence of model parameters for cementation	141
7.3.5 Comparison of sensitivity of different parameters	144
7.4 Design chart for the bearing capacity of DCM-stabilised foundations	145
7.5 Summary	146
CHAPTER 8 Conclusions and recommendations for further work	148
8.1 Conclusions	148
8.1.1 Effects of curing temperature and curing stress on strength and stiffness of cemer	nted soil
	148
8.1.2 A new model for cemented soil at small and large strains	149
8.1.3 Comparison of different constitutive models	150
8.1.4 Parametric study of DCM-stablised foundation	150
8.2 Recommendations and future studies	151
8.2.1 Suggestions for experimental study	151
8.2.2 Suggestions for theoretical constitutive model study	152
8.2.3 Suggestions for numerical study	152
References	154

List of figures

Figure 1.1 (a) Construction of DCM column (https://goo.su/6Hojx) and (b) use of DCM in retaining wall (https://goo.su/CPQLP0)
Figure 1.2 Small strain stiffness characteristics of soil (Atkinson and Sallfors, 1991)2
Figure 2.1 SEM micrograph of RT specimens cemented with (a) calcite; (b) gypsum; (c) Portland cement (Ismail et al. 2002)
Figure 2.2 SEM images of cemented Ballina clay (a) before; and (b) after shearing (Nguyen et al. 2017)
Figure 2.3 Critical state line of cemented sand (Wang and Leung 2008)14
Figure 2.4 Stress-strain and volumetric curves of cemented soil in triaxial tests for various cement contents (Wang and Leung 2008)
Figure 2.5 Variation of strength parameters with plastic shear strain (Yapage et al. 2015)18
Figure 2.6 Elastic shear modulus against mean effective stress (Trhlíková et al. 2012)20
Figure 2.7 Load applied to the cemented particles enlarges the contact area (Fernandez and Santamarina 2001)
Figure 2.8 New design charts for stiffness degradation of clays and silts: (a) static applications; (b) dynamic applications (Vardanega and Bolton 2013)23
Figure 2.9 Relationship between E ₅₀ and UCS of quicklime-stabilised soils (Kitazume 2013)
Figure 2.10 Schematic diagram of bounding surface and related concept (Dafalias and Herrmann1986)
Figure 3.1 Particle size distribution of the tested marine clay
Figure 3.2 Photographs showing the specimen preparation process: (a) cement slurry preparation; (b) mixing of marine clay and cement slurry; (c) specimen preparation using vibrator; (d) curing of specimens in curing machine
Figure 3.3 Newly designed specimen curing apparent
Figure 3.4 Diagram of unconfined compression test setup (a) overall view; and (b) local view
Figure 3.5 Apparatus for undrained triaxial shear test
Figure 3.6 Apparatus for Brazilian test

Figure 3.7 Apparatus for direct tensile test
Figure 3.8 TGA test in PolyU (Netzsch STA 449F3)
Figure 3.9 Apparatus for SEM test (Tescan VEGA3)43
Figure 4.1 SEM images of HKMC: (a) 1000x, (b) 5000x, (c) 8000x, and cemented HKMC: (d)
1000x, (e) 5000x, (f) 8000x45
Figure 4.2 Results of TG analysis on cemented HKMC at different curing temperatures: (a) TC curves; (b) DTG curves.
Figure 4.3 MIP results for the specimens at different curing temperatures48
Figure 4.4 Results of TG analysis on cemented marine clay at different curing stresses (a) TG curves; and (b) DTG curves
Figure 4.5 MIP results for the specimens at different curing stresses
Figure 4.6 Typical results of UCS tests for different cement contents: (a) stress-strain relation (b) stiffness degradation curve
Figure 4.7 Variation of (a) UCS; and (b) E ₅₀ with curing temperature and cement content51
Figure 4.8 Effects of curing temperature on stiffness degradation curves of cemented marine clay: (a) $Cc = 15\%$; (b) $Cc = 25\%$; (c) $Cc = 35\%$
Figure 4.9 Normalized modulus degradation curves of cemented soil at different curing temperatures
Figure 4.10 Influence of curing stress on (a) UCS; and (b) E ₅₀ 55
Figure 4.11 Stiffness degradation curves of cemented soil at different curing stresses(a) $T_c = 30$ °C; (b) $T_c = 40$ °C
Figure 4.12 Normalized modulus degradation curves of cemented soil
Figure 4.13 Undrained triaxial shear test results for cemented soil with ($T_c = 20$ °C, $S_c = 0$ kPa) cement content: (a) deviator stress versus axial strain; (b) excess porewater pressure versus axial strain; (c) effective stress paths; (d) small strain stiffness degradation curves59
Figure 4.14 Undrained triaxial shear test results for cemented soil ($Cc = 25\%$, $S_c = 0$ kPa) with 20°C and 30°C curing temperature: (a) deviator stress versus axial strain; (b) excess porewater pressure versus axial strain; (c) effective stress paths; (d) small strain stiffness degradation curves.
Figure 4.15 Undrained triaxial shear test results for cemented soil ($Cc = 25\%$, $T_c = 20$ °C) curing stress: (a) deviator stress versus axial strain: (b) excess porewater pressure versus axial strain
THESE TRI DEVIRIOR SITESS VEISHS RYIRI SITRID. THI EXCESS HOTEWRIET BESSSIE VEISHS WILL STEAM

(c) effective stress paths; (d) small strain stiffness degradation curves
Figure 4.16 (a) Influence of curing temperature on tensile strength; (b) influence of curing
stress on tensile strength of cemented soil
Figure 4.17 Comparison of calculated and measured (M) results: (a) Equation (4-2) and data
from the current study; (b) Equation (4-2) and data from the previous study66
Figure 4.18 Comparison of calculated and measured (M) results: (a) Equation (4-3) and data
from the current study; (b) Equation (4-3) and data from the previous study67
Figure 4.19 (a) Relationship between indirect tensile strength and UCS; (b) relationship
between direct tensile strength and UCS
Figure 5.1 Schematic diagram of the yield, maximum prestress memory and failure bounding
surfaces in the $q-p'$ plane71
Figure 5.2 The influence of parameters k and ε_{ref} on the degradation process of cementation
bonds strength74
Figure 5.3 Influence of model parameters on the prediction of G_0 : (a) parameter A ; (b)
parameter n_c
Figure 5.4 Schematic of yield, critical, dilatancy, and bounding surfaces on the stress ratio π
plane79
Figure 5.5 Comparison between the measured (M) (Saxena 1988) and computed (C) G_0 results
of cemented Monterey sand82
Figure 5.6 Comparison between the measured (M) (Yang 2008) and computed (C) G_0 results
of cemented siliceous sand at 0 confining pressure83
Figure 5.7 Comparison between the measured (M) (Trhlíková et al. 2012) and computed (C)
G ₀ results of kaolin clay83
Figure 5.8 Comparison between the measured (M) (Marri et al. 2012) and computed (C) results
of drained triaxial compression tests on cemented Portaway sand: (a-b) $Cc = 5\%$; (c-d) Cc
= 10% ; (e-f) $Cc = 15\%$ 86
Figure 5.9 Comparison between the measured (M) (Horpibulsuk et al. 2004) and computed (C)
undrained triaxial compression test results of cemented Ariake clay: (a-b) $Cc = 0\%$; (c-d)
Cc = 6%; (e-f) $Cc = 12%$.
Figure 5.10 Comparison between the measured (M) (Yao 2017) and computed (C) stiffness
degradation curves of cemented marine clay with different cement contents: (a) $Cc = 20\%$;

(b) $Cc = 30\%$; (c) $Cc = 50\%$
Figure 5.11 Comparison between the measured (M) (Marques et al. 2021) and computed (C strength and stiffness of cemented Osorio sand: (a) stress-strain behaviour; (b) degradation of stiffness. (c) volumetric strain versus shear strain
Figure 5.12 Comparison between the measured (M) (Consoli et al. 2000) and computed (C strength and stiffness of cemented weathered sandstone. (a) stress-strain behaviour; (b degradation of stiffness.
Figure 5.13 Comparison of calculation results between bounding surface model and classica elastoplastic model
Figure 5.14 Calibration of critical state parameter (a) $p'-q$ line, (b) e- $\log p'$ 93
Figure 5.15 Comparison between the measured (M) and computed (C) stress-strain curves and effective stress path of cemented marine clay. (a-b) $Cc = 15$, $T_c = 20$ °C; (c-d) $Cc = 25$, $T_c = 20$ °C; (e-f) $Cc = 25$, $T_c = 30$ °C; (g-h) $Cc = 15$, $S_c = 150$ kPa
Figure 6.1 The influence of parameters k and ε_{ref} on the degradation process of cementation bond strength
Figure 6.2 Comparison of the results of triaxial drained shear tests (Marri et al. 2012) using ful version model and basic version model (a-b) $Cc = 5\%$; (c-d) $Cc = 10\%$; (e-f) $Cc = 15\%10^4$
Figure 6.3. Comparison between the measured (M) (Yao et al. 2018) and computed (C) stiffness degradation curves of cemented marine clay with different cement contents: (a) $Cc = 20\%$ (b) $Cc = 30\%$; and (c) $Cc = 50\%$
Figure 6.4 Comparison with triaxial shear test Rios et al. (2017) using full and basic versions models. (a) stress-strain curve; (b) volume strain curve; (c) small strain modulus attenuation curve.
Figure 6.5 Comparison between the measured (M) (Ho et al. 2021) and computed (C undrained triaxial compression test results of cemented Hong Kong marine clay: (a-b) ful version model; (c-d) basic version model
Figure 6.6 (a) Schematic diagrams of the centrifuge model setup; (b) three-dimensional mode in finite element analysis
Figure 6.7 Comparison of computed results using three models and experimental test results (a) earth pressure on the quay wall, (b) deflection of the quay wall, (c) bending momen along the quay wall, (d) ground settlement behind the quay wall

Figure 6.8 Schematic diagram of physical model test setting (Fang 2006)116
Figure 6.9 Finite element model and meshing
Figure 6.10 Comparison of computed results using three models and experimental test results: (a) vertical loading stress on the foundation (b) stress comparison between DCM column and clay (c) stress ratio between DCM column and clay (d) small strain modulus of the foundation
Figure 6.11 Deformation contour of the DCM columns before loading and after loading120
Figure 6.12 Comparison of computed results using three models and experimental test results: (a) Effective stress path at the top of the DCM column at the center (b) effective stress path at the midpoint of the DCM pile at the center
Figure 6.13 Finite element model for seawall profile
Figure 6.14 Comparison of calculation results for three models: (a) settlement at point A; (b) settlement at point B
Figure 7.1 Schematic diagrams of 3D FE model for the parametric study
Figure 7.2 Comparison of computed vs. calculated results with varying area replacement ratios: (a) load-settlement curves; (b) bearing capacity of DCM-stabilised foundation; (c) Ratio of settlement
Figure 7.3 Comparison of computed vs. calculated results with varying length of DCM: (a) bearing capacity of DCM-stabilised foundation; (b) ratio of settlement
Figure 7.4 Comparison of computed vs. calculated results with soft soil stiffness: (a) load-settlement curves; (b) bearing capacity of DCM-stabilised foundation; (c) ratio of settlement
Figure 7.5 Comparison of computed vs. calculated results with varying soft soil cohesion: (a) bearing capacity of DCM-stabilised foundation; (b) ratio of settlement
Figure 7.6 Comparison of computed vs. calculated results with varying A: (a) bearing capacity of DCM-stabilised foundation; (b) ratio of settlement
Figure 7.7 Comparison of computed vs. calculated results with varying n_c : (a) bearing capacity of DCM-stabilised foundation; (b) ratio of settlement
Figure 7.8 Comparison of computed vs. calculated results with varying M : (a) bearing capacity of DCM-stabilised foundation; (b) ratio of settlement
Figure 7.9 Comparison of computed vs. calculated results with varying λ : (a) bearing capacity

of DCM-stabilised foundation; (b) ratio of settlement
Figure 7.10 Comparison of computed vs. calculated results with varying Γ : (a) bearing capacity
of DCM-stabilised foundation; (b) ratio of settlement
Figure 7.11 Comparison of computed vs. calculated results with varying h : (a) bearing capacity
of DCM-stabilised foundation; (b) ratio of settlement
Figure 7.12 Comparison of computed vs. calculated results with varying n_b : (a) bearing capacity of DCM-stabilised foundation; (b) ratio of settlement
Figure 7.13 Comparison of computed vs. calculated results with varying d_0 : (a) bearing capacity of DCM-stabilised foundation; (b) ratio of settlement
Figure 7.14 Comparison of computed vs. calculated results with varying n_d : (a) bearing capacity of DCM-stabilised foundation; (b) ratio of settlement
Figure 7.15 Comparison of computed vs. calculated results with varying p_b : (a) bearing capacity of DCM-stabilised foundation; (b) ratio of settlement
Figure 7.16 Comparison of computed vs. calculated results with varying ε _{ref} : (a) bearing capacity of DCM-stabilised foundation; (b) ratio of settlement
Figure 7.17 Comparison of computed vs. calculated results with varying k : (a) bearing capacity of DCM-stabilised foundation; (b) ratio of settlement
Figure 7.18 Sensitivity analyses of parameters on bearing capacity
Figure 7.19 Sensitivity analyses on ground settlement at: (a) $q = 100 \text{ kPa}$; (b) $q = 200 \text{ kPa}$ 145
Figure 7.20 New design chart for bearing capacity at various UCS values for (a) $\alpha = 0.2$; (b) α
$= 0.3$; (c) $\alpha = 0.4$

CHAPTER 1 Introduction

1.1 Research background

Some coastal countries and regions, such as Shanghai, Hong Kong, Japan, and Singapore, are facing a shortage of available land resources. Land reclamation is a popular method to expand land resources. Deep cement mixing (DCM) is widely used as an environmentally friendly and fast construction method in reclamation projects. Japan first adopted the technique of DCM in the land reclamation project Bruce et al. (1998). DCM has also been adopted by other Asian countries, such as China and Singapore, since the late 1970s (Kitazume and Terashi 2013). Since 2016, this technique has gained increased popularity in Hong Kong. (Wang et al. 2019a). It has been used for ground improvement works in the reclamation projects of Hong Kong, as shown in Figure 1.1, including the Three-runway System (3RS), Integrated Waste Management Facilities (IWMF), and Tung Chung New Town Extension (TCNTE)

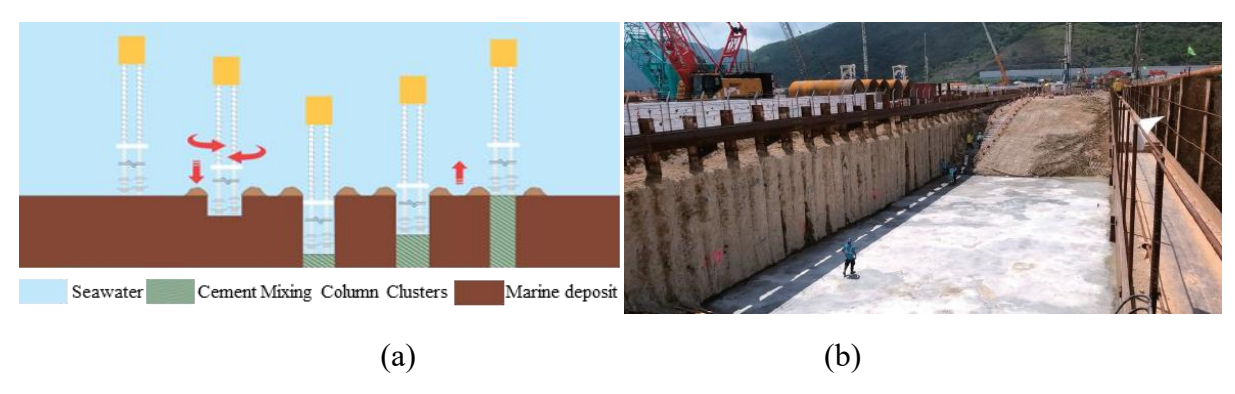


Figure 1.1 (a) Construction of DCM column (https://goo.su/6Hojx) and (b) use of DCM in retaining wall (https://goo.su/CPQLP0)

Cemented soil exhibits stiff and non-linear stress-strain behaviour before reaching its peak strength, followed by a strain-softening behaviour characterised by a reduction in strength. This post-peak strain-softening behaviour should be considered in the design of DCM to prevent sudden or brittle failure when subjected to compressive, tensile, shearing, or bending loading modes. According to the data in existing literature (Bergado and Lorenzo 2005b; Melentijevic et al. 2013a; Voottipruex et al. 2019; Pongsivasathit et al. 2021), the typical strain encountered in DCM-stabilised ground is mainly located within the small strain range, as shown in the Figure 1.2. The stress-strain response of soil is significantly nonlinear, and its stiffness can decrease substantially as strain levels rise (Atkinson 2000). The stiffness in the field could be either higher or lower than that adopted in the design (E_{50}), depending on the strain level in the

field. Comprehending the behaviour of cemented soils at small strains is vital for predicting foundation displacements and assessing performance under working conditions.

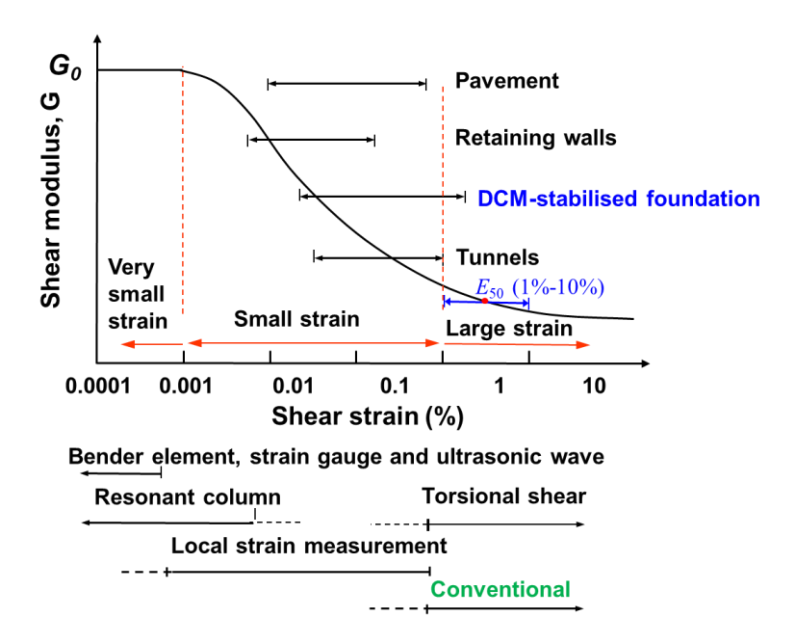


Figure 1.2 Small strain stiffness characteristics of soil (Atkinson and Sallfors, 1991)

Furthermore, DCM columns are subjected to various temperatures and stresses during insite curing. According to the field data from Japan (Van Nguyen et al. 2021) and Norway (Fiskvik Bache et al. 2022), the temperature inside DCM columns can reach 40°C due to cement hydration and last for a month. The length of DCM columns typically exceeds 10 meters, and the effective confining pressure from surrounding soils can vary widely, ranging from 0 to approximately 200-300 kPa. However, most of these studies cured specimens at room temperature (usually 20-25°C) without external loading. Ignoring the distinctions between laboratory and field curing conditions may result in inaccurate parameters and improper designs. Therefore, it is crucial to investigate the impact of curing temperature and stress on the properties of cemented soils. In terms of the experimental study, the effects of curing temperature and curing stress on stiffness within small strains have been studied by only a few studies and have not been fully understood due to limited data. As far as the authors are aware, no research has examined the effects of curing temperature on the stiffness degradation of cemented soil within small strains. Therefore, more research is required to fully understand the influence of curing temperature and stress on the strain-dependent stiffness of cemented clay, particularly at small strains.

Regarding the theoretical study, many constitutive models have been developed for cemented soil based on valuable experimental results. A common feature of these models is incorporating a cementation strength parameter that increases with cement content and decreases with plastic strain. Such a parameter is used to modify different components of a constitutive model, particularly the yield surface. Most of the existing constitutive models were proposed within the classical elastoplastic framework (Horpibulsuk et al. 2010b; Nguyen et al. 2014; Namikawa and Mihira 2007; Hirai et al. 1989) concentrating on the strain-softening and dilatancy properties of cemented soil. However, these models cannot be easily used by engineers since they are too complicated and have many input parameters. Moreover, these models cannot well capture the nonlinear stress-strain behaviour and stiffness degradation in the small strain range since only elastic deformation is predicted when the stress state is inside the yield surface. Several advanced models have recently been developed based on the bounding surface theory (Ravanbakhsh and Hamidi 2013; Xiao et al. 2017; Zhang et al. 2023a). These models improve the prediction of gradual yielding and soil behaviour under cyclic loading. However, the development of these bounding surface models did not pay particular attention to the mechanical behaviour of cemented soil at small strains.

In the application of FEM for DCM engineering design, the selection of constitutive models is a crucial factor influencing the results. Currently, the MC model is the most commonly used model in the simulation of boundary value problems for DCM (Yapage et al. 2014; Jamsawang et al. 2015; Wu et al. 2020). Some researchers (Voottipruex et al. 2019) have also employed the Hardening Soil (HS) model to simulate DCM. The primary issue with using the MC and HS models is that they are insufficient for accurately characterizing the significant strain-softening behaviour of cemented soil, particularly the stress redistribution phenomenon that may occur after strain-softening. Another advanced model is the concrete model (Waichita et al. 2020; Long and Chong 2024; Zhao et al. 2023), which can also be used to simulate the strain-softening behaviour of cemented materials. Complex constitutive models, like the concrete model, often require many parameters. For example, the concrete model has 26 parameters, which limits their practical application. In summary, despite the development of numerous advance models for simulating cemented soil, research on their application in numerical simulations remains constrained.

In the engineering design of a DCM-stablised foundation, current design guidelines generally adopt simplified or empirical methods. In FHWA (2013), the settlement is calculated under equal strain conditions using a linear elastic equation. When evaluating the bearing capacity of the DCM-stablised foundation for the upper structure, only the unconfined compressive strength (UCS) of DCM is considered. The contribution of the soft soil to the overall strength is ignored.

1.2 Research objectives and strategy

The principal objective of this study is to investigate the impact of curing conditions on the properties of cemented marine clay and improve the theoretical modelling of cemented soils. More specifically, it aims to

- (i) investigate the strength and small strain stiffness of cemented soil cured under various temperatures and stresses, reflecting field conditions;
- (ii) develop a constitutive model incorporating the small strain behaviour and strain-softening of cemented soil;
- (iii) develop a numerical code based on the proposed theoretical model; and
- (iv) conduct parametric studies of DCM-stablised ground using the proposed advanced constitutive model to improve design methods in current engineering practice.

To meet these objectives, a new temperature and stress-controlled curing apparatus was developed for specimen preparation. After 28 days of curing, all specimens underwent a series of tests, including unconfined compression tests, undrained triaxial tests, Brazilian splitting tests, and direct tensile tests. Strain gauges, local and global LVDTs were employed to measure small strain stiffness. Microscopic techniques such as Scanning Electron Microscopy (SEM), Thermogravimetric Analysis (TGA), and Mercury Intrusion Porosimetry (MIP) were utilized to investigate the mechanisms of curing temperatures and stresses enhancing the strength and stiffness of cemented soil.

A new constitutive model for cemented soil was proposed within the bounding surface framework to simulate its stress-strain behaviour across both small and large strains. To facilitate model selection based on experimental data and engineering requirements, the model was simplified by reducing the number of parameters. This simplification involved the exclusion of state-dependent behaviour and the elimination of the linkages between soil parameters and cement content, and the changes in elastic modulus due to cementation degradation were also removed. Furthermore, the proposed model was implemented into ABAQUS as a user-defined soil model subroutine for case studies and parametric analysis. Through these studies, bearing capacity design charts were developed for DCM-stabilised foundations. The research strategy is shown in Figure 1.3.

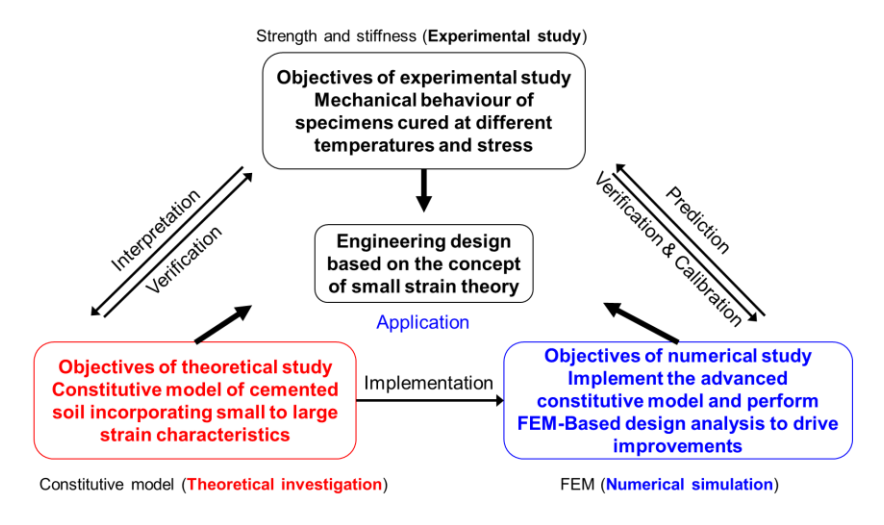


Figure 1.3 Research methodology and strategy

1.3 Thesis organization

The experimental and theoretical results are analysed and presented in this thesis. The outline is as follows:

Chapter 1 provides an overview of the background, scientific challenges, objectives, research content, and thesis layout.

Chapter 2 reviews the literature on the bonding mechanisms of cemented soil, examining its mechanical behaviour in terms of strength, modulus, and strain-softening. It also covers current theoretical models, numerical simulations, and engineering design methods for DCM.

Chapter 3 provides a comprehensive overview of the experimental setup for this study. It includes the testing programme, the properties of the materials used, and the development of a novel temperature and stress-controlled apparatus.

Chapter 4 presents the results of the mechanical tests on cemented soil under different stress paths. The primary focus is on the stress-strain behaviour, particularly the strength and small strain stiffness. Additionally, the mechanisms of curing stress and temperature on the strength and stiffness of cemented marine clay are explained using the results from microstructural tests.

Chapter 5 develops a constitutive model for cemented soils suitable for small and large strains. The model is extended to a general stress space and implemented into a FEM programme. Details about the mathematical formulations, parameter calibration, and model validation are reported.

Chapter 6 introduces the implementation and validation of a modular version of the constitutive model, enabling users to select models based on test data and engineering requirements. The performance and advantages of the proposed model are highlighted by simulating different boundary value problems using the full version model, the basic version

model, and the MC model.

Chapter 7 presents a parametric study of DCM-stabilised foundations. This study aims to improve current design methods in engineering practice by comparing results from FEM using the proposed model with those obtained from design guidelines. The focus is on the load-settlement curves and the bearing capacity of the DCM-stabilised foundation.

Chapter 8 summarises the major conclusions of this study and suggests some future studies in this area.

CHAPTER 2 Literature review

This chapter starts by exploring the mechanisms of cementation, enhancing the strength and stiffness of cemented soil. It then summarizes the test results on the mechanical behaviour of cemented soil materials, focusing on strength and small-strain stiffness. It also reviews the existing theoretical constitutive models for cemented soil. Subsequently, the chapter examines the current numerical simulation methods and the design method for DCM-stabilised ground in engineering practice.

2.1 Mechanism of cementation effects and the microstructure of cemented soil

2.1.1 Mechanism of soil stabilisation using cement

Numerous studies have shown that the process of cementation enhances the ability of treated soft soils to withstand greater stress due to the bonding between soil particles. The behaviour of cemented soil has been extensively studied over the past 30 years (Rios et al. 2014; Abdulla and Kiousis 1997; Nagaraj et al. 1998; Acar and El-Tahir 1986; Ho et al. 2021). The primary mechanism of stabilisation is the chemical hydration reaction of cement-based particles upon contact with water, resulting in cementitious materials that can bond soil particles together (Bullard et al. 2011). Many scholars have investigated the mechanisms of cement hydration. The hydration of cement includes dissolution and precipitation within a complex chemical system, resulting in the creation of different hydrates. For example, the hydration products of Ordinary Portland Cement (OPC) include calcium silicate hydrate (C-S-H) gel, crystalline calcium hydroxide (portlandite, CH), ettringite, and mono-sulphate aluminate hydrate (AFm). The intricate chemical reaction mechanisms involved in the hydration process of cement have been elucidated through research over the past few decades, with detailed information available in Kezdi (2016).

Since cement hydration is critical to cementation, any factor that influences hydration ultimately affects the properties of cemented soil. These factors include cement content, soil type, moisture content, curing conditions, and compaction methods (Moore et al. 1970). Over the past few decades, numerous studies have investigated the mechanisms of these influencing factors and their effects on the mechanical properties of cemented soil. Woo (1971) and Noble and Plaster (1970) believed that the increase in clay content or plasticity index would reduce the bonding effects of Portland cement. According to Subramanian et al. (2020), the ratio of compressional waves to shear waves rises as the clay content increases. Ismail et al. (2002)

found that the type of binder significantly affects the properties of cemented soil. Observations using an electron microscope revealed that different types of binders form distinct cemented structures: gypsum cement creates a loosely bound and brittle sparse matrix of monoclinic crystals; portland cement generates aggregates of hydrated and partially hydrated particles, while calcite cement precipitated from CIPS (calcite in situ precipitation system) solution tends to cover the host particles with granular precipitates.

Furthermore, the results from triaxial tests show that clay treated with Portland cement exhibits ductile yield and greater dilatancy. In contrast, the calcite and gypsum cemented specimens display brittle yield and increased contraction. Water plays a crucial role in soil and cement. On the one hand, water directly participates in the chemical reaction of cement (Liu et al. 2022). However, as the water content increases, the number of internal pores and defects increases (Ho et al. 2018). Many studies have examined the effects of water content on strength (Ribeiro et al. 2016; He et al. 2020a), stiffness (Consoli et al. 2017; Consoli et al. 2012b), and durability (Kenai et al. 2006) of cemented soil. In addition, the studies also show that the cement bonding effect is affected by the soil particle grading curve. Reddy and Gupta (2008) proved through experiments that the finer the sand, the lower the UCS of cemented sand. The optimum clay content for maximum strength of cemented red loamy soil is in the range of 14-16% (Venkatarama Reddy et al. 2007).

Curing conditions, such as curing temperature, stress, and environmental pH also affect the strength and modulus of cemented soil. The increase in curing temperature can accelerate the rate of cement hydration reactions (Fang and Fall 2018) and promote pozzolanic reactions (Zhang et al. 2014), producing more hydration products with enhanced strength and modulus (C-S-H and C-A-H). Some studies (Cui and Fall 2016; Chen et al. 2021) pointed out that curing stress can facilitate cement hydration reactions. They explained that the increased curing stress squeezes out more free water in the specimen, allowing more contact between cement particles and facilitating the cement hydration reaction.

In summary, the mechanical properties of cemented soil are influenced by various factors. Given the complexity of field conditions and the variability in the working conditions of cemented soil, including moisture content during curing, temperature conditions, and stress state, simulating the field curing conditions of cemented soil specimens is crucial for accurately assessing the performance of DCM in engineering design.

2.1.2 Micro-structure of cemented soil

The mechanical behaviour of granular materials is primarily determined by their structure

and the effective stress applied (Mitchell and Soga 2005). The term 'structure' refers to the combination of particle arrangement, known as 'fabric,' and the bonds between particles (Burland 1990). The cementation strength of cemented clay significantly affects its mechanical properties. Therefore, employing microstructural analysis techniques to investigate the structure of cemented clay is crucial for understanding and effectively utilising cemented soil in engineering applications. The commonly used microstructural analysis techniques for cemented soil include SEM, MIP, and TGA.

SEM is an effective tool for studying the microstructure of cemented soil. It is primarily used to identify cement hydration products and the bonding structures between particles. SEM has been widely utilised in recent years. Lemaire et al. (2013) compared the SEM result of untreated and cemented silt, observing that the latter agglomerate to form a thin film covering larger quartz grains, resulting in an aggregate. The surface of the cemented silt specimens exhibited a gel layer, which enhances mechanical properties. Ismail et al. (2002) examined the microstructural differences associated with varying binders, with SEM images shown in Figure 2.1. In specimens cemented with calcite, distinct cavity-like voids were present within the particles, enhancing the crushability of calcareous grains. Specimens cemented with gypsum produced long crystals with a high aspect ratio, featuring inclined ends that gradually align with the surfaces of the host particles. This characteristic may influence the bonding mechanism between the cement and soil particles, thereby affecting the overall strength of the matrix. In specimens cemented with Portland cement, the formation of semi-circular granular clumps occurred due to the accumulation of certain cement particles. The outer portions of these particles began to hydrate first, creating a partial barrier that delayed internal hydration as they hardened. In both studies by Nguyen et al. (2017) and Kamruzzaman et al. (2009), SEM tests were conducted on cemented clay both before and after shearing. The SEM image of the specimen after 28 days of curing is shown in Figure 2.2. As illustrated in Figure 2.2a, cement hydration products with acicular and network structures can be clearly observed. These cementation structures enhance the strength of the soil skeleton. Figure 2.2b shows the SEM image of soil in the shear band after undergoing undrained triaxial shearing. From the image, it is evident that the structure of the hydration product is destroyed after shearing. Therefore, accurately describing the destruction of the cementation structure is crucial for predicting the strain-softening behaviour of cemented soil. Further applications of SEM in studying the microstructure of cemented soils can be found in the following literature (Schnaid et al. 2001; DeJong et al. 2006; Chew et al. 2004; Sun et al. 2023b; Sun et al. 2024).

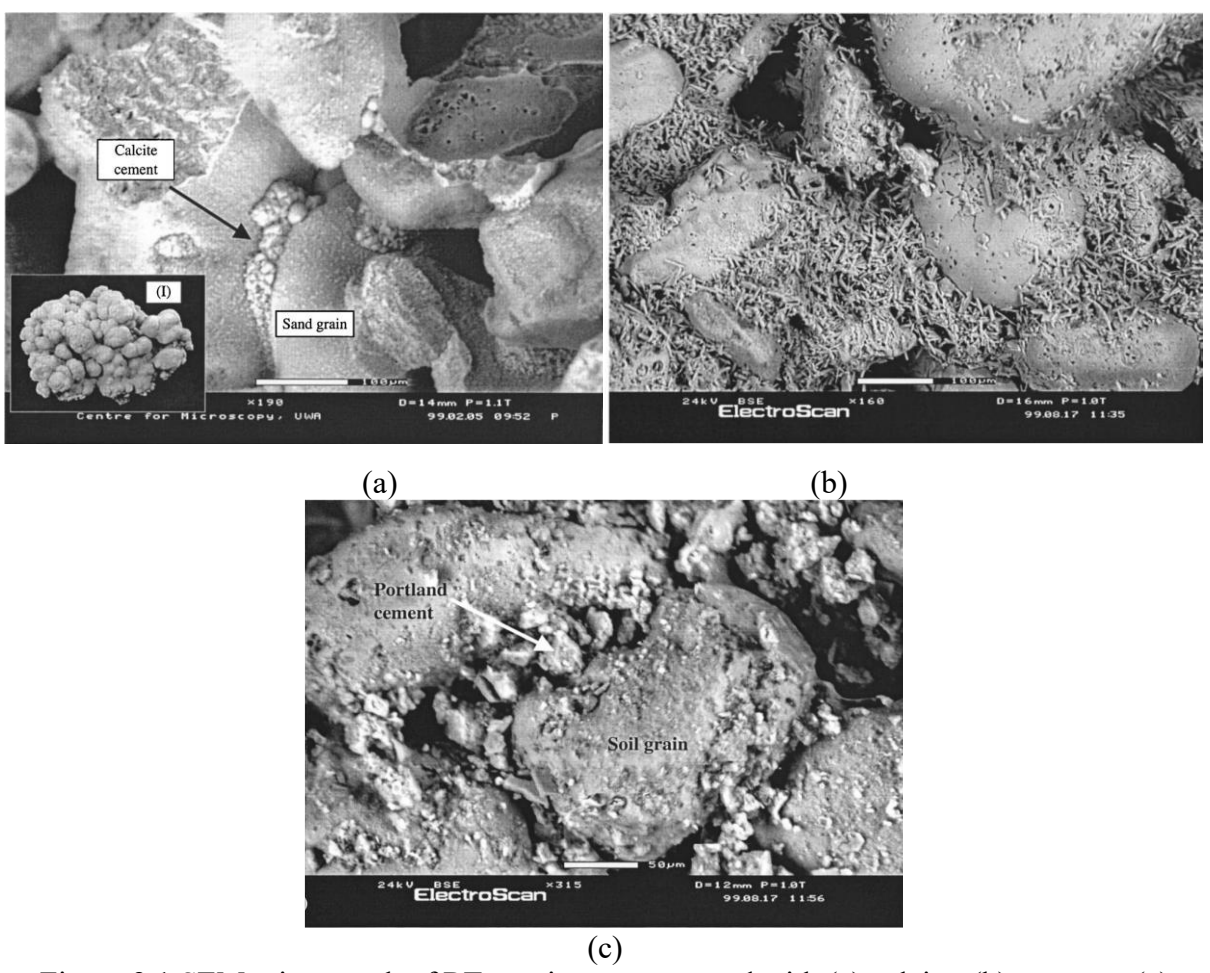


Figure 2.1 SEM micrograph of RT specimens cemented with (a) calcite; (b) gypsum; (c)

Portland cement (Ismail et al. 2002)

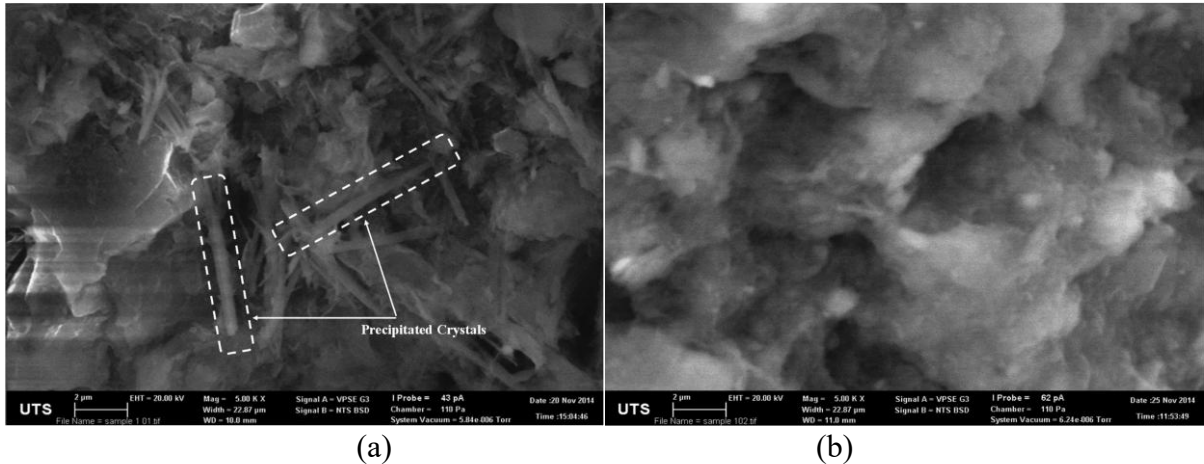


Figure 2.2 SEM images of cemented Ballina clay (a) before; and (b) after shearing (Nguyen et al. 2017)

The pore structure characteristics of the soil are closely related to the strength (Liu et al. 2023), water seepage with soil (Rao et al. 2023; Guo and Cui 2020), and compressibility (Jia et al. 2020; Delage 2010) of the soil. The pore size distribution (PSD) measured through MIP

is often used as evidence to help interpret soil behaviour (Simms and Yanful 2004). For example, Russell (2011) found that the pore size distribution affects the slope and position of the soil compression curve. Juang and Holtz (1986) proposed a probabilistic model that relates soil permeability to the pore size density function. This model highly confidently predicted the direct permeability measurements obtained in this study. Li and Zhang (2009) conducted a comprehensive study on the effects of compaction, saturation, and drying processes on the microporous structure of sandy lean clay. The MIP results indicated that the applied compressive stress during compaction significantly reduced the pore volume between aggregates while having minimal impact on the pores within the aggregates. During the closed saturation process, the soil aggregates expanded, resulting in an increase in both the size and number of internal pores. In contrast, the inter-aggregate pores decreased in size and number. In the drying process, the soil specimens contracted to a lower void ratio, reducing the radius of the internal pores within the aggregates.

Most MIP tests conducted on cementitious materials primarily aim to identify the microstructural evolution during the hardening process, ultimately linking this evolution to mechanical strength (Ouellet et al. 2007). Ouellet et al. (2007) investigated the effects of different binders and water with varying ionic compositions on the UCS of cemented clay. MIP analysis indicated that specimens using slag-based binders and water with high sulphate content exhibited the highest percentage of micropores. This phenomenon may be related to the precipitation of sulphates within the pores, significantly enhancing the strength. Wang et al. (2018) explored how coal-measure kaolinite (CMK) influences the compressive strength and permeability of cemented silty soil. The introduction of CMK led to a notable decrease in parameters such as porosity and average pore size when compared to specimens without CMK (CMK0). This effect is attributed to both physical and chemical changes in the CMK-modified cement soil. Firstly, CMK acts as a physical filler; with an average particle size of just 1.52 mm, it occupies larger pores, resulting in denser cement soil. Secondly, a pozzolanic reaction occurs between CMK and calcium hydroxide (CH), which reduces CH and generates additional C-S-H. Raja and Thyagaraj (2021) studied the optimal delay time for the best compaction performance of cemented soil. The experimental results showed that compaction delay resulted in clogging and reduced strength in SRC-stabilised expansive soil due to the formation of clogging and particle aggregation during the compaction time delay. The clogged and aggregated particles resist compressive forces, leading to a decrease in the dry density of the compacted soil. MIP analysis also confirmed that the addition of sulphates increased porosity, leading to the deterioration of SRC-stabilised soil, thereby reducing strength and compaction

density.

TGA is often used to quantitatively assess the various hydration components in cementbased materials. TGA allows researchers to accurately determine the degree of cement hydration based on the amount of hydration products. Li et al. (2022) compared OPC-cemented clay with CS-GGBS-cemented clay. The results showed that the strength of OPC paste exceeds that of CS-GGBS paste. OPC hydrates significantly faster than CS-GGBS, consuming more water and resulting in a much lower paste porosity. For stabilised clay slurry with very low binder content (60 and 80 kg/m³), the heat of hydration generated by OPC or CS-GGBS reactions is very similar; therefore, the effects of binder hydration rate on porosity are negligible. Cai et al. (2024) studied the chemical activation of ground granulated blast furnace slag (GGBS) with calcium oxide (CaO) as a low-carbon binder. The experimental results showed a significant increase in weight loss after 28 days when the binder content exceeded 5%. Wu et al. (2022) investigated the quantity of cement hydration products in kaolin and bentonite specimens treated with cement. TGA results showed that the CH content in stabilised bentonite was significantly higher than in stabilised kaolin specimens, indicating that the secondary pozzolanic reaction in stabilised bentonite mixtures is weaker than in stabilised kaolin mixtures. Wu et al. (2016) observed that the peaks of several hydrates (e.g., CSH, CAH, and ettringite) in metakaolin-modified soils were relatively high and broad, attributed to the enhanced cement hydration and the reaction between metakaolin and hydrated CH.

In summary, the mechanical behaviour of cemented soil, including its strength and modulus, is primarily influenced by its microstructure, which encompasses particle bonding and pore structure. Techniques such as SEM, MIP, and TGA offer researchers powerful tools for thoroughly evaluating cement bonding in these materials.

2.2 Mechanical behaviour of cemented soil

In recent decades, there has been growing interest in exploring techniques to artificially enhance the mechanical properties of soil to meet the increasing performance requirements for geotechnical structures. The stiffness and strength of DCM are the parameters of greatest concern to engineers and are used in the design codes. This section presents a review of the research conducted over the past few decades on the mechanical behaviour of cemented soil.

2.2.1 Strength

The UCS of cemented soil has garnered significant attention, as it is a commonly used parameter in engineering design. Numerous factors influence the UCS of cemented soil.

Jaritngam et al. (2008) have systematically categorized these factors into four principal groups, including (1) Characteristics of hardening agent and (2) soil, (3) mixing, and (4) curing conditions. One primary group of factors encompasses the inherent properties of the soil, such as the distribution of particle sizes, the amount of moisture present, and the content of organic matter. For instance, Xu et al. (2021) investigated the impact of particle size distribution curves on the UCS of cemented soil, finding that an increase in fine particle content leads to a decrease in UCS. Beckett and Ciancio (2014) reported that lower compaction moisture content can result in higher material strength. Laboratory test results from Du et al. (2021) indicate that the UCS of clay decreases by approximately 20% when the organic content increases from 0% to 5%. Studies by Tremblay et al. (2002) and Onitsuka et al. (2003) emphasize that organic acids are the primary factors reducing the cementation effect by inhibiting the pozzolanic reaction. Factors affecting the UCS of cemented soil, including moisture content, the type of binder, and the amount of binder used, have been extensively studied, as seen in the works of (Moreira et al. 2019; Nguyen et al. 2020; Beckett and Ciancio 2014). Water is a key parameter that affects the cement hydration process. Insufficient water can lead to incomplete cement hydration, while excessive moisture content can increase internal pores and inherent defects. Additionally, the cement content affects the number of cementation bonds. Consoli et al. (2010, 2013) investigated the variations in UCS of cemented soil under different porosities and cement contents. The experimental results indicated that the UCS increases with a decrease in porosity and an increase in cement content. They concluded that the ratio of porosity to cement content can be used as a control parameter to calculate the unconfined compressive strength of cemented soil materials. Diambra et al. (2017) also proposed a formula for calculating the unconfined compressive strength of cemented soil using the ratio of porosity to cement content (η/Cc) as the control parameter.

Curing conditions significantly influence the strength of cemented soil. Firstly, the strength of cemented soil increases with the curing period, which is closely related to the degree of cement hydration. However, the rate of strength development decreases over time (Gu et al. 2021). The stress level during curing also affects the strength of cemented soil (Dalla Rosa et al. 2008; He et al. 2020b; Zhao et al. 2021), as curing stress can lead to the rearrangement of soil particles, particularly in the early stages, resulting in higher density and increased contact area between solid particles (Cui and Fall 2016). An increase in curing temperature affects the strength of cemented soil as well. Zhang et al. (2014) found that higher curing temperatures enhance the strength of cemented soil by accelerating both cement hydration and the pozzolanic reaction, thereby increasing both short-term and long-term strength. Similar findings were

reported by Bi and Chian (2021).

In practical engineering applications, DCM columns work under complex stress paths. For instance, the depth of DCM typically ranges from 10 to 30 meters, with effective stress reaching 200 to 300 kPa. Additionally, tensile forces are frequently encountered, especially during DCM-supported excavation problems. Therefore, focusing on the strength of cemented soil at different stress paths, like the triaxial and tensile tests, is more representative of the behaviour of cemented soil in working conditions.

To date, the cemented soil behaviour under different stress paths has been investigated by numerous studies. Consoli et al. (2000) explored the triaxial drained shear strength under different curing stresses. The results showed a significant increase in strength with increasing curing stress. However, the cementation structure may be damaged if the confining pressure is too high. Schnaid et al. (2001) conducted drained triaxial shear tests on cemented soils with low cement content (0, 1, 3, 5%). The results showed that the increase in cement content and confining pressure significantly improved the peak strength of the cemented soil. Similar conclusions were reported in the study by Marri et al. (2012). Rios et al. (2014) compared cemented and uncemented decomposed granite, focusing on the strength at critical state under different void ratios and cement contents. The results showed that the critical state line for both cemented and uncemented soils was consistent and not affected by the cement content and density of the specimens. In contrast, other studies (Haeri and Hamidi 2009; Wang and Leung 2008; Shen et al. 2016) found that both the peak state and critical state parameters were affected by the cement content, as shown in Figure 2.3 and Figure 2.4. The increase in the critical state stress ratio and dilation trend is likely due to cementing particles remaining attached to soil particles or clusters at the critical state. This attachment increases the roughness of particle or cluster surfaces, resulting in different particle packing modes (Wang and Leung, 2008).

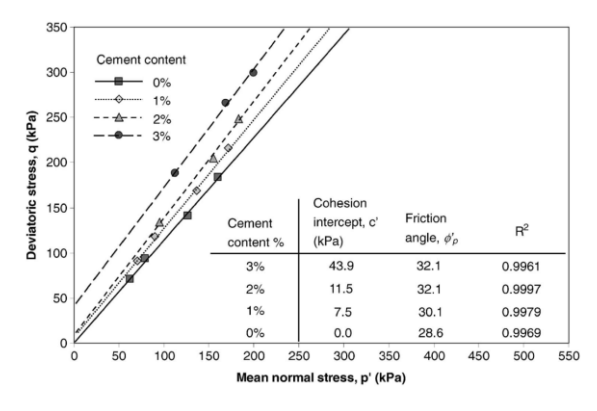


Figure 2.3 Critical state line of cemented sand (Wang and Leung 2008)

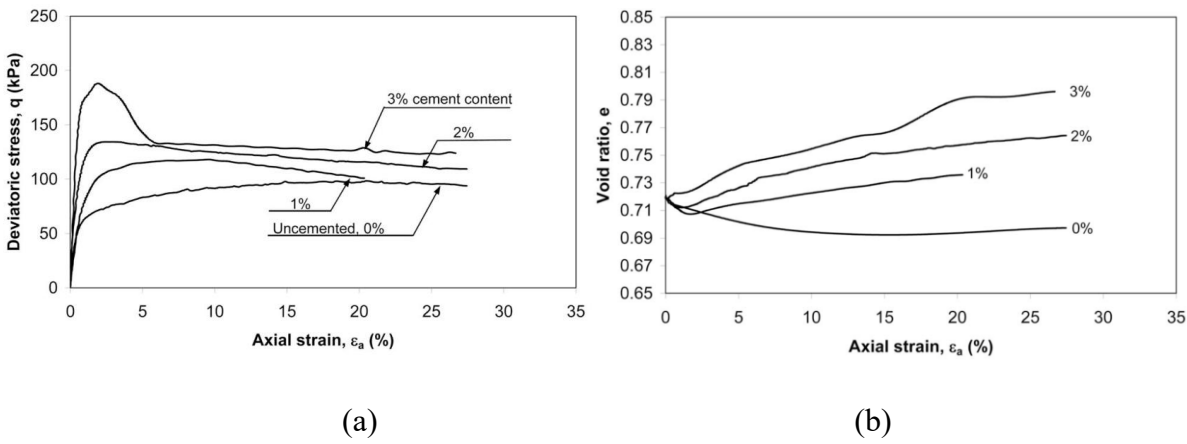


Figure 2.4 Stress-strain and volumetric curves of cemented soil in triaxial tests for various cement contents (Wang and Leung 2008)

In undrained triaxial shear tests, the conclusions regarding the effects of cement content were consistent. As the cement content increased, the peak strength increased, primarily due to the influence of cementation strength (Ho et al. 2021; Al-Zoubi 2008). However, the conclusions regarding the effects of confining pressure on undrained triaxial shear strength are inconsistent. In the experiments conducted by Kasama et al. (2006) and Ho et al. (2021), peak strength increases by approximately 40% with an increase in confining pressure of 300 kPa. However, other studies, such as Horpibulsuk et al. (2004), found the effects of confining pressure on peak strength insignificant. They explained that cementation was the primary factor determining the strength of the cemented soil. Li and Kwok (2024) conducted a series of triaxial shear tests, both consolidated undrained and drained, on field-cored DCM samples that had a high cement content. The main findings are summarised as follows: The failure envelope is nonlinear regarding peak strength. The test results of field samples showed significant dispersion. Additionally, a CT scanning system was used to visualize the internal structure of the DCM specimen, helping to explain the differences between samples. CT scan images confirmed that this was due to clay pockets within the DCM samples caused by uneven mixing, which significantly affected their stress-strain behaviour.

Several studies have also examined the isotropic compression properties of cemented soil. Rotta et al. (2003) noted that the yield stress of cemented soil during isotropic compression depends on both the void ratio and the amount of cement present. As the curing void ratio decreases, the influence of cementation on soil behavior under isotropic compression diminishes. Rios et al. (2012) also noted that for cemented soil specimens with a given dosage, the porosity/cementation index is a parameter affecting the Normal Consolidation Line (NCL). Unlike untreated clay, cemented soil has no unique NCL because the cementation structure

persists even under high stress. However, the NCLs of specimens with different porosity/cementation indices are parallel to each other. Arroyo et al. (2013) explored the coupled effects of suction and cementation on the hardening of soil under isotropic compression tests. The results showed that the effects of cementation and drying do not seem to be mutually reinforcing. Marri et al. (2012) conducted SEM tests and found that the cementation structure is not easily damaged with increasing isotropic consolidation pressure. The majority of sand particle breakage appeared to happen during shear. Consoli et al. (2000) presented data indicating that the cementation structure was compromised as confining pressure increased. This was evidenced by a decrease in the modulus of the specimens following the application of confining pressure.

Consoli et al. (2009) highlighted that system failure mechanisms triggered by tensile stress are common issues for cement-treated soil in engineering. Therefore, determining the tensile strength of cemented soil is crucial, and it has been widely investigated. Common methods for testing tensile strength include direct tensile tests, splitting tensile tests, and bending tests. Namikawa and Koseki (2007) emphasised that the strength obtained from direct tensile tests is the most representative. This is because the tensile stress distribution is linear in the split and bending tests, and the stress redistribution during deformation is ignored. Wong et al. (2022) conducted direct and indirect tensile tests on cemented kaolin and found that the direct and indirect tensile strengths are comparable. Tang et al. (2023) pointed out that direct tensile tests are much more complex than splitting and bending tests because they are highly susceptible to setting errors. Numerous studies have tried to establish correlations between direct and indirect tensile tests to UCS. For example, studies (Wang and Huston 1972; Shien et al. 2019; Consoli et al. 2015; Consoli et al. 2011) pointed out that direct tensile strength is between 10% and 20% of UCS.

In summary, existing studies have rarely investigated the effects of curing temperature and curing stress on the unconfined compressive strength (UCS) of cemented clay when specimens are cured underwater, even though this is crucial for selecting design parameters in engineering. Moreover, understanding the soil behaviour of cemented soil under various stress paths is essential for engineering design practice. For example, it remains unclear whether changes in curing conditions affect the constitutive models and soil parameters of cemented soils, which must be evaluated through comprehensive testing under different stress paths. However, there is still limited research on how curing conditions influence the strength of cemented soil under various stress paths, such as the undrained triaxial shear test.

2.2.2 Strain-softening behaviour

The cemented soil exhibits significant strain-softening behaviour, as shown in Figure 2.4. This has been observed in many experimental studies (Lo et al. 2003; Montoya and DeJong 2015; Dalla Rosa et al. 2008; Horpibulsuk et al. 2010a; Wang and Leung 2008). A strain-softening behaviour accompanying the strain localisation phenomenon is observed during shearing, as pointed out by Lo and Lee (1973) and Yerro et al. (2016). The softening of DCM columns in engineering can result in stress redistribution and underestimating the settlement in geostructures. Therefore, it is crucial to fully understand and accurately capture the strain-softening behaviour of cemented soil to ensure the safety and optimal performance of geostructures.

Unlike the softening phenomenon observed in sandy soil and over-consolidated clay, which is attributed to dilatation, the softening of cemented soil is due to the breakage of cementation bonds (Namikawa and Koseki 2006). It is generally believed that the destruction of the cemented structure is related to the accumulation of volumetric and shear strains. In the study by Nguyen et al. (2017), SEM images revealed a well-cemented structure in intact cemented specimens, whereas significant damage to the cemented structure was observed in the triaxial shear zone. However, the structure outside the shear zone remained relatively intact. Additionally, Kamruzzaman et al. (2009) conducted SEM tests on specimens subjected to oedometer consolidation and consolidated undrained triaxial shear tests, finding that increased consolidation stress led to the destruction of cementation between aggregates. As confining pressure increased, the cemented structure was damaged, but the increase in isotropic stress did not lead to the complete destruction of the cemented structure. They also noted that only through shearing could the cemented structure be destroyed.

Additionally, scholars have conducted extensive theoretical work to account for the strain-softening characteristics of cemented soil. To simulate strain-softening, a commonly used approach is to relate the cementation parameter to plastic strain (Doherty and Wood, 2020; Nguyen et al., 2014; Ravanbakhsh and Hamidi, 2013). For example, based on the Mohr-Coulomb model, Yapage et al. (2015) defined cohesion as a parameter that varies with plastic deviatoric strain, as illustrated in Figure 2.5. Implementing this model in ABAQUS and comparing the results with experimental data has proven effective in capturing strain-softening behavior. The advantages of this method are its simplicity, ease of understanding, and the requirement for only a few parameters.

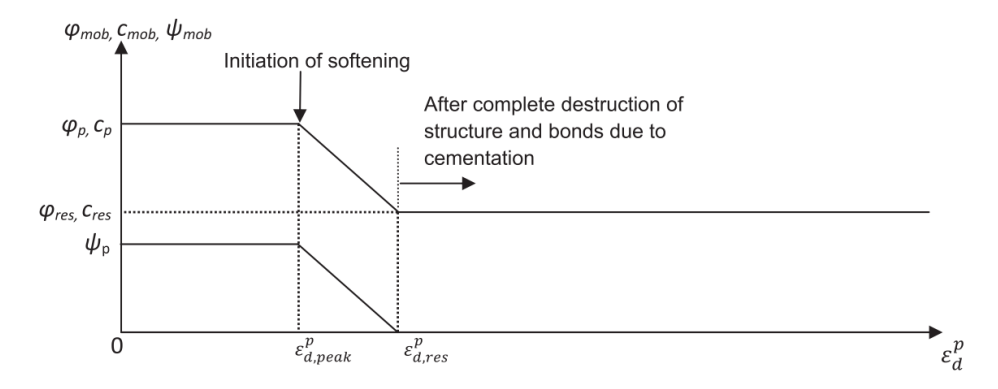


Figure 2.5 Variation of strength parameters with plastic shear strain (Yapage et al. 2015)

Based on the Cam-Clay model, Lee et al. (2004) hypothesized that the cementation effects of cemented soil generate an elliptical cementation yield surface and defined the cementation strength as a function of cumulative plastic volumetric strain and shear strain. Similarly, a parameter (p_b) was defined for the cementation strength (Doherty and Wood 2020; Nguyen et al. 2014). The degradation of cementation is defined as a function of damage strain (ε_d), as described by equation (2-1).

$$\varepsilon_d = \sqrt{\varepsilon_s^{p^2} + \varepsilon_v^{p^2}} \tag{2-1}$$

where ε_s^p = plastic shear strain; and ε_v^p = plastic volumetric strain, respectively. Namikawa and Mihira (2007) established a constitutive model based on the tensile and shear failure criteria. In their model, strain-softening during tensile and shear is focused on (Zheng et al. 2019). A detailed discussion of these constitutive models is given later.

2.2.3 Stiffness

The stress-strain response of soil is significantly nonlinear, and its stiffness can decrease substantially as strain levels rise (Atkinson 2000). To accurately predict ground movements that may affect adjacent buildings or underground infrastructure, it is crucial to have a thorough understanding of stiffness parameters under small strain conditions (Clayton 2011). To characterise the stiffness degradation process, the entire curve is divided into three parts based on the strain range: very small strain range (< 0.001%), small strain range (0.001% - 1%), and large strain range (> 1%). Numerous studies have been conducted on the stiffness of cemented soil within these three strain ranges, which will be discussed in the following sections.

2.2.3.1 Very Small strain stiffness of cemented soil

The maximum shear modulus within the very small strain range is crucial for modelling the modulus degradation curve. It is generally believed that within this very small strain range, the soil modulus does not decrease, exhibiting purely elastic behaviour. Hardin and Black (1968) initially used a functional relation expression for uncemented soil to consider the soils vibration shear modulus in general.

$$G = f(\bar{\sigma}_0, e, H, S, \tau_0, C, A, F, T, \theta, K) \tag{2-2}$$

where σ_0 = effective stress; e = void ratio; H = stress history; S = degree of saturation; τ_0 = deviatoric component; C = grain characteristics; A = amplitude of vibration; F = frequency of vibration; T = time; θ = soil structure; K = temperature. The importance of these parameters was examined in follow-up studies (Hardin and Drnevich 1972; Seed 1970). Among these parameters, the σ_0 and e are the most important parameters for maximum shear modulus calculation. So later, many researchers (Acar and Eltahir 1986; Hardin and Drnevich 1972; Viggiani and Atkinson 1995) proposed empirical equations for predicting G_{max} , which mainly considered the effects of void ratio and effective mean stress. For example, the following equation was proposed by Acar and Eltahir (1986).

$$G_{max} = \frac{S}{f(e)} (p_a)^{1-n} \sigma_0^{\ n}$$
 (2-3)

where S = stiffness coefficient; f(e) = a function reflecting the effects of the void ratio; $\sigma_0 =$ mean effective stress; $p_a =$ atmospheric pressure; and n = constant. Acar and Eltahir (1986) used the following functional form f(e) to consider the effects of the void ratio.

$$f(e) = 0.3 + 0.7e^2 (2-4)$$

The authors found that the value of n is mainly concentrated between 0.4-0.45 based on the verification of numerous experimental results.

For cemented soils, numerous studies (Bahador and Pak 2012; Consoli et al. 2012a; Khan et al. 2019; Saxena et al. 1988) have demonstrated that bonding between soil particles, known as the cementation effect, can significantly enhance the maximum shear modulus of cemented soils. Test results by Baig et al. (1997) indicated that cement content significantly impacts the modulus of cemented soil, with the elastic modulus increasing as cement content rises. In contrast, the effects of confining pressure on the modulus are minimal, especially as cement content increases, making the influence of confining pressure negligible. Similar conclusions have also been reported in this study of Trhlíková et al. (2012), as shown in Figure 2.6. According to research by Yao et al. (2019), the maximum shear modulus decreases with an increase in total water content. This is because higher total water content makes the cemented clay more porous after curing, leading to a reduction in stiffness.

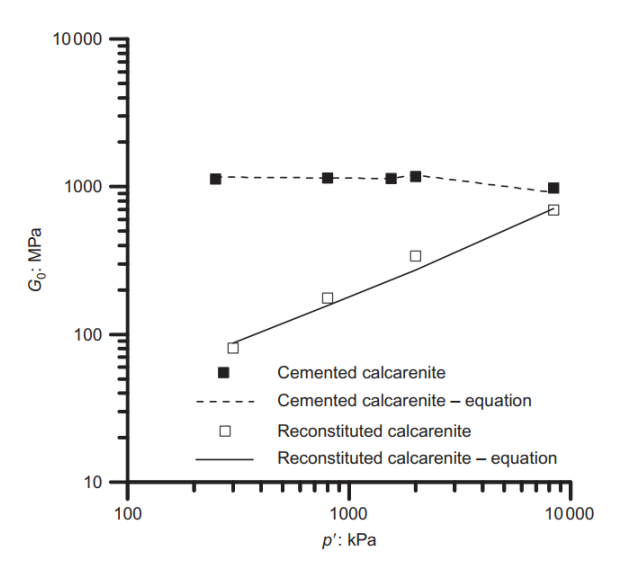


Figure 2.6 Elastic shear modulus against mean effective stress (Trhlíková et al. 2012)

To calculate the maximum shear modulus of cemented soil, researchers introduce an item to consider the cementation effect. Based on this Hertzian contact theory, as shown in Figure 2.7, Fernandez and Santamarina (2001) proposed an equation for calculating shear modulus considering the effects of curing stress. For the condition of loading before cementation

$$\frac{E_T}{G_m} = \frac{1}{1 - \nu_m} \sqrt{(Cc + 1)^{\frac{2}{3}} - 1 + \left[\left(\frac{3(1 - \nu_m)}{2} \right) \frac{\sigma^{\frac{2}{3}}}{G_m} \right]^2}$$
 (2-5)

where v_m = Poisson's ratio, and G_m = the shear modulus of the material, Cc = cement content, σ = the applied external stress.

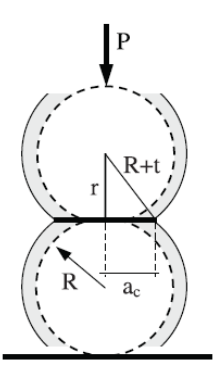


Figure 2.7 Load applied to the cemented particles enlarges the contact area (Fernandez and Santamarina 2001)

Acar and Eltahir (1986) introduced a stiffness coefficient S to account for this cementation effect.

$$G_{max} = R \frac{s}{f(e)} (p_a)^{1-n} \sigma_0^{\ n}$$
 (2-6)

where R = stiffness ratio (Sc/S); Sc and S = stiffness coefficient for cemented and uncemented

specimens, respectively. The variation of stiffness ratio is best expressed with the following equation (2-7).

$$R = 1 + C^{0.49} - 2.0C^{0.1}e^{4.6} (2-7)$$

where C = the degree of cementation; and e = void ratio. Salvati and Pestana (2006) directly use cement content as a variable to calculate this maximum shear modulus.

$$\frac{G_{max}}{p_{at}} = G_b e^{-1.3} \left(\frac{p}{p_{at}} + a_{cc} C c^2 \right)^n$$
 (2-8)

where G_b = constant; Cc = pertange of cement by weight; and a_{cc} = constant to describe the cementing agent and process. It is very convenient in engineering design to directly use the cement content as a variable to calculate the shear modulus.

Trhlíková et al. (2012) combined the isotropic compression curve and the critical state line of cemented soil. They introduced a structural parameter *s* to calculate the shear modulus of cemented soil based on the calculation of the shear modulus of the reconstituted soil.

$$\frac{G_{max}}{p_r} = G_b \left(\frac{p'}{p_{at}}\right)^n \left(\frac{p'_e}{p'}\right)^m \left(\frac{s}{s_f}\right)^l \tag{2-9}$$

where p_{at} = the reference pressure (1 kPa); and p'_e = the yield stress; p' = mean effective stress; l, n and m = dimensionless soil parameters; s = a parameter characterizing soil structure. s is calculated by the following equation.

$$s = \frac{p_e'}{p_e^*} \tag{2-10}$$

$$p'_e = exp\left[\frac{N-\ln{(1+e)}}{\lambda^*}\right]$$
 (2-11)

where p_e^* = the Hvorslev equivalent pressure for the reconstituted soil. When the structure is destroyed, s=s=1.

Zhang et al. (2023a) modified the formula of Richart et al. (1970) to use the bonding strength p_b as a parameter to calculate the maximum shear modulus.

$$G = G_0 exp \left(\sqrt{\frac{p_b}{p' + p_b}} \right) \frac{(2.97 - e)^2}{1 + e} (p' p_a)^{0.5}$$
 (2-12)

where G_0 = a non-negative model constant; p' = mean effective stress; p_a = Atmospheric pressure equal to 101 kPa. Cemented soil can bear certain tensile stress due to the existence of bonding between soil particles. Considering this, there is a common shortcoming in the existing equations for calculating the maximum shear modulus at very small strains. The existing formulas may be miscalculated when the p' value becomes negative.

2.2.3.2 Small strain stiffness of cemented soil

According to data in existing literature, typical strain ranges encountered in DCM columuns (Bergado and Lorenzo 2005a; Liu et al. 2015; Liu et al. 2012; Melentijevic et al. 2013b; Pongsivasathit et al. 2021; Voottipruex et al. 2019) are mainly within the small strain range, as summarized in Table 2.1. Comprehending the behavior of cemented soils at minor strain levels is vital for predicting foundation displacements and assessing performance under working conditions. Previous studies have shown that geotechnical materials exhibit highly non-linear behaviour, with modulus significantly decreasing as strain increases. Cemented soil materials exhibit similar behaviour in the small strain range. Acar and El-Tahir (1986) determined the small strain stiffness of cemented soil using resonant column and CU tests on cemented sand. They found that increased cementation strength leads to a higher degradation rate of modulus with increasing strain. Sargent et al. (2020) compared the modulus degradation behaviour of the Lanton alluvial layer before and after cement treatment. The elastic limit strain of the original clay was approximately 0.01%, but after cementation, the elastic limit strain increased to about 1%. This finding is inconsistent with the earlier conclusions of Acar and El-Tahir (1986). Subramaniam and Banerjee (2020) compared the shear modulus of cemented specimens with different cement contents under effective confining pressures of 100-300 kPa. The normalized modulus degradation curves show that as confining pressure increases, the rate of stiffness degradation with strain decreases. Yang and Woods (2015) conducted resonant column tests on cemented sand with varying cement and water contents, finding that porosity is a crucial parameter affecting cemented sand. The shear modulus of cemented clay with higher porosity decreases more slowly compared to that with lower porosity.

Table 2.1 Strain range of DCM columns in the literature

Reference	Infrastructure	Length	Maximum	Maximum
		(m)	displacement (m)	Strain
Voottipruex et al. (2019)	Retaining wall	8	0.025	0.30%
Bergado and Lorenzo	DCM column	9m	0.163	1.80%
(2005)				
Pongsivasathit et al. (2021)	DCM wall	16.5	0.081	0.50%
Yamashita et al. (2011)	DCM column	29	0.02	0.07%
Liu et al. (2012)	DCM column	16.5	0.24	1.40%
Navin (2005)	DCM column	12.192	0.09652	0.80%
Melentijevic et al. (2013)	DCM column	8	0.12	1.50%
Liu et al. (2015)	DCM column	28	0.175	0.63%

Several simple empirical formulas have been proposed to describe the small strain modulus

degradation curves of cemented soil (Marques et al. 2021; Yao et al. 2018; Vardanega and Bolton 2013). For instance, Vardanega and Bolton (2013) proposed a model to describe the shear modulus degradation of clay by summarising a large amount of data, as shown in Figure 2.8.

$$\frac{G}{G_{max}} = \frac{1}{1 + \left(\frac{\gamma}{\gamma_{ref}}\right)^{\alpha}} \tag{2-13}$$

where G_{max} = maximum shear modulus; G = shear modulus; γ = shear strain; γ_{ref} = reference strain, which is related to the plasticity index. Although the equation was used based on a large dataset of clay and silt, it is also referenced for the modulus degradation of cemented soil. For example, Marques et al. (2021) used a similar form to equation (2-13) for cemented sand.

$$\frac{G}{G_{max}} = \frac{1}{1 + a \left(\frac{\gamma}{\gamma_{ref}}\right)^b} \tag{2-14}$$

where a and b = model parameters by fitting the curve. These two parameters are incorporated to improve the simulation of stiffness degradation in cemented soil.

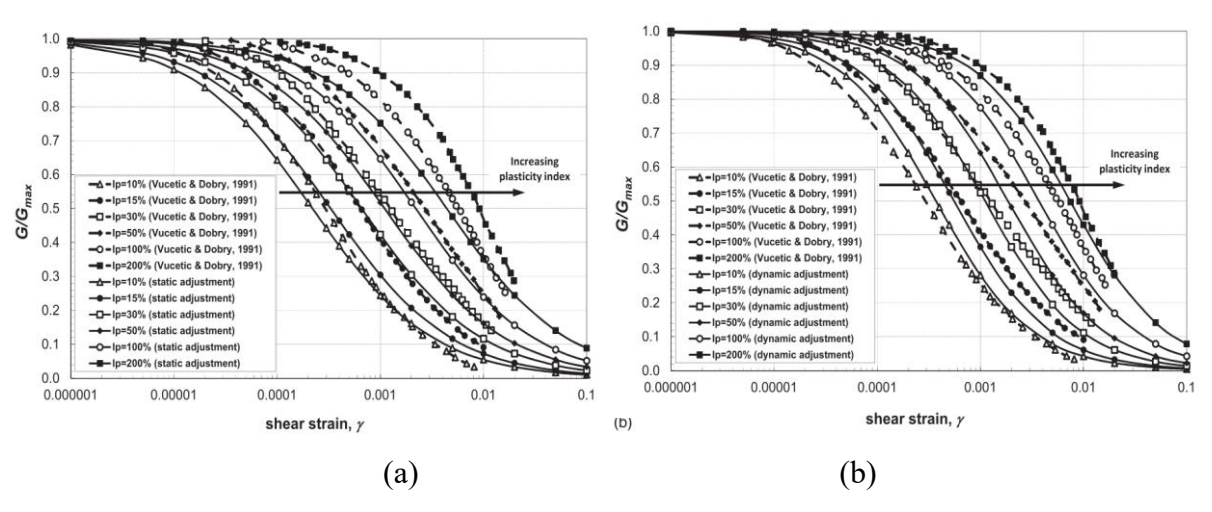


Figure 2.8 New design charts for stiffness degradation of clays and silts: (a) static applications; (b) dynamic applications (Vardanega and Bolton 2013)

2.2.3.3 Stiffness parameter of cemented soil used in engineering design

Accurate measurement of small strain stiffness typically requires precise instrumentation, making it complex to measure in conventional experiments. Such measurements necessitate specialised testing equipment or precise local strain measurements, undoubtedly increasing the complexity of engineering design. In current engineering practice, the commonly used modulus parameter is E_{50} , corresponding to the secant Young's modulus at the stress point of 50% of the UCS. The influence of E_{50} has been extensively studied in uncemented soils. Maeda and Miura (1999) indicated that E_{50} decreases with increasing confining pressure. Mallawarachchi et al.

(2014) conducted triaxial shear tests on undisturbed soil specimens, revealing that E_{50} increases with effective confining pressure. Ding et al. (2024) investigated the effects of erosion on the E_{50} of coral sand. They found that the secant modulus E_{50} decreases with the reduction of fine particle content, possibly because of the reduced contact area within the soil skeleton as fine particles diminish.

Many studies have provided E_{50} test data on cemented soil with different soil types and cement contents. In the study by Yilmaz and Ozaydin (2013), when the cement content is below 2.5%, E_{50} shows slight sensitivity to the curing period. In contrast, when the cement content exceeds 7.5%, E_{50} increases significantly with the curing period. Luis et al. (2019) compared cemented soil using OPC and fly ash. The results showed that, under the same confining pressure, the E_{50} of OPC-treated cemented soil is greater than that of fly ash-treated soil, and the ratio of E_{50} to E_{0} is approximately 0.9. Zhou et al. (2019) found that E_{50} significantly increases with confining pressure when it is below the yield stress. However, once the stress exceeds the yield stress, E_{50} initially decreases significantly with increasing confining pressure before gradually increasing again. This is likely because, at high-stress levels, the cementation structure is damaged, leading to a significant decrease in E_{50} .

Do et al. (2021) pointed out that soil type affects the variability of E_{50} . In their study, four types of soil were used, and the results showed that cemented sandy soil exhibits greater variability in E_{50} than cemented clayey soil. For engineering practical applications, E_{50} is often statistically related to UCS. Yoobanpot et al. (2020) identified a linear relationship between E_{50} and UCS, with $E_{50} = 68$ UCS. However, Kitazume (2013) also emphasized that the ratio of E_{50} to UCS for cemented soil exhibits significant variability, with values ranging from 100 to 1000, as shown in Figure 2.9.

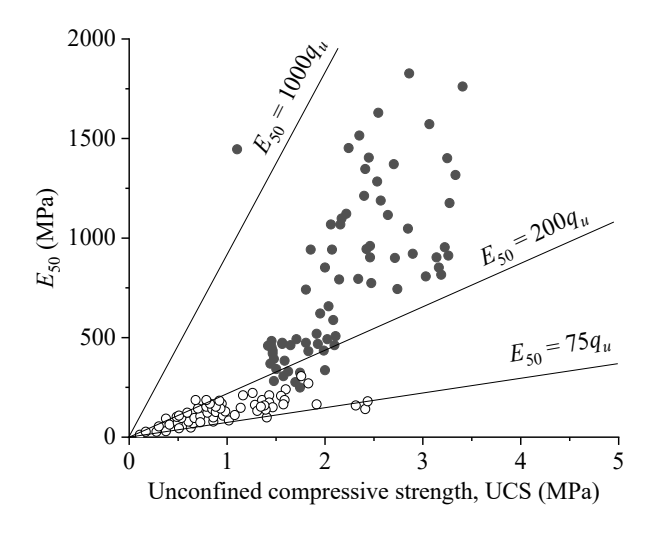


Figure 2.9 Relationship between E₅₀ and UCS of quicklime-stabilised soils (Kitazume 2013)

2.3 Constitutive modelling for cemented soil

Given the extensive application of cemented soil in engineering, many theoretical models have been developed to facilitate its use. These models include perfect elastoplastic and classical elastoplastic models, as well as advanced models such as the bounding surface and hypoelastic models. This section provides an introduction to these models.

2.3.1 Models based on the classical elastoplasticity framework

Scholars have improved existing uncemented soil models to simulate the behaviour of cemented soil. The primary approach is to define the bond strength to modify the yield surface shape, accounting for the presence of bond strength that decreases with increasing plastic strain. The simplest model is the extended MC model (Yapage and Liyanapathirana 2019). In the extended MC model, the strength parameters are defined to vary with strain to simulate strain softening. Additionally, some studies have modified existing constitutive models to incorporate the critical state concept to explain the significant strain-softening and dilation of cemented soil. Horpibulsuk et al. (2010a) modified the Cam-Clay model to consider the bonding strength in the yield surface formula. To simulate the strain-softening behaviour, they proposed one equation to describe the damage to the cementation structures.

$$dp_b = -2\left(\frac{p_b}{p_{bin}}\right) \frac{|dp'|}{3\sqrt{\frac{q}{p'}-M}}$$
 (2-15)

where p_{bin} = the value of the initial cementation strength; q = deviatoric stress; p' = mean effective stress; M = critical state stress ratio. Similarly, these studies (Horpibulsuk et al. 2010; L. Nguyen et al. 2017; Nguyen et al. 2014; Xiao et al. 2017) also proposed equations for cementation degradation, successfully capturing the experimental behaviour of strain-softening and dilatation.

Furthermore, several models have introduced new definitions for yield surfaces and flow rules specifically to simulate the soil behaviour of cemented soil better. Hirai et al. (1989) defined two yield surfaces based on the strength criterion and combined the non-associative flow rule to simulate the deformation behaviour of cemented sand. The first yield surface consideration is the shear-induced hardening yield surface.

$$f_1 = \sqrt{J_2} + \omega R(\theta) \bar{I}_1^{\alpha} \tag{2-16}$$

where J_2 = second invariant of deviatoric stress; ω and α = model parameters; \bar{I}_1 = the first invariant of stress.

The second yield surface is perpendicular to the hydrostatic axis and is used to describe the

hardening behaviour caused by volumetric strain.

$$f_2 = \bar{l}_1 + k_1 \tag{2-17}$$

where k_1 = an isotropic hardening function.

Kavvadas and Amorosi (2000) propose a model that considers the critical state theory, utilising a bonding strength envelope to characterize the contribution of cementation. They used the non-sphericity surface to account for the anisotropy induced by cementation and conceptualized cemented soil as a structural entity. It distinguishes between the concept of "yield" and the occurrence of structural failure. The bond strength envelope is defined in their study as follows:

$$F(\boldsymbol{\sigma}, \boldsymbol{\sigma}_{K}, \alpha) = \frac{1}{c^{2}}(\boldsymbol{s} - \boldsymbol{s}_{K}) : (\boldsymbol{s} - \boldsymbol{s}_{K}) + (\boldsymbol{\sigma} - \boldsymbol{\sigma}_{K})^{2} - \alpha^{2} = 0$$
 (2-18)

where σ = stress tensor; s = deviatoric stress tensor; ; σ_{K} = stress tensor of the center of the bond strength envelope; s_{K} = deviatoric stress and tensor of the center of the bond strength envelope; α = size of the bond strength envelope; c = eccentricity of the bond strength envelope. The model shows satisfactory performance by comparing simulations of drained and undrained shear tests on heavily over-consolidated clay.

In conclusion, the above-mentioned constitutive models are proposed based on the classical elastic-plastic model. The disadvantage is that only elastic behaviour can be predicted when the stress state is within the yield surface. Many advanced models have been proposed to address this limitation, which will be introduced in the next section.

2.3.2 Models based on the advanced constitutive model theory

Classical models can only predict elastic strain when the stress state is within the yield surface. The non-linear behavior of soil at small strains (less than 1%), including the strain-dependent stiffness, might not be completely represented. Non-linear soil behaviour at small strains (less than 1%), such as the degradation of shear modulus with strain, may not be fully captured. In addition, the response of soils under cyclic loading and unloading cannot be accurately modelled. Dafalias and Herrmann (1986) have made significant progress in constitutive modelling by applying the bounding surface concept to simulate soil behaviour. In bounding surface theory, soil behaviour is characterised by the distance from the stress point to the bounding surface, as shown in Figure 2.10. Hence, the bounding surface model allows for plastic deformation even when the stress state is within the bounding surface. To date, numerous studies have extended the application of bounding surface models to predict soil behaviour, including saturated (Khalili et al. 2005; Bardet 1986; Zhang et al. 2023b) and

unsaturated soils (Moghaddasi et al. 2021; Russell and Khalili 2006; Zhou et al. 2015).

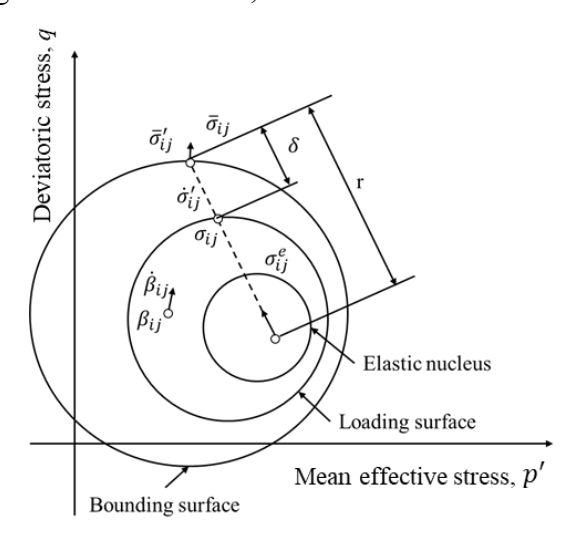


Figure 2.10 Schematic diagram of bounding surface and related concept (Dafalias and Herrmann1986)

In recent years, some researchers have applied the bounding surface model to simulate the behaviour of cemented soils. Park and Kutter (2016) proposed a constitutive model based on the Cam-Clay model, where the bounding surfaces have the same form as the yield surface in the Cam-Clay model. In their model, cemented clay is defined as a structured soil, and decementation is controlled by modelling the degradation of structural parameters related to the isotropic compression line. However, their model neglects the tensile strength of cemented soil. A similar approach was also used by Xiao et al. (2017). In the model proposed by Bandyopadhyay and Pillai (2020), the bounding surface is defined as tensile strengthdependent to improve the simulation of the true cohesion of cemented soil. However, the degradation of cementation was ignored in their study. Ma et al. (2022) proposed a bounding surface plasticity model to capture the stress-strain response of polystyrene (EPS) stabilised sand. Using Rowe's plastic dilatancy method within the critical state soil mechanics framework, the typical volumetric deformation mechanisms of EPS mix ratios at different confining pressures are studied. Zhang et al. (2023a) proposed a bounding surface model by modifying the Mohr-Coulomb failure envelope. The model focuses on the cyclic loading behaviour in cemented soils and introduces a strain liquefaction factor to improve the simulation of postliquefaction behaviour. Researchers have further extended the bounding surface model to unsaturated cemented soils. For instance, Yang et al. (2008) applied the bounding surface theory to simulate the behaviour of cemented loess, accurately predicting the strain accumulation of cemented loess under cyclic loading at different suction levels. Rahimi et al. (2016) used a simple cap-shaped yield surface as a bounding surface based on an existing

model for sand liquefaction. They modified the elastic modulus, plastic modulus, and flow rule to simulate cemented materials. Based on the MC constitutive models, Doherty and Wood (2020) proposed a model similar to the bounding surface model. Although the bounding surface was not explicitly defined in their model, the evolution of bond strength depends on the distance from the stress state to the failure envelope. Their model accounts for the time effects on bond strength development, where bond strength degrades with plastic strain development and increases with curing time.

The hypoplastic model serves as an effective alternative to the elastoplastic model. The hypoplastic theory, proposed by Kolymbas (1987), provides a new and effective framework for constructing constitutive models for soils. Unlike elastoplastic theory, hypoplastic theory does not decompose strain into elastic and plastic components, and it lacks concepts such as yield surface, flow rule, and hardening rules. Instead, it describes the stress-strain relationship of soils through a simple nonlinear tensor equation. The general form of the hypoplastic model is given by Wu and Kolymbas (1990):

$$\dot{\sigma} = \mathcal{L}: \dot{\varepsilon} + N \|\dot{\varepsilon}\| \tag{2-19}$$

where $\dot{\sigma}$ = stress tensor rate; and $\dot{\varepsilon}$ = strain tensor rate; \mathcal{L} and N = the fourth- and second-order stiffness tensors that describe the linear and nonlinear relationships between stress rate and strain rate, respectively. To simulate the various characteristics of soils, different influencing factors can be incorporated into the tensors \mathcal{L} and N.

Based on the hypoplastic model, many authors have studied various aspects of granular materials, such as stress and density dependence (Wu and Bauer 1993), cyclic loading (Bauer and Wu 1993), stability and failure (Wud and Niemunis 1994), rate dependence (Wu et al. 1993). Recently, some studies have extended the hypoplastic model to simulate cemented soil materials. For instance, Fu et al. (2022) proposed a hypoplastic constitutive model in which cementation-enhanced stiffness, strength, and dilatancy are considered. Liao et al. (2023) developed a hypoplastic theoretical framework for cemented soil models to address the poor simulation of cyclic loading in existing models. In their model, a state parameter was used to account for the effects of cementation on strength, modulus, and dilatancy. The model also considered the interrelation of cementation degradation with intergranular strain, fabric change effect, and semi-fluidized state.

However, the mechanical behaviour of cemented soil at small strains in the existing constitutive models has not been paid attention to or considered, especially the degradation of shear modulus with strain. Further theoretical and experimental research is needed to enhance

these models.

2.4 Numerical simulation and design method of DCM

2.4.1 Constitutive models used for DCM in numerical simulation

In recent years, DCM technology has garnered significant attention due to its notable advantages in environmental sustainability and construction efficiency (Yin et al. 2022; Ho et al. 2021). Extensive experimental research on cemented soil materials has been conducted, with a primary focus on the strength characteristics of cemented soil (Consoli et al. 2007; Jongpradist et al. 2010), the strain-softening behaviour (Kasama et al. 2000; Kamruzzaman et al. 2009), and the strain-dependent stiffness (Yun and Santamarina 2005; Yang and Woods 2015; Trhlíková et al. 2012). Numerous constitutive models have been proposed for cemented soil materials. These models primarily focus on behaviour like strain-softening and dilation (Nguyen et al. 2014; Rahimi et al. 2016) and responses under cyclic loading (Yang et al. 2008; Liao et al. 2023).

In the application of FEM for DCM engineering design, the selection of constitutive models is a crucial factor influencing the results. Currently, the most commonly used model for DCM in the simulation of boundary value problems for DCM is the MC model (Yapage et al. 2014, Jamsawang et al. 2015; Wu et al. 2020; Phutthananon et al. 2020; Dang et al. 2020; Wonglert et al. 2018) and HS model (Voottipruex et al. 2019). The primary issue with using the MC and HS models is that they are insufficient for accurately characterising the significant strainsoftening behaviour of cemented soil, particularly the stress redistribution phenomenon that may occur after strain-softening. Nevertheless, many engineers still prefer these models due to their simplicity and the minimal number of parameters required. To better simulate the strainsoftening behaviour, several scholars (Yapage et al. 2014; Wijerathna and Liyanapathirana 2021) have improved the MC model by defining shear strength parameters that vary with increasing strain. Another advanced model is the concrete model (Waichita et al. 2020; Long and Chong 2024; Zhao et al. 2023), which can also be used to simulate the strain-softening behaviour of cemented materials. Complex constitutive models often require more parameters. For example, the concrete model has 26 parameters, which limits their practical application. In summary, despite the development of numerous advanced models for simulating cemented soil materials, research on their application in numerical simulations remains constrained.

Field test data indicate that the strain encountered in DCM columns under working conditions is primarily within the small strain range. However, existing models do not account for the small strain property in boundary value problem analysis.

2.4.2 Numerical simulation of DCM-stabilised foundation

There have been some studies on the simulation of DCM-stabilised foundations. Existing research can be broadly divided into the following categories. Firstly, some research focuses on the load transfer mechanisms in DCM foundations under embankment. For example, the following research pointed out (Phutthananon et al. 2023; Ye et al. 2017; Zhang et al. 2020) that the DCM columns with higher stiffness can bear more load than soft soil. In addition, as the soft soil consolidates over time, the load on DCM columns progressively increase, which also accelerates the dissipation of excess pore water pressure of the surrounding soft soil (Huang and Han 2009; Han and Ye 2001).

Some studies (Yapage et al. 2015; Yapage et al. 2014; Yapage and Liyanapathirana 2014) have paid attention to the strain-softening of the DCM column. The simulation results in Liyanapathirana and Yapage (2021) show that strain-softening of DCM columns leads to significant stress redistribution. In their simulation, the settlement calculation results considering strain-softening more precisely correspond to the on-site testing results. Based on the nonlinear failure surface, Liyanapathirana and Yapage (2021) improved the analytical solution in the current design method, which assumes a linear failure surface. Zhao et al. (2023) studied the new T-shaped column-supported embankment using Plaxis. Compared to traditionally shaped columns, the T-shaped columns increased the replacement ratio of the foundation due to the enlarged cap. However, T-shaped columns reduce engineering costs as the increased material usage is confined to the top and reduces the load on the upper soil. Wu et al. (2020) used a soft soil creep model to analyse the effects of creep of the underlying soft soil on settlement.

Due to creeping, the load on the soft soil is transferred to the DCM columns via side friction, causing the soft soil to undergo unloading. This unloading process leads the soil to become over-consolidated, resulting in a reduced creep strain rate. Consequently, the effects of creep on the dissipation of excess pore water pressure are diminished.

Sakr et al. (2022) utilised PLAXIS3D to investigate the influence of design parameters such as area replacement ratio and pile dimensions (the ratio of pile length to pile diameter) on the effectiveness of DCM columns in improving foundation performance. Their study demonstrated that increasing the area replacement ratio and the pile length-to-diameter ratio significantly reduces settlement in soft soil foundations. Addressing the issue of differential settlement in high-speed railway embankments using DCM, Sedighi Moghadam et al. (2022) examined the impact of different pile types on foundation settlement under dynamic train loads.

Their simulation results indicated that TDM pile caps can prevent differential settlements on railway tracks. Achieving uniform settlement with DCM piles is only feasible at high pile densities, substantially increasing construction costs.

Ni et al. (2019) used finite element analysis to investigate the failure modes of soft soil foundations stabilised with DCM columns. They found that the failure mechanisms of pure soft soil foundations differ from those of DCM-stabilised foundations. In soft soil, the bearing capacity is proportional to the soil strength c_u , while in DCM-stabilised foundation, it is controlled by column failure strength but not proportional to the column strength.

2.4.3 Design method of DCM-stabilised foundation

Extensive research has been conducted on cemented soil, particularly regarding the strength, stiffness, and permeability of cemented soil materials under various stress paths. However, current design practices still predominantly rely on simplified analytical methods, and there are relatively few established design guidelines for DCM-stabilized foundations. This section focuses on summarizing the methods for determining the bearing capacity and settlement of DCM-stabilized ground.

In bearing capacity calculations, the modulus of soft soil is very low, meaning that mobilizing its strength requires relatively large strains. In contrast, DCM columns have a much higher modulus, allowing their strength to be mobilized at much smaller strains. Therefore, at the ultimate bearing capacity, the mobilised strength of the soft soil is quite limited. To account for this, a reduction factor is applied to the strength of the soft soil in bearing capacity calculations, as shown in Equation (2-20):

$$q_{all} = \alpha q_{dm} + \beta (1 - \alpha) q_s \tag{2-20}$$

where, q_{all} = bearing capacity of composite foundation, α = area replacement ratio, q_{dm} unconfined compressive strength of column, β = reduction factor, q_s = bearing capacities of untreated ground. According to the Chinese mainland code (JGJ 2012), different reduction factors are recommended depending on the properties of the soil between columns: for treated layers such as mud, silty soil, and flow plastic soft soil, a reduction factor of 0.1–0.4 is suggested; for other soil layers, a factor of 0.4–0.8 is recommended. In contrast, the Federal Highway Administration (FHWA, 2013) in the United States assumes that DCM columns bear the entire structural load, with no direct contribution from the soil between columns. Thus, the contribution of soft soil to bearing capacity is not considered in the FHWA specification.

Chai et al. (2010) pointed out that stress concentration on the columns may cause compression of the underlying soft soil layer, particularly for floating columns. To address this issue, a

common practice is to treat a portion of the column as soft soil in settlement calculations to avoid underestimating foundation settlement. However, there is no unified standard for determining the specific proportion of the column to be considered as soft soil in these calculations.

In the design code, the calculation of settlement for DCM-stabilised foundations is typically based on the assumption of an equal strain condition, in which the entire composite foundation is treated as having a uniform composite modulus. The composite modulus,

$$M_{comp} = \alpha E_{col} + (1 - \alpha) M_{soil}$$
 (2-21)

where E_{col} = the Young's modulus of DCM; M_{soil} = the constrained modulus of the untreated soil. A similar modulus and settlement calculation method is also adopted in the relevant Chinese mainland code. In these calculations, it is generally assumed that settlement increases linearly with increasing foundation load. However, the soil behaviour of cemented soil is highly nonlinear, which may introduce errors in settlement estimation.

In summary, the calculation of total settlement for DCM-treated foundations is currently based on relatively simple methods that have not yet undergone rigorous validation. Therefore, this study focuses on evaluating the settlement of DCM-improved foundations using advanced models for cementitious materials proposed herein. The calculated settlements are compared with current standards, and a design calculation chart is proposed.

2.5 Summary

Based on the literature review in this chapter, several limitations in the current research on cemented soil have been identified. While existing experimental studies have explored the effects of curing temperature and stress on the strength of cemented soil, there is a lack of indepth research examining how these factors affect small-strain stiffness. Most existing theoretical models effectively capture the strength, dilatancy, and strain-softening of cemented soil. However, there are currently no constitutive models specifically focused on predicting the behaviour of cemented soil within the small-strain range. In numerical studies, most research relies on simple MC models, while some employ more complex models with numerous parameters. These constitutive models often overlook the small-strain characteristics of cemented soil, leading to potentially significant computational errors that could adversely affect engineering design and safety assessments. Current design guidelines generally use simple linear elastic equations for settlement calculations, which may not adequately account for the complex mechanical behaviour of cemented soil, particularly the nonlinear soil properties. Therefore, it is necessary to improve design methods to better reflect the real soil

behaviour. By addressing these limitations, it is necessary to enhance the understanding and application of cemented soil in engineering practice.

CHAPTER 3 Test material, programme and methods

This chapter provides a comprehensive overview of the experimental setup for this study. It begins by introducing the properties of the soil materials used, emphasizing their physical and chemical characteristics. A brief overview of the development of a novel temperature and stress-controlled apparatus for specimen curing follows this. A detailed description of the testing program outlines the specific procedures and methodologies employed to ensure accurate and reliable results. Additionally, microstructural analysis methods, including SEM, MIP, and TGA, are utilized to explain the macro behaviour of the materials. The chapter concludes with a detailed discussion of the test methods.

3.1 Test material and specimen preparation

3.1.1 Test material

The binder used is Type I Ordinary Portland Cement (OPC), and its chemical composition is summarised in Table 3.1. The marine clay was sampled from Lamma Island, Hong Kong. To keep the largest particle size below one-fifth of the specimen diameter (50 mm in this study), particles exceeding 5 mm were eliminated through wet sieving without using a dispersant, following the GEO 3 (2023) guidelines. The physical properties of the marine clay are summarised in Table 3.2, and the particle size distribution curve is shown in Figure 3.1. According to the Unified Soil Classification System of ASTM (2006) D2487, it is classified as a fat clay (CH). In addition, the loss on ignition (LOI) value for the tested marine clay is 4.31%, classifying it as a mineral soil with a certain amount of organic matter (Huang et al. 2009).

Table 3.1 Chemical compositions of the cement binder

Component	SiO_2	Fe ₂ O ₃	Al ₂ O ₃	CaO	MgO	SO ₃
Percentage (%)	20.00	3.04	5.53	64.30	1.28	4.49

Table 3.2 Physical properties of the marine clay

Specific L	Liquid	Plastic	tic Plasticity t (%) index (%)	LOI (%)	Particle size distribution (%)		
gravity	1				Sand	Silt	Clay
gravity	(,0)	(/0)			content	content	content
2.62	63.9	28.2	35.7	4.31	16.7	61.0	22.3

It has been well-recognized that clay content can affect the cementation effects. For example, Woo (1971) found that increasing clay content and plasticity index would reduce the

bonding effects. Subramanian et al. (2020) demonstrated that the ratio of compressional wave to shear wave increases with the increase in clay content for cemented soils. The tested marine clay is found to have a clay content of 22%. The current study does not specifically investigate the effects of clay content on cemented marine clay.

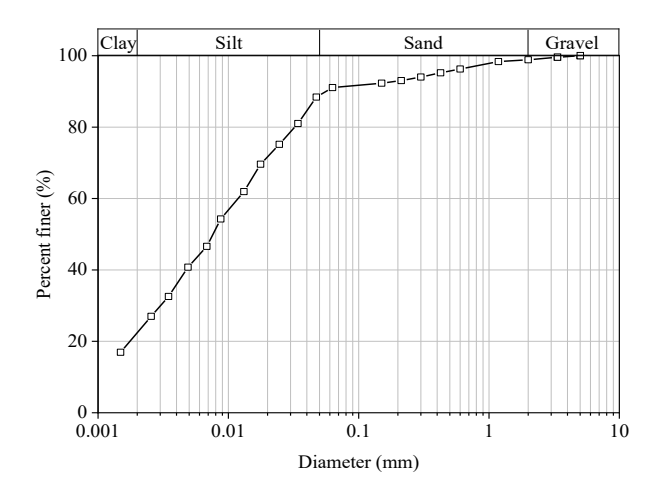


Figure 3.1 Particle size distribution of the tested marine clay

3.1.2 Specimen preparation

The specimen preparation involves five major steps, including clay slurry preparation, cement slurry preparation, soil-cement mixing, specimen moulding, and curing. The total time required for specimen preparation is approximately 30 minutes, which is shorter than the initial setting time of Type I OPC (45 minutes). The specimen preparation details are as follows:

- 1. A specific amount of sieved marine clay was taken from a sealed container after being mixed with a portable mixer. The initial water content was controlled at 65%, with reference to the typical in-situ water contents of the tested marine clay.
- 2. The required amounts of cement powder and water were weighed and mixed in a 1:1 mass ratio to form a cement slurry (Wang et al. 2019a), as shown in Figure 3.2.
- 3. A mixer was used to blend the marine clay and cement (see Figure 3.2b) at low speed (e.g., 135 RPM) for 2 minutes and then at high speed (e.g., 220 RPM) for 3 minutes, refer to the procedure outlined in GEO 3 (2023). The mixer was stopped for 60 seconds, and a spatula was used to scrape the mixture from the sides of the mixing bowl and the mixer attachment, pushing it back to the center of the bowl. Mixing continues at high speed (e.g., 220 RPM) for 5 minutes.
- 4. Once thoroughly mixed, the marine clay-cement mixture was immediately placed into moulds lubricated with petroleum jelly. Each mould was filled in three layers of approximately equal thickness. A vibrating table (60 Hz) was used to eliminate air bubbles,

following the methods in ASTM (2013) standard C192.

5. The mould containing the cement-soil mixture was set up in a curing apparatus, as shown in Figure 3.2d.



Figure 3.2 Photographs showing the specimen preparation process: (a) cement slurry preparation; (b) mixing of marine clay and cement slurry; (c) specimen preparation using vibrator; (d) curing of specimens in curing machine.

3.1.3 A new temperature and stress-controlled curing apparatus

This curing apparatus was newly developed in this study, and its details are shown in Figure 3.3. It is able to control the curing temperature and stress. A temperature-controlled water bath was employed to maintain temperature stability during the curing process.

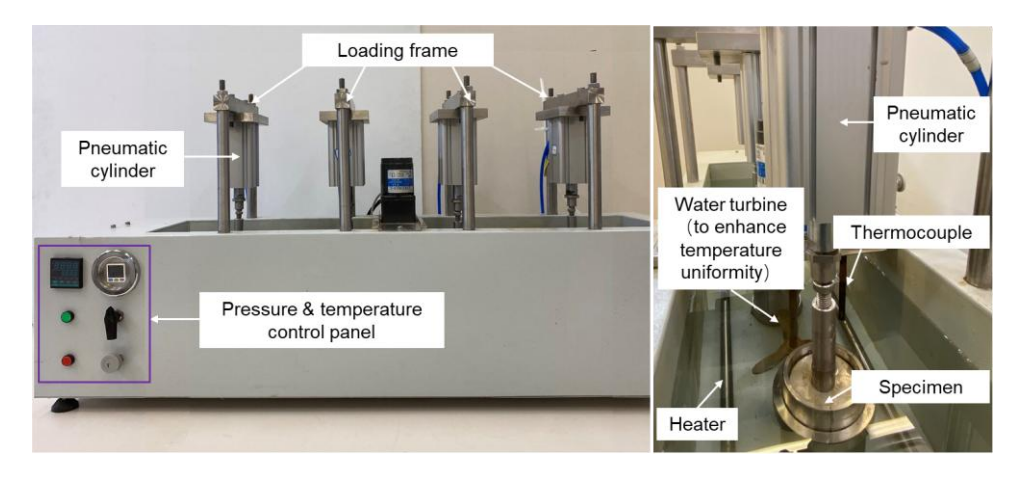


Figure 3.3 Newly designed specimen curing apparent

A heater was installed at the bottom of the water bath, and its heating rate was regulated based on the reading of a thermocouple with an accuracy of 0.1°C, which was positioned at the mid-height of the water bath. In addition, a water turbine was used to keep the water in motion to ensure uniform temperature distribution within the water tank. When the temperature reached equilibrium, the two thermocouples at different positions showed almost identical measurements and fluctuated by less than 0.1°C. On the other hand, the vertical curing stress was applied using pneumatic cylinders. The air pressure inside each pneumatic cylinder was

maintained constant throughout the curing process to ensure the desired curing stress. Before specimen curing, the friction of the cylinder telescopic rod was measured using a load cell. The results showed that the friction of the cylinder was negligible (less than 5 N).

3.2 Test programme

A comprehensive experimental program was designed and summarised in Table 3.3, considering the effects of three factors: curing temperature, curing stress, and cement content. As aforementioned, the temperature inside DCM columns can reach 40°C due to cement hydration. Therefore, this study selected three curing temperatures (i.e., 20, 30, and 40°C) ranging from room temperature to 40°C. The effective confining pressure from surrounding soils to DCM can reach several hundred kPa, depending on several factors, such as the DCM length, the unit weight, and the lateral stress coefficient of surrounding soils. The maximum stress in a typical DCM is approximately 200-300 kPa (El Kamash et al. 2014; Jamsawang et al. 2016; Phutthananon et al. 2022), so three curing stress levels (i.e., 0, 150, and 300 kPa) were selected for the planned tests. The detailed test program is summarised in Table 3.3.

Table 3.3 Test program for unconfined compression test

Curing temperature, T_c	Curing	stress,	S_c	Cement	content,	Сс	Repeatability test
(°C)	(kPa)			(%)			
20	0			15			/
20	0			25			2
20	0			35			/
30	0			15			/
30	0			25			2
30	0			35			/
30	150			25			2
30	300			25			2
40	0			15			/
40	0			25			2
40	0			35			/
40	150			25			2
40	300			25			2

Considering that the depth of DCM columns typically ranges from 10 to 20 meters and the stress arising from infrastructures, the maximum effective stress is around 300 kPa. Therefore, effective confining pressures of 200 kPa and 400 kPa were used in the triaxial tests. For the curing conditions of specimens in the undrained triaxial shear tests, the selected temperatures

were 20°C and 30°C, and the applied stresses were 0 kPa and 150 kPa. The selected testing conditions are sufficiently representative, as tests were conducted under two distinct confining pressures, curing temperatures, and curing stress conditions, effectively minimizing the experimental workload. Additionally, to evaluate the tensile properties of the cemented soil, direct tensile tests and indirect tensile tests (Brazilian splitting test) were conducted, with the same curing condition as those of triaxial rests. The test programme for undrained triaxial shear and tensile tests is summarized in Tables 3.4 and 3.5.

Table 3.4 Test program of undrained triaxial shear tests

	Cement	content,	Curing temperature,	Curing stress,	Confining
Number	<i>Cc</i> (%)		T_c (°C)	S_c (kPa)	pressure σ_c (kPa)
1	15		20	0	200
2	15		20	0	400
3	25		20	0	200
4	25		20	0	400
5	25		30	0	200
6	25		30	0	400
7	25		30	150	200
8	25		30	150	400

Table 3.5 Test program of Brazilian tensile test and direct tensile tests

	Cement	Curing	Curing	stress	Number	of
Number	content (%)	temperature (°C)	(kPa)		specimen	
1	25	20	0		2	
2	25	30	0		2	
3	25	30	150		2	
4	25	30	300		2	
5	25	40	0		2	
6	25	40	150		2	
7	25	40	300		2	

3.3 Test procedures and apparatuses

3.3.1 Unconfined compression tests

After 28 days of curing, the specimen underwent checks for flatness, perpendicularity, and parallelism before unconfined compression (UC) tests. The UC tests were conducted using the TRI-SCAN 100 device. The loading rate was set to 0.2 mm/min, consistent with the rate used by Ribeiro et al. (2016) and Cardoso et al. (2017) in their unconfined compression tests on

cemented soil. The vertical strain of specimens was measured using a combination of strain gauges and local and global LVDTs, as depicted in Figure 3.4. The working range of the sensors was divided into three intervals: 0.001% - 0.1% (strain gauge with a strain accuracy of 0.0001%), 0.1% - 1% (local LVDT with a strain accuracy of 0.01%), and > 1% (global LVDT with a strain accuracy of 0.1%).

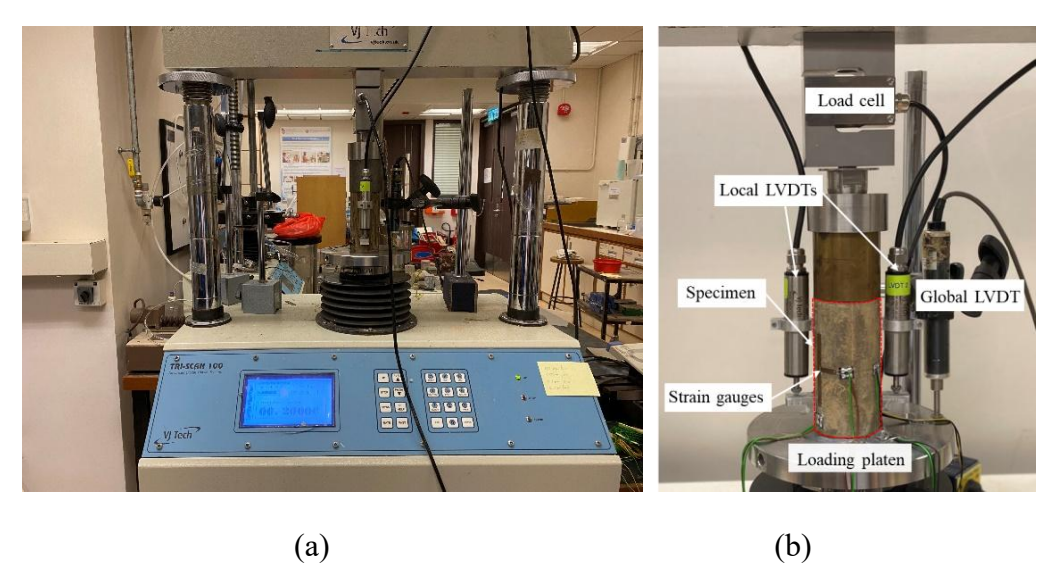


Figure 3.4 Diagram of unconfined compression test setup (a) overall view; and (b) local view 3.3.2 Consolidated undrained triaxial shear tests

Consolidated undrained shear tests (CU) were conducted, consisting of three major steps: saturation, consolidation, and undrained shearing. The test procedures followed those outlined in GEO 3 (2023). In the saturation stage, the Skempton B value was used to verify the saturation state of cemented specimens. GEO 3 (2023) requires the B value to be at least 0.95. During the saturation phase, a back pressure of 300 kPa and a cell pressure of 310 kPa were applied. Both pressures were gradually increased in steps while keeping the drainage valves open, allowing water from the burette connected to both ends of the specimen to flow into it. The increment of the cell and back pressure was set at was used to prevent unwanted prestressing of the specimen during back pressure application. The effective pressure was maintained at 10 kPa. Ultimately, the total cell pressure and back pressure reached 310 kPa and 300 kPa, respectively. After 24 hours of saturation, the B-value was determined. A specimen was deemed saturated if the B-value was 0.95 or higher, or if a graph of the B-value against back pressure showed no further rise in B-value with increased back pressure.

The objective of the consolidation phase was to enable the specimen to achieve equilibrium. Once the saturation phase was finished, the axial load piston was adjusted to make contact with the specimen cap. Drainage was enabled from both ends to minimize consolidation time. The

maximum back pressure remained constant, while the cell pressure was increased until the difference between total and back pressure matched the target effective consolidation pressure (200 and 400 kPa). Volume change and deformation readings were plotted against the square root of elapsed time on a logarithmic scale. Consolidation continued until the volume change readings stabilized and at least 95% of the excess pore pressure was relieved, typically taking about one day.

Following consolidation, the axial load piston was repositioned to contact the specimen cap. During the shearing phase, the cell pressure was maintained constant as the axial load piston moved downward against the specimen cap, with controlled axial strain as the loading criterion. No drainage was allowed during shearing, and excess pore water pressure was monitored. Additionally, local LVDTs were employed to accurately measure the nonlinear stiffness of cemented clay, as illustrated in Figure 3.5.

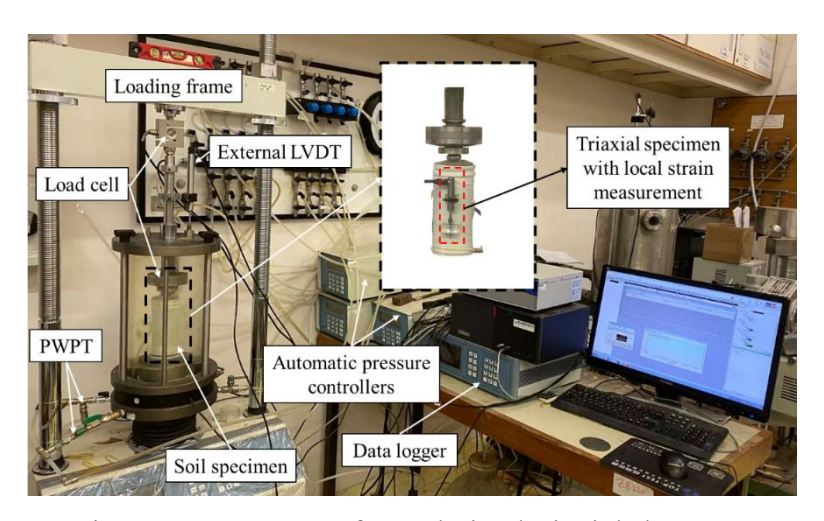


Figure 3.5 Apparatus for undrained triaxial shear test

3.3.3 Brazilian test

The Brazilian tensile test was conducted based on ASTM D3697 (2016) using the equipment shown in Figure 3.6. The specimen used for testing was a circular disk, with its thickness-to-diameter ratio (t/D) ranging from 0.2 to 0.75. Therefore, specimens with a diameter of 50 mm and a length of 25 mm were used.

First, the specimen was indicated by marking a diametral line on each end of the specimen. Second, bearing strips were needed. The purpose of the bearing strips was to ensure that the load applied to the specimen was a line load. The thickness of the bearing strips was 3 mm, and the width was less than 8% of the specimen diameter. After that, the specimen was set up. The specimen was positioned between the two bearing strips, aligned with the loading direction along the diametral line. To ensure contact, a preload was performed first.

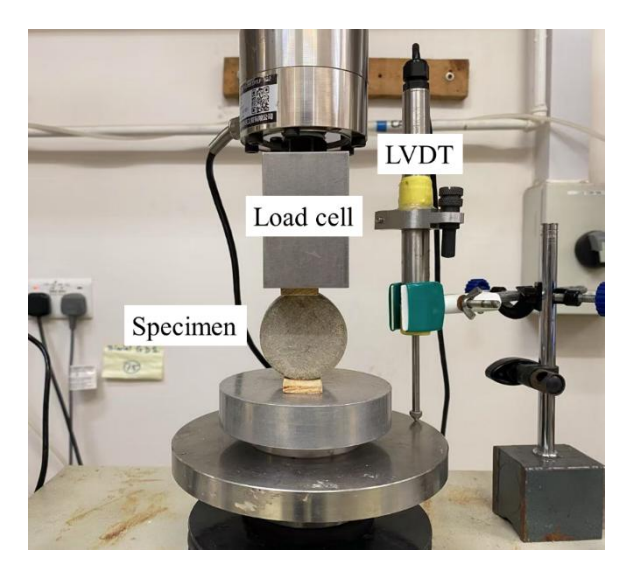


Figure 3.6 Apparatus for Brazilian test

3.3.4 Direct tensile test

The direct tensile test was based on ASTM (2008) using the equipment shown in Figure 3.7. The preparation of test specimens for the direct tensile test followed the ASTM method (2019). Metal caps were glued to the test specimen to ensure that the cap axes aligned with the longitudinal axis of the specimen. Epoxy resin was used as a suitable bonding medium. The epoxy resin layer should not be thicker than 1.5 mm at each end, and it must maintain a consistent thickness to ensure the metal caps' top surfaces are parallel on both ends of the specimen. Once the epoxy resin has hardened enough to surpass the tensile strength of the cemented soil, the specimen is placed in the testing machine, ensuring proper alignment of the load transfer system. The specified tensile load or deformation is applied smoothly and at a constant rate, ensuring failure occurs between five and 15 minutes. Details such as the type and location of failure, time to failure, and the maximum load the specimen endured during the test are recorded with 1% accuracy.

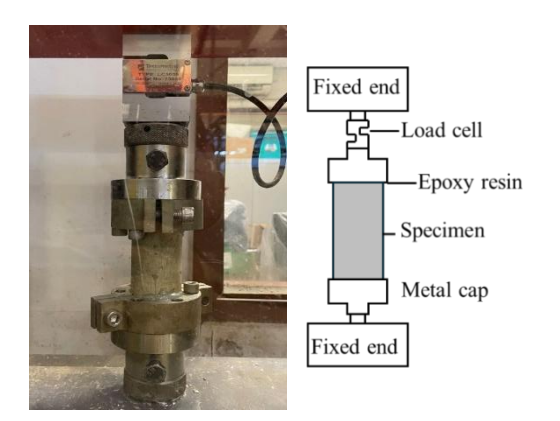


Figure 3.7 Apparatus for direct tensile test

3.3.5 Microstructural analysis

To prepare specimens for the TG analysis, cemented specimens were first frozen by immersing them in liquid nitrogen at -195°C for 5 minutes. After freezing, the specimens underwent freeze-drying at -85°C and 0.133 mbar using a Labconco Freezone 2.5 Plus freeze-drier for 48 hours. Some freeze-dried specimens were then ground into a fine powder (about 10 mg) for TG analysis (Netzsch STA 449F3), as shown in Figure 3.8, to determine the mineral contents. The temperature during testing was raised from 30°C to 1000°C at a rate of 10°C per minute. To avoid carbonation of the specimens, nitrogen gas was introduced at a flow rate of 50 mL per minute throughout the heating process. Further details of the test method can be found in Scrivener et al. (2018).

The specimens for SEM and MIP tests were prepared using a method similar to the TG analysis, with one major difference. In contrast to the specimen preparation for TG analysis, the specimen preparation procedures for SEM and MIP testing require the exchange of water with ethanol (immersed in ethanol for 3 days) before freezing in liquid nitrogen, following the method of Han et al. (2014). The main purpose of this step was to prevent the volume expansion of pore water during liquid nitrogen freezing from damaging the cementation structure. After the liquid nitrogen treatment, the parallel specimens were freeze-dried in the freeze-drier. The morphologies were analysed using an SEM (TESCAN VEGA 3), as shown in Figure 3.10, to investigate the micro-topography of cemented specimens. The pore size distribution was determined through MIP (Micromeritics Autopore V 9600) tests. In the analysis of MIP test data, a contact angle of 140° and a surface tension of mercury of 0.480 N/m was used.



Figure 3.8 TGA test in PolyU (Netzsch STA 449F3)



Figure 3.9 Apparatus for SEM test (Tescan VEGA3)

CHAPTER 4 Effects of curing condition on stiffness and strength

This chapter presents the experimental results for cemented marine clay under various curing conditions, specifically at three curing temperatures (20, 30, and 40°C) and three curing stress levels (0, 150, and 300 kPa). Microscopic test methods, including TGA, SEM, and MIP are employed to examine the effects of curing temperature and stress on the composition and microstructure of the cemented marine clay. The mechanical behaviour of the cemented clay is investigated through unconfined compression tests, triaxial tests, Brazilian splitting tests, and direct tensile tests. The unconfined compression and undrained triaxial tests focused on the effects of curing temperature and stress on strength and small strain modulus. Meanwhile, the Brazilian splitting and direct tensile tests primarily examined tensile strength. The mechanisms by which curing temperature and stress influence strength and stiffness are discussed based on microstructure tests.

4.1 Curing condition effects on the microstructure of cemented soil

4.1.1 Comparison of SEM results between uncemented and cemented clay

SEM analysis was conducted to examine its microstructure to better understand the macro behaviour of cemented marine clay. Figure 4.1 shows SEM images of uncemented and cemented marine clay. At a magnification of 1000x, Figure 4.1a, the marine clay exhibits a microstructure with exposed inter-aggregate pores. Figure 4.1c shows SEM images of uncemented marine clay at magnifications of 5000x and 8000x, respectively. It observed widely distributed clay/silt aggregates in the specimens. Figure 4.1d displays the SEM results of cemented marine clay at a magnification of 1000x, where the inter-aggregate pores are filled with cement hydration products. Compared to the SEM image of uncemented marine clay, the structure of cemented marine clay appears more compacted, and the inter-aggregate pore size is significantly reduced. Figure 4.1e and Figure 4.1f show SEM results of cemented soil after magnifications of 5000x and 8000x, revealing that the clay particles and silt grains are covered with reticulated morphology (Calcium silicate hydrate) and prismatic crystals (ettringite).

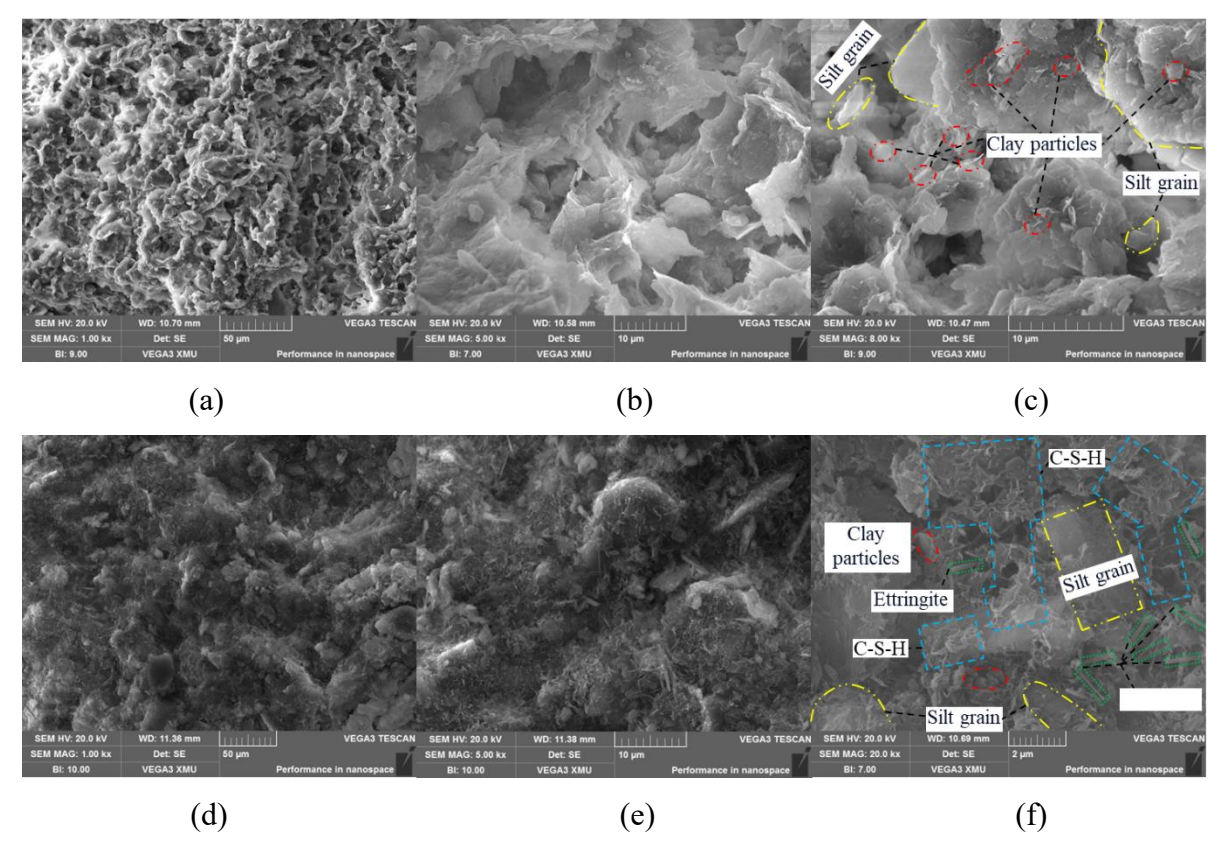


Figure 4.1 SEM images of HKMC: (a) 1000x, (b) 5000x, (c) 8000x, and cemented HKMC: (d) 1000x, (e) 5000x, (f) 8000x

4.1.2 Effects of curing temperature

Figure 4.2 shows an in-depth investigation of the mechanism of curing temperature, in which TG and differential thermogravimetry (DTG) curves of the cemented marine clay at different curing temperatures are presented, with the mass loss of various components. Specifically, the mass losses correspond to calcium silicate hydrate (C-S-H) (40-600°C), ettringite (AFt) (80-180°C), Friedel's salt (F's salt) (200-300°C) (Shen et al. 2017; Sun et al. 2023), calcium hydroxide (CH) (400-500°C), and calcite (600-800°C). Based on the weight loss data in Table 4.1, it is evident that weight loss is greater at higher curing temperatures. Specifically, the total weight loss is 12.4% for specimens cured at 20°C, while it is 14.5% for specimens cured at 30°C, suggesting that more hydration products are generated at higher curing temperatures.

The amount of CH, which is an important parameter for analysing the cementation effects, can be calculated following the approach of Scrivener et al. (2018) and Sun et al. (2024):

$$CH(\%) = \frac{74}{18} (W l_{(400-500)} - 0.8 * W l_{MD(400-500)})$$
 (4-1)

where CH(%) = the content of CH; $Wl_{(400-500)}$ and $Wl_{MD(400-500)}$ = the total mass loss

percentage of the cemented specimens and pure marine clay between 400-500°C, respectively. According to this equation, the CH content can be estimated as the total weight loss of cemented specimens between 400-500°C minus the weight loss of uncemented specimens in the same temperature range. The coefficient of 0.8 accounts for the mass percentage of marine clay in cemented specimens (Sun et al. 2023a). In addition, some minerals in the marine clay may participate in the cement hydration reaction, resulting in an underestimation of the CH value. However, the clay contains minerals with distinct decomposition characteristics: kaolinite decomposes at 450-650°C, illite at 500-800°C, and montmorillonite at 500-700°C. Therefore, the weight loss of uncemented marine clay between 400-500°C is predominantly attributed to the dehydroxylation of kaolinite. Since kaolinite is an inert component in clay that contributes negligibly to the cement hydration reaction (Mehta and Monteiro 2006; Talabi et al. 2012; Nawaz et al. 2022), the error due to the cement hydration reaction can be considered negligible.

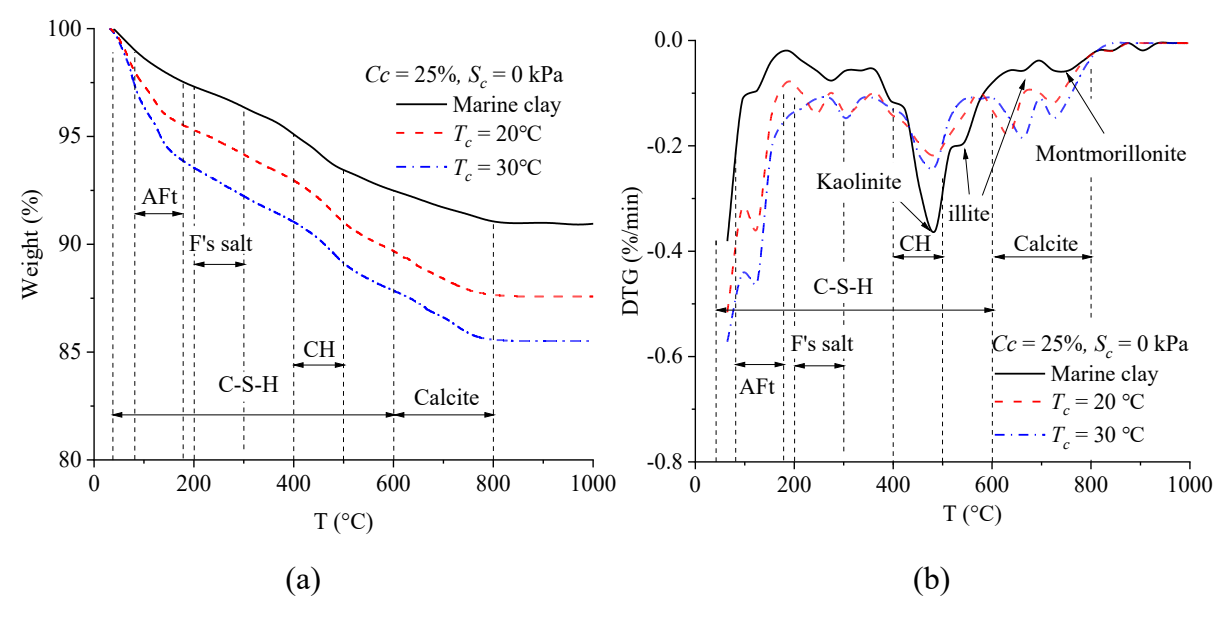


Figure 4.2 Results of TG analysis on cemented HKMC at different curing temperatures: (a) TG curves; (b) DTG curves.

The CH content calculated using Equation (4-1) at 30°C is expected to be higher than that at 20°C. However, the results in Table 4.1 show that the CH contents for specimens cured at both temperatures are nearly identical, with CH contents of 2.97 and 2.96 for specimens cured at 20°C and 30°C, respectively. This finding suggests that the additional CH produced at 30°C was consumed in other reactions. Given that CH is only consumed in pozzolanic reactions (Zhang et al. 2014), increasing the curing temperature can promote pozzolanic reactions, thereby generating more strength-enhancing products. The elevated curing temperatures

promote pozzolanic reactions may be attributed to two reasons: (1) with an increase in the curing temperature, the rate of hydration increases, producing more calcium hydroxide that raises the pH value of the environment; (2) at a higher temperature, silicates and aluminates are easier to dissociate to participate in pozzolanic reactions (Maltais and Marchand 1997, Zhang et al. 2014).

Table 4.1 Comparison of the weight loss for different specimens

Specimen	Curing	T_c	Curing stress, S_c (kPa)	Weight loss (% of original)		
	temperature, (°C)			400-500°C	0-1000°C	CH content (%)
Pure marine clay	/		/	1.62	9.11	/
	20°C		0 kPa	2.02	12.38	2.97
Cemented marine clay	30°C		0 kPa	2.01	14.48	2.96
marme ciay	30°C		300 kPa	1.99	14.36	2.86

Figure 4.3 shows the MIP test result. The specimen cured at 20°C showed a bimodal distribution curve, defining two peaks at pore radius of 180 and 0.14 µm. When the curing temperature is 30 and 40°C, the pore size distribution changes from bimodal to unimodal. The transition from a bimodal PSD to an unimodal distribution is largely dependent on the curing temperature. This phenomenon can be attributed to two primary reasons. Firstly, an increase in curing temperature enhances the degree of cement hydration, resulting in a greater production of hydration products. Secondly, elevated curing temperatures promote the pozzolanic reaction, producing reticulated morphology compounds (calcium silicate and calcium aluminate) that can effectively improve the pore structure by covering and connecting the aggregates. As illustrated in the SEM image in Figure 4.1f, reticulated morphology compounds more effectively encapsulate the particle aggregates and fill the inter-aggregate pores.

The pore radius corresponding to the peak value of the density function decreases to 0.11 µm and 0.06 µm at 30 and 40°C, respectively. Generally, the density function for a pore diameter smaller than 0.1 µm increases with higher curing temperatures, while the density function for a pore diameter larger than 0.1 µm decreases, indicating the growth of cementitious products fills the larger pores, consistent with the conclusions of Horpibulsuk et al. (2009). The higher the curing temperature, the smaller the total infiltration volume. The experimental results show that the void ratio of cemented marine clay only decreases by 2% when the curing temperature increases from 20 to 40°C.

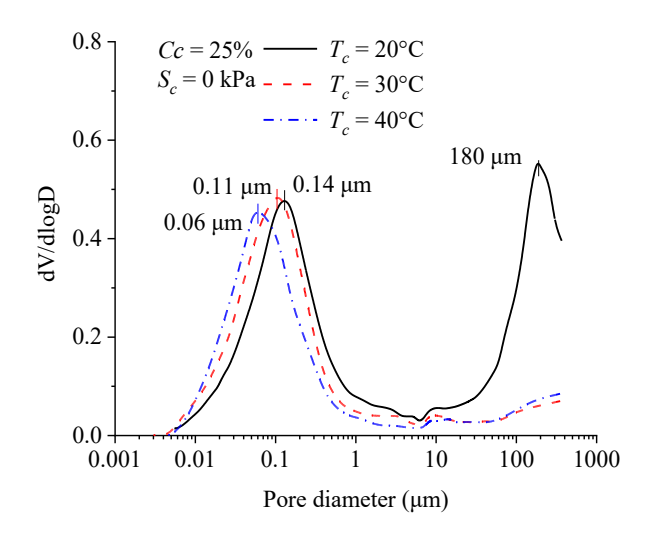


Figure 4.3 MIP results for the specimens at different curing temperatures

4.1.3 Effects of curing stress

TG analysis was conducted on the specimens under different curing stresses. This study conducted two TG analysis experiments in each test condition, as shown in Figure 4.4. The TG curves for the first and second tests exhibit consistent trends, and the difference in the total weight loss is relatively small, with a maximum error of 2%. As shown in Figure 4.4, the TG test results of specimens cured with and without confinement are basically consistent. It means there is no significant difference in the total amount and composition of the hydration product. The data shown in Table 4.1 indicates that the difference in the total amount of hydration products is less than 0.8% for specimens cured at stresses of 0 and 300 kPa, which suggests that curing stress has no obvious effects on the cement hydration reaction.

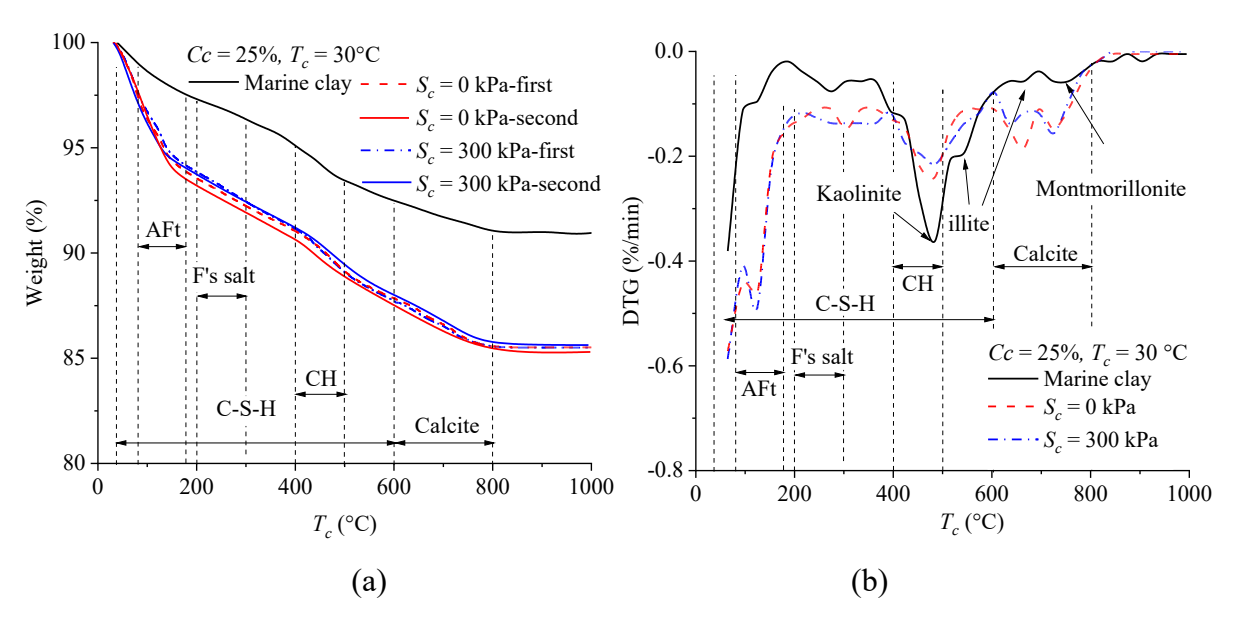


Figure 4.4 Results of TG analysis on cemented marine clay at different curing stresses (a) TG curves; and (b) DTG curves.

Some studies (Cui and Fall 2016; Chen et al. 2021) pointed out that curing stress can facilitate cement hydration reactions. They explain that the increased curing stress squeezes out more free water in the specimen, allowing more contact between cement particles and facilitating the cement hydration reaction. However, TG analysis results in Figure 4.4 show that the curing stress effects on cement hydration differ from the findings of Cui and Fall (2016) and Chen et al. (2021). The reason for this difference may be due to different curing conditions. In the current study, the specimens were cured underwater, while Cui and Fall (2016) and Chen et al. (2021) cured specimens in the air. Compared to specimens cured in air, those cured underwater have sufficient free water to sustain the progress of the cement hydration reaction.

Figure 4.5 shows the MIP test results. As the curing stress increases, the pores are significantly compressed. The maximum pore diameter is less than 200 μ m for the specimens curing with confinement, while the maximum pore diameter is greater than 200 μ m for the specimens without confinement. The pore size density function exhibits an unimodal curve, and the pore size distribution is mainly concentrated in the range of 0.01 μ m to 1 μ m. When the curing stress increases from 0 to 300 kPa, the pore size density decreases with the increase of curing stress. The population pores diameters at 0, 150, and 300 kPa are 0.11 μ m, 0.06 μ m, and 0.05 μ m, respectively, indicating that curing stress alters the pore structure inside the cemented marine clay. As shown in Figure 4.5, the pore size density corresponding to a pore diameter of 0.05-2 μ m significantly decreases, while the density corresponding to a pore diameter of 0.005-0.05 μ m slightly increases.

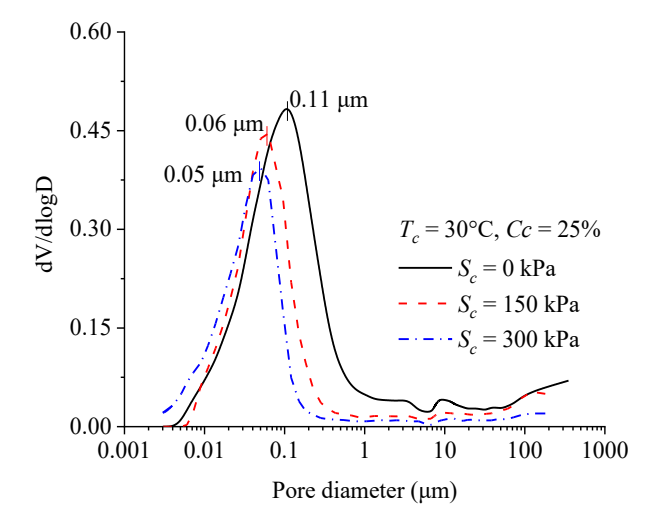


Figure 4.5 MIP results for the specimens at different curing stresses

According to the study of Sun et al. (2024b), pores in the 5-50 nm range mainly represent inner-aggregate pores, while pores with diameters from 50 nm to 2 µm include inter-aggregate pores in kaolinite and C-S-H, as well as capillary pores (Zeng et al. 2012; Yu et al. 2016;

Dewitte et al. 2022). Hence, the MIP results here suggest that increased curing stress compresses the aggregate pores, potentially contributing to the formation of a more stable cemented structure.

4.2 Interpretations of unconfined compression test and microstructure test results

4.2.1 Effects of cement content on the unconfined compression test behaviour

Figure 4.6 shows the stress-strain relationship of cemented marine clay with varying cement contents obtained from unconfined compression tests. As anticipated, the UCS increases with an increase in cement content, attributed to the growing cementation bonds as the cement content rises. The specimens demonstrate a brittle failure mode after reaching the peak strength, occurring at a strain of approximately 1.5%, due to the inherent brittleness of the cementitious matrix (Ismail et al. 2002).

Figure 4.6b illustrates the corresponding stiffness degradation curves. The secant Young's modulus is the ratio of vertical stress to vertical strain. It was observed that specimens with higher cement content exhibit a higher modulus during compression. Moreover, an important parameter of the stiffness degradation curve is the elastic threshold strain (ε_e), which represents the point below, where soil behaviour is predominantly elastic with an almost constant modulus, and the internal structure of the soil remains almost unchanged. In this study, ε_e was determined as the axial strain corresponding to $E_{sec}/E_0 = 0.95$, following the method used by Clayton and Heymann (2001). The obtained ε_e value is around 0.01%, and it slightly increased with an increase in cement content.

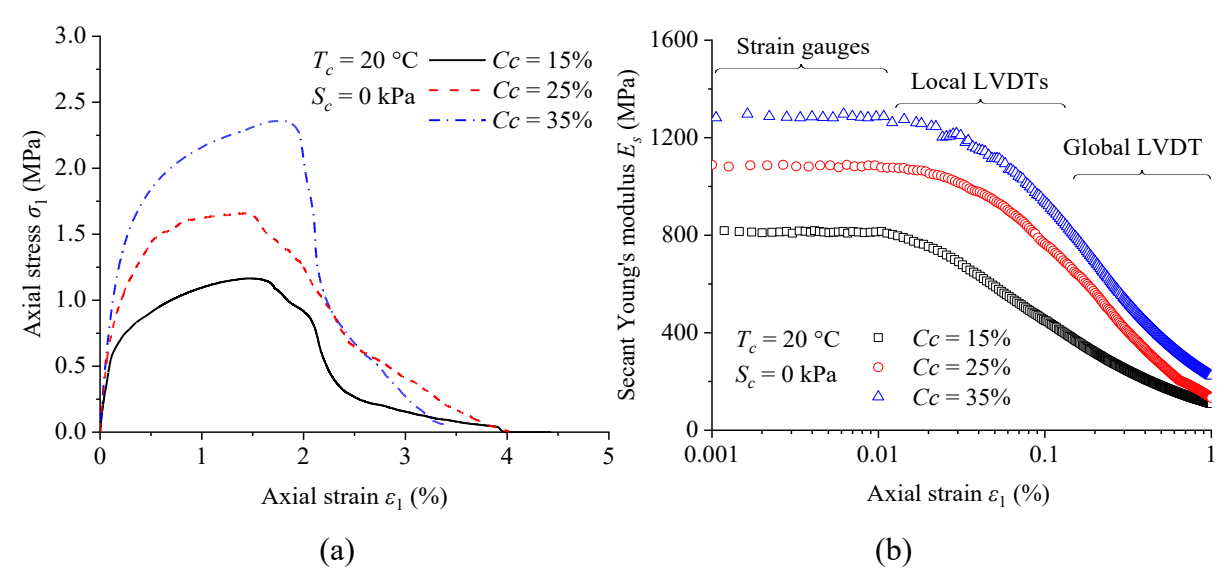


Figure 4.6 Typical results of UCS tests for different cement contents: (a) stress-strain relation; (b) stiffness degradation curve

4.2.2 Effects of curing temperature on the unconfined compression test behaviour

Figure 4.7 illustrates the UCS and E_{50} of specimens at different curing temperatures. As the curing temperature increased from 20 to 40°C, the UCS nearly doubled, and the E_{50} increased by approximately 50%. The increase in strength and stiffness with rising curing temperature can be attributed to the accelerated rate of cement hydration at elevated temperatures, producing more hydration products. Furthermore, higher temperatures promote pozzolanic reactions, which generate additional strength-enhancing hydration products. These hydration products fill the pores, effectively linking soil particles and aggregates, thereby increasing the contact stiffness and contact area between the soil particles. Consequently, both the strength and modulus were significantly improved. These observations are elucidated by the results of TG analysis and MIP tests.

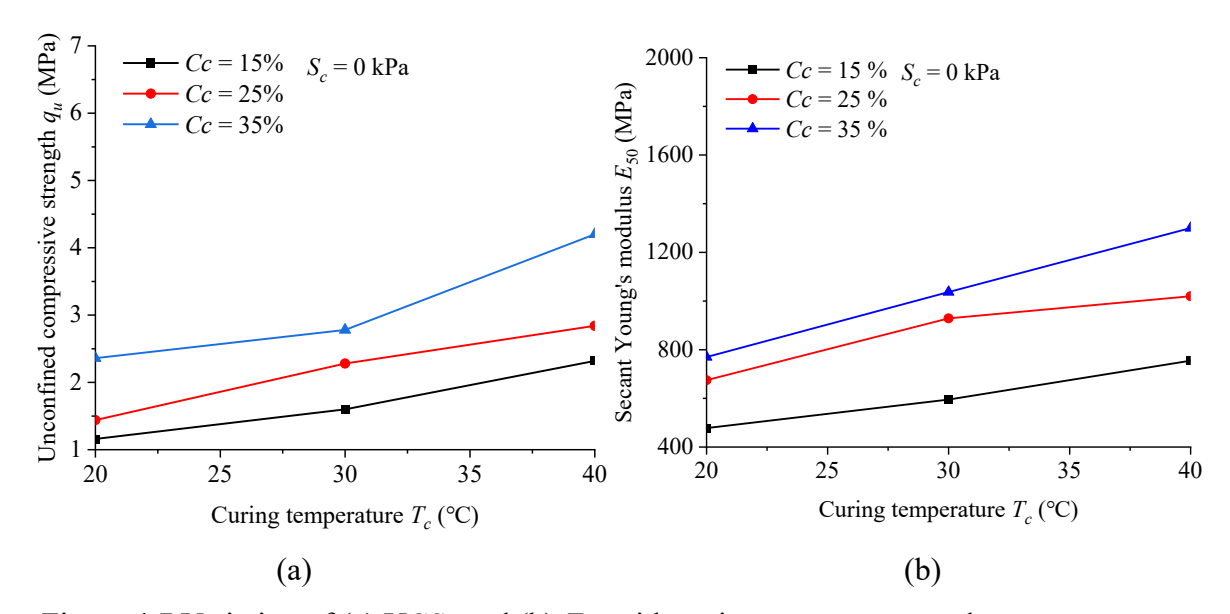


Figure 4.7 Variation of (a) UCS; and (b) E_{50} with curing temperature and cement content

Figure 4.8 depicts the degradation curves of secant Young's modulus within small strain range. When the axial strain is below approximately 0.01%, the soil behaviour is essentially elastic, and the shear stiffness remains almost constant at each curing temperature. However, when the strain exceeds 0.01%, the modulus degrades rapidly with increasing axial strain. Specimens cured at higher temperatures consistently exhibit a higher secant modulus, regardless of the strain amplitude.

To examine the potential influence of curing temperature on the stiffness degradation rate, the secant Young's modulus E is normalized by E_0 . Figure 4.8 shows the degradation curve of E/E_0 , with the results from the specimens with 15% cement content as an example. The change in curing temperature slightly affects the degradation curve. Firstly, the elastic threshold strain

decreases with increasing curing temperature. Secondly, the degradation curves for different curing temperatures intersect within the small strain range. Compared with specimens cured at a lower temperature, the stiffness degradation rate for specimens cured at a higher temperature is initially larger and subsequently becomes smaller (see Figure 4.8).

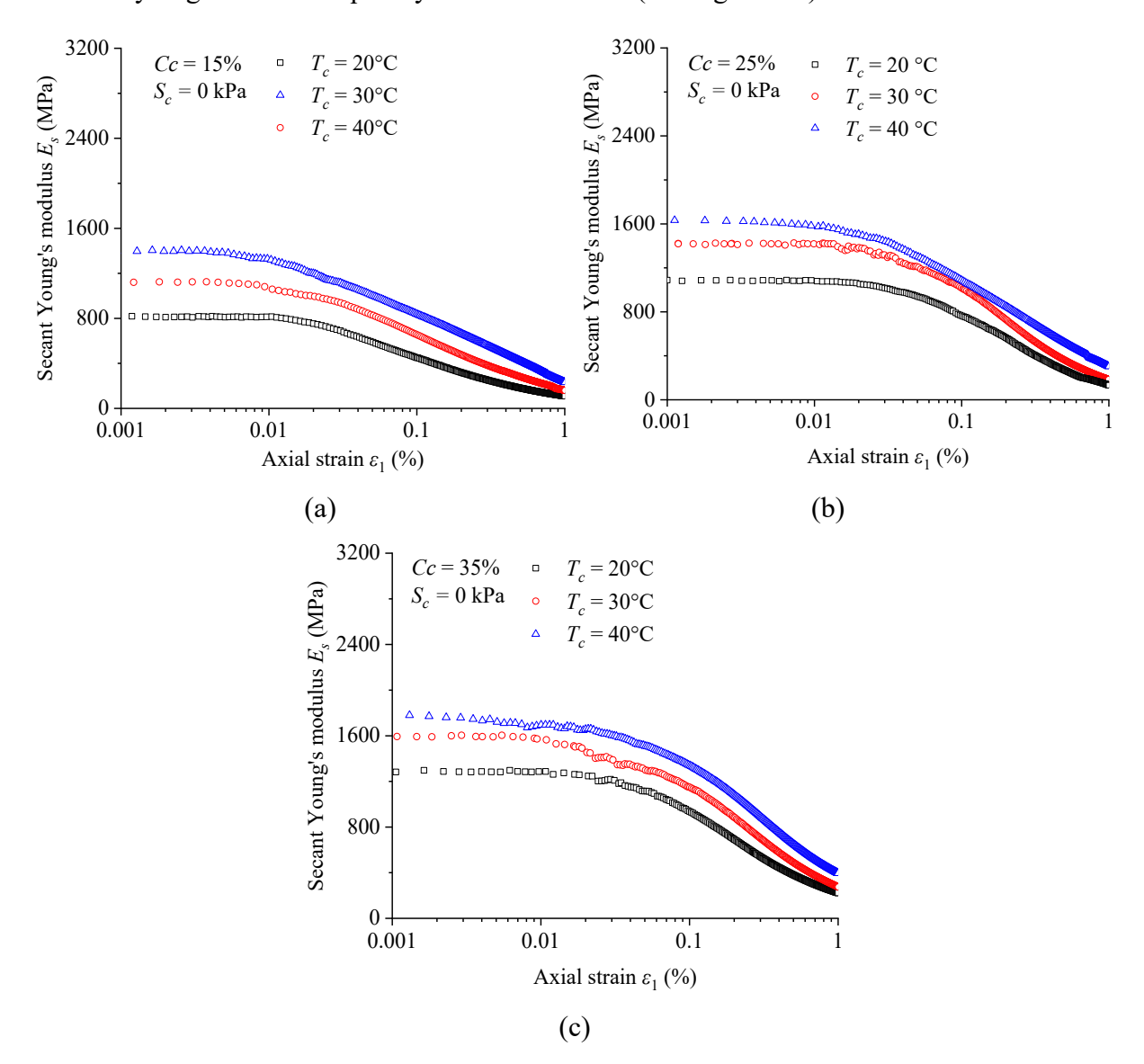


Figure 4.8 Effects of curing temperature on stiffness degradation curves of cemented marine clay: (a) Cc = 15%; (b) Cc = 25%; (c) Cc = 35%

This difference in stiffness degradation rates may be due to the fact that the stiffness degradation is affected by different mechanisms. When the strain is relatively small, the primary cause of stiffness degradation is the breakage of inter-particle bonds. Specimens cured at higher temperatures have more cementation bonds, a more uniform pore size distribution, and fewer large pores, as confirmed by the TG analysis and MIP test results. Consequently, these specimens are more strain-sensitive, resulting in a smaller elastic threshold and higher

degradation rate when the strain is relatively small. When the strain is relatively large, the rearrangement of soil particles becomes the major reason for the stiffness degradation. As explained before, the stiffness degradation induced by particle rearrangement is comparable, so the normalized stiffness degradation rate with large E_0 is smaller.

Figure 4.9 presents the normalized modulus reduction curves of specimens cured at different temperatures. By comparing these curves, it can be observed that at small strains, the modulus reduction increases with higher curing temperatures. However, as the strain approaches approximately 1%, the modulus reduction curves for specimens cured at different temperatures tend to converge. This phenomenon can be attributed to the fact that the mechanisms governing modulus reduction differ between small and large strain levels. At small strains, the reduction in modulus is primarily due to changes in the cementation structure, and higher curing temperatures result in a denser pore structure in the specimens, leading to a higher initial modulus. In contrast, at larger strains, the reduction in modulus is mainly caused by the rotation and movement of soil particles. As a result, the modulus reduction curves of the three specimens become increasingly comparable at higher strain levels. To further analyse the stiffness degradation characteristics of uncemented marine clay, predictions by the equation of Vardanega and Bolton (2013) are incorporated in Figure 4.9 for comparison.

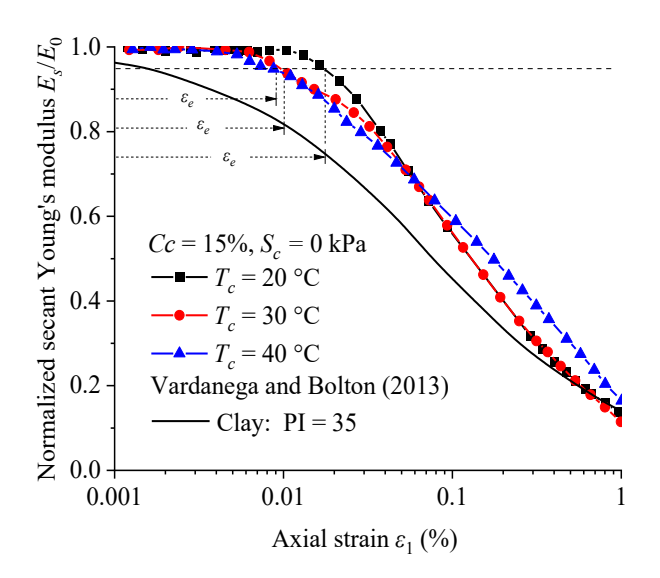


Figure 4.9 Normalized modulus degradation curves of cemented soil at different curing temperatures

Vardanega and Bolton (2013) summarised the shear modulus-strain response data of 21 uncemented fine-grained soils, including clay and silt, and proposed a hyperbolic model to model the shear modulus degradation curve of fine-grained soils. Their study demonstrated that using the plasticity index (PI) of uncemented fine-grained soil as a model parameter yields

sufficiently accurate predictions of shear modulus degradation. Assuming the degradation of shear modulus aligns with the degradation of Young's modulus, the degradation of Young's modulus of the test marine clay can be estimated. The PI of the marine clay is 35, and its degradation curve is shown in Figure 4.5. Compared to the uncemented marine clay, the E/E_0 values of the cemented specimens are generally higher. However, the difference reduces with increasing strain. The primary reason is that cement hydration products bond soil particles together, significantly enhancing soil stiffness (Clough et al. 1981). At smaller strains, the damage to the cementation bonding is negligible, resulting in a relatively lower rate of modulus degradation. However, as the strain increases, the generation of plastic volumetric and deviatoric strain (Suebsuk et al. 2010) leads to the deterioration of the cemented structure. Consequently, as the strain increases, the modulus gradually converges to that of uncemented soil.

4.2.3 Effects of curing stress on the unconfined compression test behaviour

Figure 4.10 illustrates the variation of UCS and E_{50} with curing stress. Both UCS and E_{50} show a significant increase with the rise in curing stress. As the curing stress increases from 0 to 300 kPa, the UCS nearly doubles, and the E_{50} increases by approximately 50%. The increase in UCS and E_{50} is attributed to the reduction in void ratio and the enhanced cementation bonds during curing, which have the most significant influence on the stability of the soil skeleton (Fernandez and Santamarina 2001), as demonstrated by the TG analysis and MIP test results. Moreover, the data indicates that with a curing temperature of 30°C, as the curing stress increases from 0 to 150 and 300 kPa, the UCS increases by 29% and 92%, respectively. With a curing temperature of 40°C, the UCS increases are 70% and 115% for the same increments in curing stress. These comparisons suggest that an increase in curing temperature magnifies the effects of curing stress. The higher the curing temperature, the more hydration products are produced, contributing to the effective bonding between soil particles. This, in turn, amplifies the effects of curing stress on the cementation bonds.

Figure 4.11 illustrates the stiffness degradation curves of specimens subjected to different curing stresses. As the strain increases, the Young's modulus of the specimens rapidly decreases, reaching approximately 25% of its maximum value when the strain reaches 1%. Specimens subjected to higher curing stresses consistently exhibit higher modulus. For example, the elastic Young's modulus of specimens cured at 300 kPa is 1.7 times that of specimens cured at 0 kPa.

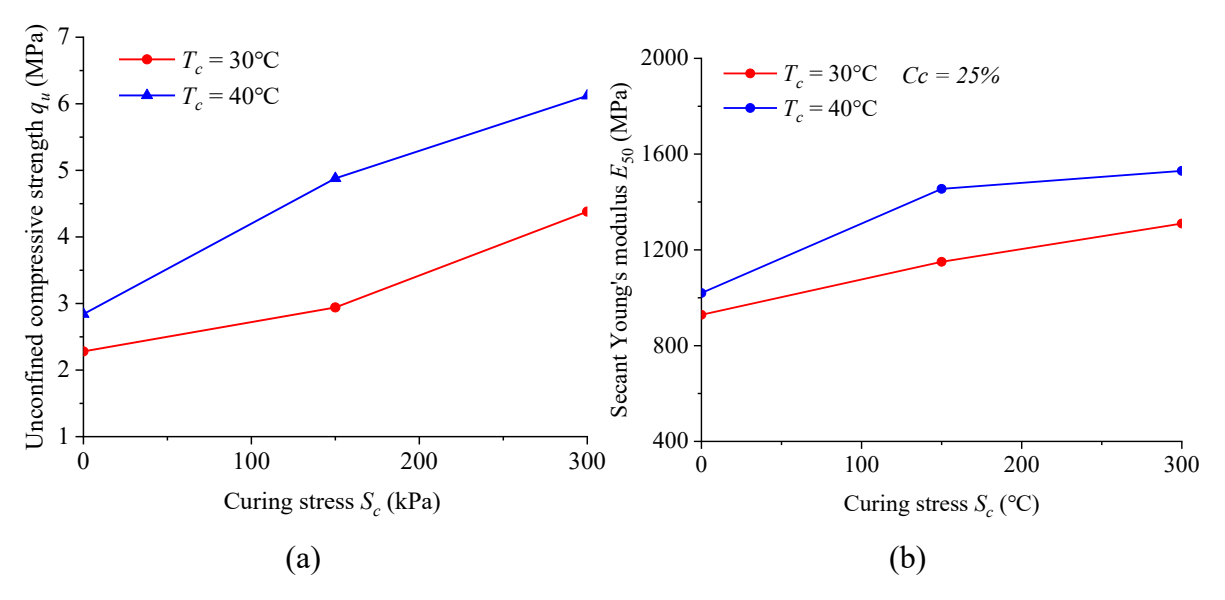


Figure 4.10 Influence of curing stress on (a) UCS; and (b) E_{50}

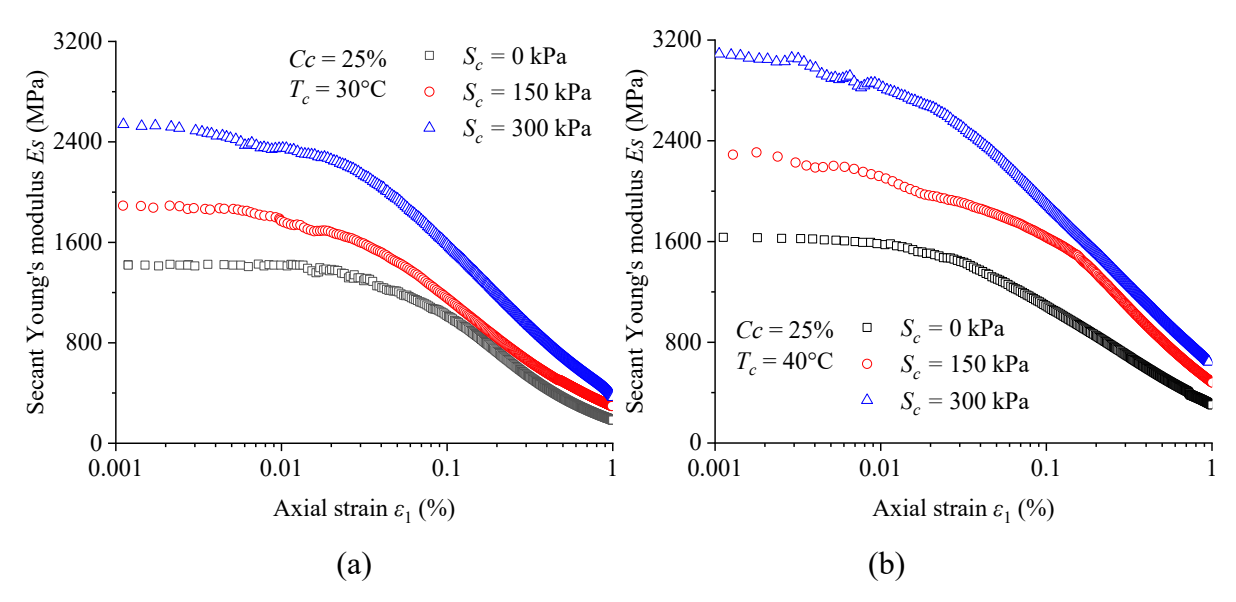


Figure 4.11 Stiffness degradation curves of cemented soil at different curing stresses(a) $T_c = 30^{\circ}\text{C}$; (b) $T_c = 40^{\circ}\text{C}$

Figure 4.12 presents the normalized Young's modulus decay curve, demonstrating that as the curing stress increases, the elastic threshold strain decreases, and the rate of stiffness degradation increases.

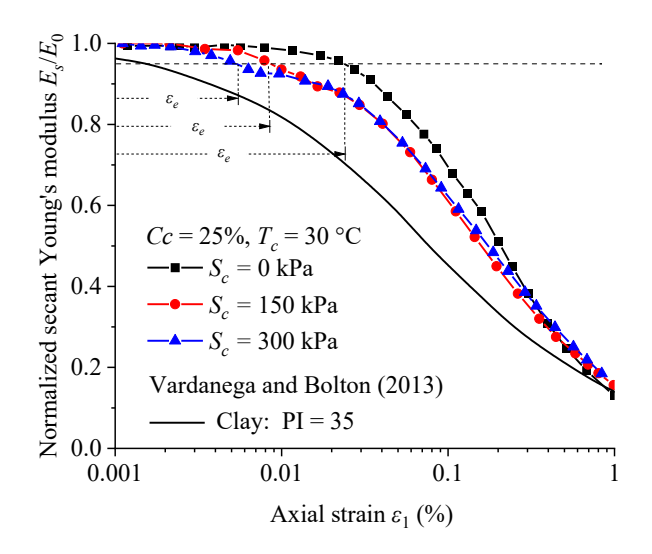


Figure 4.12 Normalized modulus degradation curves of cemented soil.

The difference is minor for specimens cured at 150 and 300 kPa. Compared to pure clay, the stiffness of cemented marine clay exhibits a slower degradation rate within a smaller strain range. At 1% strain, the normalized modulus degradation curve of the cemented marine clay converges with that of pure marine clay. This trend is consistent with the results of Subramaniam and Banerjee (2020) for specimens under low confining pressure. The results suggest that the bonding between soil particles influences the nonlinearity of stiffness. The elastic threshold strain decreases with increasing curing stress because the higher curing stress leads to a refined pore structure of the specimens, as confirmed by the subsequent MIP test results. The cementation structure is more susceptible to damage for the specimens with a refined pore structure as the strain increases. It may be because stiffness degradation is affected by both the destruction of the cementation structure and the rearrangement of soil particles. At relatively small strains, the destruction of the cementation structure is the major reason for stiffness degradation. When the strain is relatively large, the rearrangement of soil particles becomes the major reason for the stiffness degradation. As explained before, the stiffness degradation induced by particle rearrangement is comparable, so the normalized stiffness degradation rate with large E_0 decreases gradually.

4.3 Interpretations of undrained triaxial shear test results

4.3.1 Effects of cement content on the undrained triaxial shear behaviour

Figure 4.13a shows the stress-strain behaviour under undrained triaxial shear conditions with varying cement contents. As the cement content increases from 15% to 25%, the peak strength significantly increases by 25%, attributed to the enhanced cementation bonds resulting from the higher cement content. The strength of the specimen with 15% cement content is

slightly higher at higher confining pressure, which is consistent with the behaviour of uncemented soil influenced by confining pressure. In contrast, the strength of the specimen with 25% cement content is almost unaffected by confining pressure. Similar behaviour has been reported in other studies (Horpibulsuk et al. 2004), attributing this phenomenon to the cementing effects being too strong relative to the effects of confining pressure. Consequently, the increase in strength due to confining pressure is not observed. Additionally, a more important reason might be the increase in pore water pressure, which will be discussed in detail later when introducing the pore pressure variation curve.

The peak strength rapidly reached approximately 1% axial strain. As the confining pressure increases, the strain corresponding to the peak strength gradually decreases. In the unconfined compression test, the peak strength is reached at approximately 1.5% strain, whereas in the undrained triaxial shear test, it is reached at approximately 1% strain. This difference may be due to the change in boundary conditions, as the undrained shear condition allows the material to reach peak strength at a smaller strain. After the peak strength, the stress exhibits brittle behaviour similar to that observed in unconfined compression tests. Approximately 80% of strain-softening occurs within the 1.5% to 2% strain range. Within the range of confining pressures used in this study, the strain-softening behaviour of the samples did not show a clear trend of being affected by the confining pressure. The possible reason is that cementation degradation dominates the strain-softening, and cementation degradation may be strain-dependent rather than confining pressure-dependent. Another reason could be that the confining pressure is too low to reflect its influence. Notably, there is no transition from brittle to ductile failure with increasing confining pressure, as reported in previous studies (Consoli et al. 2000).

Figure 4.13b shows the variation of excess pore water pressure with strain during the triaxial shear process, while Figure 4.13c presents the effective stress path curves of the undrained triaxial shear tests. These two aspects are explained together to better understand the undrained triaxial shear behaviour of cemented soils. In Figure 4.9c, the entire shearing process is divided into three stages.

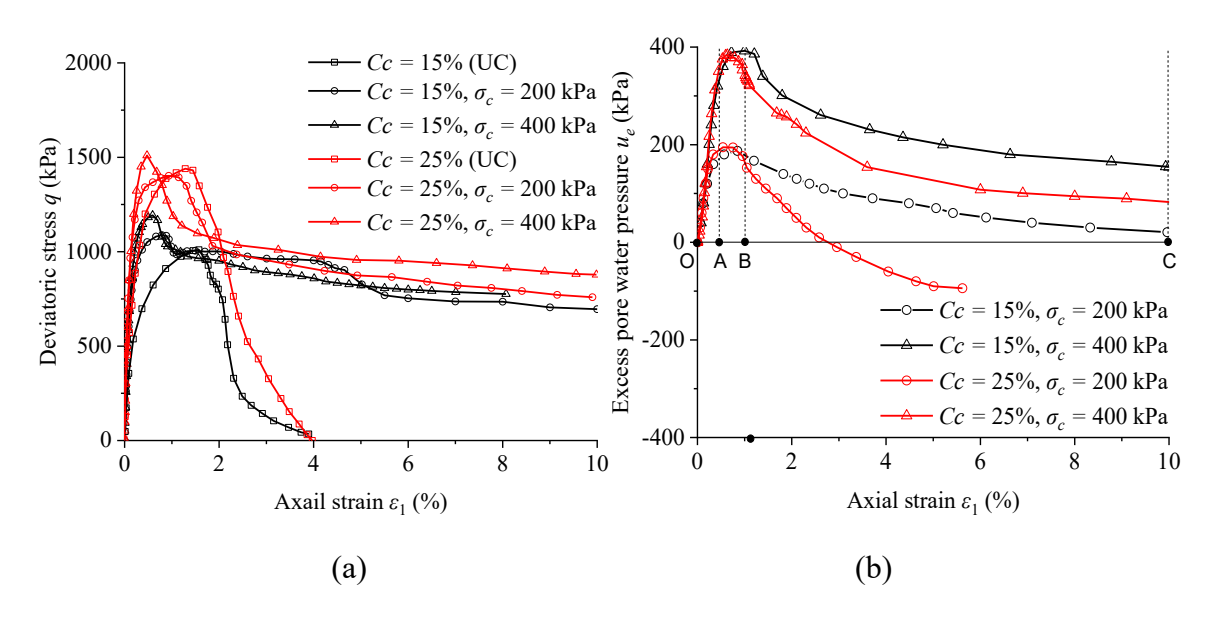
In Stage 1 (OA), the effective stress path increases vertically, and the pore water pressure gradually rises to approach the effective confining pressure after consolidation. When the stress path approaches the tension cut-off line, it indicates that the effective confining pressure is almost zero. During Stage 1, the specimen exhibits elastic behaviour, with the stress path increasing almost vertically.

In Stage 2 (AB), the stress path grows to the peak strength along the tension cut-off line,

accompanied by shear dilatancy, with the effective confining pressure equal to zero. This stage corresponds to a small plateau on the excess pore water pressure curve, where the excess pore water pressure is close to the initial confining pressure. This explains why the triaxial shear strength is relatively unaffected by confining pressure; when the stress reaches peak strength, the effective confining pressure is nearly zero. Horpibulsuk et al. (2004) observed similar behaviour in their study and attributed the confining pressure-independent strength to the dominance of cementation in determining strength during triaxial tests.

After the stress reaches peak strength, it begins to decrease, marking the onset of Stage 3 (BC), the strain-softening part. Throughout this stage, the mean effective stress path is primarily located on the right side of the peak strength point, indicating a trend of dilatancy accompanying the strain softening. Compared to specimens with 15% cement content, those with 25% cement content exhibit a faster decrease in pore pressure, suggesting that increased cement content results in a greater dilatancy trend.

Figure 4.13d presents the secant modulus degradation curves for different specimens. Throughout the small strain range, specimens with higher cement content consistently exhibit higher modulus, indicating that cement content significantly enhances the stiffness of the specimens. Under different confining pressure conditions, the modulus and its degradation curves of the specimens remain relatively unchanged. There are two main reasons for this: first, the effective confining pressure is almost zero within the small strain range, as discussed above; second, previous studies (Yun and Santamarina 2005; Trhlíková et al. 2012) have pointed out that various factors, including confining pressure and fabric, such as void ratio and the bonding between soil particles influence soil stiffness. When the inter-particle bonding is strong, the effects of confining pressure is less significant.



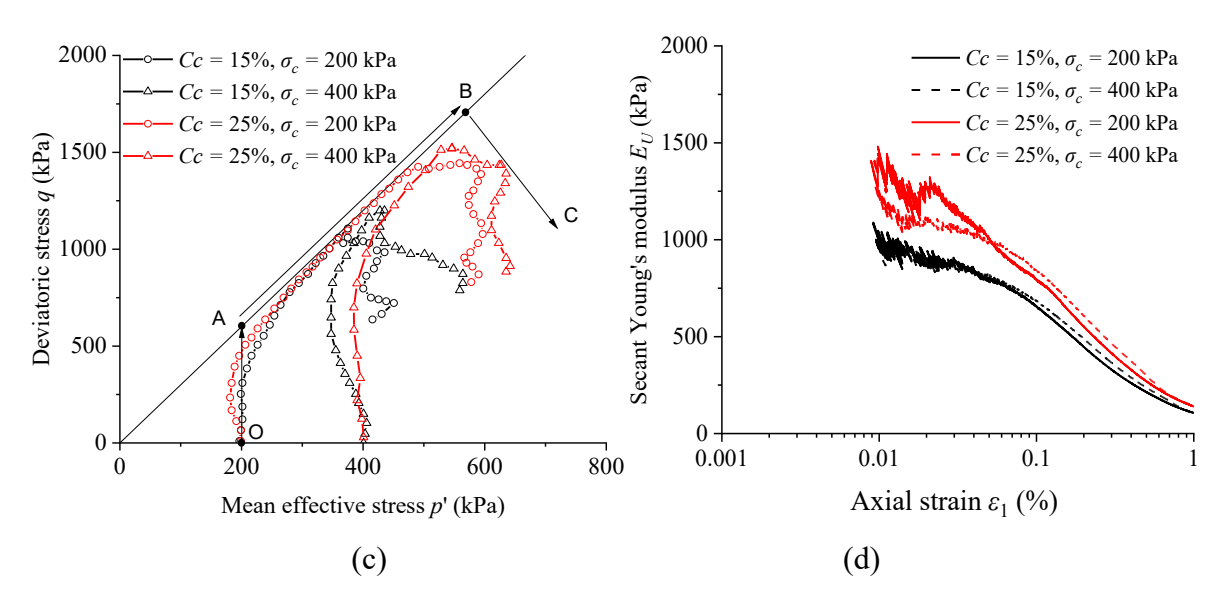


Figure 4.13 Undrained triaxial shear test results for cemented soil with ($T_c = 20$ °C, $S_c = 0$ kPa) cement content: (a) deviator stress versus axial strain; (b) excess porewater pressure versus axial strain; (c) effective stress paths; (d) small strain stiffness degradation curves.

4.3.2 Effects of curing temperatures on the undrained triaxial shear behaviour

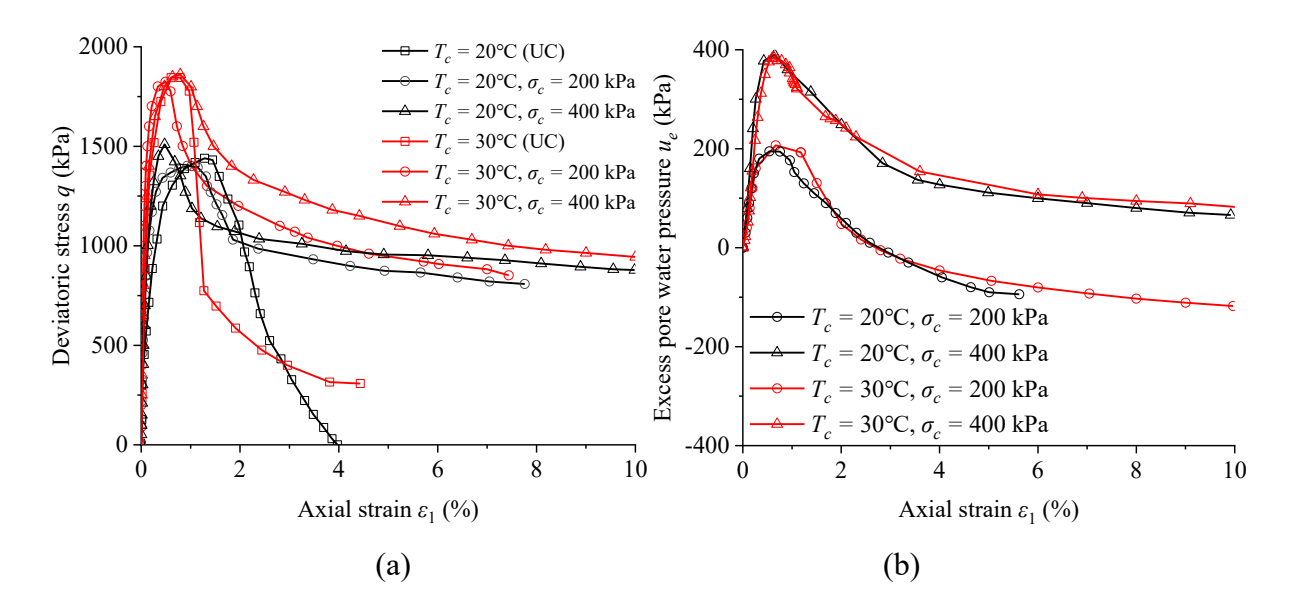
Figure 4.14 compares the triaxial shear behaviour of specimens under different curing temperatures and confining pressures. Figure 4.10a shows the stress-strain curves, indicating that increasing the curing temperature from 20°C to 30°C significantly enhances the unconfined and undrained triaxial shear strength of the specimens. This enhancement is due to the elevated curing temperature accelerating the cement hydration rate, producing more cementitious material within the 28-day curing period at 30°C. Interestingly, the increase in strength due to confining pressure was not apparent; the strength was lower under a confining pressure of 400 kPa. This may be attributed to variations in specimen quality, such as uniformity.

Additionally, the critical state strength of the specimens slightly increases with the rise in curing temperature. According to critical state theory, a smaller void ratio at the critical state (*e-lnp'* curve) corresponds to a higher mean effective stress. The increase in curing temperature leads to more hydration products filling the pores of the specimens, reducing the void ratio, and thus slightly increasing the strength at the critical state. The curing temperature did not significantly affect the strain-softening part. In the unconfined compression test, the stress-strain curve completes its degradation at around 4% strain, whereas in the triaxial test, the curve gradually transitions to the critical state at approximately 10% strain. However, the primary stress reduction occurs between 1% and 2% strain.

Figure 4.14b shows the variation in excess pore water pressure with strain. Constrained by the tension cut-off line, the excess pore water pressure initially increases to approach the initial

effective confining pressure after consolidation and then gradually decreases. The comparison of the excess pore water pressure changing curves for specimens cured at 20°C and 30°C reveals that curing temperature does not significantly influence the dilatancy properties. The effective stress path in Figure 4.14c shows that the mean effective stress does not consistently show a trend of increase or decrease during the strain-softening process. This may be due to the gradual connection of closed inner and inter-aggregate pores. Regardless of the dilation or contraction trend, significant strain softening is observed. This suggests that the breakage of the cementation structure primarily causes strain softening.

Figure 4.14d shows the modulus degradation curves for specimens cured at different temperatures. The increase in curing temperature results in an increase in modulus across the entire small strain range. The elevated curing temperature accelerates the cement hydration process, producing more cementitious material that enhances the bonding between soil particles. Additionally, changes in confining pressure have negligible effects on the small strain modulus for specimens cured at different temperatures. Therefore, factors affecting cementation, such as temperature and specimen quality, are the key factors controlling the stiffness of cemented soil.



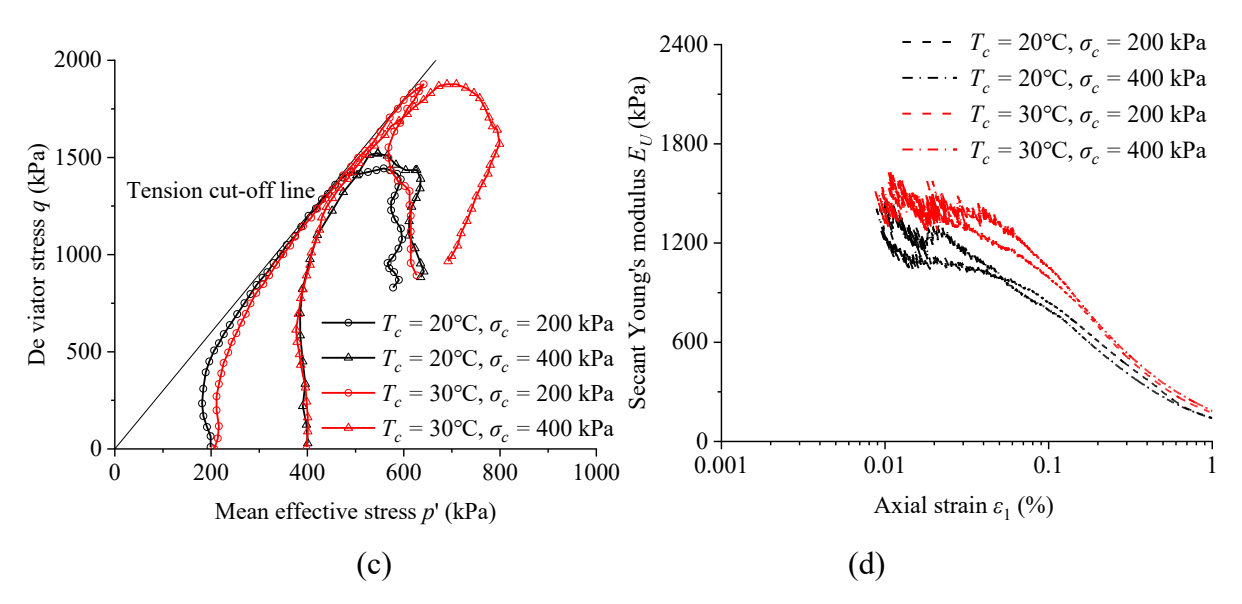


Figure 4.14 Undrained triaxial shear test results for cemented soil (Cc = 25%, $S_c = 0$ kPa) with 20°C and 30°C curing temperature: (a) deviator stress versus axial strain; (b) excess porewater pressure versus axial strain; (c) effective stress paths; (d) small strain stiffness degradation curves.

4.3.3 Effects of curing stress on the undrained triaxial shear behaviour

Figure 4.15 presents the results of undrained shear tests on specimens subjected to varying curing stresses. The stress-strain curves in Figure 4.15a demonstrate that increasing the curing stress significantly enhances the peak strength of cemented soil. Specifically, a 150 kPa increase in curing stress results in a 50% increase in strength, suggesting that the strength of deeper DCM columns may be higher or that their potential strength has not been fully mobilized. Compared to curing temperature, curing stress has a more pronounced effect on the critical state strength. With a 150 kPa increase in curing stress, the critical state strength increases by about 100%. This increase is attributed to the significant reduction in the void ratio due to the application of curing stress. Test data shows that when the curing stress increases to 150 kPa, the void ratio decreases from approximately 1.6 to 1.2. Consequently, in Figure 4.15a, a smaller void ratio corresponds to a significantly higher mean effective stress at the critical state. The increase in curing stress and confining pressure does not affect strain softening. Peak strength is reached at around 1% strain, with major strength degradation occurring within the 1-4% strain range. This suggests that strain is the key parameter controlling decementation.

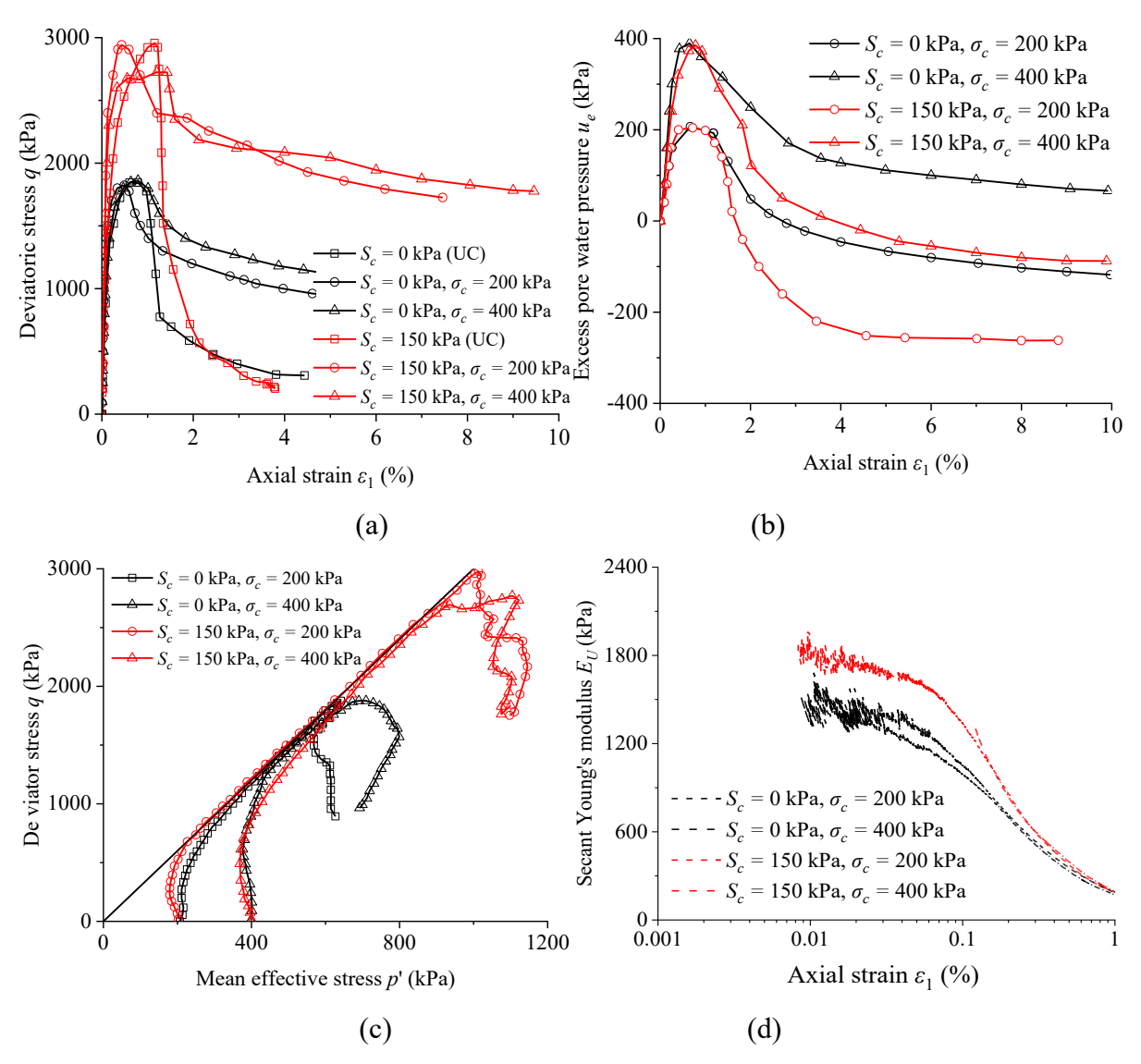


Figure 4.15 Undrained triaxial shear test results for cemented soil (Cc = 25%, $T_c = 20$ °C) curing stress: (a) deviator stress versus axial strain; (b) excess porewater pressure versus axial strain; (c) effective stress paths; (d) small strain stiffness degradation curves.

The pore water pressure results, shown in Figure 4.15b, exhibit a trend consistent with other specimens in this study. The pore water pressure increases initially, reaches a peak value equal to the initial effective confining pressure after consolidation, and then decreases. The undrained triaxial shear strength attains its peak value when the effective confining pressure is approximately zero. Consequently, the undrained shear strength is governed by the bond strength and is nearly consistent with the unconfined compressive strength. It is evident that higher curing stresses result in greater dilatancy of the specimens, as the pore water pressure is more negative for the specimens with 150 kPa curing stress. This may be attributed to the increase in density with higher curing stress. The higher the soil density, the more pronounced its dilatancy.

The effective stress paths of specimens under various curing stresses are illustrated in Figure 4.15c. Initially, typical elastic behaviour is exhibited, as the axial strain increases, the effective stress path rises vertically. Subsequently, a plastic hardening process occurs, accompanied by dilatancy behaviour. After reaching peak strength, the effective stress path decreases, indicating significant internal structural damage. Limited dilatancy behaviour is still observed throughout the strain-softening process, which does not affect the strength reduction. Previous studies (Houlsby 1991; Bolton 1987) have shown that dilatancy dominates strain softening. The test results of this study indicate that for cemented soils, cementation is the primary factor influencing strain softening. Figure 4.15d illustrates the small strain modulus degradation curves. The impact of curing stress on the modulus is more significant than that of confining pressure.

4.4 Interpretations of tensile test results

Figure 4.16 compares the direct tensile strength (DTS) and indirect tensile strength (Brazilian tensile strength, BTS) of cemented clay under various curing conditions. Figure 4.16a illustrates the relationship between BTS and DTS of specimens subjected to different curing temperatures. The data indicate that the BTS of cemented clay significantly increases with curing temperature. Specifically, when the curing temperature rises from 20°C to 30°C, the average BTS increases by approximately 15%. However, a further increase in curing temperature to 40°C results in a 50% increase in tensile strength. Consoli et al. (2014) observed that the rate of tensile strength increase reduces with higher curing temperatures when the binder dosage remains constant. The results of this study differ from those reported by Consoli et al. (2014). Unlike the study of Consoli et al. (2014), where specimens were cured in air, the specimens in this study were cured in a water tank, ensuring sufficient water for the cement hydration process throughout. Previous studies (Zhang et al. 2014; Chau et al. 2024) have proposed that the mechanism by which curing temperature influences the strength of cemented soil involves accelerating the cement hydration rate and enhancing specific chemical reactions that require water.

The test results indicate that the average DTS slightly increases with curing temperature, but the increase is much smaller than that of the BTS. When the temperature rises from 20°C to 40°C, the average DTS increases by about 10%, while the BTS increases by 50%. Previous studies have discussed the reasons for the differences between BTS and DTS, attributing them to the different stress states in these two tests (Li and Wong 2013) and pre-existing microcracks (Erarslan and Williams 2012). Direct tensile strength is primarily affected by pre-existing

microcracks. Consequently, due to the numerous internal defects present in the specimen, the DTS does not increase as significantly as the compressive strength.

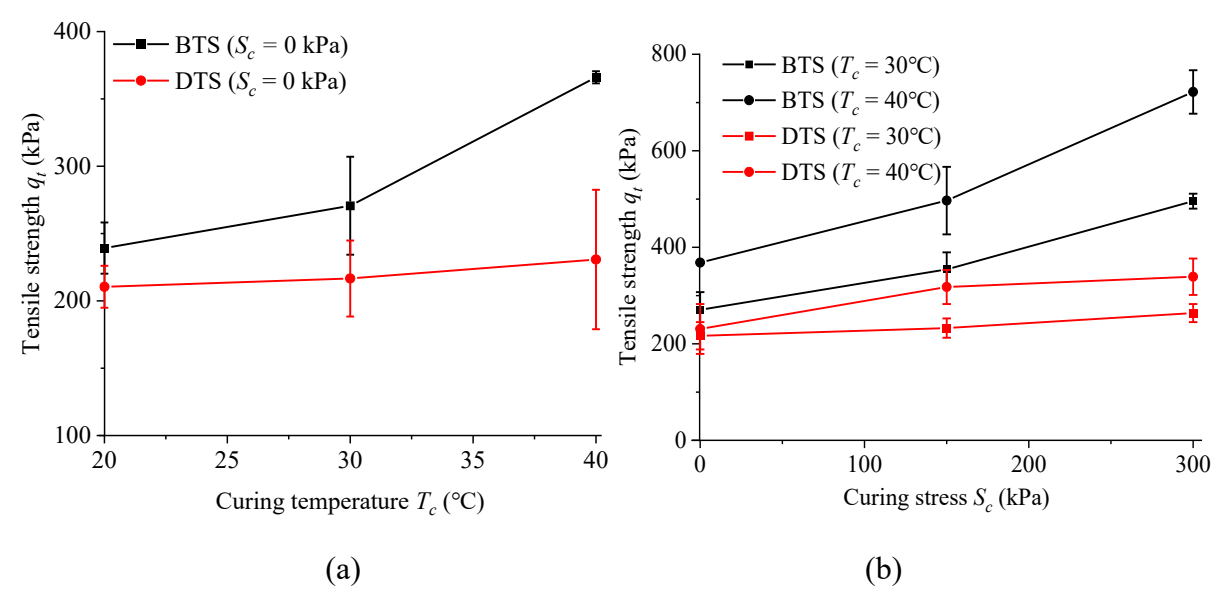


Figure 4.16 (a) Influence of curing temperature on tensile strength; (b) influence of curing stress on tensile strength of cemented soil

However, BTS is less sensitive to pre-existing defects. Figure 4.16b compares the BTS and DTS of specimens under different curing stresses. As the curing stress increases, the average BTS rises significantly, with an approximate 80% increase in strength as the curing stress increases from 0 to 300 kPa. This increase is substantial in both the 0-150 kPa and 150-300 kPa ranges. However, the DTS primarily increases when the curing stress rises from 0 to 150 kPa, showing a 30% increase in tensile strength. When the curing stress increases from 150 to 300 kPa, the average tensile strength increases by only about 10%. The increase in curing stress leads to an increase in strength, primarily because higher curing stress reduces the void ratio, significantly decreasing the pre-existing defects within the specimen.

4.5 Correlation between stiffness and strength

4.5.1 Correlation between UCS and E₅₀

Different aspects of the small strain behaviour of cemented marine clay have been discussed in detail. The results can provide valuable insights and data for theoretical modelling. From the perspective of engineering designs following current design methods, the stiffness of cemented soil is usually assumed to be constant with the use of E_{50} (Kitazume and Terashi 2013).

On the one hand, the test data shows that the corresponding strain for E_{50} typically falls in

the strain range of 0.3% to 0.5%. When the strain increases to this range, the modulus decreases to about 30% of its initial value. This simplified approach of using E_{50} is not always appropriate. For example, E_{50} may be too conservative for DCM-stablised foundation where the encountered strains are mainly located within smaller strains (Phutthananon et al. 2023). In contrast, for deep excavation in DCM-treated ground (Meepon et al. 2016), the strain could be much greater than 0.5%. The use of E_{50} could overestimate soil stiffness and underestimate the ground deformation. Therefore, the selection of modulus needs to be determined based on the expected strain values. If E_{50} is used, a correction factor should be applied.

On the other hand, it is crucial to estimate E_{50} accurately in the current engineering practices. Two approaches for determining the E_{50} value are described below. Approach 1 utilizes the empirical linear relationship between UCS and E_{50} from the current design guidelines. For instance, both FHWA (2013) and the SCDOT (2022) suggested that the E_{50} should be 300 times the UCS for the wet mixing method, whereas, for the dry mixing method, it should be 150 times the UCS. Based on these design guideline recommendations, Equation (4-2) was proposed:

$$E_{50} = kq_u \tag{4-2}$$

where k = the coefficient representing the linear relationship between E_{50} and the qu, which can be determined by curve fitting. To evaluate the performance of Equation (4-2), previously published data (Swasdi et al. 2007; Bushra and Robinson 2013; Mansour et al. 2015) and tested data in the current study (summarised in Tables 4.2) were utilized, with a primary focus on studies of cemented clay.

Figure 4.17a and 17b compare the test results with the calculated results using Equation (4-2). The maximum discrepancy between the test data from this study and the calculated results from Equation (4-2) is around 40%. For data from the literature, the maximum error is approximately 100%. In current engineering practice, the input parameters are mostly determined without considering the influence of curing temperature and stress (FHWA 2013; SCDOT 2022). For cemented marine clay in the current study, the ratio of E_{50} to UCS is 280, which is close to the value recommended by guidelines (Bruce et al. 2013; SCDOT 2022) for the wet mix method. Therefore, Equation (4-2) could still be used as long as the increase in strength with curing temperature and stress is properly considered.

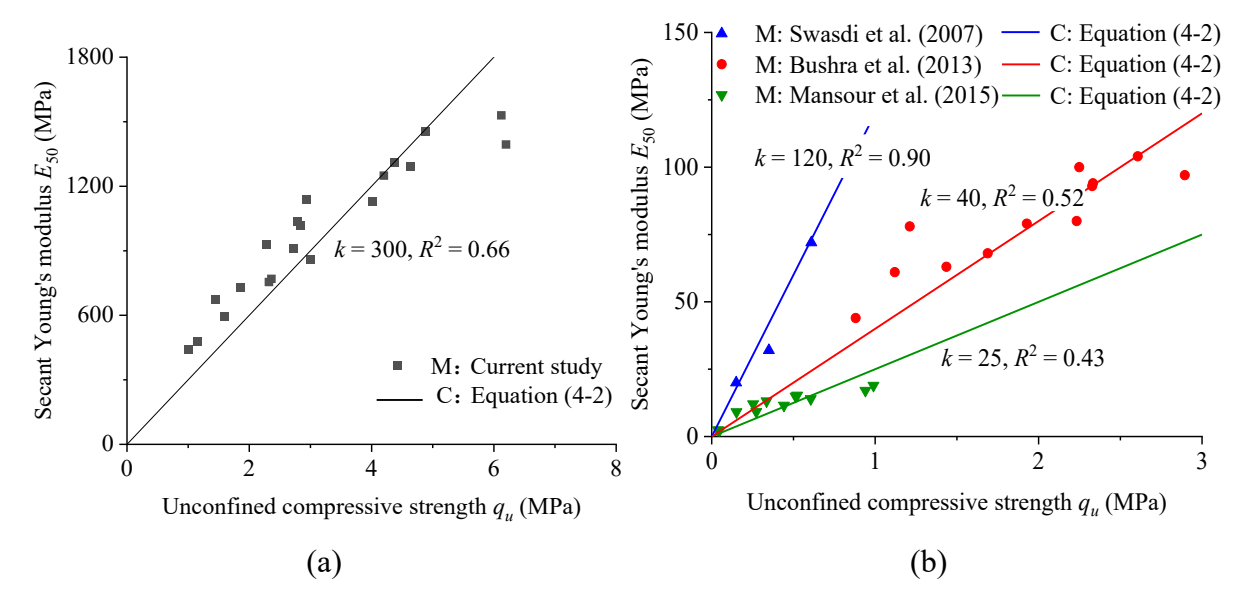


Figure 4.17 Comparison of calculated and measured (M) results: (a) Equation (4-2) and data from the current study; (b) Equation (4-2) and data from the previous study

The above approach may be used in engineering practice to estimate E_{50} . However, the coefficient of determination R^2 between the calculated and measured results is low for some cemented soils. Hence, an alternative approach has been proposed in this study. The test results show that the stiffness of cemented soil is not only controlled by cementation but also affected by other factors, such as void ratio. So far, many formulas have been proposed to calculate the elastic shear modulus incorporating density, stress, and cementation effects. Using a similar mathematical form and considering the mean effective stress corresponding to E_{50} is qu/6 in UC tests, the following equation is proposed for E_{50} .

$$E_{50} = A(1+e)^{-1.3} \left(\frac{q_u}{p_r}\right)^{0.5} \tag{4-3}$$

where A and n_s = model parameters; e = the void ratio; q_u = the unconfined compression strength; and p_r = a reference pressure taken as 100 kPa here. In the formula, the term q_u represents the quantitative cementation and incorporates the mean effective stress on E_{50} . This alternative method can be used when accurate analysis is desired and more data is available. The comparison between the measured and predicted E_{50} using Equation (4-3) is shown in Figure 4.18. The parameters used are also included in the figures. Compared to Equation (4-2), Equation (4-3) provides better modulus prediction results. This significant improvement is due to incorporating the density effects and using a nonlinear equation for E_{50} calculation.

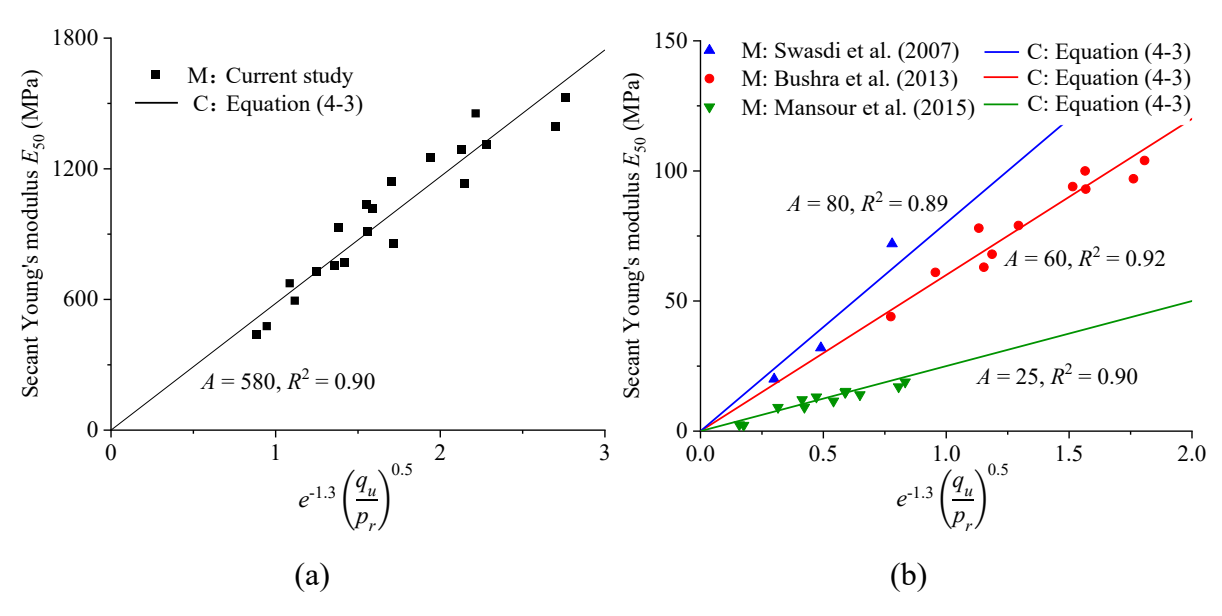


Figure 4.18 Comparison of calculated and measured (M) results: (a) Equation (4-3) and data from the current study; (b) Equation (4-3) and data from the previous study

4.5.2 Correlation between UCS and tensile strength

Figure 4.19 illustrates the relationship between tensile strength and UCS. Both DTS and BTS exhibit considerable variability, which is represented in the figure by average values with error bars. In Figure 4.19a, the variation of BTS with increasing UCS is shown. The average ratios suggest a slight decrease as UCS increases: when UCS is approximately 1 MPa, the BTS/UCS ratio is about 0.17, while at a UCS of 6 MPa, the ratio stabilizes around 0.10. Similarly, Figure 4.19b shows that the DTS/UCS ratio decreases from about 0.15 at a UCS of 1 MPa to 0.06 as UCS increases. The primary reason for this trend is that internal defects may close under compressive loading, having minimal impact on compressive strength. In contrast, stress concentrations at internal defects can significantly reduce tensile strength during tensile testing. DTS, in particular, appears more sensitive to internal defects than BTS. Due to the limited amount of tensile strength data, it is not possible to draw a strong conclusion regarding the effects of curing temperature and curing stress on the tensile-to-compressive strength ratio. However, the available results indicate that tensile strength is more sensitive to these factors than compressive strength. Therefore, relying solely on Brazilian tensile strength test results to represent the tensile strength of cemented soil may not be conservative. Some engineering practices (Suzuki 1982; Kivelo 1998) suggest using a tensile strength value of 10% to 15% of UCS, which may overestimate the actual tensile strength.

Table 4.2 Summary of main properties of tested specimens

Curing temperature, T_c (°C)	Curing stress, S_c (kPa)	Cement content,	Void ratio (after curing), <i>e</i>		q _u (MPa)		E50 (MPa		- E ₀ (MPa
			Test 1	Repeated test	Test 1	Repeated test	Test 1	Repeated test	- 20 (MI u
20	0	15	1.68	1.68	1.16	1.01	478	439	816
20	0	25	1.62	/	1.44	/	675	/	1080
20	0	35	1.58	/	2.36	/	770	/	1292
30	0	15	1.67	/	1.60	/	595	/	1120
30	0	25	1.60	1.60	2.28	1.86	929	729	1417
30	0	35	1.56	/	2.78	/	1037	/	1600
30	150	25	1.44	1.42	2.94	2.99	1140	857	1890
30	300	25	1.27	1.30	4.38	4.00	1310	1131	2540
40	0	15	1.65	/	2.32	/	755	/	1390
40	0	25	1.54	1.53	2.84	2.72	1020	911	1620
40	0	35	1.53	/	4.20	/	1250	/	1780
40	150	25	1.42	1.45	4.88	4.64	1455	1290	2269
40	300	25	1.23	1.28	6.12	6.19	1530	1394	3081

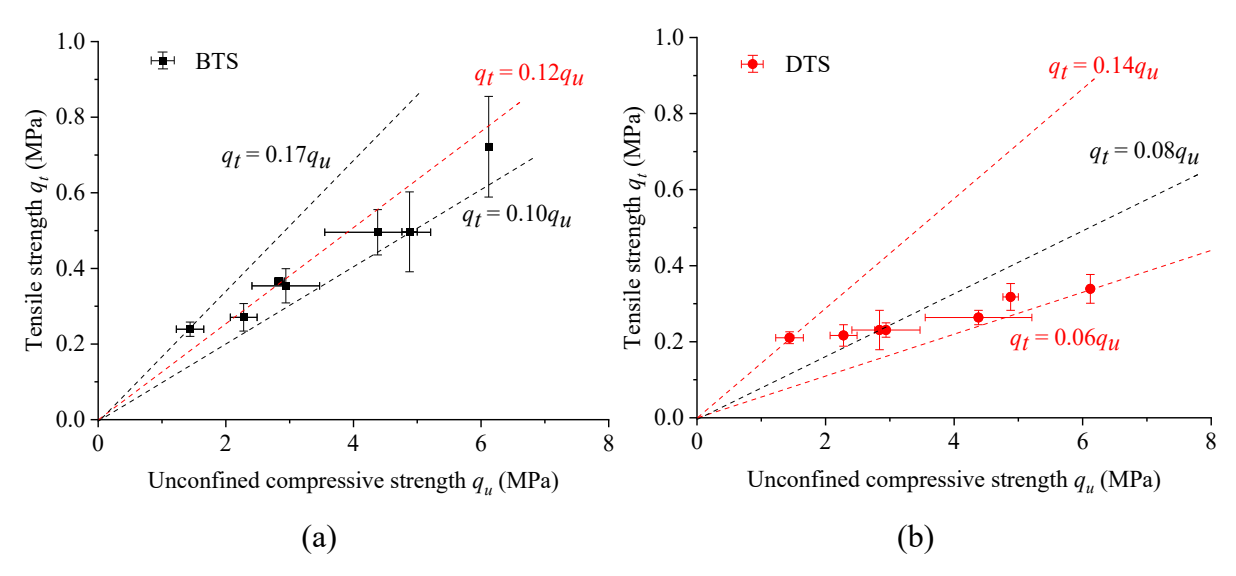


Figure 4.19 (a) Relationship between indirect tensile strength and UCS; (b) relationship between direct tensile strength and UCS

4.6 Summary

As the curing temperature rises from 20 to 40°C, the UCS of cemented marine clay doubles. The strength increase is mainly attributed to the accelerated cement hydration and enhanced pozzolanic reactions resulting from the elevated curing temperature. In particular, the pozzolanic reaction produces more Calcium Silicate Hydrate gel, significantly contributing to the strength gain. Furthermore, the UCS of cemented marine clay doubles as the curing stress increases from 0 to 300 kPa. The increase in curing stress does not affect the cement hydration reaction. Instead, it primarily contributes to pore compression and the formation of more effective cementation structures.

E₀ increases by about 50% as the curing temperature rises from 20°C to 40°C and by 80% when the curing stress increases from 0 to 300 kPa. Accompanying the increase in curing temperature and stress is a decrease in the elastic threshold strain corresponding to the modulus attenuation curve. The reduction of elastic threshold strain is caused by the increase in curing temperature and stress, which leads to smaller pore sizes, as demonstrated by MIP test results. Specimens with smaller pores are more easily damaged with increasing deformation. With further strain increase, the modulus degradation curve of cemented clay initially maintains a high decay rate and then gradually slows down. When the strain reaches 1%, the stiffness converges to approximately 20% of the maximum value. This behaviour may be because, at larger strains, the cementation structure is significantly damaged, and particle rearrangement and pore compression may dominate the stiffness degradation.

As the curing temperature and stress increase, both E_{50} and UCS significantly rise, but their

ratio remains relatively constant. The linear equation recommended by design guidelines (i.e., $E_{50} = 300$ UCS) can be used in engineering practice for approximation. Alternatively, the newly proposed nonlinear equation from this study can be used to predict E_{50} with higher accuracy. This nonlinear equation incorporates the density effects and can improve prediction accuracy with a single parameter compared to the linear equation.

In undrained triaxial shear tests, the peak strength and modulus increase significantly with higher curing temperatures, consistent with observations in unconfined compression tests. The critical state strength also increases with higher curing temperatures due to a reduced void ratio at the critical state. The application of curing stress increases density, enhances overall strength and stiffness, and leads to more pronounced dilatancy behaviour, as evidenced by the faster decrease in pore water pressure during shear tests. The failure of cementation induces significant strain-softening, even in the presence of shearing dilatancy. The influence of confining pressure on strength is negligible because the cementation strength dominates, and the effective stress approaches zero at peak strength.

The test results indicate that the tensile strength of cemented soil generally increases with higher curing temperatures and stresses, accompanied by considerable variability. The ratio of BTS to UCS is approximately 0.12, while the ratio of DTS to UCS is approximately 0.08. The ratio of both direct tensile strength (DTS) and indirect tensile strength (BTS) to unconfined compressive strength (UCS) decreases as UCS increases, which may be attributed to the differing sensitivities of compressive strength and tensile strength to internal defects. During compression tests, internal defects close, which does not affect compressive strength. However, tensile strength is reduced due to stress concentration at internal defects.

CHAPTER 5 A bounding surface model for cemented soil at small and large strains

Many constitutive models have been proposed to characterize the mechanical behavior of cemented soil at large strains (exceeding 1%). However, the highly non-linear stress-strain response at small strains has received less focus, despite its significance for accurately assessing the serviceability of various infrastructures. This study presents a bounding surface model designed to simulate the behavior of cemented soil across both small and large strain ranges. In this study, a bounding surface model was developed to simulate cemented soil behaviour from small to large strains. To capture the degradation of the modulus in the small strain range, a new formula for calculating the shear modulus and a new formula for describing the cementation degradation are proposed. The test results in Chapter 4 and the literature were used to verify the new model. In this chapter, model formulations and parameter calibration are described in detail.

5.1 Mathematical formulations

The proposed model is formulated in the triaxial stress space. The soil stress state is defined using the effective mean stress (p') and deviator stress (q). The deformation is described through the volumetric strain (ε_v) and deviator strain (ε_q) . For the sign convention, compressive stress and strain are considered positive.

5.1.1 Elastoplasticity

Following the bounding surface plasticity theory proposed by Dafalias and Herrmann (1986), the total strain consists of elastic and plastic parts:

$$\begin{cases} d\varepsilon_v = d\varepsilon_v^e + d\varepsilon_v^p \\ d\varepsilon_q = d\varepsilon_q^e + d\varepsilon_q^p \end{cases}$$
 (5-1)

where $d\varepsilon_v$ = total increments of volumetric strain; $d\varepsilon_v^e$ = elastic increments of volumetric strain; and $d\varepsilon_v^p$ = plastic increments of volumetric strain; $d\varepsilon_q$ = total increments of deviator strain; $d\varepsilon_q^e$ = elastic increments of deviator strain; and $d\varepsilon_q^p$ = plastic increments of deviator strain. The incremental elastic strains are calculated using the following formulation:

$$\begin{cases} d\varepsilon_q^e = \frac{dq}{3G_0} \\ d\varepsilon_v^e = \frac{dp'}{K} \end{cases}$$
 (5-2)

where K = the bulk modulus; and G = the shear modulus. The incremental plastic strains are expressed as follows:

$$\begin{cases} d\varepsilon_{\nu}^{p} = D\Lambda \\ d\varepsilon_{q}^{p} = \Lambda \end{cases}$$
 (5-3)

where $D = d\varepsilon_v^p/d\varepsilon_q^p$ is the dilatancy index; and Λ = the non-negative loading index. The dilatancy and loading index can be obtained from the flow rule and the hardening law, which are explained later.

5.1.2 Bounding and yield surfaces

As summarised and illustrated by (Dafalias and Herrmann, 1986), the main feature of bounding surface models is the dependency of the plastic modulus on the distance between actual and 'imaged' stress states. In addition to this general feature, each bounding surface model has some specific features regarding the definition and description of the bounding surface (Zhou et al. 2015). The current model adopts the approach of Wang et al. (1990). Two bounding surfaces are defined in the p'-q plane, as shown in Figure 5.1, both of which intersect with the horizontal axis at the point (p_b , 0). The variable p_b is defined as cementation bond strength and is used to describe the effects of cementation on soil strength. Its initial value and loading-induced evolution are discussed in the next section.

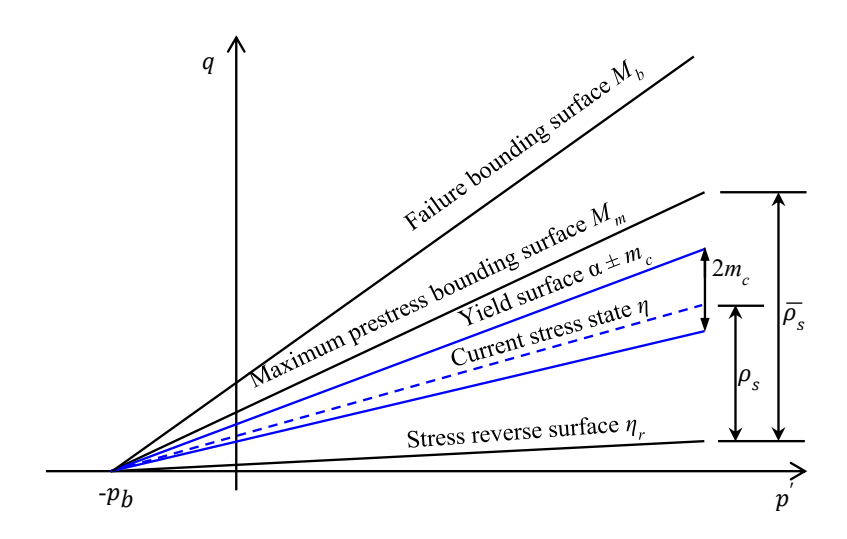


Figure 5.1 Schematic diagram of the yield, maximum prestress memory and failure bounding surfaces in the q-p' plane

The first bounding surface is the maximum prestress memory bounding surface. It can be described as follows:

$$F_s = q - M_m(p' + p_b) (5-4)$$

where M_m = the maximum value of stress ratio in the stress history, defined as $q/(p'+p_b)$.

The other one is the failure bounding surface, which is mathematically defined as follows:

$$\overline{F}_s = q - M_b(p' + p_b) \tag{5-5}$$

$$M_b = M_c exp(-n_b \Psi) \tag{5-6}$$

where M_c = the critical state stress ratio; M_b = the attainable peak stress ratio; and n_b = a positive model parameter used to define the influence of the state parameter on the strength. The location of the failure bounding surface depends on the state variable Ψ , which is defined later. According to equation (5-6), M_b is below and above M_c when Ψ is positive and negative, respectively.

Furthermore, a yield surface is defined in the p'-q plane using equation (5-7) representing the elastic range under shearing (Zhou et al. 2015). Within this elastic range, soil deformation is considered elastic.

$$f_t = \left| \frac{q}{p' + p_b} - \alpha \right| - m_c \tag{5-7}$$

where p_b = the cementation bond strength, as defined above, and its determination is given in the next section; m_c = a model parameter governing the size of the elastic region (Figure 5.1). Following some previous studies (Dafalias and Manzari 2004; Zhou et al. 2020), a default and constant value of 0.01 is used for this parameter. This simplification barely affects the model prediction because the elastic range of soils with constant stiffness is usually very small (in the order of 0.001%). On the other hand, the variable α corresponds to the back stress ratio (Dafalias and Manzari 2004), which depends on the stress path. When the stress state is on the yield surface, and the soil is subjected to continuous shearing, soil behaviour is elastoplastic and α changes to ensure that the stress state remains on the yield surface. For other cases, soil behaviour is elastic, and α maintains constant. The determination and evolution of α were described by Zhou et al. (2020) in detail.

The current model does not define bounding and yield surfaces for compression, assuming that soil behaviour under loading and unloading at a constant stress ratio is elastic. In this way, only the changes in stress ratio $(q/(p'+p_b))$ can cause significant particle rearrangements, which are macroscopically modelled as plastic shear and volume changes (Dafalias and Manzari 2004; Taiebat and Dafalias 2008). For most practical purposes, the plastic strain due to a stress increase under a constant stress ratio can be neglected (Wang et al. 2019b), especially for cemented soils with a high yield stress during constant stress ratio compression. It is worth mentioning that this simplification has been widely adopted in previous research (Manzari and

Dafalias 1997; Dafalias and Manzari 2004; Doherty and Wood 2020; Zhang et al. 2023a). This method can keep the model relatively simple and reduce at least two model parameters related to the hardening and dilatancy during constant stress ratio compression.

5.1.3 Cementation bond strength

The cement hydration and pozzolanic reactions produce cementation bonds between soil particles, which can significantly improve soil strength and stiffness (Clough et al. 1981; Doherty and Wood 2020). The unconfined compression strength of cemented soil is usually considered a power function of cement content (Consoli et al. 2007). Similarly, the relationship between initial cementation bond strength p_{b0} and cement content is modelled using a power function:

$$p_{b0} = k_{pb} C c^{\beta} \tag{5-8}$$

where Cc = the cement content; k_{pb} = a constant soil parameter used to determine the magnitude of the bond strength at different cement contents; the power β = a soil parameter that characterizes the sensitivity of bond strength to cement content. Some experimental investigations have shown that the presence of curing stress (i.e. confinement during the cement hydration reaction) leads to a significant increase in bond strength (Cuccovillo and Coop 1999; Vatsala et al. 2001; Yun and Santamarina 2005; Nweke 2017). This influence is considered by changing the value of k_{pb} and β in the proposed model. On the other hand, changing confinement after curing can lead to cementation degradation, which is explained below.

An accurate prediction of cementation bond strength degradation is very important for predicting the mechanical behaviour of cemented soil. Suebsuk et al. (2010) and Zhang et al. (2023a) related the debonding process to plastic deviator strain for simplicity, and this cannot reflect the debonding induced by plastic volumetric strain. In the current model, the cementation bond strength p_b is modelled as a function of damage strain following the approach of (Baudet and Stallebrass 2004):

$$\varepsilon_d = \sqrt{\varepsilon_s^{p^2} + \varepsilon_v^{p^2}} \tag{5-9}$$

$$p_b = p_{b0} \exp\left(-\left(\frac{\varepsilon_d}{\varepsilon_{ref}}\right)^k\right) \tag{5-10}$$

where ε_d = the damage strain; k and ε_{ref} = two parameters used to describe the rate of p_b degradation. According to equation (5-10), ε_{ref} is the damage strain required for p_{b0} reducing to $\frac{p_{b0}}{e}$ (e: Euler number), which is generally in the range of 1% to 10% based on test data. The

parameter k is related to the non-linearity of the cementation bond strength-damage strain relation. A larger k describes a slower degradation at the early loading stage but a faster decay at the later stage. Based on experimental results in the literature, it is found in this study that the value of k should be greater than 1 to model the behaviour of cemented soil over a wide strain range.

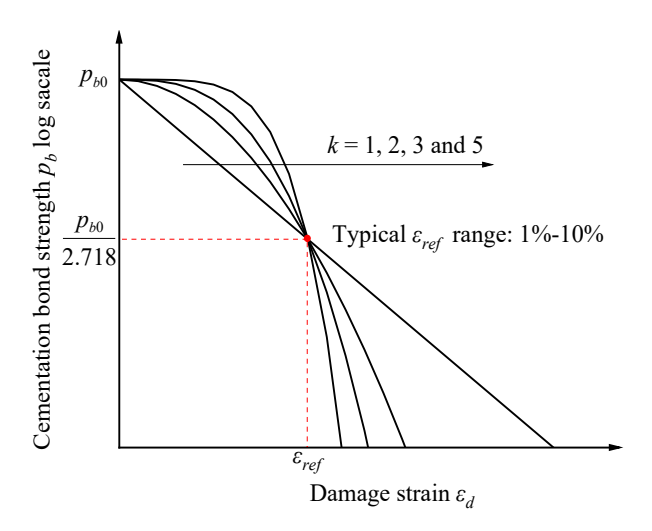


Figure 5.2 The influence of parameters k and ε_{ref} on the degradation process of cementation bond strength

5.1.4 Elastic moduli

According to equation (5-2), K and G_0 are required to compute the incremental elastic strains. For the elastic moduli of uncemented soil, the mean stress and void ratio are usually incorporated (Oztoprak and Bolton 2013; Zhou et al. 2015). Cementing bonds can further affect soil stiffness (Lo and Wardani 2002). So far, several equations have been proposed (Pestana and Salvati 2006; Trhlíková et al. 2012) to calculate the G_0 of cemented soil. However, they cannot reasonably predict G_0 under low and tensile stress conditions, which are quite common in cemented soil. Some equations, such as Trhlíková et al. (2012), predict a negative G_0 value when subjected to tensile stress. The following equation is proposed to solve this problem based on Zhou et al. (2015):

$$G_0 = A(1+e)^{-1.3} \left(\left(\frac{p' + p_b}{p_r} \right)^{0.5} + n_c \left(\frac{p_b}{p_r} \right)^{0.5} \right)$$
 (5-11)

where A and n_c = soil parameters for describing the shear modulus of cemented soil; e = the void ratio; and p_r = a reference pressure taken as 100 kPa here. There are two parameters in equation (5-11): A and n_c . Their influence on the predicted G_0 value is shown in Figure 5.3. The test result of cemented Monterey sand treated with Type I Portland cement (Saxena et al. 1988) is included for comparison. As shown in Figure 5.3a, the computed G_0 value increases

with increasing A. The computed curves at different A values are parallel at a given n_c . In addition, the incremental rate of G_0 with increasing stress is lower at a higher cement content, consistent with experimental results (Saxena et al. 1988; Pestana and Salvati 2006; Trhlíková et al. 2012). The computed results at different n_c values are shown in Figure 5.3b. n_c represents the sensitivity of G_0 to the cementation. When n_c is larger, G_0 is more sensitive to p_b .

In addition, the bulk modulus K is defined by G_0 and Poisson's ratio v in equation (5-12):



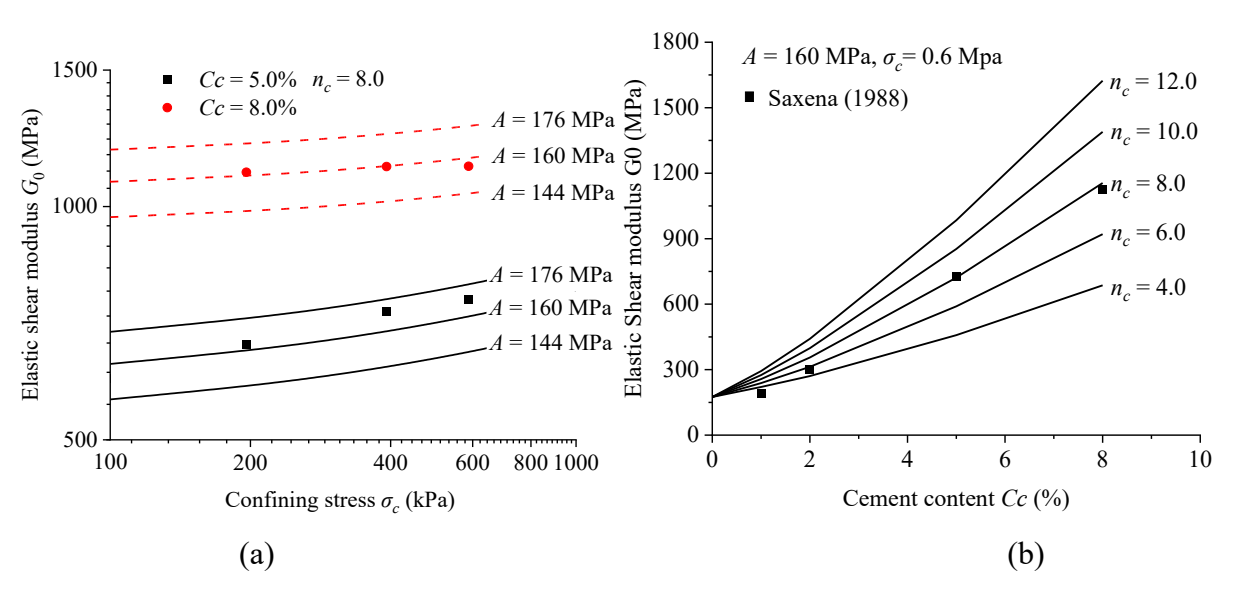


Figure 5.3 Influence of model parameters on the prediction of G_0 : (a) parameter A; (b) parameter n_c

5.1.5 Critical state and state parameter

Critical state lines (CSL) are important reference states in a state-dependent constitutive model. The cementation bonds are assumed to have been fully destroyed (i.e. $p_b=0$) when the soil reaches a critical state. Projections of the CSL in the p'-q plane is modelled as a straight line:

$$q = M_c p' \tag{5-13}$$

where M_c = the stress ratio at the critical state, which can be determined from the critical state friction angle.

Projections of the CSL on the e-lnp' plane is described by the following equation:

$$\begin{cases} e_{cs} = \Gamma_c - \lambda \ln\left(\frac{1 \, kPa}{p_r}\right) & (p' \le 1 \, kPa) \\ e_{cs} = \Gamma_c - \lambda \ln\left(\frac{p'}{p_r}\right) & (p' > 1 \, kPa) \end{cases}$$
(5-14)

where Γ_c = the intercept of the CSL on the e-ln p' plane at the reference pressure of cemented

soil; λ = the gradient of the CSL on the *e-ln p'* plane. This equation predicts a bilinear relationship between e and ln p', mainly because experimental studies in the literature (Papadopoulou and Tika 2008) show that the critical state void ratio does not change significantly with ln p' when the effective mean stress is relatively low. In the current study, when $p' \leq 1 \, kPa$, the critical state void ratio is assumed to be constant for simplicity.

The influence of cement content on the CSL has attracted great attention. Existing data generally show that M_c and Γ_c increases with increasing cement content (Mohsin 2008; Subramaniam et al. 2019; Schnaid et al. 2001; Zhang et al. 2023a). The increase is likely because cementing particles are still attached to soil particles/clusters at the critical state. The change in soil fabric may increase the roughness of particle/cluster surfaces and result in different particle packing modes (Wang and Leung 2008). The observed changes in CSL are also likely related to strain localization. Cemented soils are more prone to strain localization than uncemented soils (Rinaldi and Santamarina 2008; Jiang et al. 2011), obscuring the path to attaining CSL. Given the above considerations, the current model adopts the method of Zhang et al. (2023) to model a linear increase in M_c and Γ_c with cement content:

$$M_c = M_U + k_M C_c (5-15)$$

$$\Gamma_c = \Gamma_U + k_\Gamma C_c \tag{5-16}$$

where M_U and Γ_U = the critical state stress ratio and void ratio of uncemented soil, respectively; k_M and k_Γ = non-negative model constants, respectively, controlling the changes in critical state stress ratio and void ratio with cement content. It should be highlighted that the current model incorporates the variation of CSL with cement content. If the cement content of one soil does not affect CSL, its behaviour can also be simulated with $k_M = 0$ and $k_\Gamma = 0$.

Based on these critical state formulations, a state parameter (Ψ) (Been and Jefferies, 1985) is defined in equation (5-17). It refers to the difference between the current void ratio e and e_c with the same values of p':

$$\Psi = e - e_c \tag{5-17}$$

The values of Ψ are positive and negative for the soil state on the wet and dry sides of the CSL, respectively.

5.1.6 State-dependent dilatancy

Following Li (2002), the dilatancy is determined by equation (5-18):

$$D = \frac{d_0}{M} \left(M_d \left(\frac{\overline{\rho}_S}{\rho_c} \right)^{0.5} - \eta_c \right) \tag{5-18}$$

$$M_d = Mexp(n_d \Psi) \tag{5-19}$$

where d_0 and n_d = soil parameters; η_c = the stress ratio defined as $\eta_c = q/(p' + p_b)$; M_d = the stress ratio at which phase transformation occurs under the preliminary shearing (Zhou et al. 2020). Phase transformation is the transition of soil behaviour from contractive to dilative during shearing (Ishihara et al. 1975). To account for the effects of loading and unloading history on the shear behaviour, equation (5-19) incorporates the term $\sqrt{\frac{\overline{\rho}_s}{\rho_s}}$. In the case of primary shearing, $\sqrt{\frac{\overline{\rho}_s}{\rho_s}} = 1$.

As discussed earlier, the dilatancy tendency increases with increasing cement content. This behaviour can be modelled by equation (5-18), governed by an upward shift of the critical state line in the $v - \ln p'$ plane with increasing cement content. A larger Γ_c value results in a smaller Ψ and a lower M_d . Consequently, the phase transformation occurs at an earlier shearing stage and a higher dilatation value.

5.1.7 Hardening law and condition of consistency

The loading index Λ in equation (5-3) is determined using the condition of consistency and hardening law. In this model, the evolution of the bounding surface Fs directly depends on the plastic deviator and volumetric strains. During the primary shearing, when yielding is occurring with the stress state on Fs, the condition of consistency suggests that:

$$\frac{\partial F_S}{\partial p'}dp + \frac{\partial F_S}{\partial q}dq + \frac{\partial F_S}{\partial p_b}\frac{\partial p_b}{\partial \varepsilon_q^p}d\varepsilon_q^p + \frac{\partial F_S}{\partial M_m}\frac{\partial M_m}{\partial \varepsilon_q^p}d\varepsilon_q^p + \frac{\partial F_S}{\partial M_m}\frac{\partial M_m}{\partial \varepsilon_v^p}d\varepsilon_v^p = 0 \qquad (5-20)$$

The plastic modulus K_p is introduced and defined in equation (5-21). The evolution of the bounding surface F_S during the shearing process is controlled by M_m and p_b .

$$K_p = -\left(\frac{\partial F_S}{\partial p_b} \frac{\partial p_b}{\partial \varepsilon_q^p} + \frac{\partial F_S}{\partial M_m} \left(\frac{\partial M_m}{\partial \varepsilon_q^p} + \frac{\partial M_m}{\partial \varepsilon_v^p} D\right)\right)$$
(5-21)

By substituting equations (5-4) to (5-21), the value of Λ can be determined by equation (5-22).

$$\Lambda = \frac{1}{K_p} \left(\frac{\partial F_S}{\partial p'} dp' + \frac{\partial F_S}{\partial q} dq \right) = \frac{1}{K_p} (dq - M_m dp')$$
 (5-22)

To calculate K_p , $\frac{\partial F_S}{\partial p_h}$ and $\frac{\partial F_S}{\partial M_m}$ can be obtained by differentiating equation (5-4):

$$\frac{\partial F_S}{\partial p_b} = -M_m \tag{5-23}$$

$$\frac{\partial F_S}{\partial M_m} = -(p + p_b) \tag{5-24}$$

where $\frac{\partial p_b}{\partial \varepsilon_q^p}$ = a function of dp_b and $d\varepsilon_q^p$, which can be determined by differentiating equations (5-9) and (5-10):

$$\frac{\partial p_b}{\partial \varepsilon_q^p} = -p_{b0} \exp\left(-\frac{\varepsilon_d}{\varepsilon_{ref}}\right)^k k \left(\frac{\varepsilon_d}{\varepsilon_{ref}}\right)^{k-1} \frac{\sqrt{1+D^2}}{\varepsilon_{ref}}$$
(5-25)

The term $\frac{\partial M_m}{\partial \varepsilon_q^p} + D \frac{\partial M_m}{\partial \varepsilon_v^p}$ corresponding to the influence of the shearing mechanism on the stress ratio M_m . In the study of Zhou et al. (2015), the change of M_m induced by shear was simplified, which is only related to the plastic volumetric strain. According to Zhou et al. (2015), $\frac{\partial M_m}{\partial \varepsilon_p^p} + D \frac{\partial M_m}{\partial \varepsilon_v^p}$ is defined as follows for simplicity:

$$\frac{\partial M_m}{\partial \varepsilon_q^p} + D \frac{\partial M_m}{\partial \varepsilon_v^p} = \frac{hG}{M_m} \left(M_b \frac{\overline{\rho_s}}{\rho_s} - M_m \right)$$
 (5-26)

According to equations (5-23) through (5-26), the plastic modulus K_p can be obtained:

$$K_{p} = (p + p_{b}) \frac{hG}{M_{m}} \left(M_{b} \frac{\overline{\rho_{s}}}{\rho_{s}} - M_{m} \right) - M_{m} p_{b} \exp \left(-\left(\frac{\varepsilon_{d}}{\varepsilon_{ref}} \right)^{k} \right) k \left(\frac{\varepsilon_{d}}{\varepsilon_{ref}} \right)^{k-1} \frac{\sqrt{1+D^{2}}}{\varepsilon_{ref}}$$
(5-27)

5.1.8 Tension cut-off

The current models incorporate the tension cut-off as follows:

$$\begin{cases}
\sigma_1' - \sigma_t \le 0 \\
\sigma_2' - \sigma_t \le 0 \\
\sigma_3' - \sigma_t \le 0
\end{cases}$$
(5-28)

where σ_t = the tensile strength.

5.2 Multiaxial Generalization

The model presented was extended to three dimensions was compiled into the finite element software for analysing boundary value problems. This section introduces the key formulas in the general stress space.

For a given effective stress rate $d\sigma = ds + dp'I$, The deviatoric stress s is defined by $s = \sigma - p'I$, where p is the hydrostatic pressure defined by $p = (1/3)tr\sigma$, and I is the identity tensor. The elastic strain obtained by

$$d\varepsilon_{v}^{e} = \frac{dp'\delta_{ij}}{3K} \tag{5-29}$$

$$d\varepsilon_q^e = \frac{ds}{2G_0} \tag{5-30}$$

Combining all the above the basic constitutive equations (5-2) of the SANISAND-Z model

under triaxial conditions can now be expressed as follows:

$$\dot{\varepsilon}_q = \dot{\varepsilon}_q^e + \dot{\varepsilon}_q^p \tag{5-31}$$

$$\dot{\varepsilon}_v = \dot{\varepsilon}_v^e + \dot{\varepsilon}_v^p \tag{5-32}$$

$$\dot{\varepsilon}_q^p = \Lambda \tag{5-33}$$

$$\dot{\varepsilon}_{V}^{p} = D\Lambda \tag{5-34}$$

Determining the plastic modulus in the general stress space is crucial, and this involves establishing the mapping rule for the recovery modulus. In the multiaxial stress space, the parameter (M) is interpolated between its values (Mc) and (Me) by means of the Lode angle, according to the proposition by Argyris et al. (1974), which ($c_M = Me /Mc$) following Taiebat and Dafalias (2010). The critical state stress ratio varies with the stress ratio in the loading direction, as shown in Figure 5.4.

$$M_{\theta}^{a} = M^{a} \frac{2c}{(1+c)-(1-c)cos(3\theta)}$$
 (5-35)

$$c_M = \frac{M_e}{M_c} \tag{5-36}$$

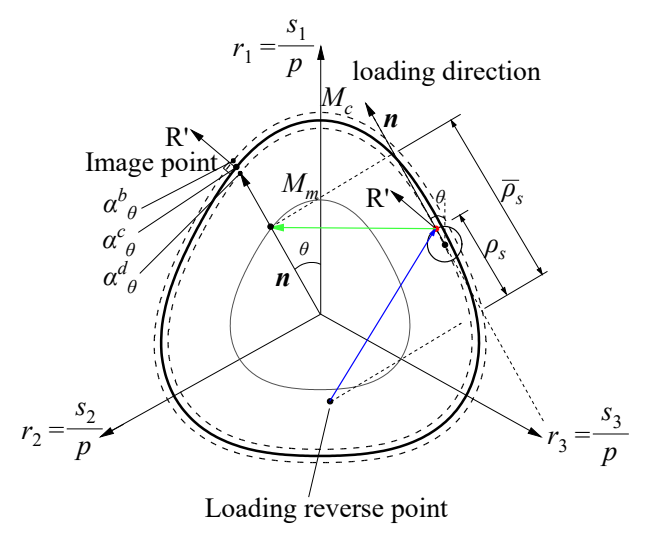


Figure 5.4 Schematic of yield, critical, dilatancy, and bounding surfaces on the stress ratio π plane

Following (Li and Dafalias, 2002), the dilatancy is determined by equation (5-19):

$$D = \frac{d0}{M_{\theta}} \left(\alpha_{\theta}^{d} \left(\frac{\overline{\rho}_{S}}{\rho_{S}} \right)^{0.5} - \alpha \right) : \boldsymbol{n}$$
 (5-37)

The mapping rule in this study primarily references the work of Dafalias and Manzari

(2004). The image point is determined by the loading direction, which is defined by the line connecting the back stress ratio to the current stress ratio, represented as the n vector in the figure. From point O, a line parallel to the loading direction intersects the M_m surface at the image point. In three-dimensional space, the distance ratio is the projection of these two lines in the n direction, as shown by (ρ_s) and $(\bar{\rho}_s)$ in Figure 5.4.

According to the flow rule, the plastic strain increment $d\varepsilon_{ij}^p$ is given by.

$$d\varepsilon_{ij}^{p} = \langle L \rangle \frac{\partial Q}{\partial \sigma_{ij}^{p}} = \langle L \rangle \left(\frac{\partial Q}{\partial p} \frac{\partial p}{\partial \sigma_{ij}} + \frac{\partial Q}{\partial q} \frac{\partial q}{\partial \sigma_{ij}} \right) = d\varepsilon_{v}^{p} \frac{\partial p}{\partial \sigma_{ij}} + d\varepsilon_{s}^{p} \frac{\partial q}{\partial \sigma_{ij}} = \left(D_{s} \frac{\partial p}{\partial \sigma_{ij}} + \frac{\partial q}{\partial \sigma_{ij}} \right) d\varepsilon_{s}^{p}$$
 (5-38)

where σ_{ij} = the stress tensor; Q = the plastic potential; L = the loading index; <> is known as Macauley brackets; D_s is the soil dilatancy ratio.

For mathematical convenience, several tensor variables are defined as follows.

$$A_{ij} = \frac{\partial p}{\partial \sigma_{ij}} = \frac{1}{3} \delta_{ij} \tag{5-39}$$

$$B_{ij} = \frac{\partial q}{\partial \sigma_{ij}} = \frac{3}{2q} s_{ij} \tag{5-40}$$

$$C_{ij} = D_s \frac{\partial p}{\partial \sigma_{ij}} + \frac{\partial q}{\partial \sigma_{ij}} = D_s A_{ij} + B_{ij}$$
 (5-41)

where δ_{ij} = the Kronecker delta. Substituting equations (5-40) into equation (5-39) yields

$$d\varepsilon_{ij}^p = C_{ij}d\varepsilon_s^p \tag{5-42}$$

Then, the stress–strain relationship can be written as:

$$d\sigma_{ij} = D^{e}_{ijkl}d\varepsilon^{e}_{kl} = D^{e}_{ijkl}(d\varepsilon_{kl} - d\varepsilon^{p}_{kl}) = D^{e}_{ijkl}(d\varepsilon_{kl} - C_{kl}d\varepsilon^{p}_{s})$$
 (5-43)

The condition of consistency of the maximum bounding surface in equation requires that

$$\frac{\partial F_S}{\partial \sigma_{ij}} D^e_{ijkl} \left(d\varepsilon_{kl} - C_{kl} d\varepsilon_S^p \right) + \left(\frac{\partial F_S}{\partial p_b} \frac{\partial p_b}{\partial \varepsilon_q^p} + \frac{\partial F_S}{\partial p_b} \frac{\partial p_b}{\partial \varepsilon_v^p} D + \frac{\partial F_S}{\partial M_m} \frac{\partial M_m}{\partial \varepsilon_q^p} \right) d\varepsilon_S^p = 0$$
 (5-44)

The tensor form of the stress–strain relationship can be obtained as follows:

$$\frac{\partial F_S}{\partial \sigma_{ij}} D^e_{ijkl} \left(d\varepsilon_{kl} - C_{kl} d\varepsilon_S^p \right) + \left(\frac{\partial F_S}{\partial p_b} \frac{\partial p_b}{\partial \varepsilon_q^p} + \frac{\partial F_S}{\partial p_b} \frac{\partial p_b}{\partial \varepsilon_v^p} D + \frac{\partial F_S}{\partial M_m} \frac{\partial M_m}{\partial \varepsilon_q^p} \right) d\varepsilon_S^p = 0$$
 (5-45)

$$\frac{\partial F_S}{\partial \sigma_{ij}} D^e_{ijkl} d\varepsilon_{kl} - \frac{\partial F_S}{\partial \sigma_{ij}} D^e_{ijkl} C_{kl} d\varepsilon_s^p - K_p d\varepsilon_s^p = 0$$
 (5-46)

$$d\varepsilon_s^p = \frac{\frac{\partial F_S}{\partial \sigma_{ij}} D_{ijkl}^e d\varepsilon_{kl}}{\frac{\partial F_S}{\partial \sigma_{ij}} D_{ijkl}^e C_{kl} + K_p}$$
(5-47)

$$d\sigma_{ij} = D^{e}_{ijkl}d\varepsilon^{e}_{kl} = D^{e}_{ijkl}\left(d\varepsilon_{kl} - d\varepsilon^{p}_{kl}\right) = \left(D^{e}_{ijkl} - \frac{D^{e}_{ijkl}C_{kl}\frac{\partial F_{S}}{\partial \sigma_{ij}}D^{e}_{ijkl}}{\frac{\partial F_{S}}{\partial \sigma_{ij}}D^{e}_{ijkl}C_{kl} + K_{p}}\right)d\varepsilon_{kl} \quad (5-48)$$

The formula for the plastic modulus in the general stress space needs to consider the critical state stress ratio, which varies with the stress path direction, and the mapping rule.

$$Kp = -\left(\frac{\partial F_S}{\partial p_b} \frac{\partial p_b}{\partial \varepsilon_q^p} + \frac{\partial F_S}{\partial p_b} \frac{\partial p_b}{\partial \varepsilon_v^p} D + \frac{\partial F_S}{\partial M_m} \frac{\partial M_m}{\partial \varepsilon_q^p}\right) = \frac{hG}{M_m} \left(\left(\boldsymbol{\alpha}_{\theta}^b \left(\frac{\overline{\rho}_S}{\rho_S} \right)^{0.5} - \boldsymbol{\alpha} \right) : \boldsymbol{n} \right) - M_m p_b exp \left(-\left(\frac{\varepsilon_d}{\varepsilon_{ref}} \right)^k \right) k \left(\frac{\varepsilon_d}{\varepsilon_{ref}} \right)^{k-1} \frac{\sqrt{1+D^2}}{\varepsilon_{ref}}$$

$$(5-49)$$

5.3 Calibration of model parameters

In total, 16 parameters are needed in the proposed model, as shown in Table 5.1. 10 of them were adopted in the reference model proposed by Zhou et al. (2015) for uncemented soil, and they can be calibrated following the method of Zhou et al. (2015). Six new parameters are used in the proposed model to simulate cementation effects, and they can be determined using the following methods:

- (1) Parameters k_M and k_Γ describe the effects of cement content on the stress ratio and void ratio at the critical state. To calibrate k_M , it is necessary to measure the critical stress ratio M_c through triaxial shear tests at different cement contents Cc. Then, the relationship between M_c and Cc is fitted using equation (5-15) to determine k_M . Similarly, k_Γ can be obtained by fitting the relationship between Γ_c and Cc with equation (5-16).
- (2) Parameters k_{pb} and β can be calibrated using the results of unconfined compressive tests at different cement contents. Following the method of previous researchers (Horpibulsuk et al. 2004), the initial bond strength p_{b0} can be approximated as follows:

$$p_{b0} = \frac{q_u}{2M} \tag{5-50}$$

The measured relationship between p_{b0} and Cc can be fitted using equation (5-8) to determine the value of k_{pb} and β .

(3) The other two parameters (ε_{ref} and k) is calibrated from the relationship between bond strength and damage strain. As shown in Figure 5.2, ε_{ref} can be determined at the point where $p_b = p_{b0}/e$, and k can be estimated by fitting the strength degradation using equation (5-10). In case the $p_b - \varepsilon_d$ relation is not available, the stress-strain relationship $\sigma_{axial} - \varepsilon_{axial}$ (softening section) from unconfined or triaxial compression tests can be used as an alternative.

5.4 Model validation using test data in the literature

5.4.1 Elastic shear modulus

Saxena et al. (1988) studied the elastic moduli of Monterey No. 0 sand treated with Type I Portland cement by resonant column tests. The calculated and measured results of G_0 at different stress conditions are compared. As shown in Figure 5.5, in the log $G_0 - \log p'$ plane, G_0 increases linearly with increasing p'. The incremental rate is smaller for higher cement content, demonstrating coupling effects between the stress and cementing bonds on G_0 . In equation (5-11), the term $\left(\frac{p'+p_b}{p_r}\right)^{0.5} + n_c p_b^{0.5}$ is used to account for the coupling effects of stress and cementation. At a larger p_b value, the role of stress becomes relatively less important.

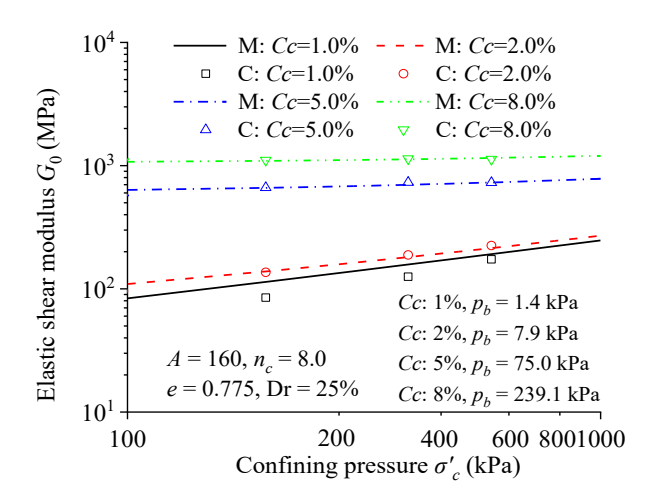


Figure 5.5 Comparison between the measured (M) (Saxena 1988) and computed (C) G_0 results of cemented Monterey sand.

Yang (2008) investigated the effects of void ratio on the elastic shear modulus of cemented sand through bender element and resonant column tests. Their study used type III Portland Cement to stabilise Puerto Rico sand. Figure 5.6 compares the measured and calculated results at three relative densities (Dr = 60%, Dr = 80%, Dr = 100%). The calculated results are determined using equation (5-11) with the parameters shown in Figure 5. In the log G_0 - e plane, G_0 decreases linearly with an increasing void ratio, and the decremental rate is almost independent of cement content. At a given void ratio, G_0 increases with increasing cement content. The above behaviour is well captured by equation (5-11).

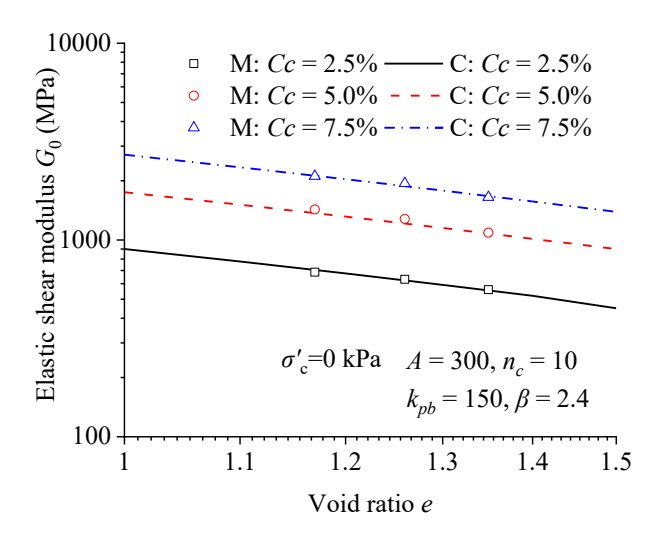


Figure 5.6 Comparison between the measured (M) (Yang 2008) and computed (C) G_0 results of cemented siliceous sand at 0 confining pressure.

To further demonstrate the capability of equation (5-11), this study compares the computed and measured G_0 results of isotropic compression tests on kaolin clay treated with 4% ordinary Portland cement. The test results are obtained from Trhlíková et al. (2012) and shown in Figure 5.7. Equation (5-11) gives a good prediction for the uncemented specimen. For the cemented clay, the equation does not capture the experimental results well in the stress range of 100 to 1000 kPa. The discrepancies are likely because the proposed model predicts an elastic soil behaviour during isotropic compression for simplicity, as illustrated above. Hence, the degradation of bonding during isotropic compression cannot be considered.

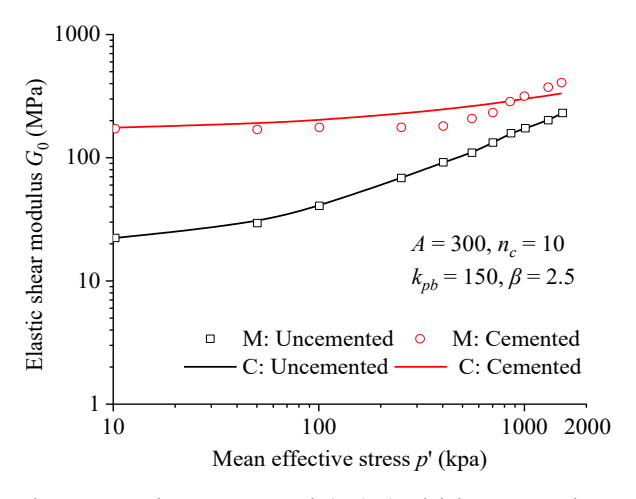


Figure 5.7 Comparison between the measured (M) (Trhlíková et al. 2012) and computed (C) G_0 results of kaolin clay.

5.4.2 Stress-strain relation and dilatancy during drained shearing

Marri et al. (2012) conducted triaxial drained shear tests on Portaway sand at different Ordinary Portland Cement contents (5, 10, 15%) and confining pressures (1, 4, 8, 12 MPa).

The relative densities of the three specimens were 88%, 82%, and 79% at cement contents of 5%, 10%, and 15%, respectively. A wide range of high stress is simulated for two reasons. Firstly, cemented soils may be subjected to high stress in some engineering problems, such as deep pile foundations, especially offshore piling, deep mine shafts, high earth dams, and deep oil-bearing strata (Marri et al. 2012). Secondly, the model performance over a wide stress range can be evaluated.

The model parameters are calibrated and shown in Table 5.1 based on the test results. Figure 5.8 compares the measured and computed results. The proposed model can well capture the stress-strain and volume change behaviour during shearing. The cemented sand exhibits clear strain-softening behaviour when the confining pressure is relatively low. This behaviour is because p_b plays a dominant role, and the peak strength is higher than the critical state shear strength. On the contrary, under higher confining pressure, the role of p_b is overweighted by that of p'. Cementation bonds have been fully degraded before reaching the peak state, so a strain-hardening behaviour is observed.

With an increase in cement content, strain-softening is more obvious. This increase is because the p_b value increases with the cement content, which leads to the failure bounding surface in Figure 5.8 shifting towards the left. Furthermore, with the increase in cement content, the soil becomes slightly more dilative. This trend is captured by the model, mainly due to the upward movement of the critical state line in e-lnp' plane, in equation (5-14). A larger Γ_c value results in smaller Ψ and M_d , leading to earlier phase transformation and higher dilatancy.

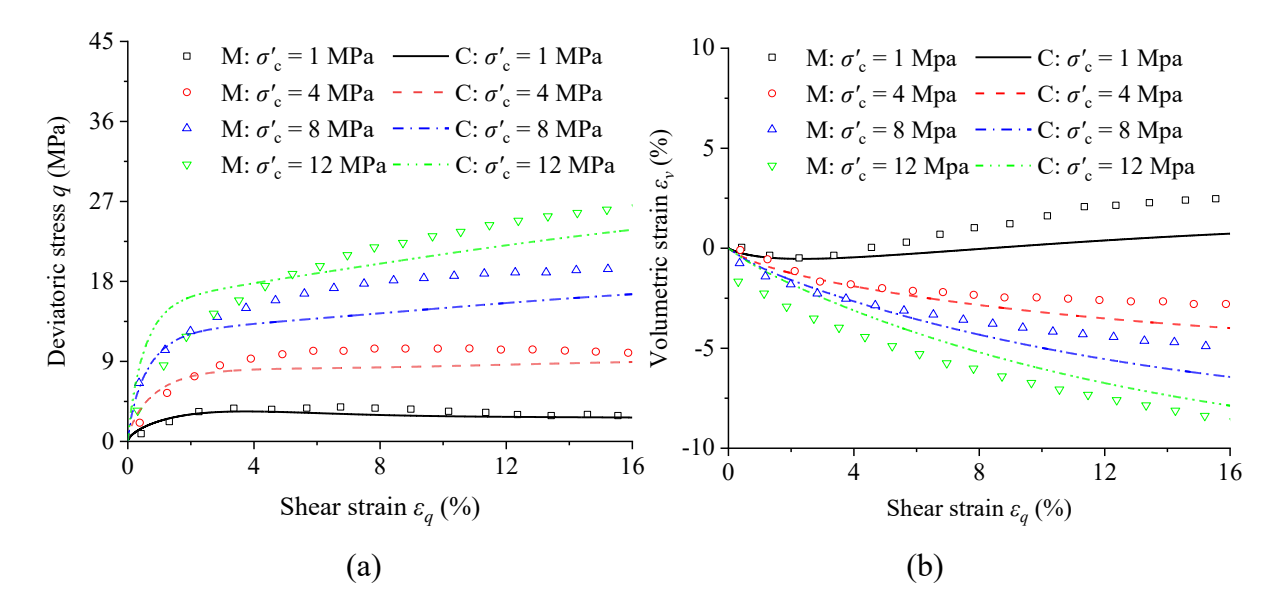


Table 5.1 Summary of model parameters for soils reported in the literature

Parameter	Symbol	Portaway sand (Marri et al. 2012)	Ariake clay (Horpibulsuk et al. 2004)	Singapore marine clay (Yao 2017)	Osorio sand (Marques et al. 2021)	Weathered sandstone (Consoli et al. 2000)	Calcareous sediments, (Mohsin et al. 2008)
Elasticity	A (MPa)	200	150	130	380	460	200
	ν	0.1	0.1	0.1	0.1	0.1	0.1
	n_c	1.0	1.0	2.8	1.0	1.0	5.0
	m_U	0.02	0.02	0.02	0.02	0.02	0.02
Critical state	M_U	1.20	1.58	0.90	1.32	1.39	1.5
	k_M	2.0	0.7	1.0	0.1	0.3	1.0
	λ	0.08	0.40	0.20	0.02	0.02	0.2
	$\Gamma_{\!U}$	2.1	4.8	3.0	2.8	1.7	1.7
	$k_{arGamma}$	0.1	1.8	0.5	2.0	1.0	0.6
Flow rule	n_d	2	3	1	3	5	10
	d_0	1.0	0.05	0.1	0.05	0.01	0.2
Hardening	nb	3.0	1.0	1.0	0.5	2.0	0.5
law	h	0.1	0.7	1.0	0.8	0.1	0.3
Cementation parameter	ε_{ref}	0.06	0.10	0.06	0.03	0.08	0.03
	k	2.0	2.0	0.8	4.0	1.8	1.5
	k_{pb} (MPa)	68	300	1.3	11	22	40
	β	1.5	2.6	1.5	1.0	1.4	1.9

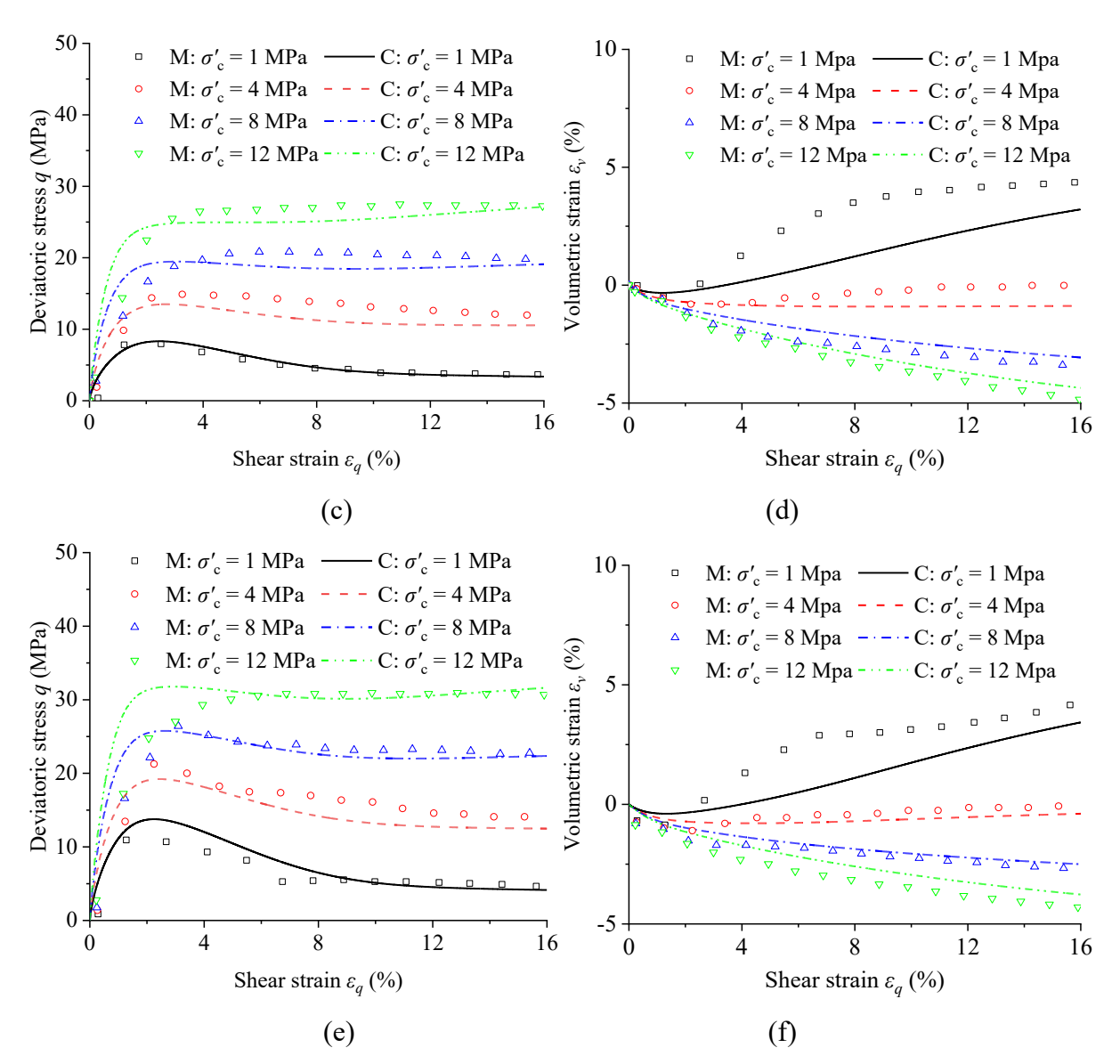


Figure 5.8 Comparison between the measured (M) (Marri et al. 2012) and computed (C) results of drained triaxial compression tests on cemented Portaway sand: (a-b) Cc = 5%; (c-d) Cc = 10%; (e-f) Cc = 15%.

5.4.3 Stress-strain relation and effective stress path during undrained shearing

Horpibulsuk et al. (2004) studied the effects of cementation on clay improved using Type I Portland cement through undrained triaxial tests. Isotopically consolidated undrained triaxial compression tests were conducted on specimens with 6% cement content after 28 days of curing. It revealed that the cementation enhances the strain-softening behaviour. Figure 5.9 compares the calculated results and measured data. The calibrated parameters are summarised in Table 5.1.

As shown in Figure 5.9, the stress path of cemented soil exceeds the CSL due to cementation. After reaching the peak shear strength, the specimens exhibit strain-softening

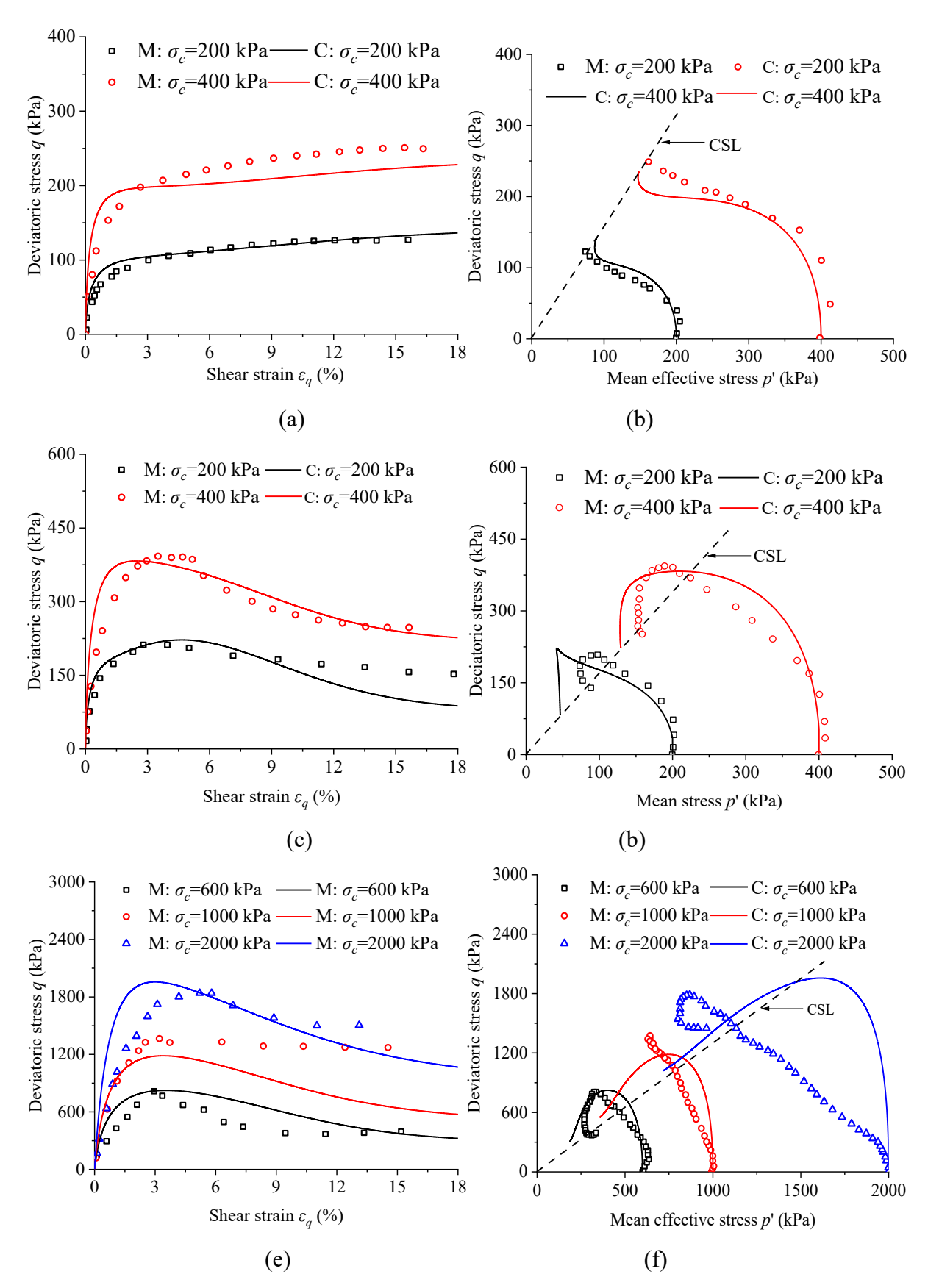


Figure 5.9 Comparison between the measured (M) (Horpibulsuk et al. 2004) and computed (C) undrained triaxial compression test results of cemented Ariake clay: (a-b) Cc = 0%; (c-d)

$$Cc = 6\%$$
; (e-f) $Cc = 12\%$.

behaviour due to the destruction of cementation bonds, and then the strength degrades to the CSL. The proposed model captures this behaviour well, with some differences, mainly in the cement content of 12%. The discrepancy between the computed and measured results may be because cementation effects on the dilatancy are modelled in a simplified and indirect approach (i.e., considering the effects of cementation on the state parameter in Eqs. (5-18) and (5-19)). Cementation may alter dilatancy through other mechanisms (e.g., changes in soil particle number and fabric) (Martinez and DeJong 2009; Rios et al. 2014). Some advanced flow rules could be used to improve the modelling of the dilation behaviour, such as bond strength-dependent dilatancy, e.g., Horpibulsuk et al. (2004).

5.4.4 Stiffness at very small strains and small strains

Yao (2017) studied the elastic shear modulus G_0 and its degradation curves of cemented Singapore marine clay with different Ordinary Portland Cement contents and confining pressures. Figure 5.10 compares the measured and calculated secant modulus results. The secant modulus is the ratio of q to $3\varepsilon_q$, where q and ε_q are shear stress and deviator strain, respectively. The calibrated parameters are summarised in Figure 5.10.

As shown in Figure 5.10, the elastic shear modulus in the very small strain range (< 0.001%) is accurately modelled under different confining pressures. The good performance can be mainly because equation (5-11) can reasonably consider the effects of effective mean stress and cementation on the elastic shear modulus. In addition, there are some minor differences between the measured and computed results, probably because equation (5-10) models the relationship between bond strength (p_{b0}) and cement content in a simplified approach. It underestimates the p_{b0} value at relatively lower cement content and overestimates the p_{b0} value at relatively higher cement content.

The degradation curves of the secant shear modulus in the small strain range (0.001% – 1%) are well captured, attributed to two merits of the models: (i) the elastic shear modulus can be determined accurately using Equation (5-11); (ii) Equation (5-10) reasonably characterises the degradation of p_b . These two aspects are important to predicting shear modulus at very small strains and modelling shear modulus degradation at small strains. They were not fully incorporated into existing models for cemented soil.

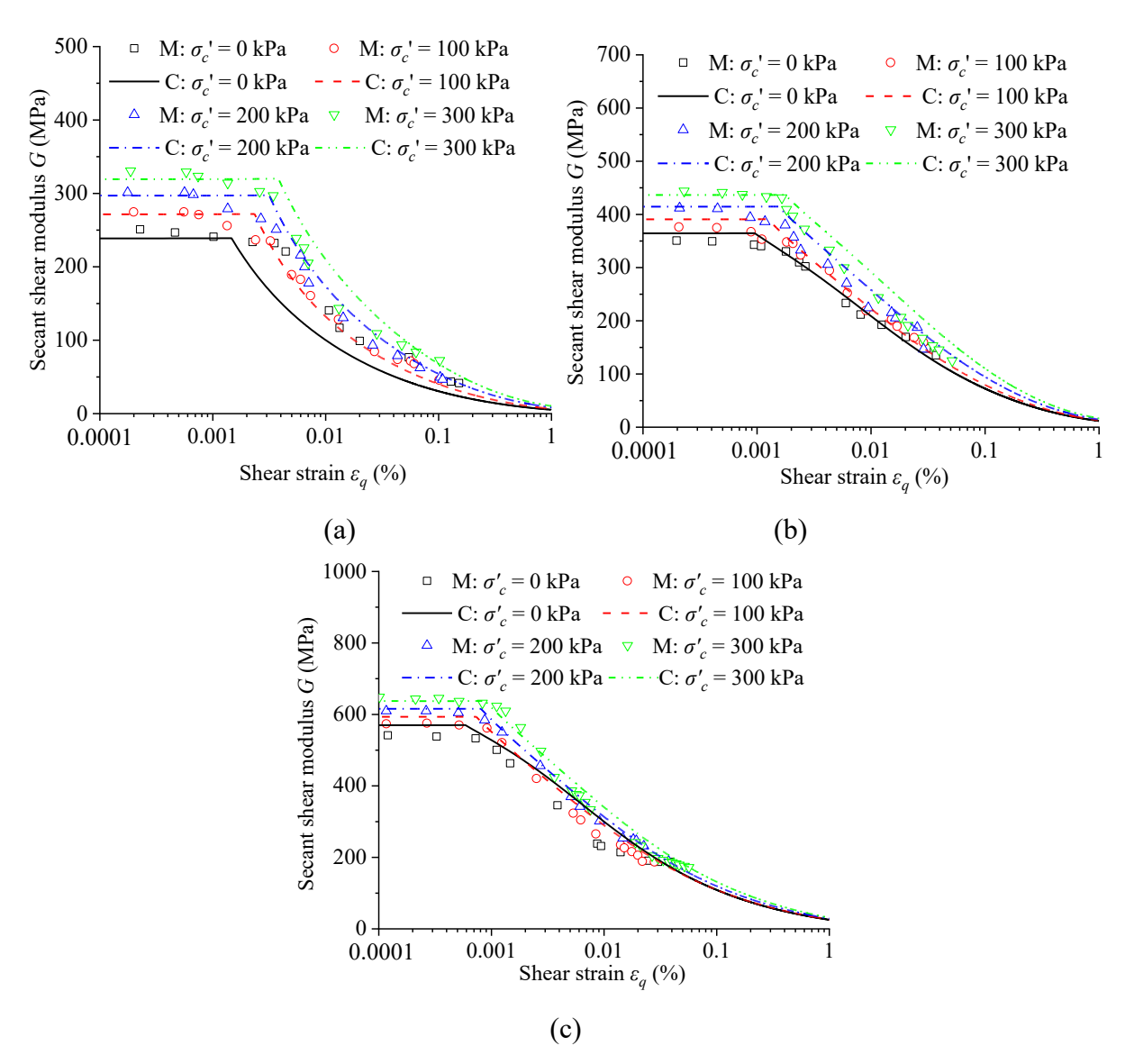


Figure 5.10 Comparison between the measured (M) (Yao 2017) and computed (C) stiffness degradation curves of cemented marine clay with different cement contents: (a) Cc = 20%; (b) Cc = 30%; (c) Cc = 50%.

5.4.5 Mechanical behaviour of cemented soil from small to large strains

Marques et al. (2021) conducted triaxial tests to study cemented sand's strength and small strain stiffness behaviour. Early-strength Portland cement (Type III) was the binder to shorten the test duration. The measured and calculated results are compared in Figure 5.11. The calibrated parameters are summarised in Figure 5.11. The influence of parameter k, in equation (5-11), on the small strain stiffness degradation curve is studied. As shown in Figure 5.11, in the case of k = 4 and $k_{pb} = 40$, both the stress-strain curve and the degradation curve of small strain stiffness are well captured.

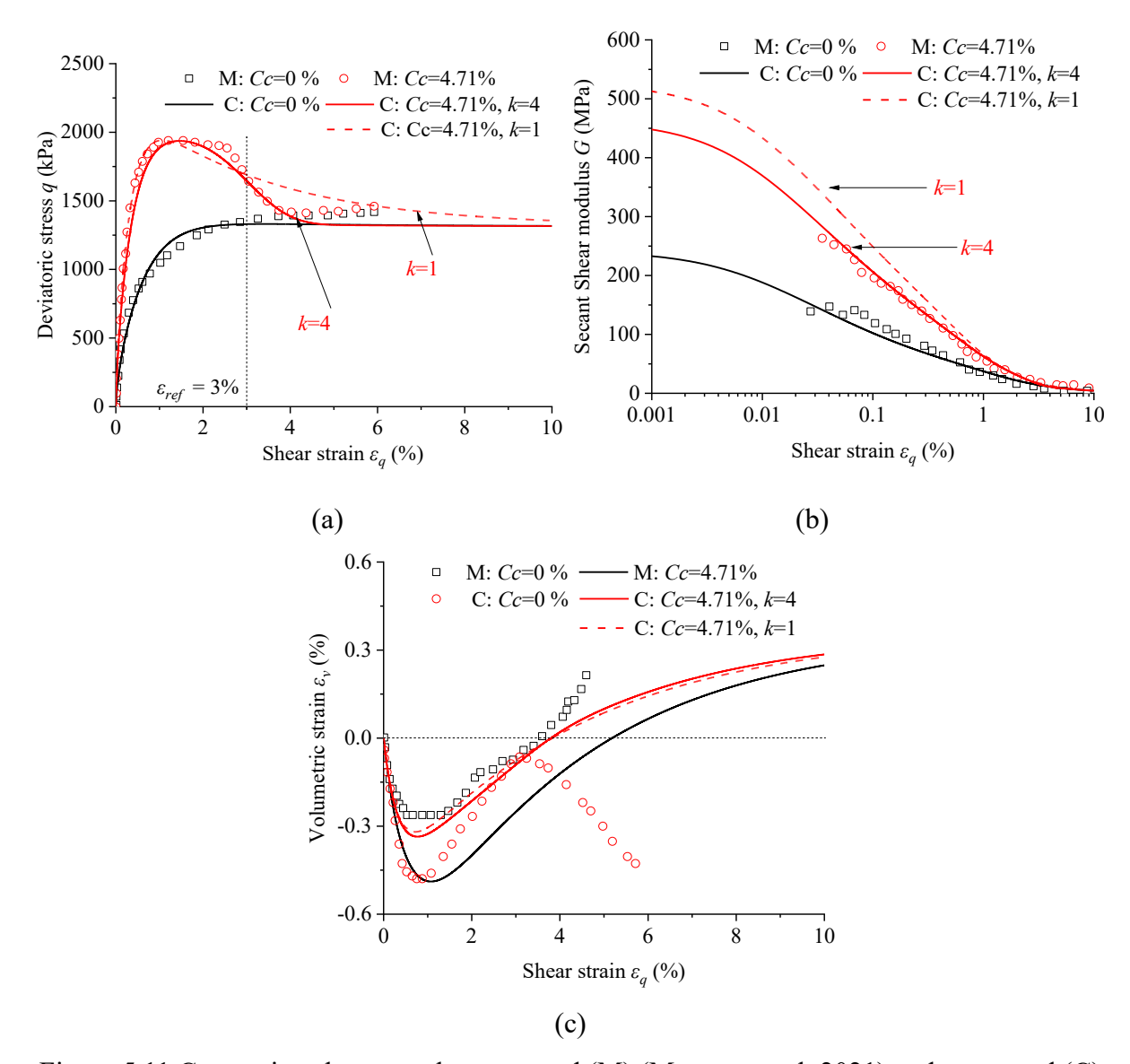


Figure 5.11 Comparison between the measured (M) (Marques et al. 2021) and computed (C) strength and stiffness of cemented Osorio sand: (a) stress-strain behaviour; (b) degradation of stiffness. (c) volumetric strain versus shear strain.

The case with k = 1, which is a common assumption in existing models, predicts faster and slower degradation before and after ε_{ref} than the case with k = 4, respectively, as shown in Figure 5.2. With k = 1, a larger p_{b0} is required to capture the peak strength of cemented soil. When k = 1, $k_{pb} = 56$ is required for modelling the peak strength, but this overestimates the small strain stiffness. In other words, if k = 1 is assumed, it is challenging to predict the behaviour of cemented soil over a wide strain range well. In addition, there are some obvious differences between the measured and computed volumetric strains, as shown in Figure 5.11c. This limitation is likely because the influence of cement content on dilatancy is modelled in a simplified approach, as discussed above. Moreover, cemented soils often exhibit strain

localization during shearing, especially during softening (shear strain > 1% in Figure 5-11). The specimen is not an ideal representative element, causing differences between the measured and computed results at strains above 1%.

Consoli et al. (2000) conducted triaxial tests on cemented and weathered sandstone with 3% cement content. The results are used for further validating the proposed model. The calibrated parameters are summarised in Figure 5.12. Figure 5.12 shows the measured and computed results. Overall, the model prediction curve and the test results show consistent trends. There are some discrepancies between the computed and measured results. This limitation is likely because the current model adopts a linear failure bounding surface (see equation (5-5) for simplicity, while the failure envelope of cemented soils can be highly nonlinear (Wu et al. 2017; Sharma et al. 2011).

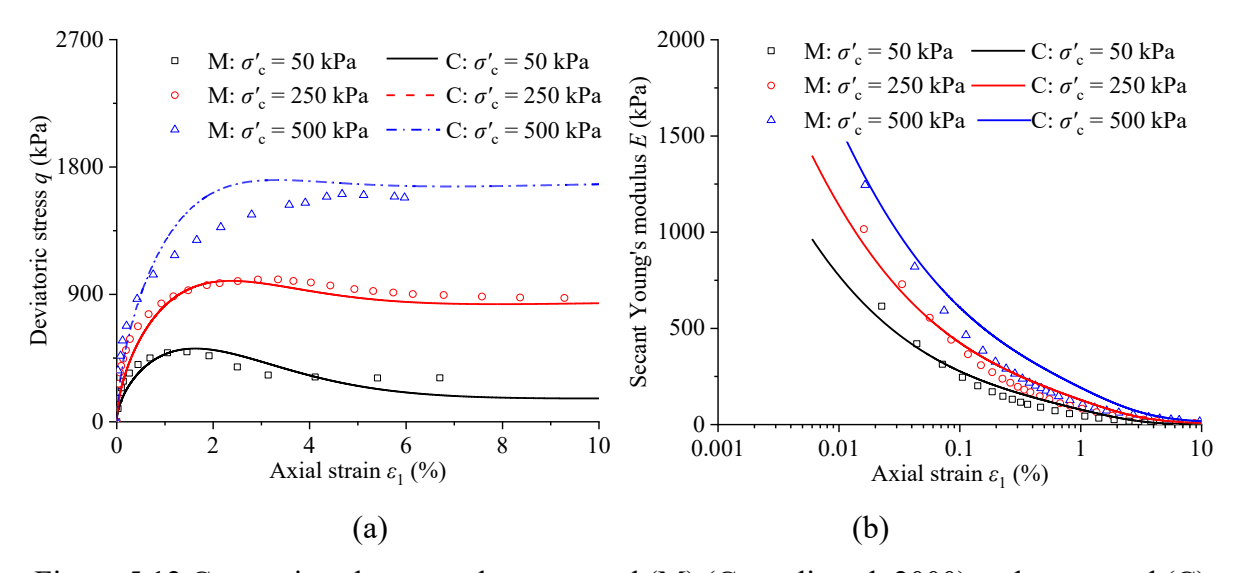


Figure 5.12 Comparison between the measured (M) (Consoli et al. 2000) and computed (C) strength and stiffness of cemented weathered sandstone. (a) stress-strain behaviour; (b) degradation of stiffness.

5.4.6 Stress-strain behaviour during the loading and reloading process

Unlike the classical elastoplastic theory, which assumes elastic soil behaviour within the yield surface, the bounding surface plasticity theory allows for gradual yielding when the stress path is inside the bounding surface. The two theories are compared to simulate a laboratory test reported by Mohsin (2008). Calcareous sediment treated with 10% gypsum was tested in triaxial apparatus at an effective confining pressure of 600 kPa. A specimen was subjected to three cycles of deviatoric stress. The measured and computed results are shown in Figure 5.13. The experimental results clearly show gradual yielding and irreversible deformation during reloading. Furthermore, the specimen failed during reloading even though the deviatoric stress

did not exceed the maximum deviatoric stress applied during the first loading. The failure is mainly attributed to the degradation of bond strength. The bounding surface plasticity model can capture these phenomena well. In contrast, soil responses during the unloading and reloading processes are reversible when the classical elastoplasticity framework is used. The above features cannot be simulated.

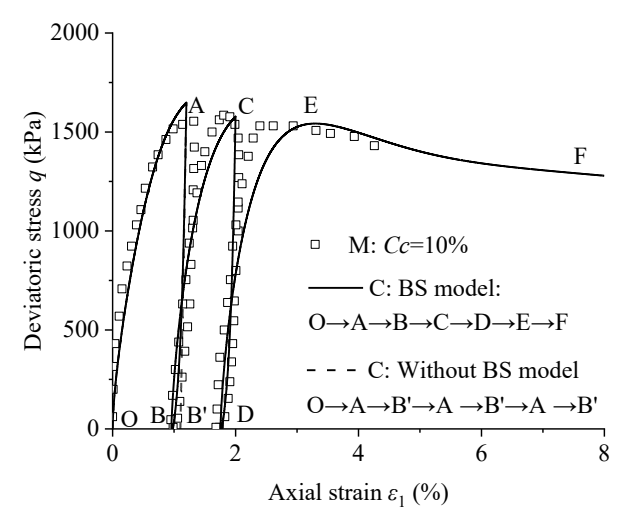


Figure 5.13 Comparison of calculation results between bounding surface model and classical elastoplastic model

5.5 Model validation using test data from the current study

The model validation using experimental data in the literature did not consider the effects of curing temperature and stress. Therefore, it is necessary to validate the model using test data from specimens subjected to various curing temperatures and stresses. This validation aims to verify the model using data that accounts for curing stress and temperature, and to analyze their effects on the cementation parameters within the advanced theoretical framework. For the curing conditions of specimens in the undrained triaxial shear tests, the selected temperatures were 20°C and 30°C, and the applied stresses were 0 kPa and 150 kPa. The selected testing conditions are representative enough that similar conclusions could be obtained for other conditions, while effectively minimizing the number of experimental tests.

Firstly, the model parameters are calibrated. Figure 5.14a plots the critical state line in p'-q plane. It shows that the increase in cement content and curing temperature does not significantly affect the critical stress ratio. An increase in curing stress slightly increases the critical state stress ratio. Given the change of critical stress ratio with different curing temperatures and stresses, the same set of critical state parameters was used in the theoretical model computation. Figure 5.14b plots the critical state line in the e- $\ln p'$ plane. The results

show that changes in curing temperature and curing stress do not significantly affect the position of the critical state line. Apart from the critical state parameters, other parameters are calibrated. It should be noted that in Chapter 5, the effects of curing temperature and curing stress on soil parameters were not considered. Therefore, specimens subjected to different curing temperatures and stresses are treated as a new type of cemented soil. The calibrated parameters are summarized in Table 5.2. The calibration results indicate that the parameter mainly affected by curing temperature and curing stress is p_b , while other parameters remain consistent.

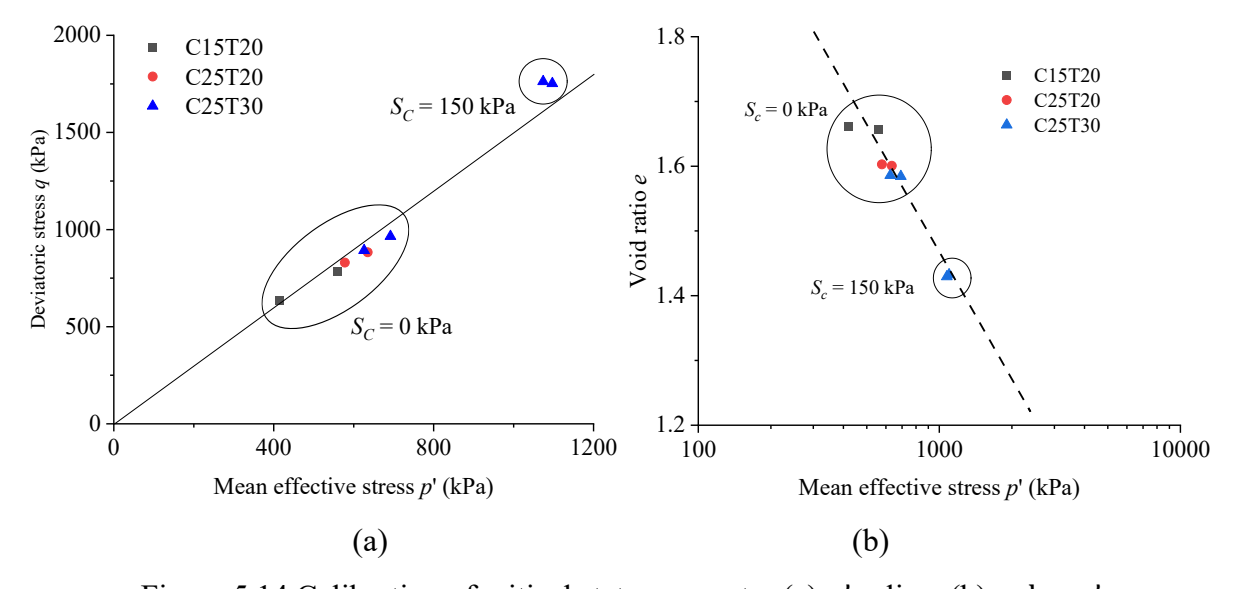


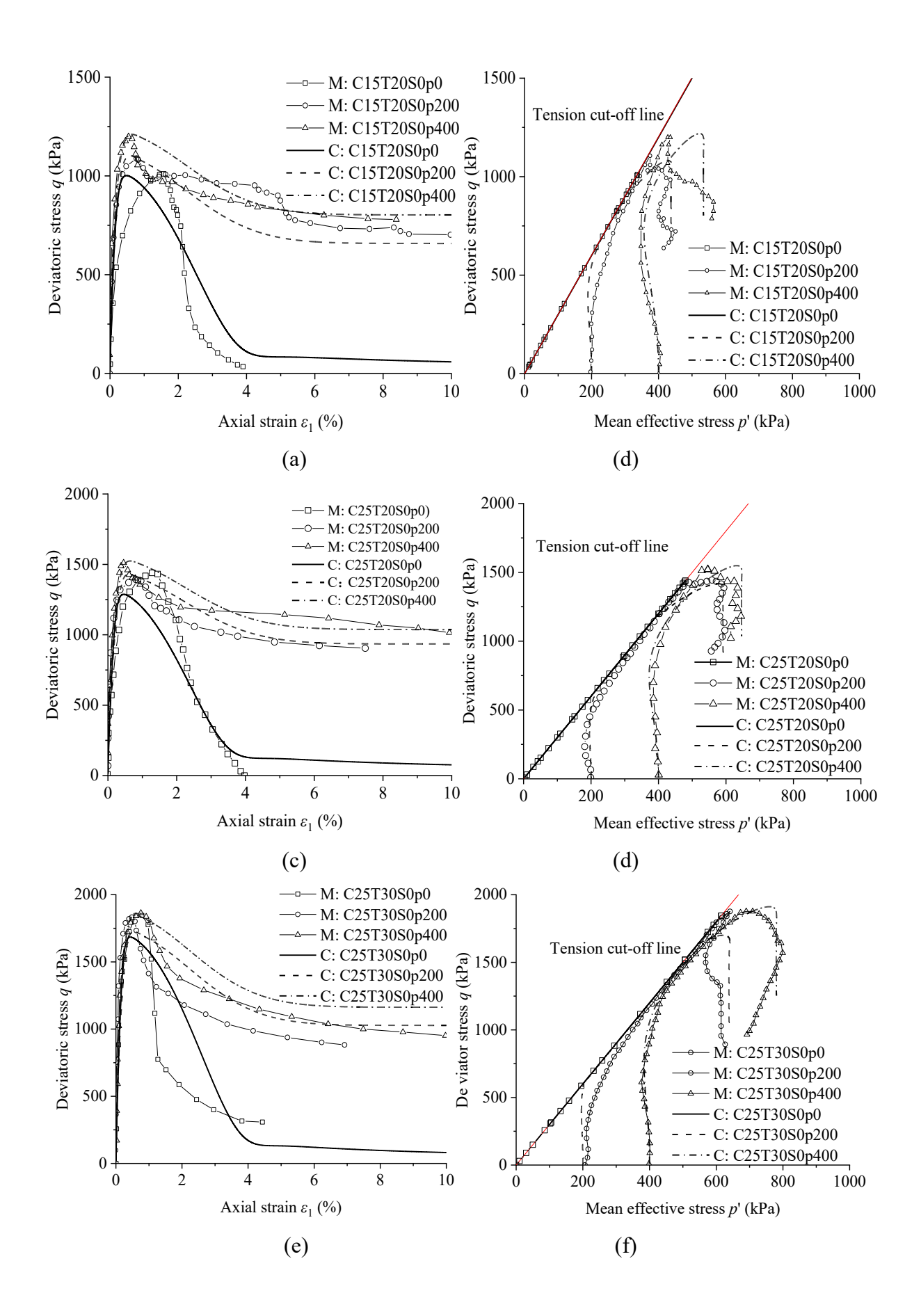
Figure 5.14 Calibration of critical state parameter (a) p'-q line, (b) $e-\log p'$

Figure 5.15 presents a comparison between the computed results and the experimental data. The computed stress-strain curves and stress paths match the experimental results well. This alignment is primarily attributed to the model ability to capture cementation degradation and incorporate critical state theory. In the computed results, strain softening is mainly caused by cementation failure, with the stress state already attaining the e-lnp' line, resulting in a predominantly vertical reduction in the effective stress path. Additionally, in the undrained triaxial shear test, the stress at the critical state is mainly influenced by the void ratio. The proposed model within the bounding surface framework has been successfully validated against experimental data. The calibration process and subsequent computations demonstrate that the model can effectively predict stress-strain behaviour and stress paths of cemented soil.

Table 5.2 Summary of model parameters for the tested Hong Kong marine clay

Parameter	Symbol	Value
	A (MPa)	160
Elasticity	ν	0.3
	n_c	1.6
	M_{U}	1.6
	k_{M}	/
Critical state	λ	0.26
	Γ_U	3.3
	$k_{arGamma}$	/
T1 1	$n_{\rm d}$	3.0
Flow rule	d_0	0.5
II	n_b	0.8
Hardening law	h	3
	\mathcal{E}_{ref}	0.03
	k	2.0
Cementation parameter	k_{pb} (MPa)	/
	β	/
	p_b (kPa, C15T20S0)	450
	p_b (kPa, C25T20S0)	560
	p_b (kPa, C25T30S0)	750
	p_b (kPa, C25T30S150)	1200

Note: when the curing condition is changed, only the value of p_b is affected, with the values of other parameters remaining unchanged.



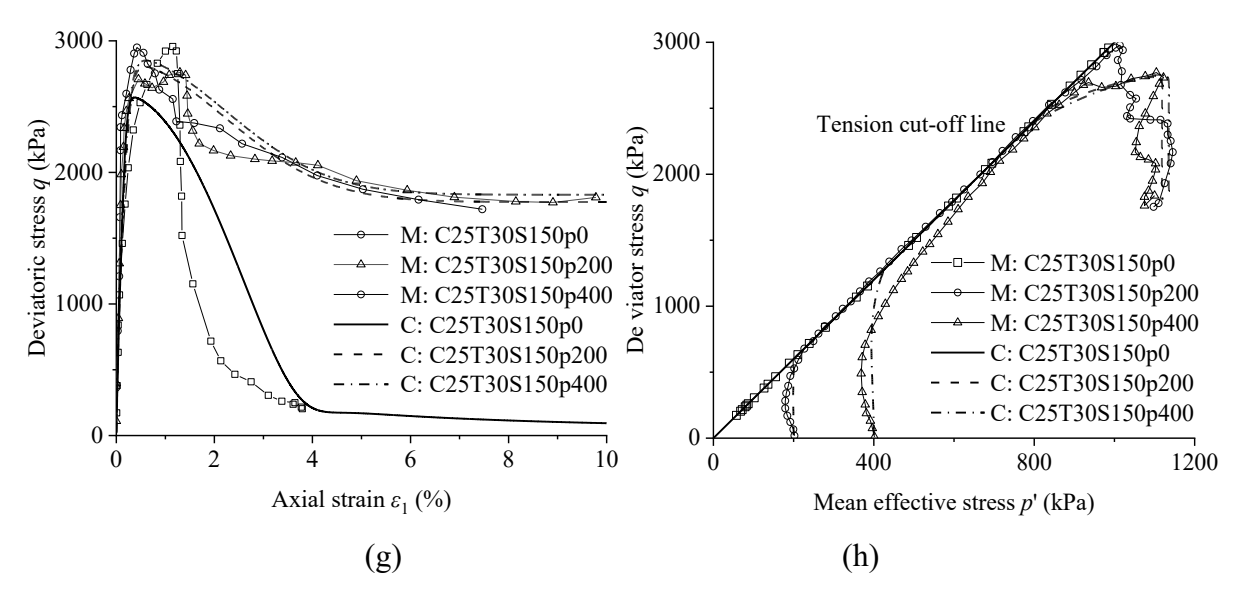


Figure 5.15 Comparison between the measured (M) and computed (C) stress-strain curves and effective stress path of cemented marine clay. (a-b) Cc = 15, $T_c = 20$ °C; (c-d) Cc = 25, $T_c = 20$ °C; (e-f) Cc = 25, $T_c = 30$ °C; (g-h) Cc = 15, $S_c = 150$ kPa.

5.6 Summary

Based on the bounding surface plasticity theory, a new state-dependent model is developed to simulate the cemented soil behaviour at both small and large strains. The size and position of the bounding surface are modified to incorporate the cementation effects. Some new equations are proposed to improve the modelling of the small strain behaviour of cemented soil, such as (i) the elastic shear modulus under both tensile and compressive stress conditions; (ii) the non-linear degradation of bonding strength (p_b) with damage strain (ε_d) in the $\ln p_b - \varepsilon_d$ plane. Seven new parameters are added to simulate the behaviour of cemented soil. These parameters can be calibrated based on laboratory tests. For the convenience of engineering design, the value of some model parameters is correlated with cement content.

The model has been used to predict the behaviour of cemented soils at both small and large strains. The computed results are compared with the experimental results of cemented sands and clays along various stress paths.

The proposed models have several key advantages. Firstly, it can accurately capture the stiffness degradation behaviour of cemented soil in the small strain range. Secondly, the use of bounding surface plasticity theory allows it to simulate nonlinear soil behaviour well during unloading and reloading. Thirdly, the strain-softening behaviour is well simulated based on the newly proposed bonding degradation equation. The proposed model is expected to improve the analysis of the serviceability limit state of infrastructures involving cemented soil.

CHAPTER 6 Model implementation in a modular approach and comparisons among different models

In engineering applications, models with a large number of parameters often face significant limitations. For instance, calibrating these parameters is often complex and challenging, and the models are typically difficult to comprehend. Therefore, this chapter introduces a modular approach to the constitutive model (basic version model), which can be selected based on the availability of input parameters. The primary objectives of this chapter include comparing the results of the full version model and the basic version model, as well as comparing these models with the Mohr-Coulomb (MC) Model. Subsequently, these three models are used to simulate various boundary conditions, including centrifuge tests, laboratory model tests, and a field case in Hong Kong. The aim is to evaluate the effectiveness of the proposed models and to assess the discrepancies in computational results arising from the use of different constitutive models. All analyses are conducted using the commercial software ABAQUS.

6.1 Implementation of the newly proposed model in a modular approach

The theoretical model in Chapter 5 currently consists of 16 parameters due to its comprehensive nature. It is essential to reduce the number of model parameters, considering the difficulties in parameter calibration and the need for convenience in engineering applications. There are two primary strategies to achieve this objective.

Firstly, the model in Chapter 5 establishes correlations between soil parameters and cement content. Specifically, three stiffness and strength parameters are functions of cement content. The model uses the same set of parameters to simulate cemented soil with different dosages. However, this capability is not necessary in most engineering practices because cemented soil with distinct dosages is often treated as different materials. By deactivating this capability, three parameters can be eliminated, simplifying the comprehensive model to have 13 parameters.

Secondly, the full version of the model can adopt a modular approach, consisting of the base version along with two additional modules. These modules can be selected based on the availability of the model parameters to implement the model into FEM programs. This concept is described as follows:

(1) A basic version of the model is developed by simplifying the comprehensive model. Despite the simplification, key features of cemented soil, such as the modelling of strainsoftening and nonlinear stiffness at small strains, are still incorporated. This basic version is detailed in the next part.

(2) Two optional modules with varying complexity and parameter numbers are provided, which have the flexibility to choose whether to turn these modules on or off.

6.2 Basic version of the proposed model

6.2.1 Elastoplasticity

In the basic version model, the calculation of strain uses a decoupled approach, where the total strain is divided into elastic and plastic components.

$$\begin{cases} d\varepsilon_v = d\varepsilon_v^e + d\varepsilon_v^p \\ d\varepsilon_q = d\varepsilon_q^e + d\varepsilon_q^p \end{cases}$$
 (6-1)

where $d\varepsilon_v$ = total increments of volumetric strain; $d\varepsilon_v^e$ = elastic increments of volumetric strain; and $d\varepsilon_v^p$ = plastic increments of volumetric strain; $d\varepsilon_q$ = total increments of deviator strain; $d\varepsilon_q^e$ = elastic increments of deviator strain; and $d\varepsilon_q^p$ = plastic increments of deviator strain.

The incremental elastic strains are calculated using the following formulation:

$$\begin{cases} d\varepsilon_q^e = \frac{dq}{3G_0} \\ d\varepsilon_v^e = \frac{dp'}{\kappa} \end{cases}$$
 (6-2)

where K = the bulk modulus; and G = the shear modulus. They can be calculated from elastic Young's modulus and Poisson's ratio. In the modified formula, Young's modulus and Poisson's ratio are used as model parameters, and these two parameters are constant and are not affected by confining pressure and bond strength attenuation.

$$\begin{cases} d\varepsilon_v^p = D\Lambda \\ d\varepsilon_q^p = \Lambda \end{cases} \tag{6-3}$$

$$K = \frac{E_0}{3(1-2v)} \tag{6-4}$$

$$G_0 = \frac{E_0}{2(1+\nu)} \tag{6-5}$$

The incremental plastic strains are expressed as follows:

$$\begin{cases} d\varepsilon_v^p = D\Lambda \\ d\varepsilon_q^p = \Lambda \end{cases} \tag{6-6}$$

where $D = d\varepsilon_v^p/d\varepsilon_q^p$ is the dilatancy index; and Λ = the non-negative loading index. The dilatancy and loading index can be obtained from the flow rule and the hardening law, which

are explained later.

6.2.2 Bounding and yield surfaces

For the basic version model, two bounding surfaces are defined in the p'-q plane. The first bounding surface is the maximum prestress memory bounding surface, which accounts for the stress history up to the maximum stress, consistent with the model's definition. It can be described as follows:

$$F_s = q - M_m(p' + p_b) (6-7)$$

The second bounding surface is the failure bounding surface. After simplification, the failure bounding surface is unaffected by shear dilatancy behaviour, meaning that state-related soil behaviour characteristics are excluded from the model, which is mathematically defined as follows:

$$\overline{F}_{S} = q - M_{C}(p' + p_{b}) \tag{6-8}$$

where M_c = the critical state stress ratio and is defined as consistent with the attainable peak stress ratio in the basic version model.

Furthermore, a yield surface is defined in the p'-q plane using equation (6-8) representing the elastic range under shearing (Zhou et al. 2015). Within this elastic range, soil deformation is considered elastic.

$$f_t = \left| \frac{q}{p' + p_h} - \alpha \right| - m_c \tag{6-9}$$

6.2.3 Cementation bond strength and its degradation

In the full version model, cementation degradation is described using two parameters. According to experimental data on various cemented soils from Hong Kong, Japan, Singapore, Norway, and other places, the parameter k can be set to a default value of 1. By using only one other parameter, ε_{ref} , it is also possible to simulate a good cementation strength degradation curve. Therefore, the basic version modulus degradation formula for basic version model is Equation (9).

$$p_b = p_{b0}e^{-\frac{\varepsilon_d}{\varepsilon_{ref}}} \tag{6-10}$$

where p_{b0} = the initial cementation bond strength; ε_d = the damage strain.

Figure 6.1 illustrates the impact of different ε_{ref} values on cementation degradation rate when k = 1. It can be observed that, with k = 1, the cementation strength decreases linearly with increasing strain in the logarithmic scale. Additionally, as ε_{ref} decreases the cementation

degradation rate increases. This indicates that the ε_{ref} is potentially able to control the cementation degradation rate.

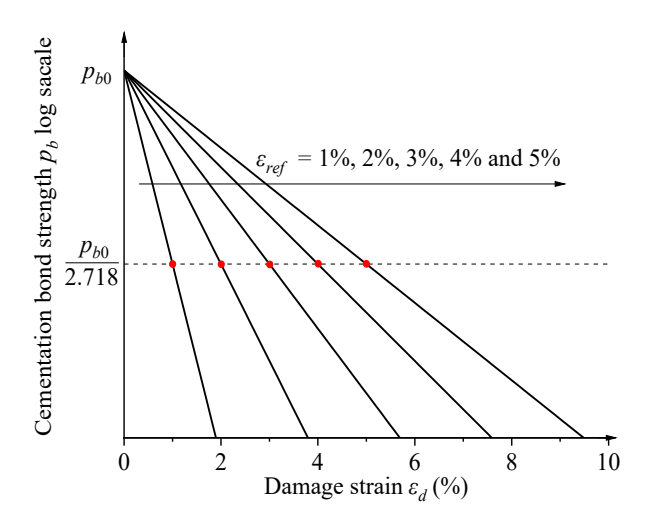


Figure 6.1 The influence of parameters k and ε_{ref} on the degradation process of cementation bond strength

6.2.4 Critical state

In the basic version model, the critical state line (CSL) is simplified to retain only its projection on the p'-q plane, modelling it as a straight line. This simplification is particularly suited for strongly bonded cemented soils, where the bonding between particles primarily governs the strength. Previous experiments have demonstrated that the shear dilatancy behaviour is not a key factor affecting the stress strain behaviour, regardless of whether the soil is drained or undrained. By focusing on the projection of the CSL on the p'-q plane, the model can more accurately represent the behaviour of these soils under various loading conditions without the need for additional complexity for the flow rule.

$$q = M_c p' \tag{6-11}$$

$$M_c = \frac{6\sin(\phi)}{3-\sin(\phi)} \tag{6-12}$$

where M_c = the stress ratio at the critical state, which can be determined from the critical state friction angle.

6.2.5 Determination of dilatancy

As discussed earlier, the proposed model requires the determination of the dilation relation (see Equation (6-5)). For simplicity, the flow rule in the Cam-Clay Model is used. The equation of the flow rule does not require an additional parameter in that the number of parameters is kept to a minimum:

$$D = \frac{M_c^2 - \eta_c^2}{2\eta_c} \tag{6-13}$$

where η_c = the stress ratio defined as the ratio of q to $(p'+p_b)$.

6.2.6 Determination of loading index

In the basic version model, the determination of the loading index is formally consistent with the equations in the full version model. The plastic modulus can be determined by incorporating the simplified elastic modulus, modulus degradation formula, flow rule, and other elements from the basic version model into the equations of the full version model.

6.2.7 Tension cut-off

The current models incorporate the tension cut-off as follows:

$$\begin{cases}
\sigma_1' - \sigma_t \le 0 \\
\sigma_2' - \sigma_t \le 0 \\
\sigma_3' - \sigma_t \le 0
\end{cases}$$
(6-14)

where σ_t = the tensile strength.

6.3 The calibration of the seven model parameters is described as follows:

- (1) q_u is the unconfined compressive strength, which can be determined from unconfined compression tests.
- (2) For the friction angle φ , at least two triaxial tests are needed at different confining pressures.
- (3) The tensile strength σ_t can be determined from indirect or direct tensile tests.
- (4) E_0 is elastic Young's modulus, which can be calibrated from unconfined compression tests with small strain measurements by strain gauges or local LVDT. If test data is unavailable, users may employ the semi-empirical correlation between E_0 and q_u .
- (5) *v* is the Poisson's ratio. It can be calculated from the measured vertical and radial strains in unconfined compression tests. If test data is unavailable, *v* may take a typical value.
- (6) The parameter h controls the plastic modulus. It can also be determined through unconfined compression or triaxial shear tests using the stress-strain relationship before the peak state. Two assumptions are introduced: (a) The destruction of cementation before peaks is negligible, and hence, the second term in equation (5-27) is assumed to be zero; (b) The elastic shear strain is negligible when the mobilised strength is close to the peak value. Given these two assumptions, the stress point reaching 90% strength can be selected to calculate the value of h. With primary shearing corresponding to $\frac{\overline{\rho_s}}{\rho_s} = 1$ and Mm = η_{90} , h yields

$$h = \frac{q_{90} - \eta'_{90} p'_{90}}{\frac{G}{\eta'_{90}} (M_c exp(-n_b \Psi) - \eta'_{90})}$$
(6-15)

(7) The parameter ε_{ref} is related to the relationship between bond strength and damage strain. ε_{ref} is the damage strain at which p_b equals to p_{b0} divided by e. This parameter can be determined using the post-peak stress-strain relationship, i.e., the relationship between axial stress σ_{axial} and axial strain ε_{axial} from the softening section of unconfined compression tests. This method assumes that the $p_b - \varepsilon_d$ and $\sigma_{axial} - \varepsilon_{axial}$ relationships exhibit similar behaviour based on the following three features: (i) the total strain closely approximates the plastic strain during the softening process; (ii) the volumetric strain in unconfined compression tests is typically small, resulting in similar axial, deviatoric, and damage strains; (iii) the values of $\frac{p_b}{p_{b0}}$ and $\frac{\sigma_{axial}}{q_u}$ in the softening process of unconfined compression tests are close. In this calibration method, ε_{ref} is estimated as the axial strain corresponding to the point where the axial stress decreases to q_u/e during the strain-softening process.

6.4 Optional modules

The constitutive model has been developed in a modular version, allowing for flexibility in its application. In addition to the basic version model described in section 6.2, two independent modules have been incorporated, which can be selectively activated based on the availability of input parameters and the requirements of engineering problems. For each module, Table 6.1 summarizes the relevant model functions and additional parameters. The formulas for these two additional modules have been detailed in Chapter 5, so they would not be repeated here.

Table 6.1 Capability and input parameters of optional modules

Optional module	Capability	Additional parameters
(1) State-dependent stiffness and strength	Modelling soils with different initial water contents/densities with a single set of parameters	λ , Γ_c , n_d , d_0 , n_b
(2) Correlation between elastic modulus and UCS	Considering the change of elastic shear modulus during bonding degradation	A, $n_c(E_0)$ in the basic version is not required if these two parameters are used)

6.5 Comparison of different models

6.5.1 Simulating drained triaxial shear tests

The drained triaxial shear tests conducted by Marri et al. (2012), which focused on specimens with three different cement contents, were compared. Figure 6.2 shows the simulation results of triaxial tests for the full and basic versions models, with model parameters summarised in Tables 6.2 and 6.3. By comparing the stress-strain curves, it was observed that both models predict satisfactory results. The primary reasons are as follows: Firstly, the shear strength of cemented soil is mainly controlled by the cementation effect. Both models utilize the cementation parameter (p_b) to predict strength behaviour accurately. Secondly, both models employ the framework of the bounding surface model, which can predict gradual yield behaviour. Additionally, h is a positive model parameter influencing the growth of plastic strain. As shear strain increases, a larger h value leads to a higher plastic modulus, resulting in smaller plastic strain and a more rapid increase in shear stress with strain. These two characteristics ensure a good simulation of the stress-strain behaviour of cemented soil.

Figure 6.2b, d, and f compare the computed volumetric strain curves using the full and basic versions models. The full version model can better predict volumetric changes as it considers state-dependent dilatancy behaviour, which has been detailed in Chapter 5 and is not elaborated here. The results shown in the figure indicate that the basic version model cannot simulate the significant dilatancy behaviour of cemented soil. The primary reasons are, firstly, the removal of state-dependent dilatancy behaviour in the basic version model, and the dilatancy defined in this study is related solely to the stress ratio. Cemented soil is stiff, and with increasing strain, the stress state quickly approaches the failure envelope. Consequently, the dilatancy coefficient is almost zero in the strain-softening part, making it challenging to predict volumetric expansion behaviour.

Yao et al. (2018) utilized the bender element test, resonant column test, and local strain measurement to determine the modulus degradation curve of cemented clay within a small strain range. Figure 6.3 compares the small strain modulus computed results of the full version model and basic version model in the study of Yao et al. (2018), with model parameters summarised in Tables 6.2 and 6.3. The comparison reveals that the full version model effectively simulates soil behaviour, including the stress effects on stiffness and significant stiffness degradation at small strains. In contrast, the basic version model does not perform well in simulating the stress effect on stiffness.

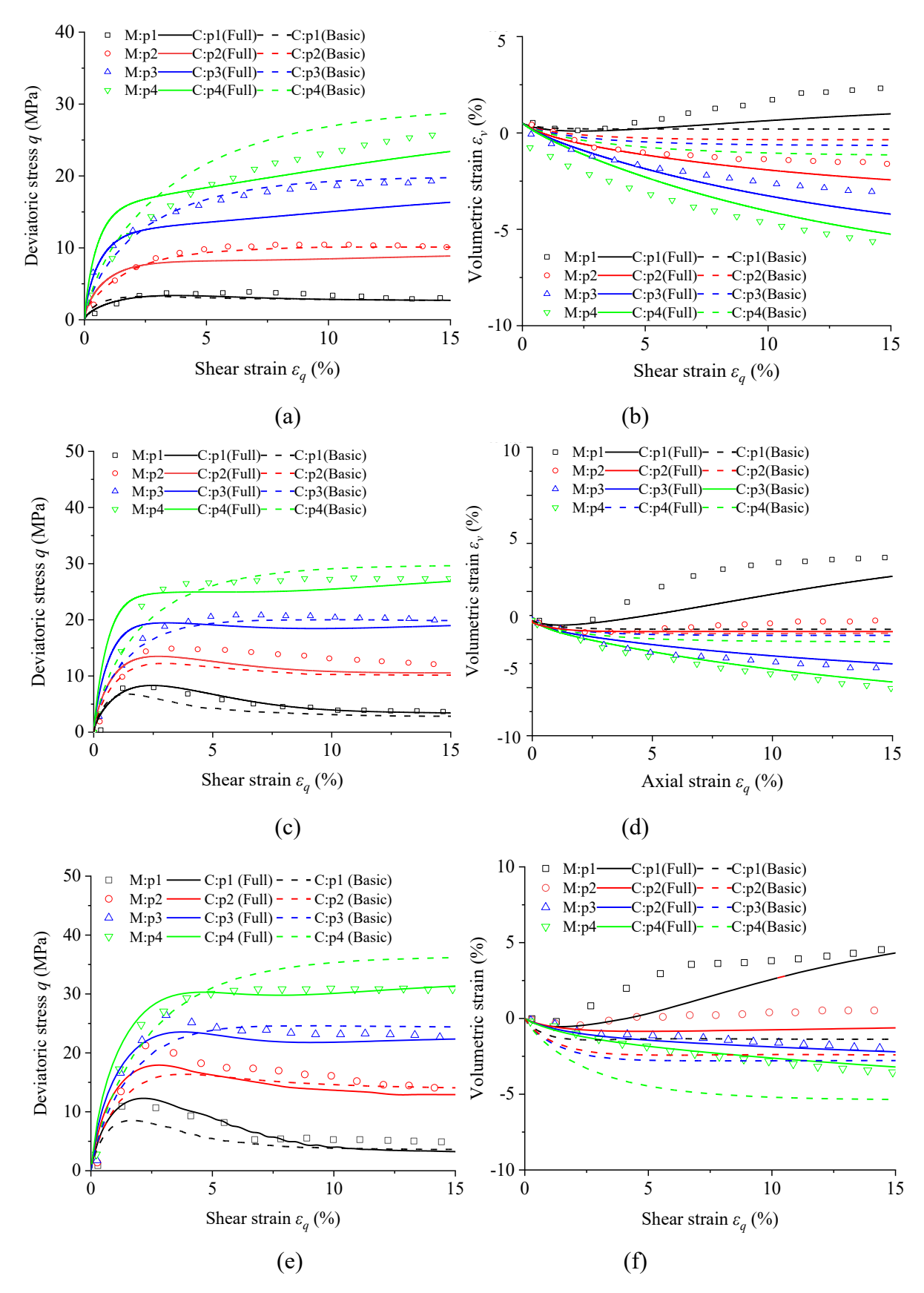


Figure 6.2 Comparison of the results of triaxial drained shear tests (Marri et al. 2012) using full version model and basic version model (a-b) Cc = 5%; (c-d) Cc = 10%; (e-f) Cc = 15%

The primary reason for this difference is that the elastic modulus of the cemented soil in the basic version model is set as a constant, ignoring the variation of the elastic modulus as the cementation and stress change. Simplifying the effects of stress on modulus is a reasonable approach. This simplification is justified by previous research, which has demonstrated that cementation predominantly determines the modulus of strongly cemented soil and is independent of confining pressure. Therefore, the computed result is not significantly compromised after simplification.

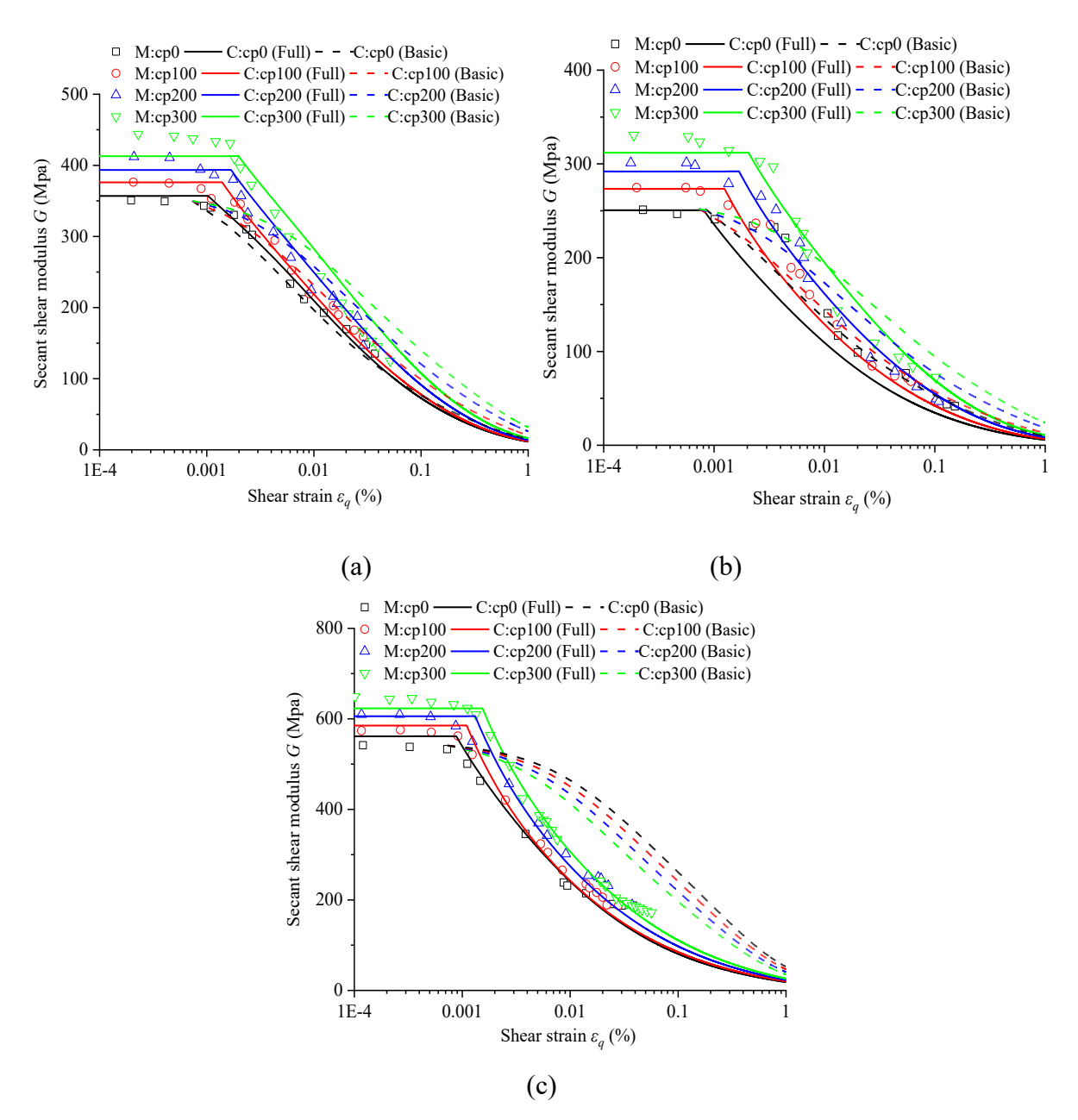


Figure 6.3. Comparison between the measured (M) (Yao et al. 2018) and computed (C) stiffness degradation curves of cemented marine clay with different cement contents: (a) Cc = 20%; (b) Cc = 30%; and (c) Cc = 50%.

The study conducted by Rios et al. (2017) provides comprehensive data on stress-strain curves, volumetric deformation, and small strain modulus for cemented soil. Therefore, the measured data in their study were selected for comparison to evaluate the model performance in different aspects. The model parameters of the full version model and basic version model are summarised in Tables 6.2 and 6.3. For the MC model, the friction angle is selected as the critical state angle of 32 degrees. According to the ideal MC strength calculation formula proposed by Vermeer and De Borst (1984), the cohesion in the model is calculated to be 520 kPa.

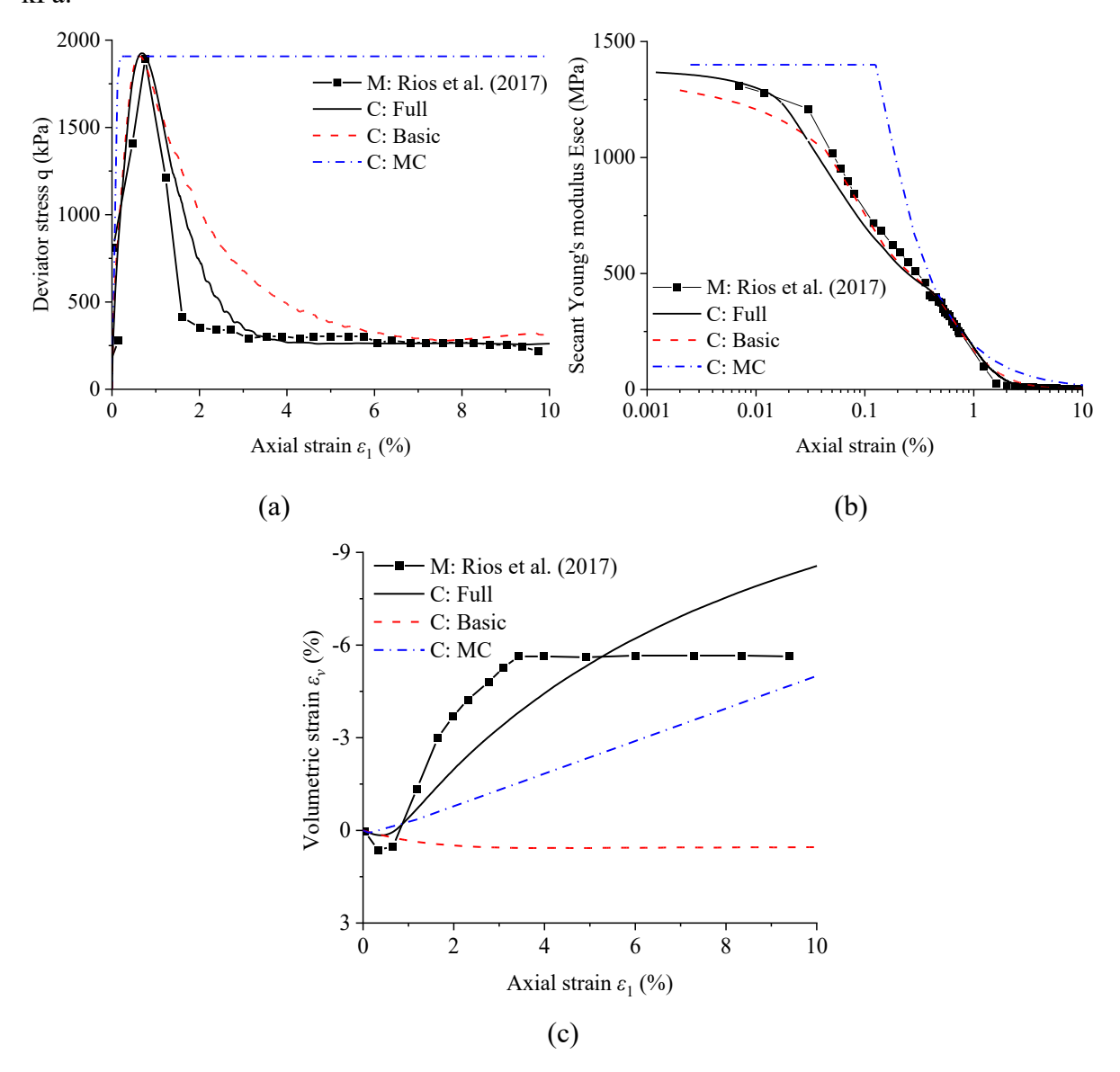


Figure 6.4 Comparison with triaxial shear test Rios et al. (2017) using full and basic versions models. (a) stress-strain curve; (b) volume strain curve; (c) small strain modulus attenuation curve

Comparative analysis of the stress-strain curves reveals that the MC model has major

limitations in simulating strain-softening, as shown in Figure 6.4a. There is no strain softening behaviour in the MC result, potentially leading to an overestimation of the bearing capacity of DCM columns in practical engineering and neglecting the stress transfer from DCM to the surrounding soil. Figure 6.4b illustrates the comparison between the calculated curve of the small strain modulus and the test results. The proposed bounding surface models predict modulus degradation starting from very small strains. However, the ideal elastoplastic (MC) model predicts only elastic behaviour when the stress is within the yield surface, resulting in the modulus exhibiting plastic degradation only after the peak strength.

A comparative analysis of the volumetric strain curves reveals that the full version model is the most effective in simulating irreversible volumetric changes. In contrast, the MC model simulates shear strain using a constant dilation angle, which, under significant strain, may result in an overestimation of irreversible volumetric strain. The basic version of the model is the least effective in predicting dilation behaviour. This is due to the removal of state-dependent dilation behaviour and the use of a simplistic dilation formula, resulting in inaccurate predictions. This comparison demonstrates that the bounding surface model provides higher accuracy in predicting material behaviour, particularly within the small strain range. In contrast, while the ideal elastoplastic model offers reasonable elastic predictions initially, its accuracy significantly diminishes as the stress approaches the yield surface.

6.5.2 Simulating undrained triaxial shear tests

To validate the model performance under different stress paths, the computed results were compared with undrained triaxial shear tests. Ho et al. (2021) conducted these tests on cemented samples, using four initial effective confining pressures. The comparison between the computed and test results is shown in Figure 6.5. Both the undrained stress-strain curves and the effective stress paths were analysed. Figure 6.5a compares the stress-strain curve between the computed results of the full version model and the test results. The test results indicate that the undrained triaxial shear strength significantly increases with an increase in confining pressure. When the stress increases from 100 to 400 kPa, the strength increases by approximately 30%. The computed results predicted a slight increase in strength with confining stress, which is attributed to the critical state theory. Firstly, as the initial confining pressure increases, the strength increases. Secondly, higher initial confining pressure results in a lower void ratio after consolidation, which enhances dilatancy and which enhances dilatancy and thus leads to higher strength.

The effective stress path in Figure 6.5b shows an initial elastic phase where the vertical

stress increases, followed by dilative behaviour as plasticity develops. The test data show that after the stress reaches its peak, the soil exhibits contractive behaviour, as the stress path is located to the left of the peak stress point. However, the full version model did not predict this transition from dilation to contraction. In the current model, predicting the transition between dilation and contraction during hardening and softening processes is challenging.

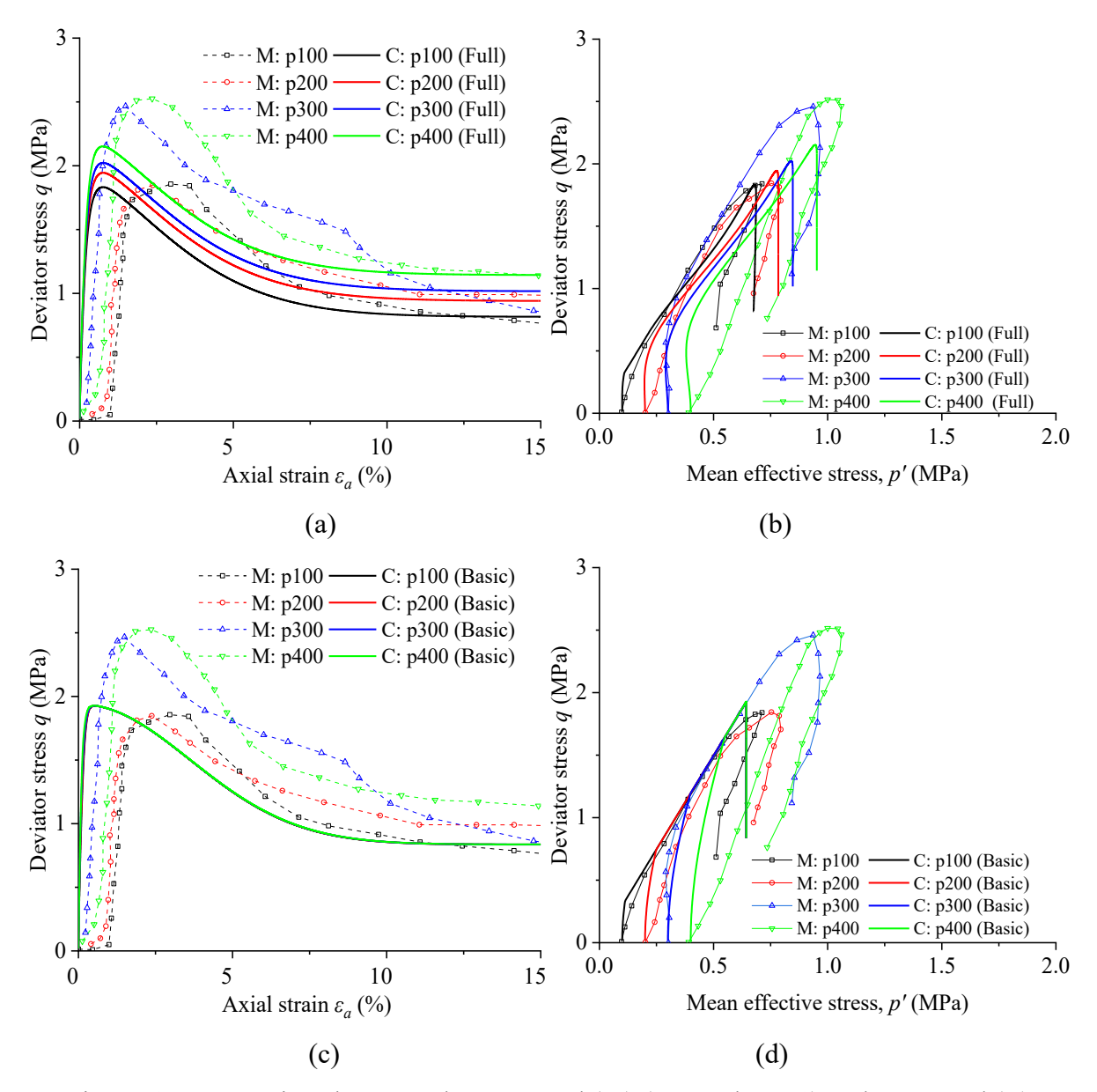


Figure 6.5 Comparison between the measured (M) (Ho et al. 2021) and computed (C) undrained triaxial compression test results of cemented Hong Kong marine clay: (a-b) full version model; (c-d) basic version model

Figure 6.5c compares the test data with the computed results of the basic version model. The comparison of the stress-strain curves shows that the simplified model can not predict the increase in strength with increasing confining pressure. This phenomenon can be explained

using the undrained shear path shown in Figure 6.5d. Initially, the nearly elastic response increases up to the tension-cutoff line. Subsequently, the mean effective stress increases along the tension line until it reaches the failure envelope, achieving peak strength. It is important to note that the effective mean stress acting on the specimen is zero when the stress state is located on the tension-cutoff line. Therefore, the strength does not increase with confining pressure. Additionally, the removal of state-dependent property implies that the increased density effects induced by consolidation confining pressure can not be considered.

6.5.3 Simulating centrifuge tests of DCM-support excavation

Validation of constitutive models through the simulation of boundary value problems is crucial. This helps in evaluating the models under more complex stress paths. This section presents a simulation of a centrifuge test involving DCM column-supported excavation conducted by Chen et al. (2023). Chen et al. (2023) studied the performance of anchored sheet pile quays reinforced with DCM columns in soft soil using centrifuge tests. The study was designed with a model scale of 1/100, with a nominal centrifuge acceleration of 100 g. The dimensions used in the model simulation corresponded to the prototype dimensions. The experimental setup is illustrated in Figure 6.6. The analysis steps are conducted using a static state analysis. The model parameters are summarised in Table 6.4 to Table 6.8.

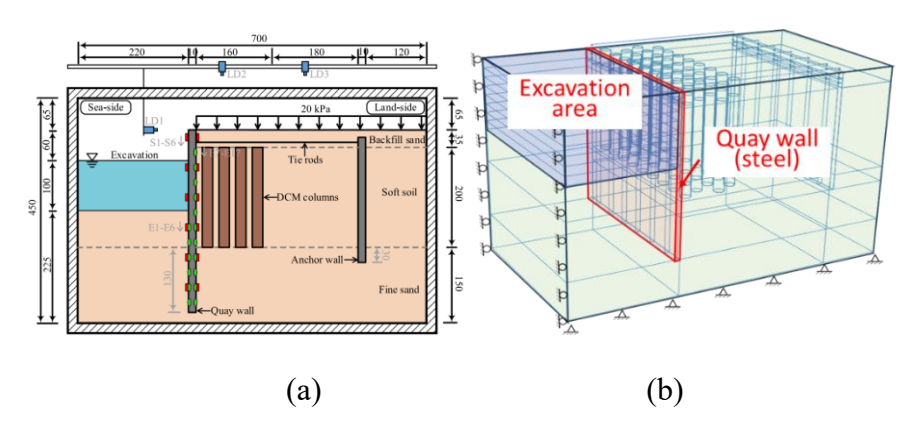


Figure 6.6 (a) Schematic diagrams of the centrifuge model setup; (b) three-dimensional model in finite element analysis

Table 6.2 Parameters used in the full version model for element testing

Parameter	Symbol	Portaway sand Marri et al. (2012)	Singapore marine clay Yao et al. (2017)	Singapore marine clay (Rios et al. 2017)	Osorio sand (Ho et al. 2021)
	A (MPa)	200	130	130	600
Elasticity	ν	0.3	0.3	0.3	0.3
Elasticity	n_c	1.0	2.8	2.8	5.0
	m_U	0.01	0.01	0.01	0.01
	M_U	1.20	0.90	0.90	1.30
	k_M	2.0	1.0	1.0	0.1
Critical state	λ	0.08	0.20	0.20	0.02
	Γ_U	2.1	3.0	3.0	3.2
	$k_{arGamma}$	0.1	0.5	0.5	2.0
Flow rule	n_d	2	1	1	3
riow rule	d_0	1.0	0.1	0.1	0.05
Hardening	n_b	3.0	1.0	1.0	0.5
law	h	0.1	1.0	1.0	0.8
	ε_{ref}	0.06	0.06	0.06	0.03
Cementation	k	2.0	0.8	0.8	4.0
parameter	k_{pb} (MPa)	68	1.3	1.3	11
	β	1.5	1.5	1.5	1.0

Table 6.3 Parameters used in the basic version model and MC model for element test

Parameters	Portaway sa	and Marri et al.	. (2012)	Singapore 1	marine clay		Singapore	marine clay	Osorio sand
				Yao et al. (2017)		(Rios et al. 20	017)	(Ho et al. 2021)
	<i>Cc</i> = 5%	<i>Cc</i> = 10%	<i>Cc</i> = 15%	<i>Cc</i> = 5%	<i>Cc</i> = 10%	<i>Cc</i> = 15%	Basic	MC	-
E_{θ} (MPa)	200	460	540	650	920	1400	1300	1360	480
ν	0.3			0.3			0.3	0.3	0.3
φ (°)	32			32			32	32	32
h	1.0			1.0			0.8	/	1.0
ε_{ref}	0.04			0.03			0.015	/	0.05
c ₀ (kPa)	400	500	800	200	350	450	1000	1000	300
$\sigma_t(\mathrm{kPa})$	40	50	80	20	30	50	100	/	30

Table 6.4 Soil parameters used in the elastic and MC models for different materials in centrifuge test

Soil Parameters	Quay wall	Anchored	Tie rod	Sand	Fine
		wall		backfilling	sand
Material model	Elastic	Elastic	Elastic	Mohr-	Mohr-
				Coulomb	Coulomb
Density, ρ (kg/m ³)	2500	2500	1	2000	2000
Young's modulus, E_0 (MPa)	2800	28000	200000	40	30
Poisson's ratio, ν	0.2	0.2	0.3	0.3	0.3
Friction angle, ϕ' (°)	/	/	/	32	29
Cohesion, c (kPa)	/	/	/	0	0

Table 6.5 Soil parameters used in the modified Cam-Clay model for HKMD in centrifuge test

Soil Parameters	Soft soil
Compression index, λ	0.1
Swelling index, κ	0.01
Density, ρ (kg/m ³)	1500
Critical state stress ratio, M	1.0
Poisson's ratio, ν	0.3

Table 6.6 Soil parameters used in the proposed full version model for cemented soil in centrifuge test

Soil Parameters	Value for DCM	Soil Parameters	Value
A (MPa)	290	ϵ_{ref}	0.06
v	0.3	p_b (kPa)	500
n_c	1.0	Density (kg/m ³)	1500
M_c	1.25	Permeability (m/d)	/
λ	0.08	β	/
n_b	3.0	K_{pb}	/
d_0	1.0	k_{M}	/
n_d	2.20	k_T	/
h	0.3		

Table 6.7 Soil parameters used in the proposed basic version DCM model for cemented soil in centrifuge test

Soil Parameters	Value
E_0 (MPa)	480
ν	0.3
φ (°)	30
h	1.0
$arepsilon_{ref}$ $ ext{c}_0 ext{ (kPa)}$	0.05
$c_0(kPa)$	300
σ_t	30

Table 6.8 Soil parameters used in the MC model for cemented soil in centrifuge test

Soil Parameters	Value
E_0 (MPa)	120
v	0.3
φ (°)	32
c (kPa)	300
$\Psi(^{\circ})$	5
σ_t	30

The steps of the numerical simulation of the excavation are the same as those in the centrifuge test and can be summarised as follows:

- (1) Initially, the quay wall and anchor wall are established within the soil layers under gravitational forces to achieve force equilibrium.
- (2) Subsequently, model replacement is executed by installing DCM columns, followed by resetting the displacements to zero.
- (3) The excavation body is then deactivated to simulate the removal of soil.
- (4) After the excavation, a load of 20 kPa is applied to the ground surface behind the quay wall to simulate the working load conditions.

Figure 6.7a compares the measured earth pressure behind the quay wall with the earth pressure calculated using three different models. As shown in Figure 6.7a, the use of DCM-supported excavation effectively reduces the earth pressure acting on the back of the quay wall. Within the DCM-supported range of 0-23.5 meters, the full version model and basic version

model show good agreement with the test results. However, the MC model predicts the largest values. For the soil beneath the DCM-improved zone, the lateral earth pressure calculated by the three models is slightly higher than the measured result and gradually approaches the lateral at-rest earth pressure. Figure 6.7b compares the lateral displacement curves along the quay wall after excavation. The overall displacement profile of the quay wall exhibits an S-shape, with the maximum displacement occurring at the top of the wall. The lateral displacement curves computed by the three models exhibit consistent trends with the test results. The MC model predicts the smallest lateral displacement at the base of the wall, followed by the basic version model. Conversely, the MC model predicts the largest lateral displacement at the top of the wall, while the basic version model predicts the smallest. However, the differences in the lateral displacement curves predicted by the three models are insignificant. In Figure 6.7c, the bending moment distribution along the depth of the quay wall also exhibits an S-shape. The bending moment is attributed to the displacement of the soil in the direction of excavation and the stress release caused by excavation. The bending moments at the top and bottom of the quay wall are approximately zero, with positive and negative peak values occurring at depths of 25 m and 13 m, respectively. The calculation results of the full version model are most consistent with the measured data, followed by the basic version model and the MC model. The MC model overestimates the maximum negative moment and underestimates the maximum positive moment. Figure 6.6d compares the calculated ground settlement results. The computed results indicate that the results from the full version model closely align with the experimental data, whereas the settlements predicted by the basic version model and the MC model are significantly lower than the experimental values. This discrepancy is likely due to the definition of elastic modulus. In the basic version model and the MC model, the elastic modulus is treated as constant, ignoring the effects of stress and cementation on stiffness, which results in an underestimation of the deformation. Overall, the calculated results align with the measured data, indicating that the full and basic versions models are appropriate for simulating the anchored sheet pile wall system.

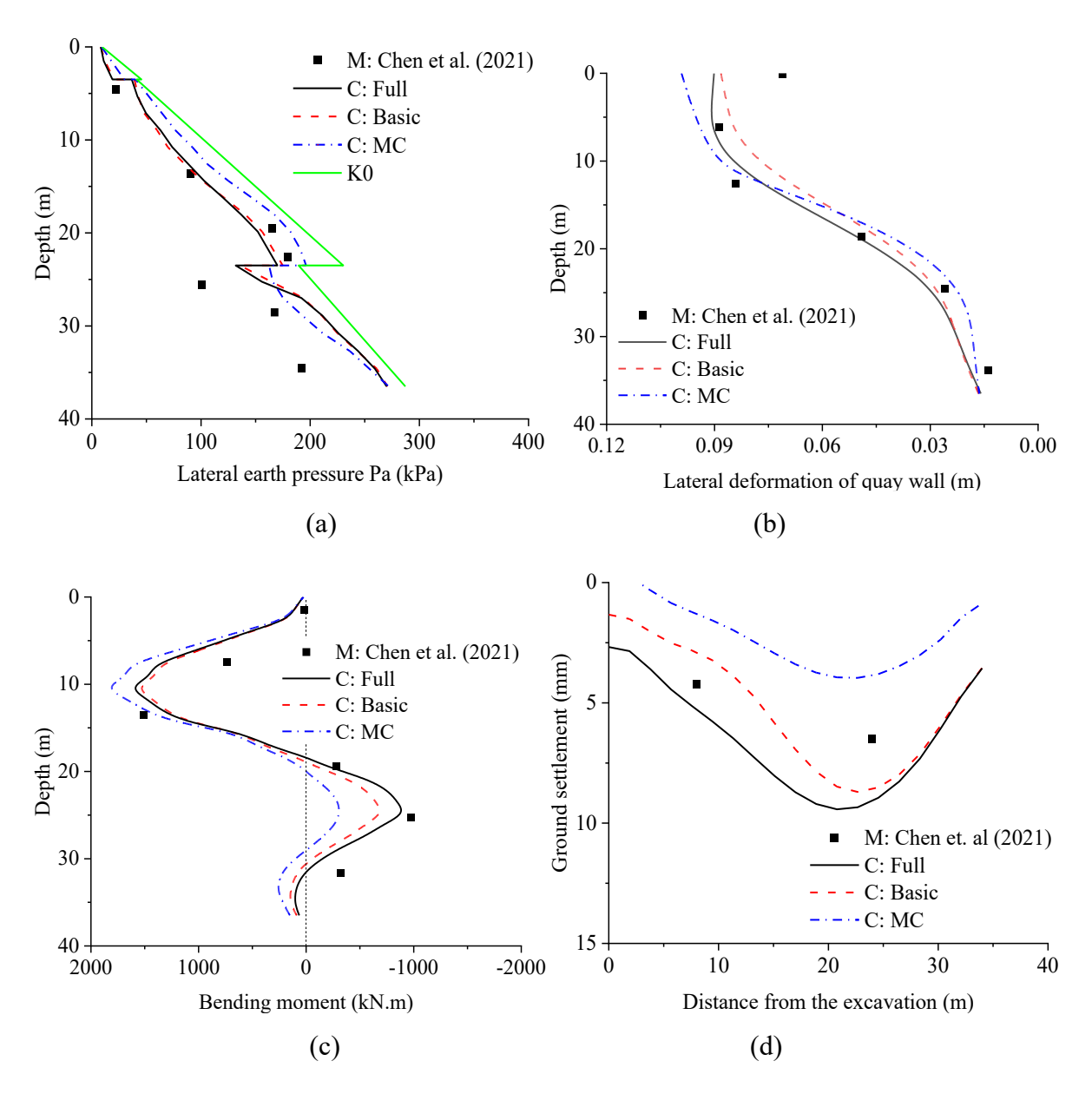


Figure 6.7 Comparison of computed results using three models and experimental test results.

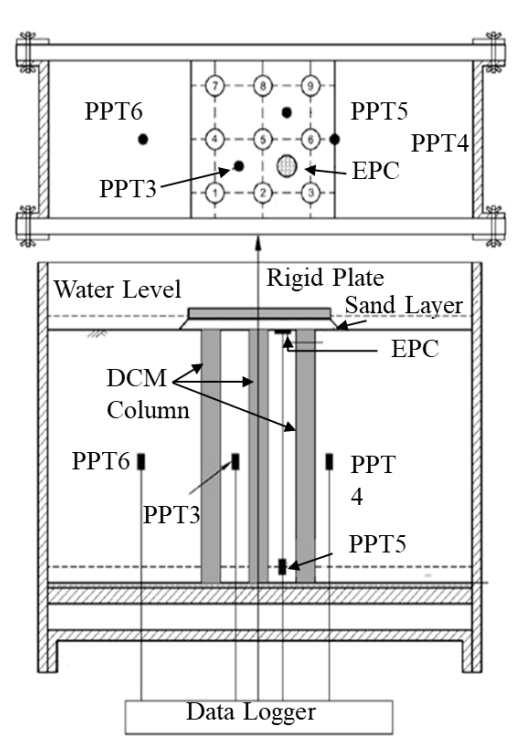
(a) earth pressure on the quay wall, (b) deflection of the quay wall, (c) bending moment along the quay wall, (d) ground settlement behind the quay wall.

6.5.4 Simulating physical model tests of DCM-supported rigid footing

To demonstrate the superiority of the model, simulations involving a shallow foundation supported by DCM (see Figure 6.8) were conducted. In this case, the strain was relatively large, with a maximum strain of 5%. Significant degradation of the cementation structure occurred at this strain level in the DCM columns. Additionally, comprehensive experimental data were also recorded, including stress distribution and pore water pressure changes. Detailed information on the experimental setup can be found in the work of Fang (2006). The numerical analysis type is a fully coupled hydromechanical analysis. The soil parameters used in the FEM

simulations are presented in Table 6.9 to Table 6.12. The primary focus is on the calculated results of stress and deformation behaviour of the foundation.

- (1) For the X-direction and Y-direction, normal displacement is constrained at Xmin, and an equivalent lateral force boundary condition is applied at Xmax. The hydraulic condition in the Xmin and Xmax, Ymin and Ymax is impermeable;
- (2) For the Zmin, displacement in all three directions—x, y, and z are constrained, and the hydraulic condition is impermeable. The analysis type is a fully coupled hydro-mechanical analysis. The soil parameters used in the simulations are summarised in Table 6.16 to Table 6.18.
- (3) For the top boundary condition, the displacement is unrestrained and permeable. The pore water pressure is always set at zero. The analysis type is a fully coupled hydro-mechanical analysis.



- Pore water pressure transducer (PPT)
- © Earth pressure cell (EPC)

Figure 6.8 Schematic diagram of physical model test setting (Fang 2006)

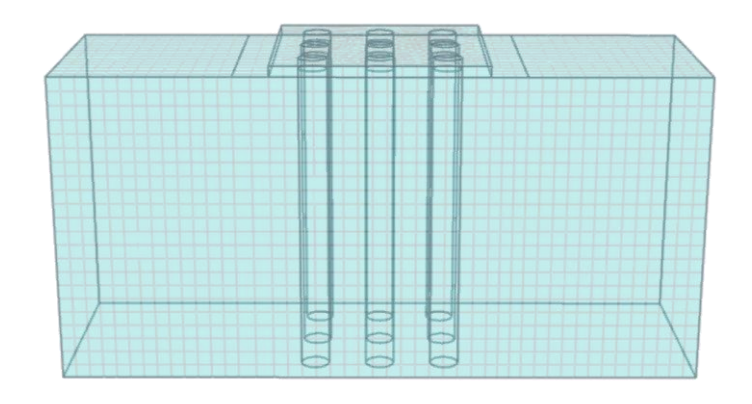


Figure 6.9 Finite element model and meshing

Table 6.9 Mechanical properties of soft soil in physical model test

Soil Parameters	Marine Deposits
Compression index, λ	0.15
Swelling index, κ	0.012
Density, ρ (kg/m ³)	1500
Critical state stress ratio, M	1.0
Poisson's ratio, ν	0.3
Permeability coefficient, k (m/d)	0.005

Table 6.10 Soil parameters used in the full version model for cemented soil in physical model test

Soil Parameters	Value for DCM	Soil Parameters	Value for DCM
A (MPa)	500	ϵ_{ref}	0.03
v	0.3	p_b (kPa)	200
n_c	2	Density (kg/m ³)	1500
M_c	1.25	Permeability (m/d)	0.003
λ	0.02	β	1.2
n_b	1	K_{pb}	/
d_0	2	k_{M}	/
n_d	1	k_T	/
h	1		

Table 6.11 Soil parameters used in the proposed basic version model for cemented soil of physical model test

Soil Parameters	Value for DCM
E_0 (MPa)	450
v	0.3
φ (°)	33
h	1.5
$arepsilon_{ref}$	0.03
$arepsilon_{ref}$ $c_{ heta}$ (kPa)	200
σ_t	20

Table 6.12 Soil parameters used in the MC model for cemented soil of physical model test

Soil Parameters	Value for DCM
E_0 (MPa)	350
ν	0.3
φ (°)	33
c (kPa)	1000
$\Psi(^{\circ})$	0.1
σ_t	100
E_0 (MPa)	350

Figure 6.10a compares the vertical load obtained from three models against vertical settlement. The test results indicate that the vertical load initially increases as settlement increases. After reaching peak strength, the stress gradually decreases at the strain of around 2%, completing the reduction at a strain of approximately 6%. This behaviour is effectively captured by both the full and basic version models. In contrast, the computed load using the MC model maintains the maximum value after attaining peak strength, demonstrating the superior performance of the proposed bounding surface models. Figure 6.10b compares the stress on the DCM columns and soft soil during loading. At the same strain level, the stress on the DCM columns is significantly higher than that on soft soil due to the higher modulus of the DCM columns. Once the stress reaches the foundation bearing capacity, the overall capacity decreases, resulting in a significant reduction of approximately 30% in the load on the columns. This reduction is primarily due to the degradation of the cementation structure in the DCM

columns. The strain-softening behaviour of DCM is accompanied by stress redistribution within the foundation, which is well captured by the full and basic version models but not by the MC model. The predictions from the three models indicate that the full and basic versions closely match the observed stress reduction, whereas the MC model does not account for the softening behaviour.

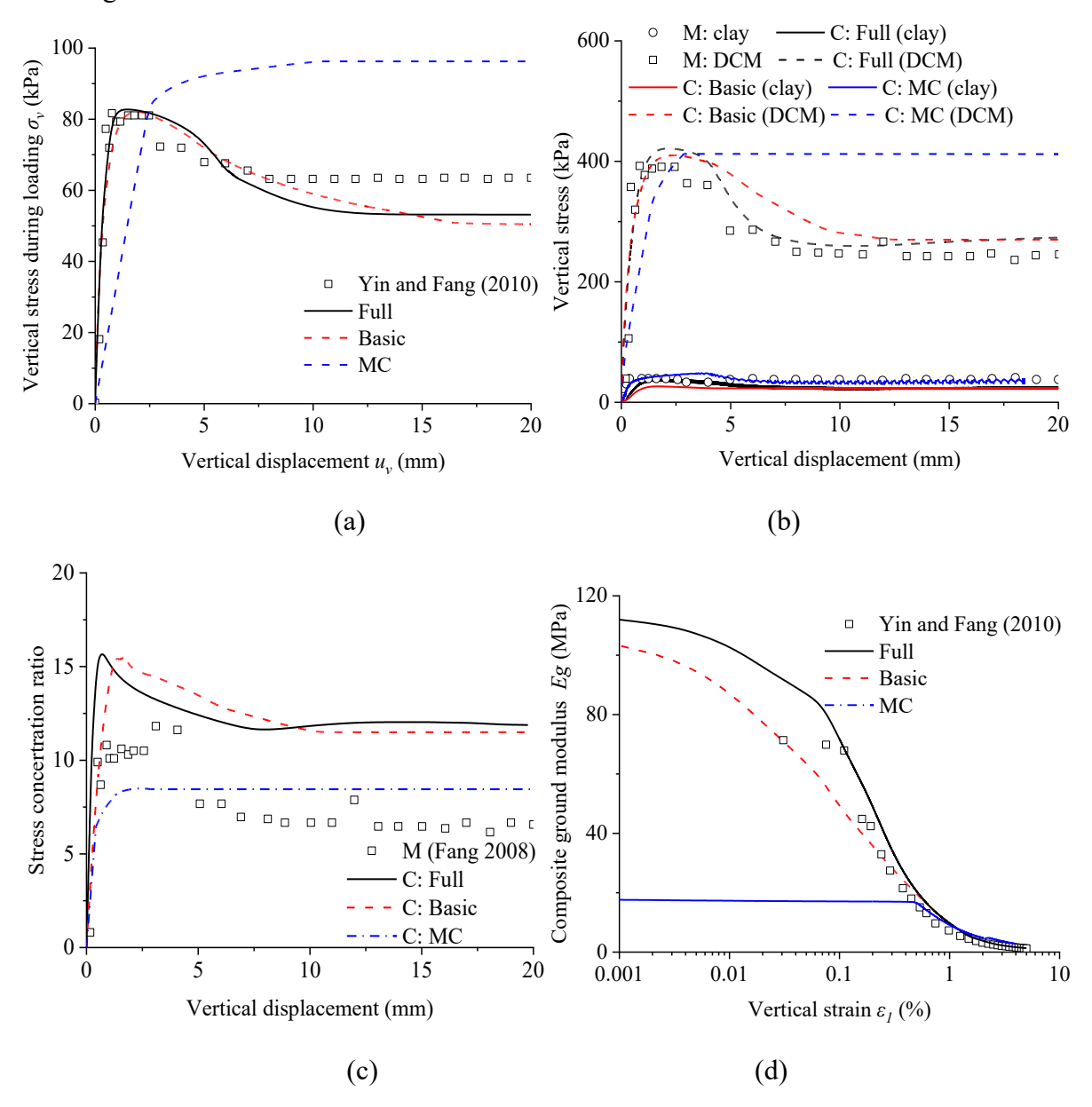


Figure 6.10 Comparison of computed results using three models and experimental test results: (a) vertical loading stress on the foundation (b) stress comparison between DCM column and clay (c) stress ratio between DCM column and clay (d) small strain modulus of the foundation

Figure 6.10c compares the stress ratio between DCM and clay. The experimental results indicate that the stress ratio initially increases and gradually decreases as the DCM column

fails. The calculated results slightly underestimate the strength of the clay, leading to an overestimation of the predicted stress ratio between the stresses acting on DCM and clay. A possible reason is that the DCM undergoes lateral deflection under compression, as shown in Figure 6.11. Consequently, during the DCM failure process, surrounding clay undergoes an unloading process, causing horizontal and vertical stresses on the clay to decrease. Although the MC model detects that this ratio aligns well with the experimental results, it overlooks the transition from strain-hardening to strain-softening.

Figure 6.10d compares the stiffness degradation curves of the composite foundation. The newly proposed models for cemented soil accurately reflect the stiffness degradation at small strains. For the MC model, the currently recommended modulus estimation method for DCM ($E = 300q_u$) in FHWA (2013) may underestimate the modulus of the cemented soil. The computed result using MC for DCM initially shows elastic deformation, subsequently transitioning into plastic deformation. However, the discrepancy between the predicted small-strain modulus and the experimental results remains significant across the entire strain range. Overall, the newly proposed full and basic version models for cemented soil effectively simulate the typical mechanical behaviour of DCM over a wide range of strains.

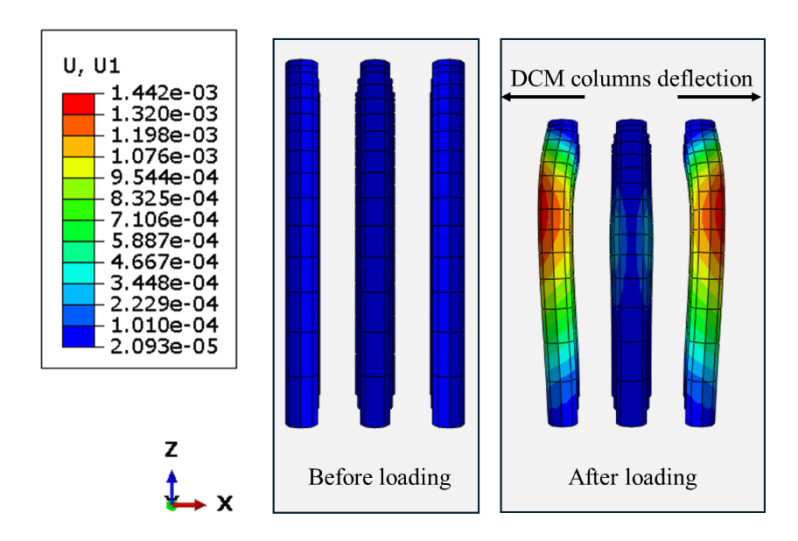


Figure 6.11 Deformation contour of the DCM columns before loading and after loading

It is noteworthy that previous comparisons show that the basic version model has been simplified in many aspects, particularly in state-dependent dilatancy, which affects the calculation of pore water pressure. The calculation results from the physical model test indicate minimal differences between full and basic version models when performing fully coupled hydromechanical analyses. The effective stress paths within the DCM columns at different positions were compared to further validate this. As shown in Figure 6.12, the stress path curves

reveal that before reaching the peak, the stress path closely follows the drained shear path, resulting in small excess pore water pressure. During the strain-softening phase, the pore water pressure dissipates gradually, and the stress path attains the drained stress path line. Therefore, it can be concluded that the proposed full and basic version models are highly reliable for fully coupled hydro-mechanical analysis.

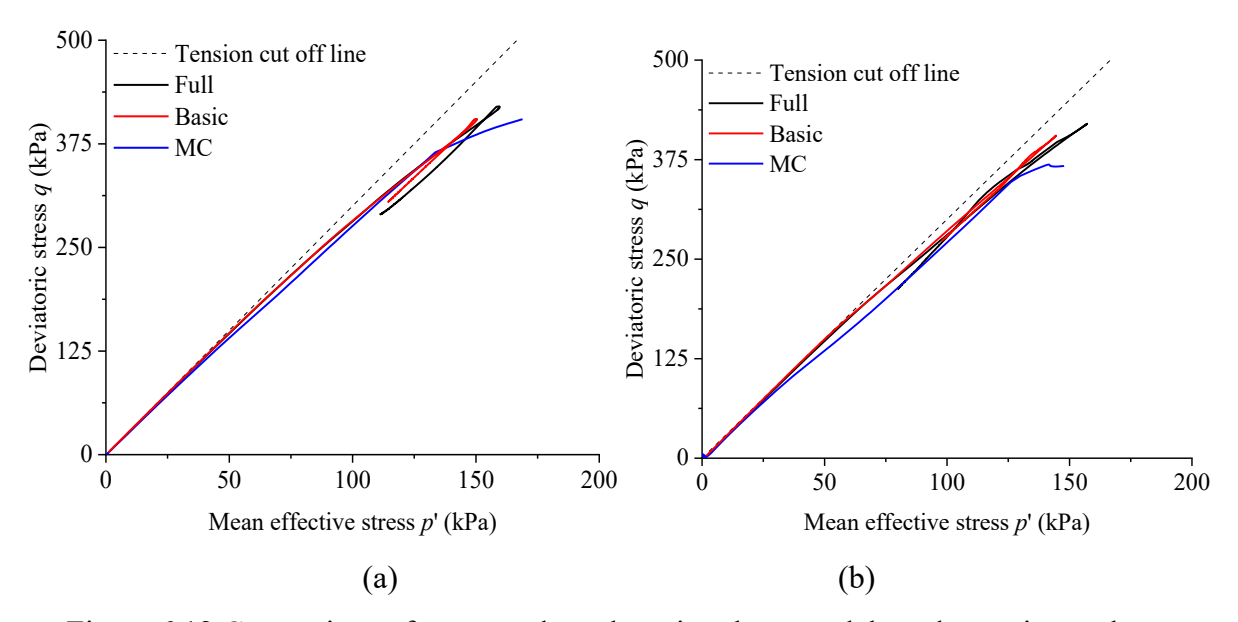


Figure 6.12 Comparison of computed results using three models and experimental test results: (a) Effective stress path at the top of the DCM column at the center (b) effective stress path at the midpoint of the DCM pile at the center

6.5.5 Simulating a field test of DCM-supported embankment

Finally, a comparison was made with the field monitoring case from a reclamation project in Hong Kong. The engineering problem involves the construction of a DCM-supported seawall and embankment. Intensive testing data on the settlement and lateral displacement at points A and B, as shown in Figure 6.13, were collected. Point B is located on the surface of the block seawall, which is constructed on the DCM-treated area. The simulation steps are divided into three phases. Step 1 involves the static equilibrium of the original strata under gravity. Step 2 includes the backfilling of soil layers after the construction of the seawall. Finally, step 3 involves the construction of the embankment slope. The entire construction process is a fully coupled hydromechanical analysis. The boundary conditions are set as follows:

- (1) for the X-direction, normal displacement is constrained at Xmin, and an equivalent lateral force boundary condition is applied at Xmax. The hydraulic condition in the Xmin and Xmax is permeable;
- (2) for the Y-direction, the normal displacement is constrained, and the permeability condition

is set to impermeable;

(3) for the Zmin, displacement in all three directions—x, y, and z are constrained, and the hydraulic condition is impermeable. The analysis type is a fully coupled hydro-mechanical analysis. The soil parameters used in the simulations are summarised in Table 6.13 to Table 6.17.

Figure 6.14 compares the computed and measured settlements from markers A and B. Figure 6.14a shows the process of increasing settlement as the excess pore water pressure dissipates at point A. Figure 6.14b shows the settlement data at different soil layers. The results show that DCM treatment significantly reduced the ground settlement. In the area without DCM treatment, the settlement is still increasing after 240 days, while in the DCM treatment area, the settlement tends to be stable at 90 days. The calculation results of the three models are basically consistent, mainly because the DCM strains in this problem are small and fall within a narrow strain range, so the strain-softening and stiffness nonlinearity do not play an important role.

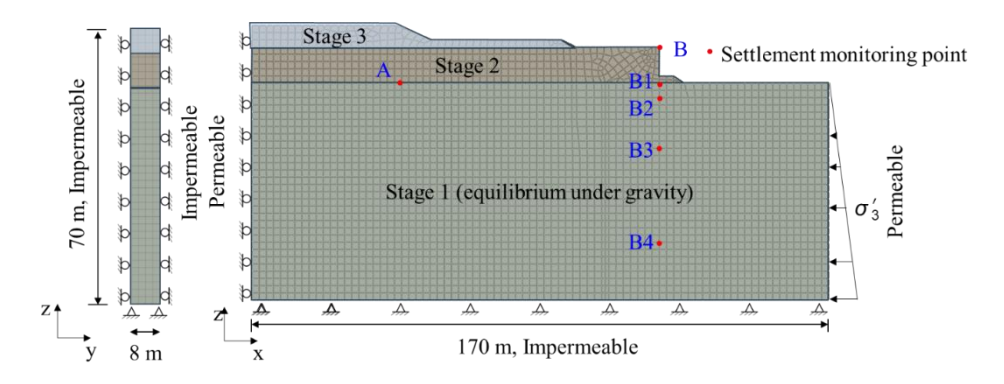


Figure 6.13 Finite element model for seawall profile.

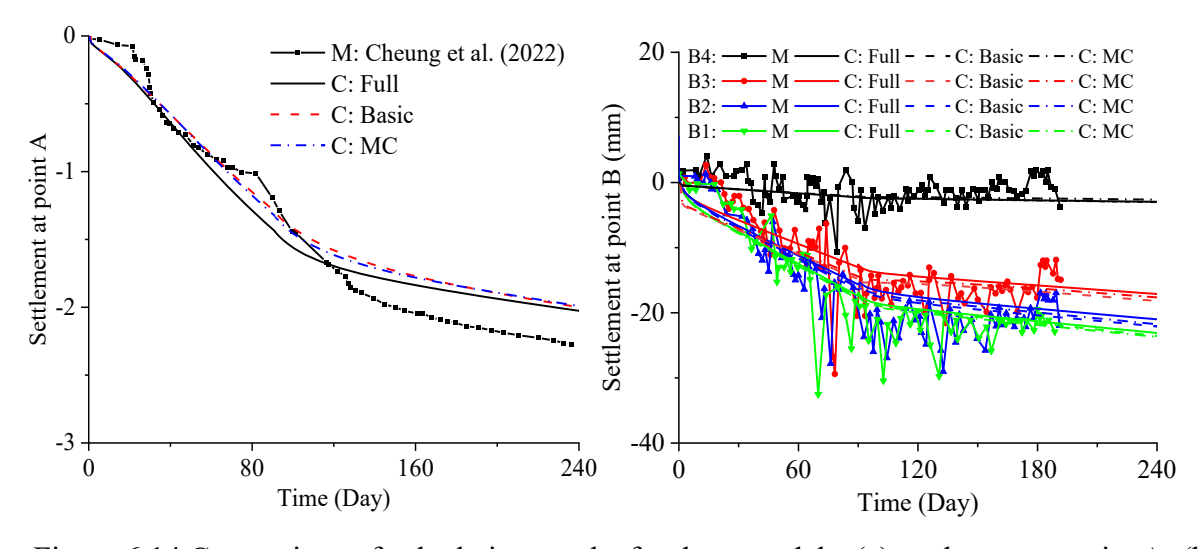


Figure 6.14 Comparison of calculation results for three models: (a) settlement at point A; (b) settlement at point B

Table 6.13 Soil parameters used in the MC model for simulation of field test

Soil Parameters	Backfill	Alluvium	Decomposed	Concrete blockwork
	material		rock	of Seawall
Material model	Mohr-	Mohr-	Mohr-	Mohr-Coulomb
	Coulomb	Coulomb	Coulomb	
Density, ρ (kg/m ³)	1800	1900	2000	2400
Young's modulus, E_0	30	20	300	30000
(MPa)				
Poisson's ratio, ν	0.3	0.3	0.3	0.3
Friction angle, ϕ' (°)	32	30	35	32
Cohesion, c (kPa)	0	20	8	10000
Permeability, k (m/day)	0.01	0.008	0.001	0.5

Table 6.14 Soil parameters used in the Modified Cam-clay model for HKMD for simulation of field test

Soil Parameters	Marine Deposits
Compression index, λ	0.15
Swelling index, κ	0.012
Density, ρ (kg/m ³)	1500
Critical state stress ratio, M	1.0
Poisson's ratio, ν	0.3
Permeability coefficient, $k \text{ (m/d)}$	0.005

Table 6.15 Soil parameters used in the proposed full version model for cemented soil of field test

Soil Parameters	Value for DCM	Soil Parameters	Value for DCM
A (MPa)	200	ϵ_{ref}	0.05
v	0.1	p_b (kPa)	variable
n_c	2	Density (kg/m ³)	1500
M_c	1.2	Permeability (m/d)	0.003
λ	0.02	β	/
n_b	0.5	K_{pb}	/
d_0	2	k_{M}	/
n_d	0.5	k_T	/
h	0.4		

Table 6.16 Soil parameters used in the proposed basic version model for cemented soil of field test

Soil Parameters	Value for DCM
E_{θ} (MPa)	450
ν	0.3
φ (°)	33
h	1.5
$arepsilon_{ref}$	0.03
$arepsilon_{ref}$ $c_{ heta}$ (kPa)	750
σ_t	75

Table 6.17 Soil parameters used in the MC model for cemented soil of field test

Soil Parameters	Value for DCM
E_{θ} (MPa)	350
ν	0.3
arphi (°)	33
c (kPa)	1000
$\Psi(^{\circ})$	0.1
σ_t	100
E_{θ} (MPa)	350

6.6 Summary

In this chapter, the proposed theoretical models were successfully implemented into a finite element programme. The accuracy and effectiveness of both the model and the programme were verified through the simulation of element tests. Subsequently, various boundary value problems, including centrifuge tests, physical model tests, and field monitoring tests, were simulated to demonstrate the advantages of the proposed theoretical model. By comparing the performance of three models in different aspects, the advantages and disadvantages of each model are summarised as follows:

- 1. The full version model encompasses comprehensive soil behaviours, including small strain behaviour, shearing dilatancy, and strain-softening of cemented soil. It performs well in both drained and undrained conditions, as well as in fully coupled hydro-mechanical analysis. However, the model requires a substantial number of parameters, resulting in a complex parameter calibration process.
- 2. The basic version model can effectively simulate small strain behaviour and strain-softening of cemented soil with a reduced number of parameters, thereby facilitating simpler engineering applications. Nevertheless, it inadequately predicts dilatancy behaviour due to the exclusion of state-dependent dilatancy properties, resulting in calculation errors, especially in undrained triaxial shear tests.
- 3. The Mohr-Coulomb model is characterised by theoretical simplicity, ease of understanding, and minimal parameter requirements. However, it fails to adequately simulate small strain characteristics and strain-softening behaviour of cemented soil.

Overall, the proposed full and basic version models are a reliable tool for geotechnical engineering applications, offering significant improvements over existing models.

CHAPTER 7 Parametric study of DCM-stabilised foundation

In this chapter, a comprehensive parametric analysis is conducted to examine the effects of various parameters on the settlement and bearing capacity of DCM-stabilised foundations. To improve design methods, results from advanced numerical models are compared with those from simple design formulations in existing design guidelines. The parameters analyzed include the area replacement ratio, the strength and stiffness of the soft soil, and the column length and model parameters for DCM columns. The comprehensive parametric study identifies key factors influencing settlement and bearing capacity. Finally, a design chart for bearing capacity is proposed.

7.1 Analytical formulations for designing DCM-stabilised foundation

Column diameter, d (m)

The guidelines provided by the Federal Highway Administration (FHWA, 2013) offer detailed design methods and case studies for DCM-stabilised foundations. The examples from FHWA (2013) were utilized in the parametric study conducted in this chapter. The model used for this study is depicted in Figure 7.1, with dimensions summarized in Table 7.1. The primary focus is on comparing the settlement under the applied load and the bearing capacity of foundations.

Parameter Reference case parametric study

Top elevation of DCM, (m) 0 /

Bottom elevation of DCM, (m) 7.6 7.6, 15.2, 22.8, 30.8

Width of embankment crest DCM, B (m) 12.2 /

Area replacement ratio, 0.2 0.2, 0.3, 0.4

Table 7.1 Summary of model dimension data

According to FHWA (2013), the settlement is assessed under equal strain conditions. The settlement of the foundation is determined using a composite modulus, which is related to the area replacement ratio, as illustrated in Equation (7-1).

1.2

$$M_{comp} = \alpha E_{dm} + (1 - \alpha) M_{soil}$$
 (7-1)

$$S_e = H_{dm} \frac{q}{M_{comn}} \tag{7-2}$$

where α = the area replacement ratio; E_{dm} = the Young's modulus of the DCM; and M_{soil} = the constrained modulus of the soil; M_{comp} = the modulus of the composite foundation; S_e = the modulus of the composite foundation; H_{dm} = depth of the stabilized ground; q = the load

applied to the top of the foundation. FHWA (2013) suggested the E_{dm} is 300 times the UCS of DCM.

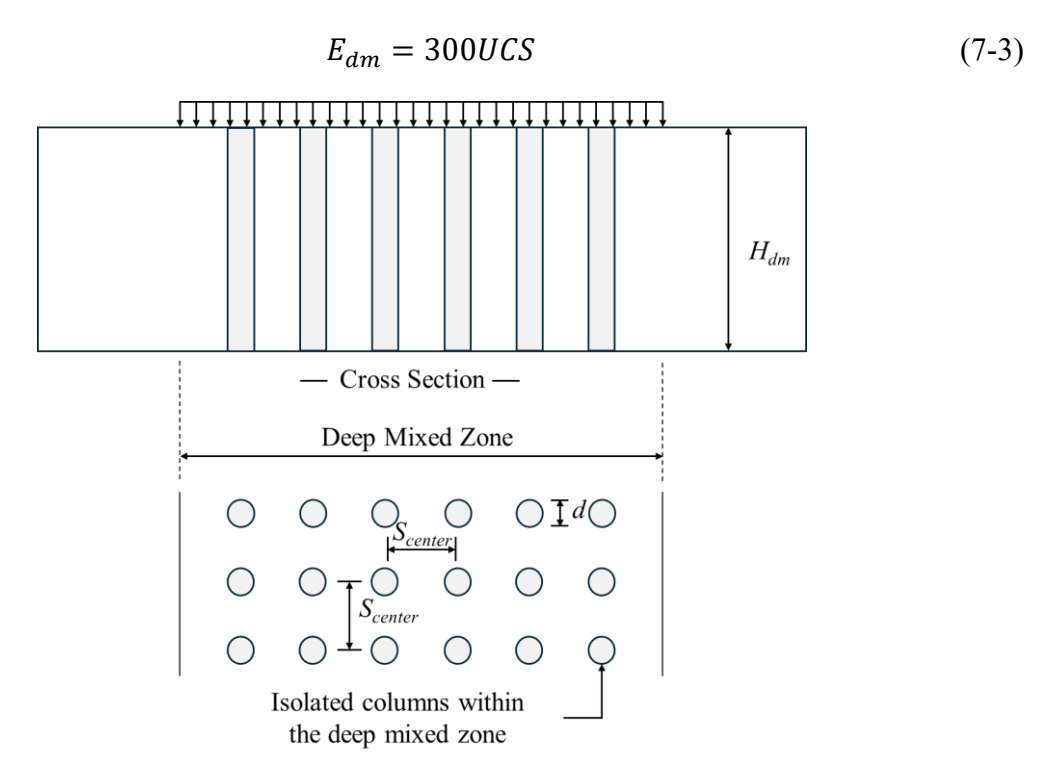


Figure 7.1 Schematic diagrams of the 3D FE model for the parametric study

According to FHWA (2013), DCM columns are typically utilized to support geotechnical structures such as retaining walls, embankments, and abutments. The DCM columns are designed to bear the entire structural load without considering support from the surrounding soils. Consequently, the bearing capacity at the failure of a single pile is equal to:

$$q_{all} = UCS * \alpha \tag{7-4}$$

where q_{all} = the bearing capacity of DCM-stablised foundation. The literature indicates that the area replacement ratio commonly used in DCM engineering ranges from 0.2 to 0.4. The diameter of DCM columns is approximately 0.6 to 1.2 meters, and their length varies from 5 to 25 meters (Jamsawang et al. 2016; Kitazume 2013; Yi et al. 2016). The parameters for DCM columns were referenced from studies on cemented soft soil in Fang (2006), while the parameters for the soft soil were obtained from FHWA (2013). All parameter values, such as diameter, length, and area replacement ratio, are summarized in Table 7.2.

Table 7.2 Mechanical properties of soft soil in parametric study

Soil Parameters	Reference case	parametric study
Density, ρ (kg/m ³)	14	14
Young's modulus, E_{θ} (MPa)	5 MPa	5, 10, 20
Poisson's ratio, ν	0.3	0.3
Friction angle, ϕ' (°)	0	0
Cohesion, c (kPa)	20	20, 30, 50

7.2 Comparisons between the results computed using advanced numerical model and simple design formulations

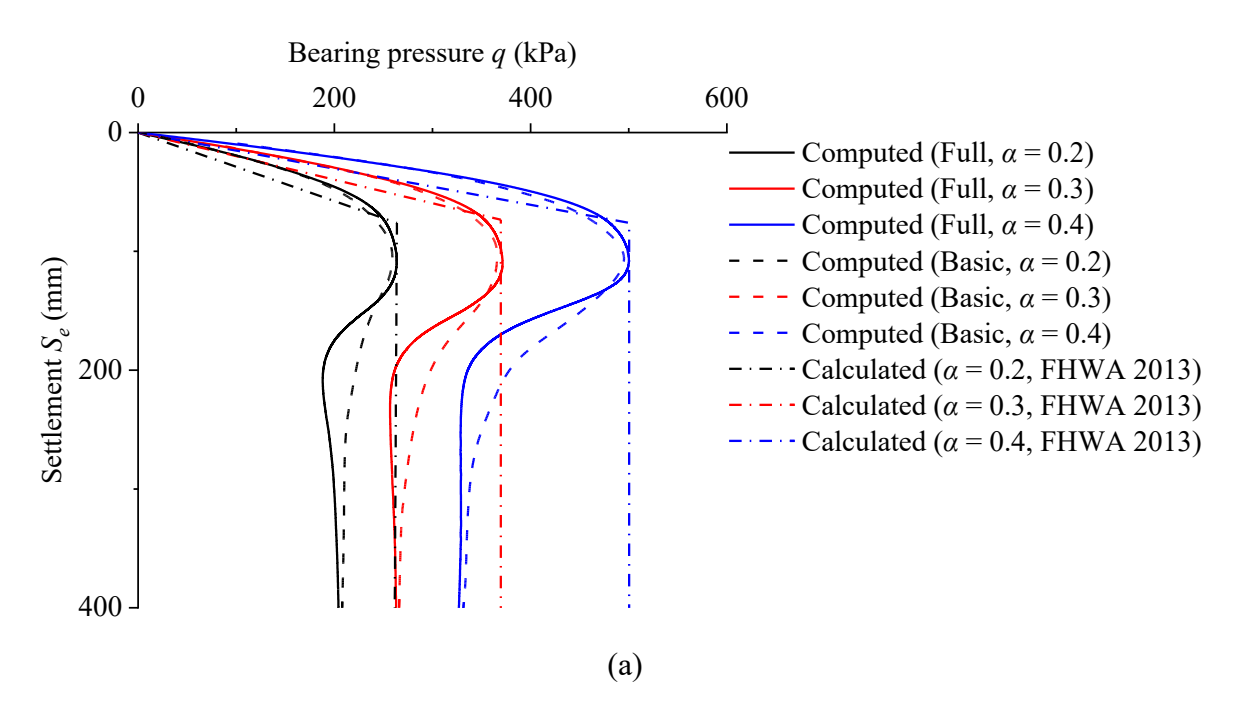
7.2.1 The influence of pile length and replacement ratio

Figure 7.2a presents the load-settlement curves for the DCM-stabilised foundation at different DCM area replacement ratios. Both the full and basic version models predict hardening and softening behaviour. As the replacement ratio increases, the bearing capacity of the foundation significantly improves, as shown in Figure 7.2a. For instance, for the calculation result using the full version model, at an area replacement ratio of 0.2, the bearing capacity is approximately 265 kPa, while at an area replacement ratio of 0.4, it nearly doubles to 500 kPa. The calculation results of the basic version model exhibit the same trend as the full version model, with the bearing capacity nearly doubling as the replacement ratio increases from 0.2 to 0.4. However, the bearing capacity calculated by the basic version model is lower than that obtained by the full version model. There are two main reasons for this discrepancy. Firstly, the basic version ignores the contribution of dilatancy to strength, resulting in a lower strength of the DCM columns. Secondly, the full version model can predict the volumetric expansion of DCM columns induced by dilatancy. This volumetric expansion leads to compressive stress on the surrounding soft soil, thereby enhancing the contribution of the soft soil to the overall strength. This behaviour cannot be simulated in the basic version model.

Figure 7.2a also compares the calculated load-settlement curves derived from Equation (7-2). Equation (7-2) may overestimate settlement at low strain levels while underestimating settlement at larger strain levels. This is because the recommended modulus for DCM in engineering is 300 times the UCS. At low strain levels, the recommended modulus underestimates the actual modulus of DCM. However, as strain increases, the modulus of DCM significantly decreases due to the development of plastic behaviours induced by cementation breakdown and soil particle rearrangement. It suggests that the linear elastic calculation

equation employed in current engineering may result in significant errors in settlement predictions. Additionally, Equation (7-2) cannot predict the reduction in bearing capacity after reaching the peak value.

Figure 7.2b compares the calculated and computed bearing capacities for supporting the superstructure. Current guidelines do not account for the contribution of soft soil in bearing capacity calculations. Consequently, the bearing capacities calculated by the full version and the basic version models are higher than the theoretical values. The full version model demonstrates a bearing capacity approximately 10% higher than the theoretical values, while the basic version model indicates an enhancement of around 5%. The primary reason for the discrepancy is that the basic version model cannot predict the dilatancy of DCM well, as discussed above. This suggests that current engineering designs, which ignore the contribution of soft soil to bearing capacity, may be conservative. Furthermore, as the area replacement ratio increases, the contribution from soft soil decreases, from approximately 10% at $\alpha = 0.2$ to about 5% at $\alpha = 0.4$, likely due to the increased DCM area and reduced soft soil area.



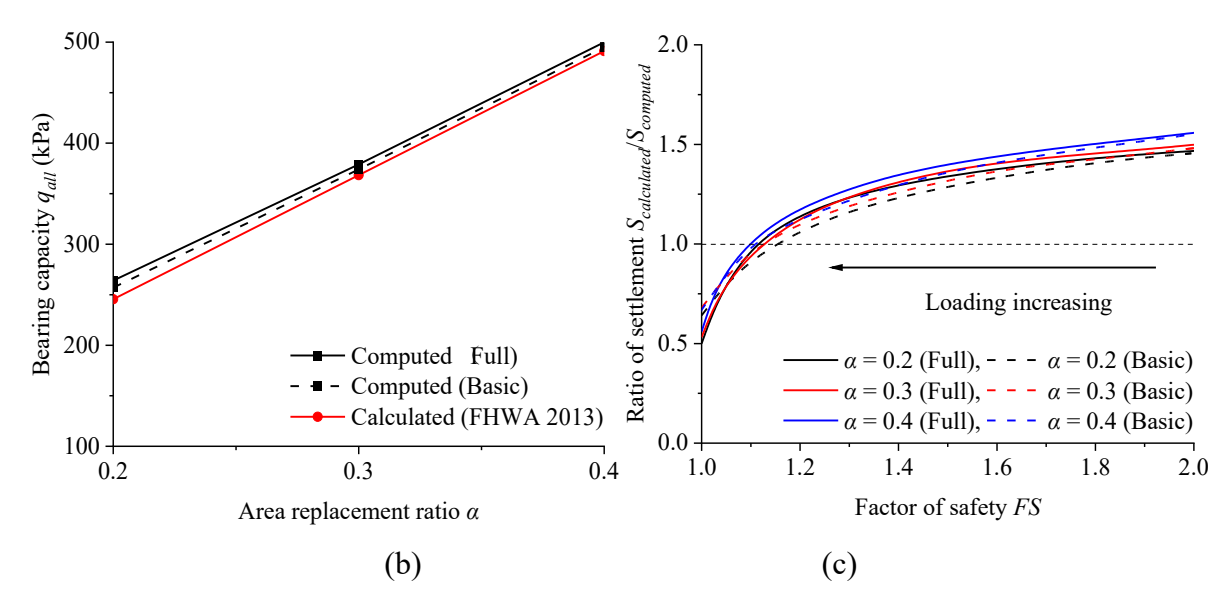


Figure 7.2 Comparison of computed vs. calculated results with varying area replacement ratios: (a) load-settlement curves; (b) bearing capacity of DCM-stabilised foundation; (c)

Ratio of settlement

Figure 7.2c compares the settlement ratio of calculated settlement using Equation (7-2) with the computed settlement obtained from FEM under varying safety factors. Following the definition in (Becker 1997; Meyerhof 1984), the safety factor is defined as the ratio of the bearing capacity to the applied press on the foundation.

$$Fs = \frac{q}{q_{all}} \tag{7-5}$$

It can be observed that the computed results using the full version model and the basic version model exhibit minor differences within the range of safety factors from 1.0 to 2.0, across various area replacement ratios. When the safety factor is 2.0, the ratio of calculated settlement to computed settlement is approximately 1.5, indicating that the theoretical calculations using Equation (7-2) tend to overestimate the actual settlement by more than 50%. Conversely, when the safety factor is 1.0, the calculated settlement significantly underestimates the actual settlement by around 40%. This discrepancy arises due to the design guidelines employing linear equations, whereas the stress-strain behaviour of cemented soil is highly nonlinear, particularly as the applied pressure approaches the bearing capacity. The safety factor recommended by FHWA. (2013) for DCM-stablised foundation ranges from 1.2 to 1.6. According to the results presented in Figure 7.2c, with a safety factor between 1.2 and 1.6, the corresponding calculated settlement is overpredicted by 0-40%, suggesting that the current design methodology may be conservative. Furthermore, the degree of overprediction slightly increases with higher area replacement ratios.

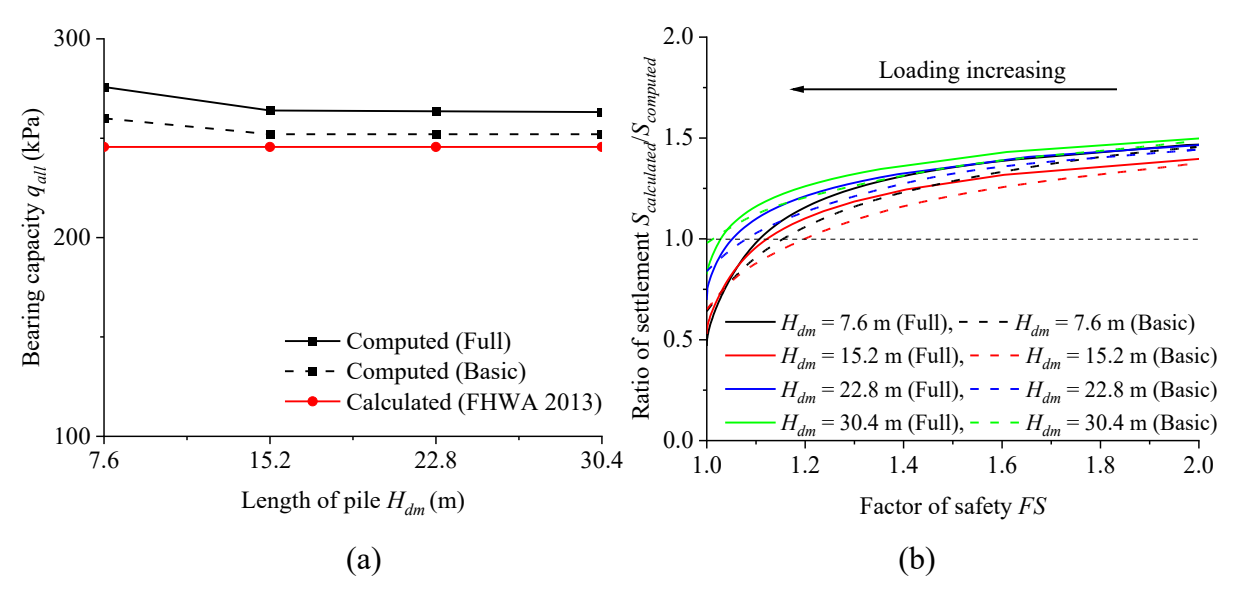


Figure 7.3 Comparison of computed vs. calculated results with varying length of DCM: (a) bearing capacity of DCM-stabilised foundation; (b) ratio of settlement

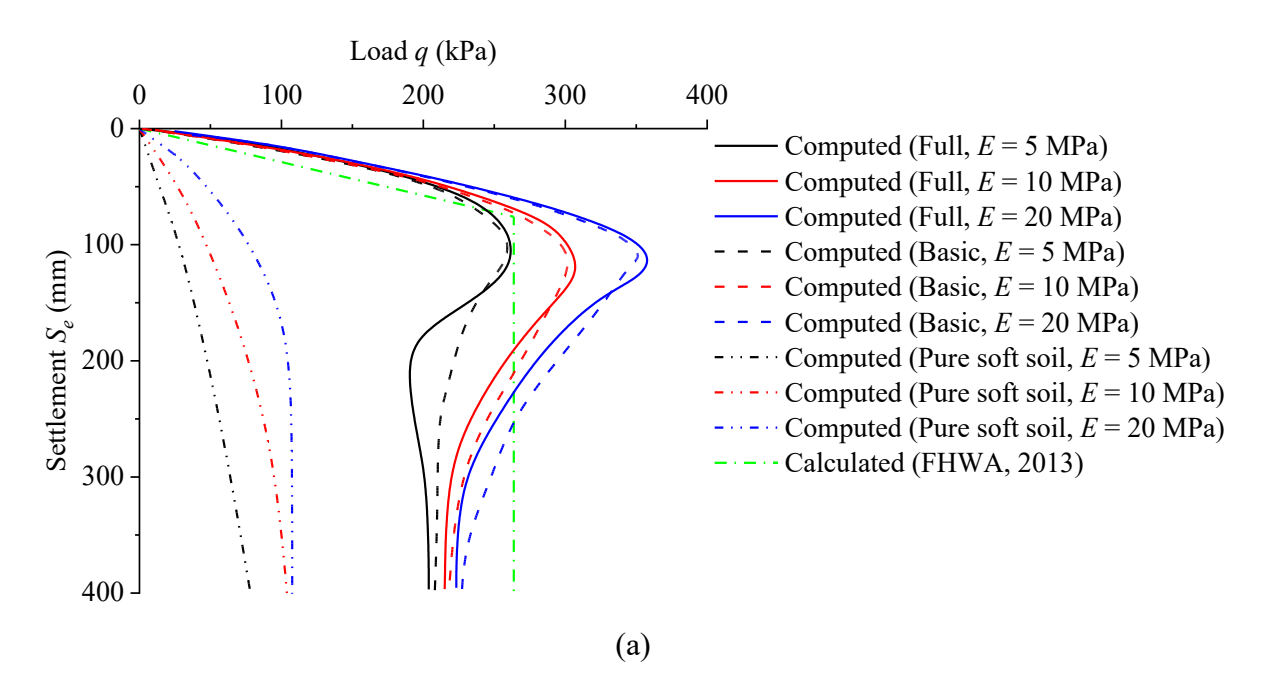
The comparison of computed and calculated results with varying DCM lengths is illustrated in Figure 7.3. The results indicate that the bearing capacity initially decreases with increasing DCM length and keeps unchanged once the length exceeds 15.2 meters. This trend is likely due to the boundary conditions in the numerical analysis, where the bottom of the FEM model is constrained in all directions (xyz), potentially limiting the mobilization of side friction for this end-bearing condition. This phenomenon contrasts with conventional floating pile foundations, which typically exhibit increased bearing capacity with longer pile lengths due to enhanced side friction. Regarding the variation of the settlement ratio with the safety factor, pile length has a minor influence. At higher safety factors (2.0), calculated settlement tends to be overestimated, whereas at lower safety factors (1.0), it may be underestimated. As pile length increases, the overestimation of settlement becomes more pronounced. This suggests that the assumption of equal strain, as stated in equation (7-2), along the DCM columns may not be suitable.

7.2.2 Influence of soft soil Parameters

In current designs, the contribution of soft soil to the bearing capacity of the DCM-supported upper structure is ignored. Figure 7.4 compares the influence of soft soil stiffness on bearing capacity, illustrating the load-settlement curves for the improved soil layer at different soft soil stiffnesses. It can be observed that an increase in soil stiffness significantly enhances the bearing capacity. For instance, in the computed results of the full version model, when the soil stiffness is 5 MPa, the bearing capacity is 265 kPa. When the soil stiffness is increased to

20 MPa, the bearing capacity rises to 360 kPa. There are two main reasons for this phenomenon. First, as the cemented strength of the soft soil increases, a higher modulus leads to quicker mobilization of soil strength. For DCM-stablised soft soil foundations, the bearing capacity is the sum of the contributions from both the DCM columns and the soft soil. Figure 7.4a presents the load–settlement curve for a pure soft soil foundation, which clearly confirms this point by showing that a higher modulus results in greater mobilization of the strength of inner-column soil as strain increases. In addition, another important factor is that an increase in the modulus of the soft soil leads to higher confining pressure around the columns, which further enhances the bearing capacity of the composite foundation. Therefore, both the quicker mobilization of soft soil strength and the increase in confining pressure contribute to the overall improvement in the bearing capacity of the composite foundation.

Figure 7.4c compares the impact of soft soil modulus on settlement calculations and the resulting settlement ratio. Overall, it can be observed that variations in soft soil stiffness have a minimal effect on the settlement ratio in both the full and basic version models. As the modulus of soft soil increases from 5 MPa to 20 MPa, the calculated settlement ratio is almost unaffected. The primary reason is that Equation (7-1) considers the contribution of soft soil stiffness to the composite modulus well because the ratio of calculated and computed settlement is almost consistent.



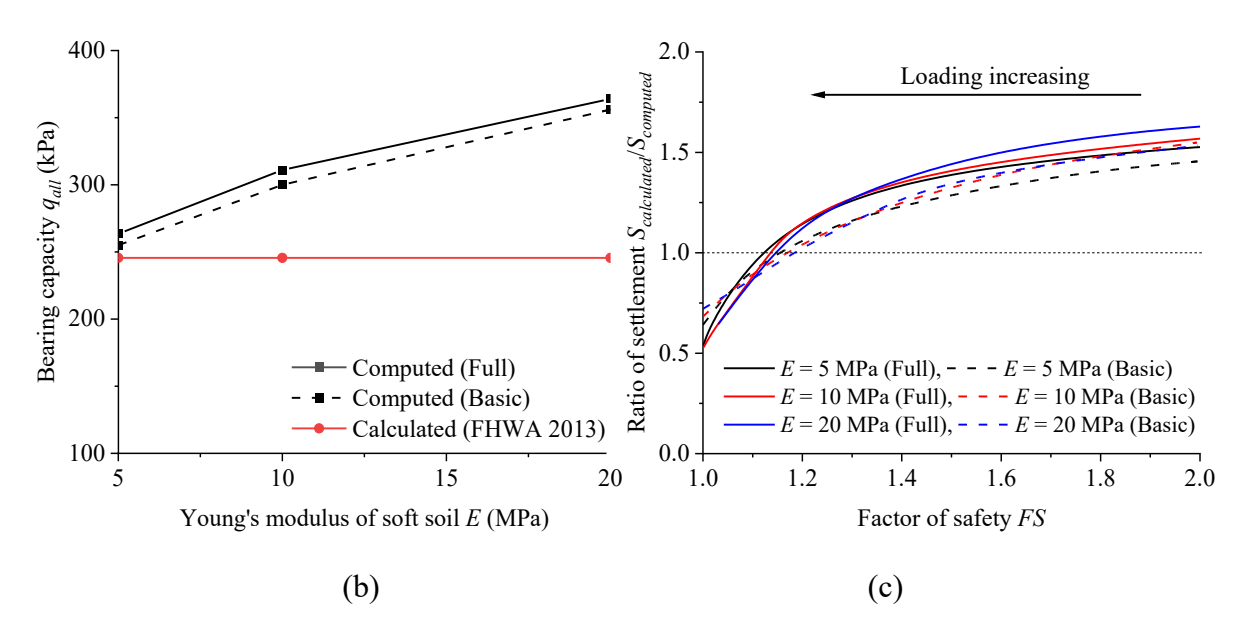


Figure 7.4 Comparison of computed vs. calculated results with soft soil stiffness: (a) load-settlement curves; (b) bearing capacity of DCM-stabilised foundation; (c) ratio of settlement

Figure 7.5a illustrates the influence of soft soil cohesion on the bearing capacity of the foundation. The computed bearing capacity gradually increases with the increase in cohesion, reflecting the contribution of the soft soil cohesion to the bearing capacity. Figure 7.5b shows the impact of changes in cohesion on the settlement ratio. The changes in cohesion have an insignificant impact, primarily because the settlement of the foundation is related to the stiffness parameters. The change in cohesion has a minimal effect on both the calculated and computed settlement.

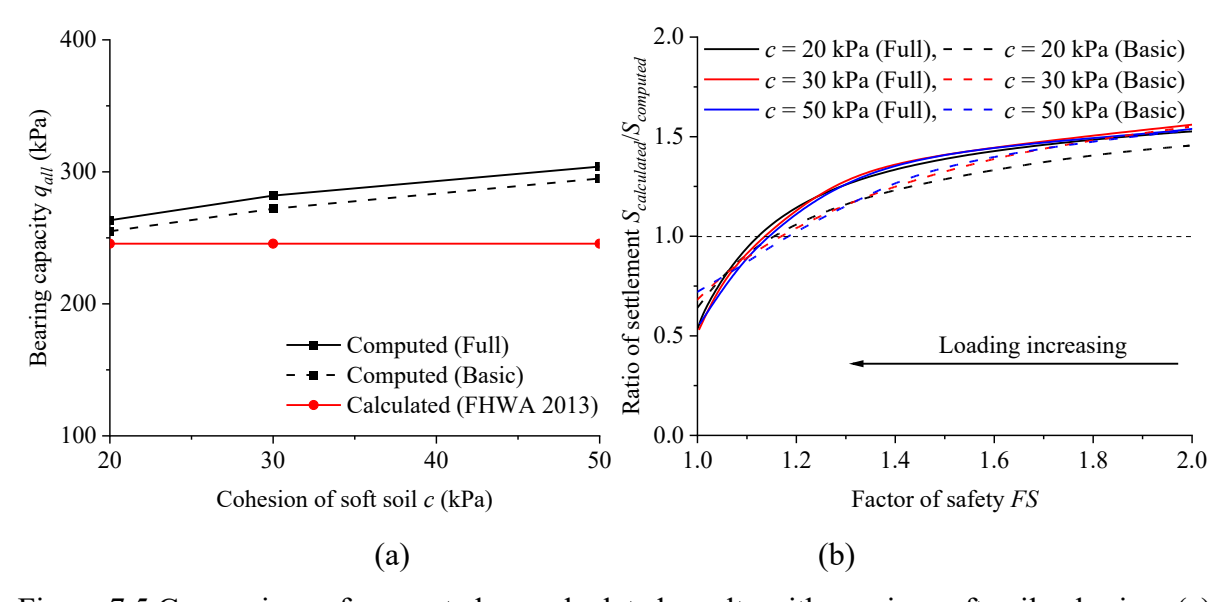


Figure 7.5 Comparison of computed vs. calculated results with varying soft soil cohesion: (a) bearing capacity of DCM-stabilised foundation; (b) ratio of settlement

The computed results for various area replacement ratios, pile lengths, and soft soil

parameters indicate that the differences between the full and basic versions models are insignificant and show a consistent trend. This difference is primarily due to the simplification of the dilatancy and modulus equations. Therefore, only the parameters in the full version model were examined in the sensitivity analysis.

7.3 Sensitivity analysis based on the advanced numerical model

7.3.1 Influence of model parameters for elasticity

In the full version model, three parameters are used to determine the elastic modulus: A, v, and n_c . The Poisson's ratio, v, for cemented soil, is approximately 0.3 and is not discussed further in this chapter. A represents the soil parameter for the elastic modulus of uncemented clay, while n_c indicates the sensitivity of the shear modulus (G_0) to cementation. A larger n_c value results in a more sensitive G_0 to changes in p_b .

The range of A values is quite broad, primarily influenced by soil type. Figure 7.6(a) illustrates the impact of different A values on bearing capacity. As A increases from 200 to 400, a slight decrease in bearing capacity is observed. This occurs because the foundation bearing capacity is the combined contribution from DCM columns and the soft soil. A higher A value indicates a higher stiffness for the DCM, allowing the peak strength of DCM to be fully mobilised at a smaller strain. However, at lower strains, the mobilised strength of the soft soil is reduced. Consequently, the overall bearing capacity is slightly decreased. Figure 7.6b compares the impact of different A values on the calculated and computed settlement ratio. It is found that while bearing capacity is almost unaffected by A, the calculated settlement ratio is significantly influenced. Since there is a linear relationship between G_0 and A, the computed settlement decreases linearly with increasing A. For the method in FHWA (2013), the Young's modulus is linearly to UCS (fully coupled). Changes in A do not cause significant variations in the Young's modulus and the calculated settlement. This explains why a larger A value results in a larger ratio of calculated and computed settlement.

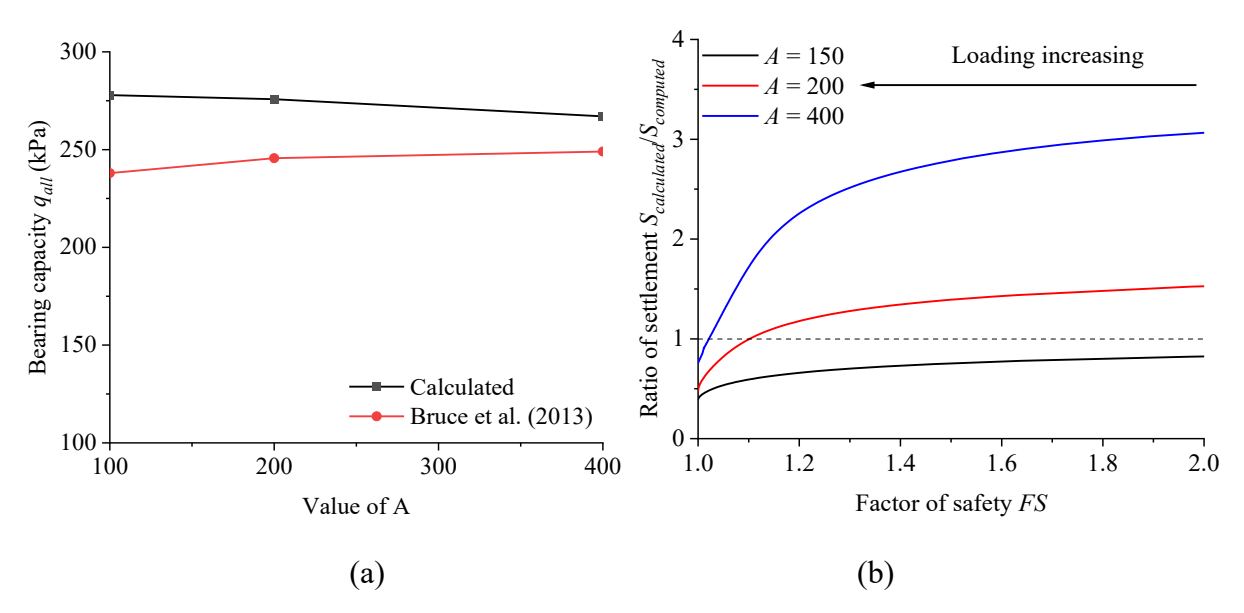


Figure 7.6 Comparison of computed vs. calculated results with varying A: (a) bearing capacity of DCM-stabilised foundation; (b) ratio of settlement

Figure 7.7 compares the effects of different n_c values on bearing capacity and settlement ratio. The typical range for n_c is 0-2. The mechanism by which n_c affects the results is similar to that of A, as both parameters influence the elastic modulus. Consequently, bearing capacity and the ratio of calculated to computed settlement show the same trend with the change of A and n_c . The minor differences may be attributed to n_c controlling the dependence of the elastic modulus on cementation.

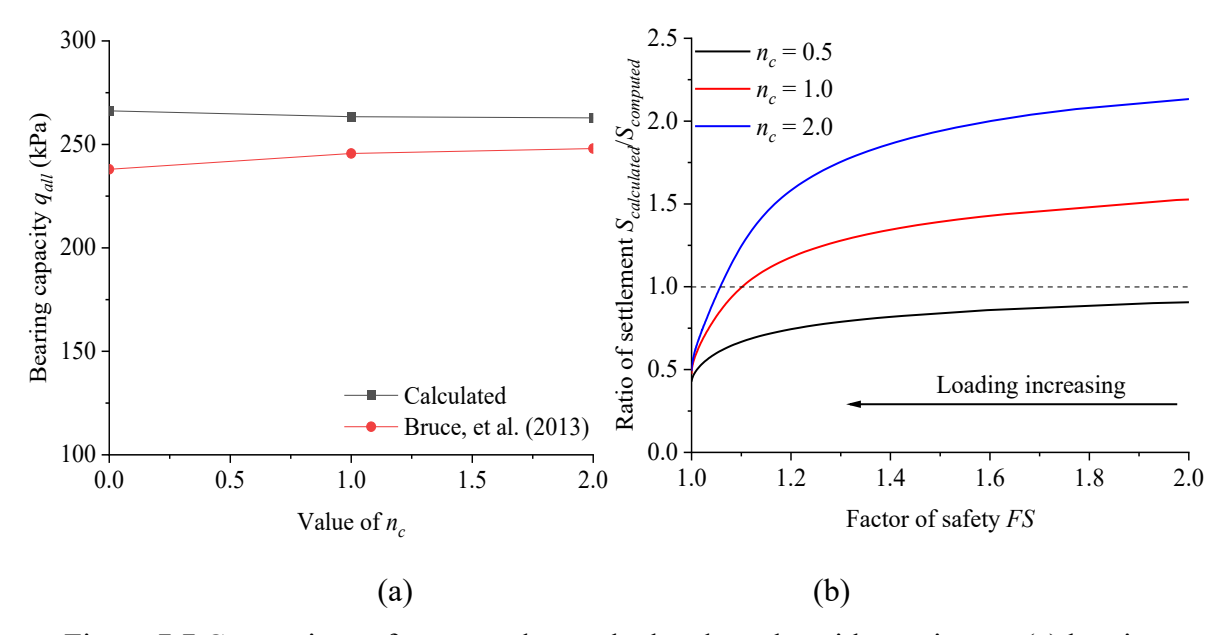


Figure 7.7 Comparison of computed vs. calculated results with varying n_c : (a) bearing capacity of DCM-stabilised foundation; (b) ratio of settlement

7.3.2 Influence of model parameters for critical state

The critical state parameters analysed include M, λ , and T. In the full version model, M represents the critical state stress ratio, while λ and Γ represent the slope and intercept of the critical state line in the e-lnp' space, respectively. According to reported experimental data, the values for M typically range from 1.1 to 1.5, λ ranges from 0.01 to 0.04, and Γ varies between 2.1 and 2.5.

Figure 7.8a shows the variation in bearing capacity with different M values. It can be observed that both the calculated and computed bearing capacities exhibit a substantial increase with increasing M, showing a nearly linear relationship. The computed results are consistently larger than the calculated values by approximately 10%, attributable to the contribution of the surrounding soft soil. Figure 7.9b illustrates the significant effects of different M values on the settlement ratio curve. The value of M significantly affects the settlement curve. In the full version model, an increase in M primarily leads to a significant increase in strength, with minimal impact on the modulus. In the current design method, the stiffness is fully coupled with the UCS using a linear equation. An increase in strength results in a significant increase in modulus, reducing the calculated settlement. This explains why a larger M value results in a smaller settlement ratio.

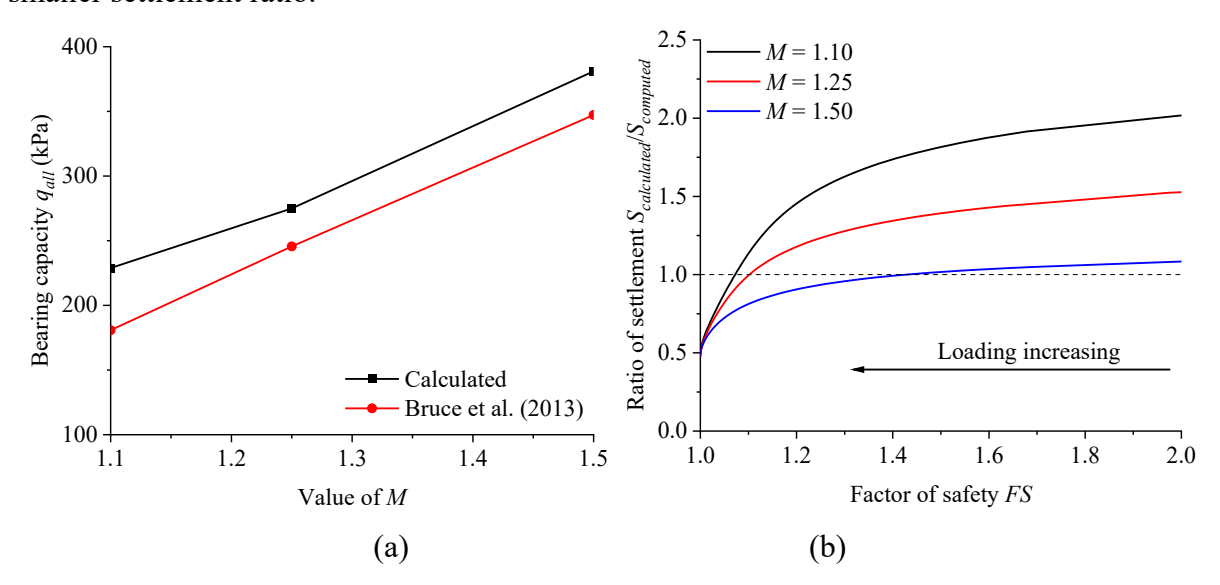


Figure 7.8 Comparison of computed vs. calculated results with varying M: (a) bearing capacity of DCM-stabilised foundation; (b) ratio of settlement

Figure 7.9a examines the effects of different λ values on the bearing capacity and settlement ratio curves. In contrast to M, an increase in λ results in a decrease in the bearing capacity of the foundation. This is because a larger λ value implies a smaller dilatancy trend at a given constant Γ value. As a result, the volumetric expansion of the DCM column decreases, leading

to a reduction in the confining pressure exerted by the surrounding soft soil on the DCM column. Compared to M, the change in bearing capacity due to variations in λ is relatively small. An increase in λ from 0.01 to 0.03 results in approximately a 10% reduction in bearing capacity. Figure 7.9b shows the effects of λ on the settlement ratio with changing safety factor. The insignificant effects are likely due to λ having a relatively minor effect on the strength and modulus of cemented soil.

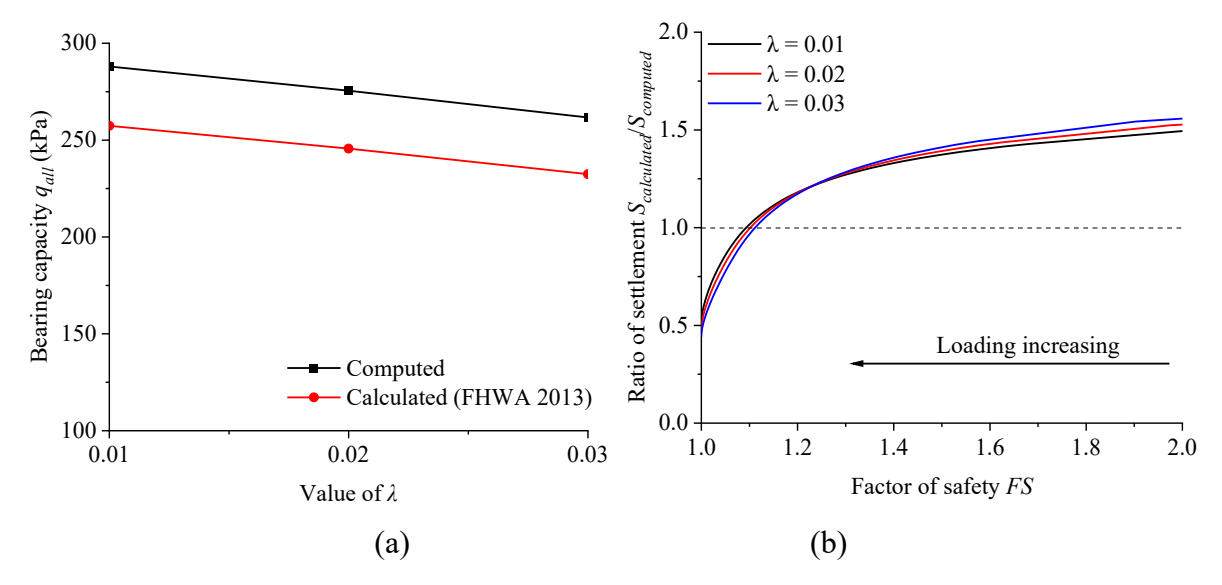


Figure 7.9 Comparison of computed vs. calculated results with varying λ : (a) bearing capacity of DCM-stabilised foundation; (b) ratio of settlement

Figure 7.10 explores the influence of varying Γ values on bearing capacity and settlement ratio. An increase in Γ is accompanied by an increase in bearing capacity. This is because a larger Γ value indicates a greater dilatancy trend, which corresponds to higher peak strengths of the DCM columns and results in greater volumetric expansion of the column material. Consequently, the DCM columns experience increased confinement from the surrounding soil. Figure 7.10b shows the effects of varying Γ values on the settlement ratio. When the safety factor is 2.0, a larger Γ results in a settlement ratio closer to 1.0. This is because, in the calculation method, as Γ increases, the E_0 of the DCM also increases, where E_0 is equal to 300 times the UCS. However, in the FEM model, an increase in Γ does not significantly affect the modulus of the DCM. Therefore, it significantly reduces the overestimated settlement using equation (7-2) in the calculation method. When the safety factor equals 1.0, the calculated settlement ratio for a larger Γ is closer to 1.0. Since a larger Γ enhances dilatancy and volumetric behaviour, it increases the constrained effect on the surrounding soft soil, thereby increasing the composite modulus of the foundation. The enhanced modulus significantly reduces the computed settlement. Consequently, the computed settlement in the FEM model decreases, and

the ratio between calculated and simulated values approaches 1.0.

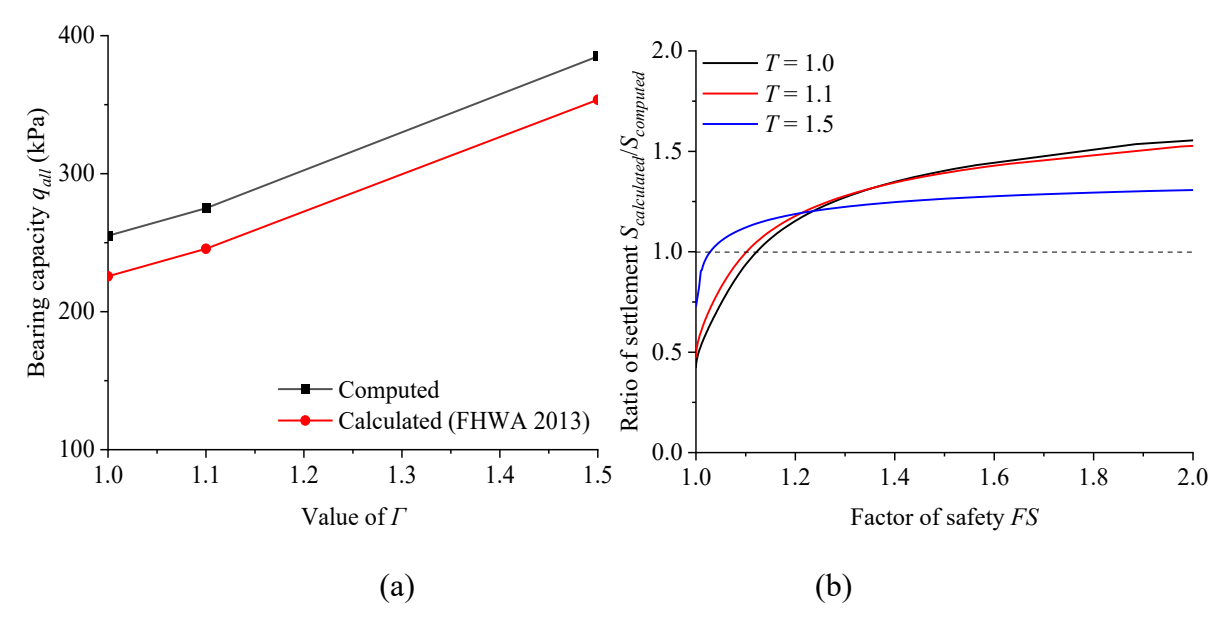


Figure 7.10 Comparison of computed vs. calculated results with varying Γ : (a) bearing capacity of DCM-stabilised foundation; (b) ratio of settlement

7.3.3 Influence of model parameters for flow rule and hardening law

The parameters controlling the hardening law are h and n_b . The parameter h primarily governs the evolution of the hardening parameter (back stress ratio). A larger h results in a higher plastic modulus and less plastic strain. Consequently, the back stress ratio mobilizes with strain more quickly. As shown in Figure 7.11a, the theoretically calculated bearing capacity increases as h increases from 1.0 to 3.0 because a larger h results in smaller plastic deformations. This means that the degradation of cementation is reduced before reaching the peak strength of DCM, thereby increasing the peak strength of DCM. However, when h increases from 3 to 5, the calculated bearing capacity does not further increase. This is because the reduction in cementation due to plasticity becomes negligible when h increases from 3 to 5. However, the computed bearing capacity is not affected by h. This is because increasing hstrengthens the DCM but simultaneously reduces the mobilized strength of the soft soil. The settlement curve in Figure 7.11b demonstrates that as h increases, the ratio of calculated to computed settlement also increases. This phenomenon occurs because a larger h value enhances the elastic modulus of DCM in the simulation, resulting in reduced settlements. Consequently, the substantial decrease in computed settlement leads to an increased ratio between the calculated and computed settlements.

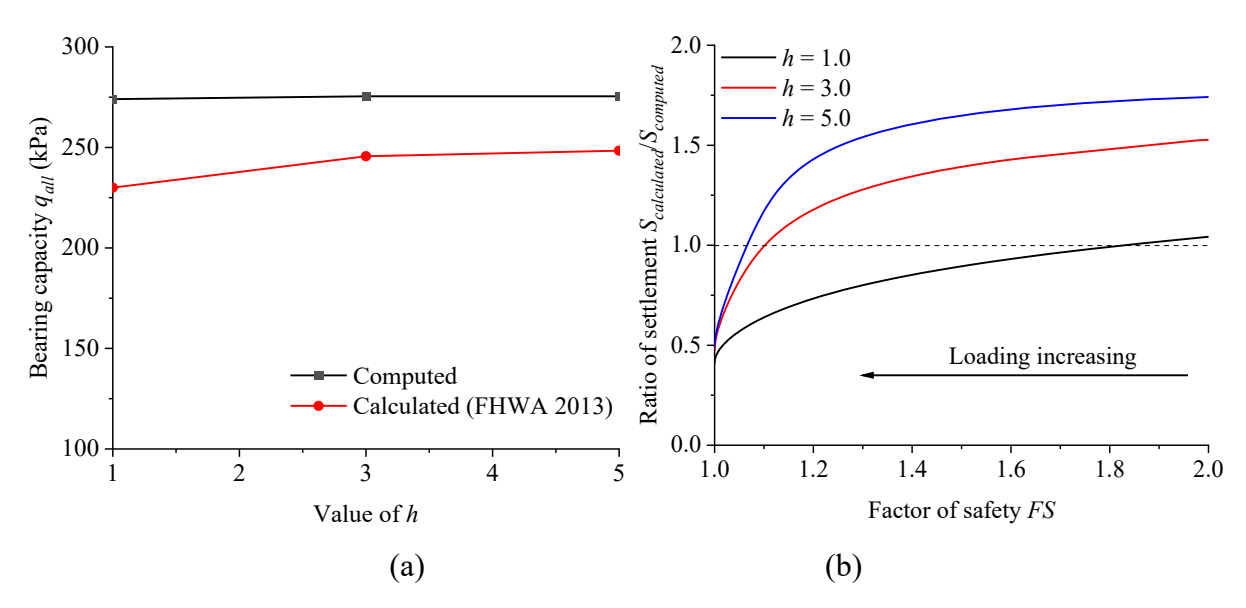


Figure 7.11 Comparison of computed vs. calculated results with varying *h*: (a) bearing capacity of DCM-stabilised foundation; (b) ratio of settlement

Figure 7.12 compares the impact of n_b on the bearing capacity and settlement. The parameter n_b primarily affects the peak strength of DCM, accounting for its dilatancy behaviour. A larger n_b results in a higher potential peak strength induced by shear dilatancy. Consequently, both the calculated and computed bearing capacities increase significantly with increasing DCM strength. However, the increase in n_b leads to a decrease in the settlement ratio. This is because the increase in n_b mainly affects the strength of DCM and does not influence the computed settlement. In the theoretical calculation method, the increase in DCM strength is accompanied by a linear increase in Young's modulus, resulting in a significant reduction in the calculated settlement. However, the computed settlement is not significantly affected by n_b .

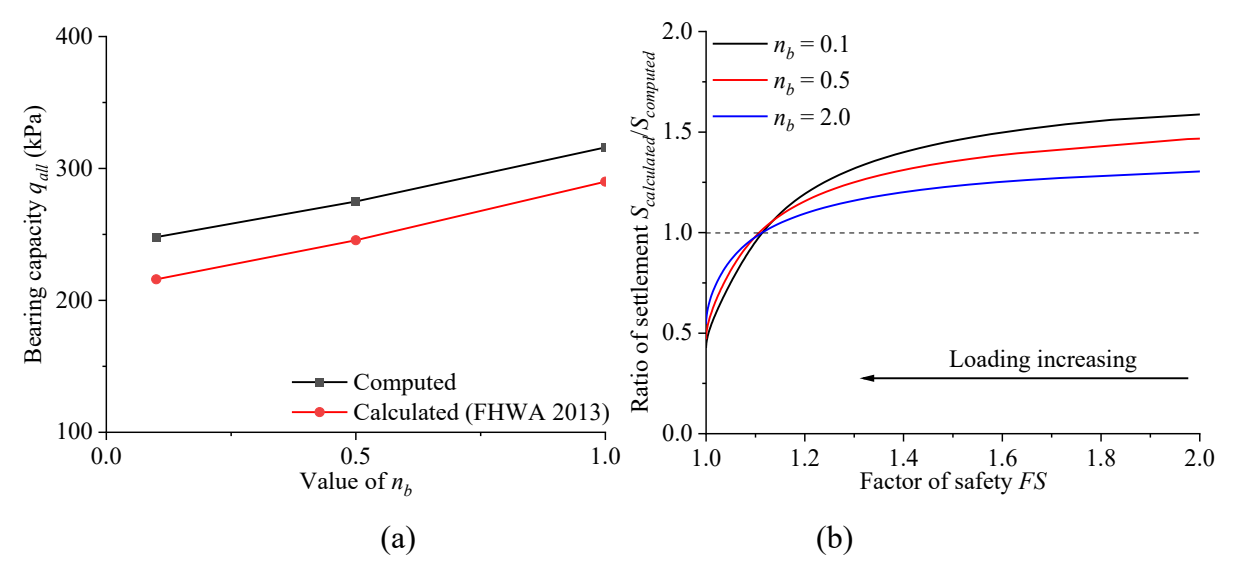


Figure 7.12 Comparison of computed vs. calculated results with varying n_b : (a) bearing capacity of DCM-stabilised foundation; (b) ratio of settlement

Figure 7.13 compares the impact of d_0 on the bearing capacity and settlement. The calculated bearing capacity decreases by approximately 4% with an increase in d_0 from 0.0 to 2.0, whereas the theoretical calculation shows only a 1% decrease in Figure 7.13a. The discrepancy arises from the reduction of the contribution from soft soil. An increase in d_0 indicates that plastic deformation develops more rapidly during shearing. This leads to the peak and critical states being reached at smaller strains, thus resulting in a small mobilised strength of the soft soil. Regarding the effects of d_0 on the settlement ratio, a larger d_0 results in a more significant degradation of cementation with increasing shear strain, leading to reduced cementation strength and stiffness (G), and larger computed settlement. Thus, the calculated and computed settlement ratio is slightly decreased in Figure 7.13b.

The mechanism by which n_d affects bearing capacity and settlement is similar to that of d_0 as both influence the dilation and degradation of cementation. Figure 7.14a shows that the impact of n_d on bearing capacity is smaller than that of d_0 . Regarding the settlement ratio curves, it is shown that as the parameter n_d increases, the settlement ratio also increases. A larger n_d results in more rapid volumetric strain, which can apply higher confining pressure on the surrounding soil. Consequently, the stiffness of the DCM-stabilised foundation increases. As the calculated settlement remains unchanged, the ratio between the calculated and computed settlements decreases.

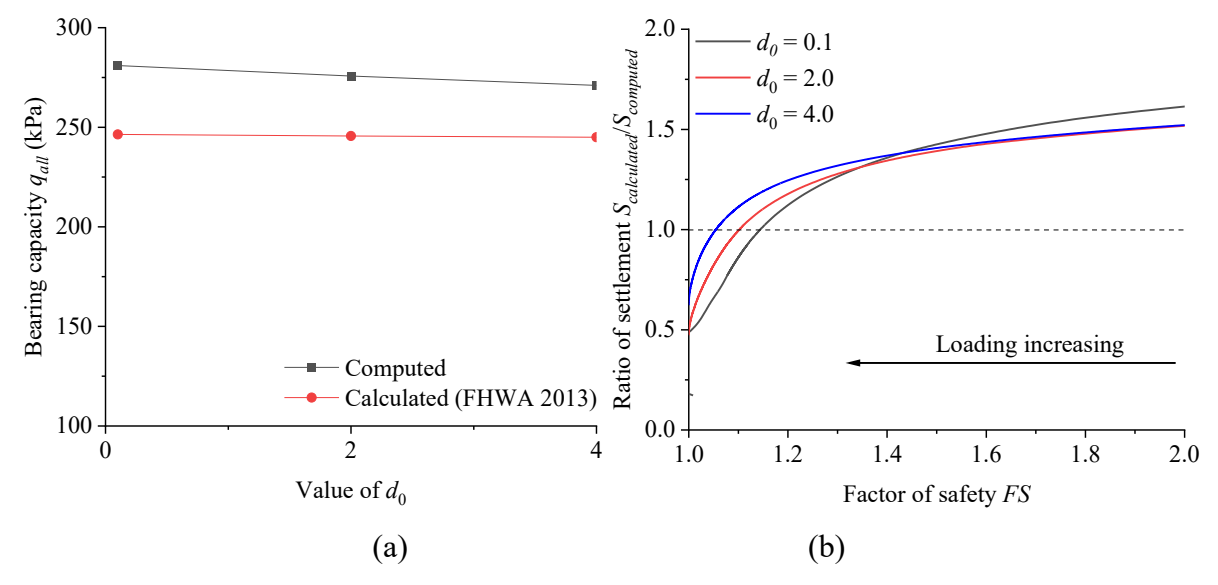


Figure 7.13 Comparison of computed vs. calculated results with varying d_0 : (a) bearing capacity of DCM-stabilised foundation; (b) ratio of settlement

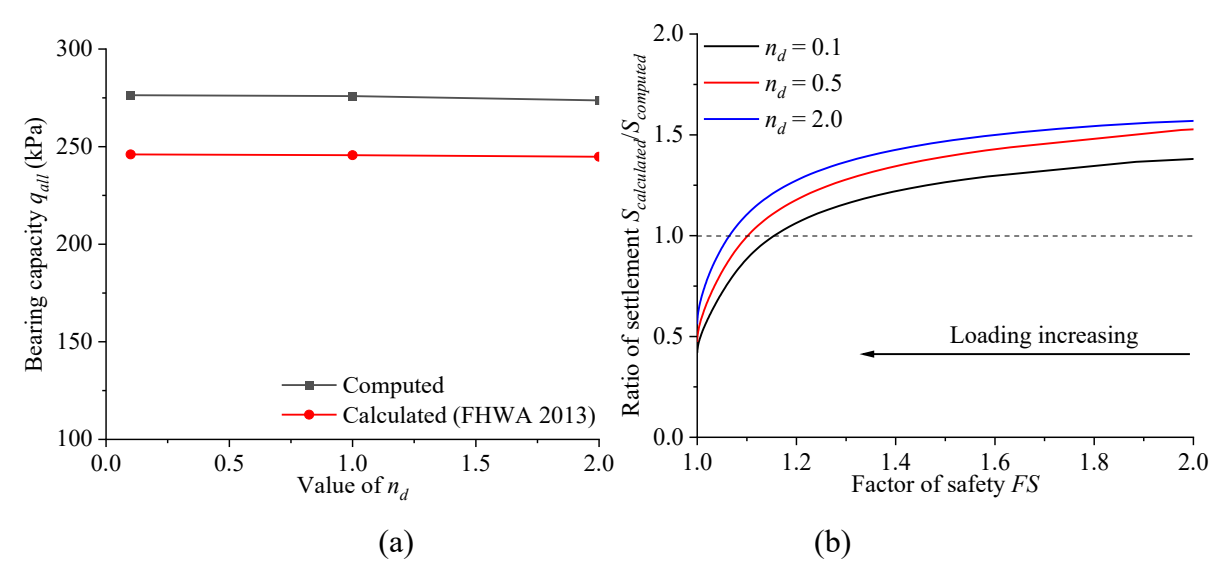


Figure 7.14 Comparison of computed vs. calculated results with varying *n_d*: (a) bearing capacity of DCM-stabilised foundation; (b) ratio of settlement

7.3.4 Influence of model parameters for cementation

In the full version model, three parameters are employed to characterise the cementation properties: k, ε_{ref} , p_b . Figure 7.15a shows the impact of p_b on bearing capacity. Numerically, p_b denotes the cementation strength. It is observed that an increase in p_b significantly enhances the bearing capacity of the foundation as expected, while concurrently reducing the discrepancy between the calculated and computed bearing capacity. This can be attributed to the substantial increase in the modulus of the DCM columns, which has higher cementation strength. Consequently, the mobilisation of DCM peak strength occurs at smaller strains. Conversely, the mobilised of soft soil strength at smaller strains is greatly reduced.

Figure 7.15b illustrates the influence of varying p_b on the settlement ratio. As p_b increases, the ratio of calculated and computed settlement decreases. It is primarily due to the different relationships between modulus and cementation strength in the design guideline and the proposed model. FHWA (2013) assumes that the modulus is 300 times the UCS and neglects cementation degradation on the modulus. In the full version model, the relationship between modulus and UCS may not be linear. As p_b increases, the difference between the modulus used in the theoretical method and the numerical model may decrease.

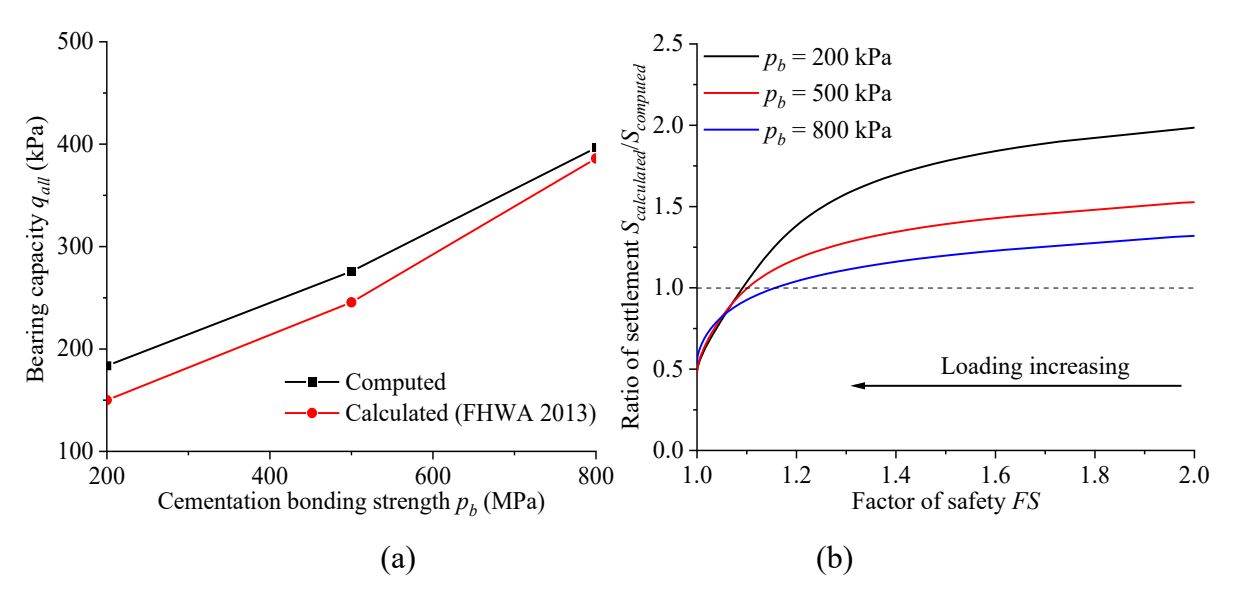


Figure 7.15 Comparison of computed vs. calculated results with varying p_b : (a) bearing capacity of DCM-stabilised foundation; (b) ratio of settlement

The parameter ε_{ref} governs the rate of cementation degradation with strain. A smaller ε_{ref} value indicates more pronounced cementation degradation with plastic deformation. Figure 7.16a illustrates the effects of ε_{ref} on bearing capacity. It is observed that when ε_{ref} increases from 0.01 to 0.04, both calculated and computed bearing capacity increase. However, when ε_{ref} increases from 0.04 to 0.10, the calculated bearing capacity remained unchanged, which is derived from the UCS value of DCM. This is because, as ε_{ref} icreasing, the degraded cementation at the peak stress point decreases, resulting in higher peak strength. However, with further increases in ε_{ref} , the degraded cementation becomes almost zero, leading to a plateau in the strength of the DCM. Conversely, the computed bearing capacity continues to rise. This is because, in addition to the increase in DCM strength, the corresponding strain required to reach the bearing capacity also increased, which further mobilized the strength of the soft soil. In summary, the theoretical calculation overlooks the contribution of soft soil to the bearing capacity of the DCM-stablised foundation. Figure 7.16b illustrates the effects of ε_{ref} on the settlement ratio curve. A larger ε_{ref} results in a smaller ratio of calculated to computed settlement. This is because a larger ε_{ref} leads to a higher UCS, and the modulus in the calculation method increases, thereby mitigating the overestimation of calculated settlement.

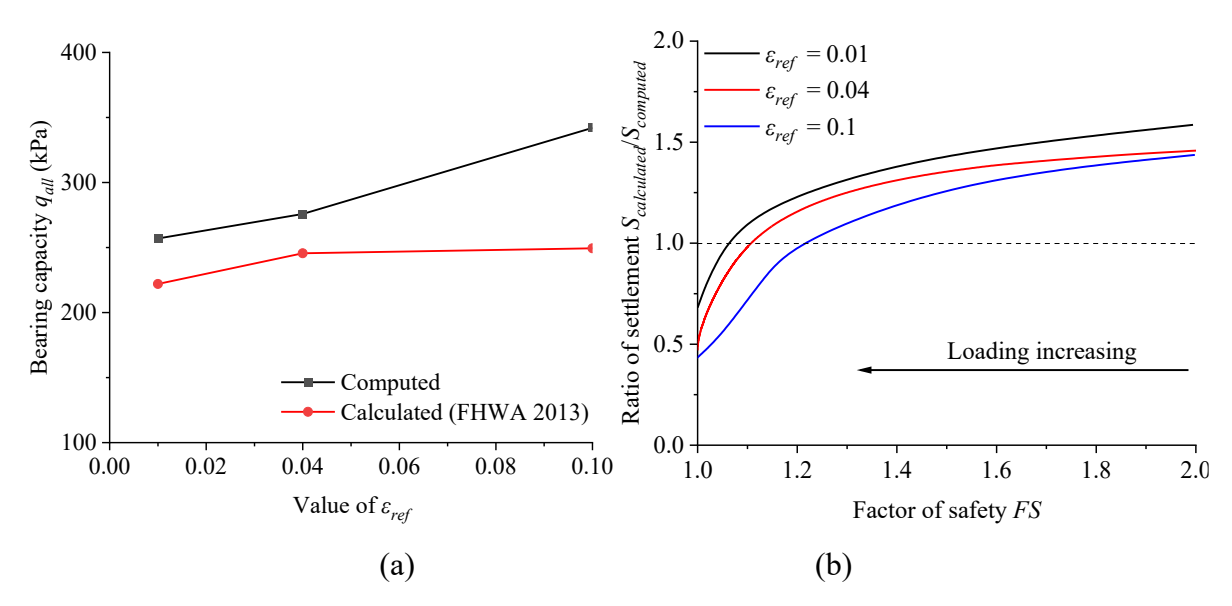


Figure 7.16 Comparison of computed vs. calculated results with varying ε_{ref} : (a) bearing capacity of DCM-stabilised foundation; (b) ratio of settlement

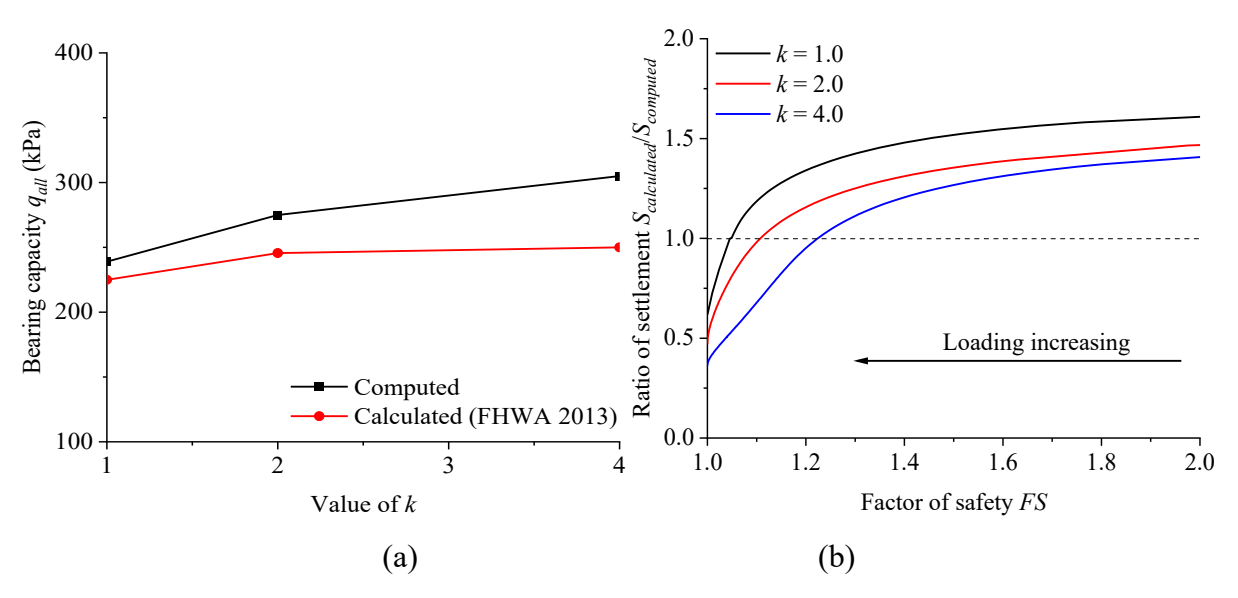


Figure 7.17 Comparison of computed vs. calculated results with varying k: (a) bearing capacity of DCM-stabilised foundation; (b) ratio of settlement

Figure 7.17a shows the influence of k on bearing capacity and settlement ratio. Both k and ε_{ref} affect the degradation of cementation with strain. If the value of k is small, cementation degrades more significantly before ε_{ref} and more slowly after ε_{ref} . With a smaller k value, significant cementation degradation occurs before reaching the peak strength of DCM, resulting in a significant reduction in total bearing capacity. Figure 7.17a shows that bearing capacity increases with an increase in k, since less cementation degrades before the peak strength. The influence of k on the settlement curve is similar to that of ε_{ref} . As k increases, the modulus in the theoretical calculation method also increases, whereas the modulus in the FEM

model is almost unaffected by the *k* value.

7.3.5 Comparison of sensitivity of different parameters

This study examines the effects of various parameters on the settlement and bearing capacity of foundations stabilised with DCM columns. To assess the relative significance of these parameters, key findings are presented using tornado diagrams, as shown in Figures 7.18 and 7.19. These diagrams demonstrate the effect of each input parameter on the output across its typical value range while keeping all other inputs at their reference values. The vertical black line in the tornado diagram indicates the outcome of the baseline scenario. Red bars extending to the right or left of this line signify a positive or negative correlation between the input parameters and the output, respectively. The tornado diagram assists designers in identifying the dominant parameters.

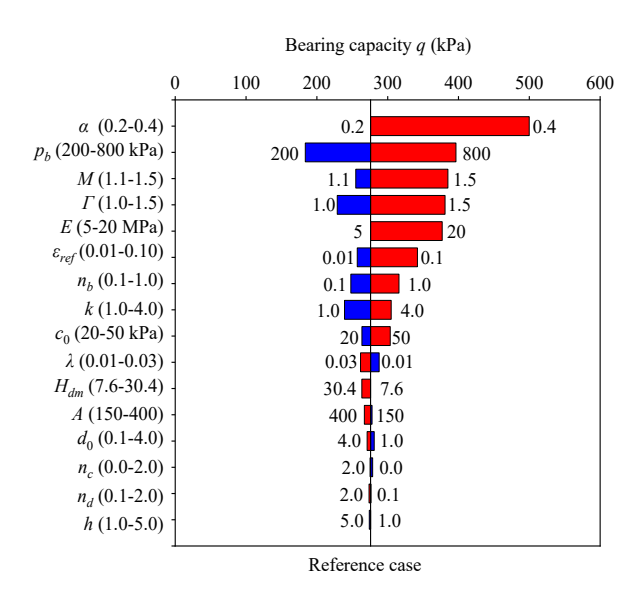


Figure 7.18 Sensitivity analyses of parameters on bearing capacity

According to Figure 7.18(a), the parameters that significantly affect the calculated bearing capacity include the cementation parameters (p_b) and critical state parameters of DCM (Γ, M) , as well as the replacement ratio (α) and soft soil stiffness(E). The sensitivity ranking decreases from top to bottom. The most sensitive parameters for bearing capacity are the area replacement ratio and cementation strength. These two parameters are also the most critical in engineering design. However, it is noteworthy that other parameters, such as the modulus of soft soil, are also important. This is why the prefabricated vertical drains method is commonly used in combination with DCM treatment.

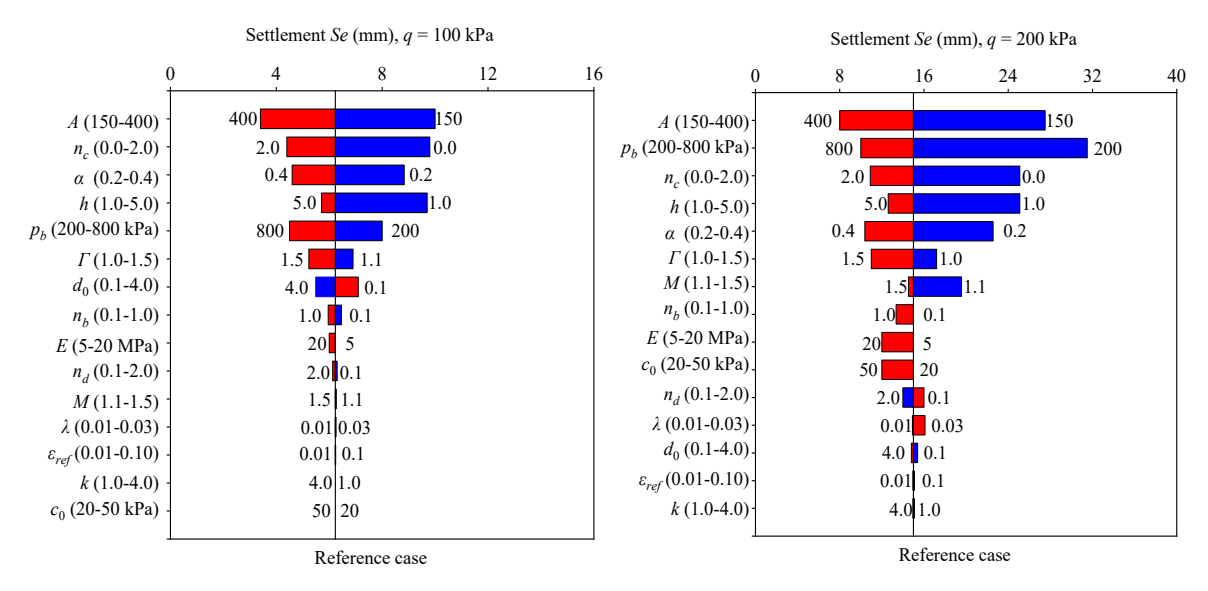


Figure 7.19 Sensitivity analyses on ground settlement at: (a) q = 100 kPa; (b) q = 200 kPa

Additionally, the sensitivity of parameters to settlement was analysed under load conditions of q = 100 and q = 200 kPa. It was found that the sensitivity of parameters differs at these two load levels. As the load increases, the number of parameters sensitive to settlement increases, primarily because the increase in load leads to the development of plasticity, thus highlighting the influence of parameters affecting plastic behaviour in the model. However, a comparison reveals that the most sensitive parameters at both load levels are those determining the elastic modulus of DCM and the DCM replacement ratio.

7.4 Design chart for the bearing capacity of DCM-stabilised foundations

Furthermore, in this chapter, a large number of finite element models were analysed within typical parameter ranges, and three key parameters were identified that govern bearing capacity: the UCS of DCM, the replacement ratio (α), and the Young's modulus of soft soil. Based on the finite element model analysis, a design chart for bearing capacity calculation is proposed, as illustrated in Figure 7.20. The three charts in the figure correspond to three different area replacement ratios, illustrating the relationship between the bearing capacity of foundations improved by DCM (Deep Cement Mixing) columns and the unconfined compressive strength (UCS) of a single column, under varying soil moduli. Each chart includes a fitted semi-empirical equation. The first term in the semi-empirical equation accounts for the increase in bearing capacity due to the addition of DCM columns, with its coefficient being the area replacement ratio consistent with current design codes. The second term considers the contribution of the soft soil to the overall bearing capacity. Finite element analysis results indicate that the contribution of the soft soil largely depends on its modulus. As the modulus

increases, the bearing capacity rises significantly. The analysis also shows that when the soft soil modulus is below 5 MPa, its contribution to the bearing capacity is relatively minor.

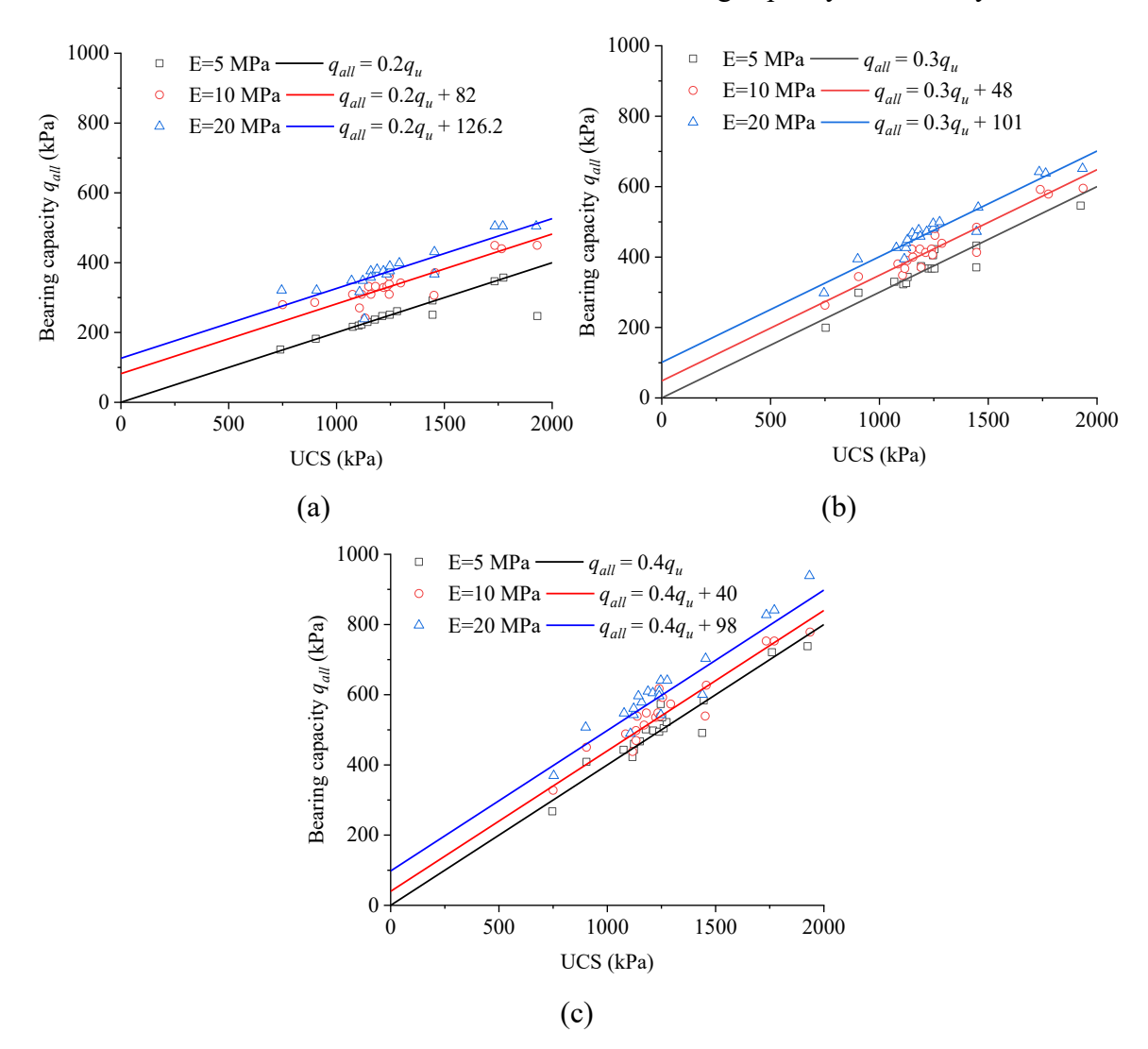


Figure 7.20 New design chart for bearing capacity at various UCS values for (a) $\alpha = 0.2$; (b) $\alpha = 0.3$; (c) $\alpha = 0.4$

7.5 Summary

This chapter presents a comprehensive parametric study of DCM-stabilised foundations. A large number of finite element models were computed to investigate the effects of various parameters on bearing capacity and settlement. These results were then compared with the calculation methods recommended by current design guidelines. To improve the current design method, this study evaluated the ratio between calculated settlement and computed settlement under different safety factor values. Finally, a design chart for bearing capacity was proposed based on the analysis of the finite element model. The differences between the full version model and the basic version model are minimal. The discrepancies are primarily due to the

simplification of equations for the modulus and the flow rule.

The results indicate that several parameters significantly affect the bearing capacity, including the replacement ratio, the modules of soft soil, and the strength and critical state parameters of DCM. Both DCM and the soft soil significantly contribute to the bearing capacity. The strength of DCM is quickly mobilized within a relatively small strain, whereas the strain required for the strength to be fully mobilized in soft soil is larger due to its low stiffness. The sum of these two terms constitutes the bearing capacity of the composite foundation.

The influence of DCM parameters on bearing capacity primarily involves three aspects: bonding strength parameters (p_b), friction angle (M), and dilation. The computed results indicate that current settlement calculation methods in design guidelines tend to overestimate settlement under higher safety factors. This is because the recommended modulus in current standards, which is 300 times the UCS, may underestimate the modulus of DCM. Additionally, the simple equation may underestimate settlement as the load increases and the safety factor decreases. The main reason is that the soil behaviour of DCM is nonlinear and the development of plasticity. Therefore, using simple calculation methods under low safety factors neglects the rapid development of plasticity.

Finally, by summarizing the computation results of numerous FEM models, which included different DCM parameters, soft soil parameters, area replacement ratios, and DCM lengths, the results showed that the bearing capacity of DCM-stabilised foundations is mainly affected by the area replacement ratio, the UCS of DCM, and the modulus of soft soil. Consequently, a design chart for bearing capacity was proposed, focusing on three different soil stiffnesses and three different replacement ratios under varying UCS values, aiming to provide guidance for design methods in engineering practice.

CHAPTER 8 Conclusions and recommendations for further work

The small-strain stiffness of cemented soil is crucial for analysing and predicting ground movements and the applicability of many geotechnical structures. Additionally, cemented soil may be subjected to complex curing temperatures and stresses during on-site curing. Therefore, it is essential to study the effects of curing temperature and stress on the small-strain stiffness of cemented soil. Previous research has often overlooked the mechanisms of curing temperature and stress under water-saturated conditions. Additionally, existing constitutive models in the literature rarely address the characteristics of cemented soil within the small-strain range. The design methods in the current DCM design guidelines employ a simple linear elastic approach. To explore and incorporate the small-strain characteristics of cemented soil in design, this study conducts comprehensive experimental and theoretical work on cemented clay. The major conclusions and recommendations for further studies are summarised in this chapter.

8.1 Conclusions

8.1.1 Effects of curing temperature and curing stress on strength and stiffness of cemented soil

When the curing temperature is increased from 20°C to 40°C, the UCS of cemented marine clay doubles. This strength enhancement is largely due to accelerated cement hydration and intensified pozzolanic reactions at higher temperatures. Specifically, the pozzolanic reaction generates more calcium silicate hydrate gel, which plays a crucial role in the increase in strength. Additionally, raising the curing stress from 0 to 300 kPa also results in a doubling of the UCS. This increase in curing stress does not impact the cement hydration process but instead promotes pore compression and the development of more effective cementation structures.

The initial elastic modulus (E_0) increases by approximately 50% as the curing temperature rises from 20°C to 40°C, and by 80% when the curing stress is elevated from 0 to 300 kPa. Alongside these increases, there is a reduction in the elastic threshold strain associated with the modulus attenuation curve. This decrease is attributed to smaller pore sizes resulting from higher curing temperatures and stresses, as shown in MIP test results. Specimens with smaller pores are more susceptible to damage as deformation increases. With further strain, the modulus degradation curve of cemented clay initially exhibits a high decay rate, which gradually slows. When the strain reaches 1%, the stiffness stabilises at about 20% of its

maximum value. This behaviour may occur because, at larger strains, the cementation structure is significantly compromised, and particle rearrangement and pore compression become the primary factors in stiffness degradation.

As curing temperature and stress increase, both E_{50} and UCS rise significantly, yet their ratio remains relatively constant. For practical applications, the linear equation recommended by design guidelines ($E_{50} = 300$ UCS) can be used. Alternatively, a newly proposed nonlinear equation from this study, which incorporates the density effect, offers improved prediction accuracy with a single parameter compared to the linear equation.

In triaxial shear tests, both peak strength and modulus increase significantly with higher curing temperatures, consistent with findings from unconfined compression tests. The critical state strength also rises with increased curing temperatures due to a lower void ratio at the critical state. The effects of confining pressure on strength is minimal because cementation strength is predominant, and effective stress approaches zero at peak strength. Applying curing stress enhances density, which enhances overall strength and stiffness, and results in more pronounced dilatancy behaviour, as indicated by the quicker reduction in pore water pressure during shearing. The breakdown of cementation leads to notable strain-softening, even when shearing dilatancy is present.

8.1.2 A new model for cemented soil at small and large strains

A novel state-dependent model (full version model) has been developed using the bounding surface plasticity theory to simulate the behaviour of cemented soil across both small and large strains. This model adjusts the size and position of the bounding surface to account for cementation effects. New equations have been introduced to enhance the modelling of small strain behaviour, including (i) the elastic shear modulus under both tensile and compressive stress conditions; and (ii) the nonlinear degradation of bonding strength with damage strain in the stress-strain plane. The model includes seven new parameters that can be calibrated through laboratory testing. For ease of engineering design, some parameters are correlated with cement content. This model has been applied to predict the behaviour of cemented soils under various stress paths, with results compared to experimental data from cemented sands and clays.

The proposed model offers several advantages. Firstly, it accurately captures the stiffness degradation of cemented soil in the small strain range. Secondly, the use of bounding surface plasticity theory effectively simulates nonlinear soil behaviour during unloading and reloading. Thirdly, the strain-softening behaviour is well-represented through the newly proposed bonding degradation equation. This model is expected to enhance the analysis of the serviceability limit

state of infrastructures involving cemented soil.

8.1.3 Comparison of different constitutive models

The full version model is implemented using a modular approach and integrated into a finite element program, which can be selected based on the availability of input parameters. The accuracy and effectiveness of both the model and the program were validated through simulations of element tests. Subsequently, various boundary value problems, such as centrifuge test, physical model test, and field test, were simulated to highlight the advantages of the proposed theoretical model. By comparing the performance of three models across different aspects, the strengths and weaknesses of each model are summarized as follows:

The full version model captures a wide range of soil behaviours, including small strain behaviour, shearing dilatancy, and strain-softening of cemented soil. It performs effectively under drained and undrained conditions and fully coupled hydro-mechanical analyses. However, it requires a large number of parameters, making the parameter calibration process complex.

The basic version model simulates small strain behaviour and strain-softening of cemented soil with fewer parameters, simplifying engineering applications. However, it does not adequately predict dilatancy behaviour due to the omission of state-dependent dilatancy properties, leading to calculation errors, particularly in undrained triaxial shear tests.

The Mohr-Coulomb model is known for its theoretical simplicity, ease of understanding, and minimal parameter requirements. However, it is inadequate for simulating small strain characteristics and strain-softening behaviour of cemented soil.

The proposed full and basic version models are reliable tools for geotechnical engineering applications, offering significant improvements over existing models.

8.1.4 Parametric study of DCM-stablised foundation

A detailed parametric study on the DCM-stabilised foundation was conducted. A total of 200 finite element method (FEM) models were analyzed to explore the effects of various parameters on bearing capacity and settlement. These results were compared with the calculation methods recommended by current design guidelines to improve the existing design method. To align with engineering design practices, the settlement ratio between calculated settlement and simulated settlement with safety factor values was analyzed. Finally, a design chart for bearing capacity was proposed based on the results of the finite element model. The differences between the full version model and the basic version model are minimal. The

discrepancies are primarily due to simplifying equations for the modulus and the flow rule.

The results indicate that several parameters significantly affect the bearing capacity, including the replacement ratio, the modules of soft soil, and the strength and critical state parameters of DCM. Both DCM and the soft soil significantly contribute to the bearing capacity. The strength of DCM is quickly mobilized within a relatively small strain, whereas the strain required for the strength to be fully mobilized in soft soil is larger due to its low stiffness. An increase in the modulus of the soft soil also leads to greater confining pressure on the DCM columns. The sum of these two terms constitutes the bearing capacity of the composite foundation.

The computed results indicate that current settlement calculation methods in design guidelines tend to overestimate settlement under higher safety factors. This is because the recommended modulus in current standards, which is 300 times the UCS, may underestimate the modulus of DCM. Additionally, the simple equation may underestimate settlement as the load increases and the safety factor decreases. The main reason is that the soil behaviour of DCM is nonlinear and the development of plasticity. Therefore, using simple calculation methods under low safety factors neglects the rapid development of plasticity.

Finally, by summarizing the computation results of numerous FEM models, which included different DCM parameters, soft soil parameters, area replacement ratios, and DCM lengths, the results showed that the bearing capacity of DCM-stabilised foundations is mainly affected by the area replacement ratio, the UCS of DCM, and the modulus of soft soil. Consequently, a design chart for bearing capacity was proposed, focusing on three different soil stiffnesses and three different replacement ratios under varying UCS values, aiming to provide guidance for design methods in engineering practice.

8.2 Recommendations and future studies

8.2.1 Suggestions for experimental study

In Chapter 4, the experimental study examines the strength and modulus characteristics of cemented clay under monotonic loading, focusing on the effects of curing temperatures and stresses. However, several limitations remain. Firstly, in Hong Kong, soil layers treated with DCM are often homogeneous, typically consisting of both depositional and alluvial layers (Wang et al. 2019a; Cheung et al. 2022). Therefore, it is crucial to investigate the influence of curing temperature and stress on different soil types. Secondly, previous research has highlighted the anisotropic properties of cemented soil, including variations in strength and modulus (Klimov et al. 2022; Shi et al. 2023). Yet, the impact of curing temperature and curing

stress on anisotropy requires further exploration. To the best of the author's knowledge, no studies have specifically addressed the influence of curing temperature and stress on the anisotropic properties of cemented soil. Thirdly, researchers suggest that under cyclic loading, the strength and modulus of cemented soil may exhibit different characteristics. While some studies have conducted cyclic loading tests on cemented soil, focusing on small strain modulus, they often overlook the effects of curing temperature and stress. Thus, it is essential to investigate the behaviour of specimens under varying curing conditions. Existing findings indicate that strain increase is a key parameter in controlling cementation degradation. However, under high-frequency cyclic loading, it is necessary to establish a comprehensive criterion to describe the degradation of cementation binding, as cementation is the most critical parameter characterizing cemented soil behaviour.

8.2.2 Suggestions for theoretical constitutive model study

The current models are designed for isotropic materials, primarily focusing on behaviour under monotonic loading. These models have been validated through extensive experimental data. For future research, here are three main recommendations for developing constitutive models for cemented soil:

Current constitutive models have considered the isotropic properties of cemented soil. However, anisotropy in strength and small strain modulus has been observed experimentally, indicating that the material behaves differently in different directions. Understanding and incorporating these anisotropic characteristics into constitutive models can provide a more accurate simulation of the behaviour of cemented soil under various loading conditions. Hence, it is essential to address the anisotropic properties of cemented soil, specifically: (1) anisotropy in strength and (2) anisotropy in small strain stiffness.

The basic version model faces issues when simulating shearing dilatancy. One approach to address this issue is enhancing the current dilatancy equation, which is based on the Cam-Clay model. One suggested improvement is establishing a linkage between the dilation equation and cementation parameters. This approach can avoid an increase in parameters and improve the prediction of dilatancy behaviour. By integrating the effects of cementation into the dilatancy model, it is possible to achieve better performance.

8.2.3 Suggestions for numerical study

In Chapters 6 and 7, isotropic models were employed for analysis. However, it is essential to consider advanced models that incorporate soil behaviours such as anisotropy and the

response of cemented soil under various loading conditions. This consideration becomes particularly important when simulating on-site loading conditions, including cyclic and other complex loading conditions. Furthermore, the numerical simulations in Chapters 6 and 7 primarily utilize constitutive models intended for homogeneous materials. Nonetheless, both field and laboratory data reveal significant variability in the properties of cemented soil (Yin et al. 2023; Yin et al. 2022; Kek et al. 2021). This variability can lead to localized failures within DCM columns (Wijerathna and Liyanapathirana 2019). Therefore, it is crucial to adopt numerical methods that account for the inherent variability of cemented soil parameters. Developing probabilistic-based design methods would also be highly advantageous from an engineering perspective.

References

- Abdulla, A. A. & Kiousis, P. D. (1997) Behaviour of cemented sands—I. Testing. *International Journal for Numerical and Analytical Methods in Geomechanics* **21(8)**:533-547.
- Acar, Y. B. & El-Tahir, E.-T. A. (1986) Low strain dynamic properties of artificially cemented sand. *Journal of geotechnical engineering* **112(11)**:1001-1015.
- Acar, Y. B. & Eltahir, E. A. (1986) Low Strain Dynamic Properties of Artificially Cemented Sand. *Journal of Geotechnical Engineering-Asce* **112(11)**:1001-1015.
- Al-Zoubi, M. S. (2008) Undrained shear strength and swelling characteristics of cement treated soil. *Jordan Journal of Civil Engineering* **2(1)**:53-62.
- Argyris, J., Faust, G., Szimmat, J., Warnke, E. & Willam, K. (1974) Recent developments in the finite element analysis of prestressed concrete reactor vessels. *Nuclear Engineering and Design* **28(1)**:42-75.
- Arroyo, M., Amaral, M., Romero, E. & Viana Da Fonseca, A. (2013) Isotropic yielding of unsaturated cemented silty sand. *Canadian geotechnical journal* **50(8)**:807-819.
- Astm (2006)Standard Practice for Classification of Soils for Engineering Purposes (Unified Soil Classification System). Annual Book of ASTM Standards, ASTM International West Conshohocken, PA, USA.
- Astm (2008) Standard test method for direct tensile strength of intact rock core specimens. ASTM International.
- Astm (2013) ASTM C192: Standard practice for making and curing concrete test specimens in the laboratory.) ASTM international West Conshohoken, PA, USA.
- Astm (2019)D4543 Standard Practices for Preparing Rock Core as Cylindrical Test Specimens and Verifying Conformance to Dimensional and Shape Tolerances.
- Atkinson, J. (2000) Non-linear soil stiffness in routine design. *Geotechnique* **50(5)**:487-508.
- Atkinson, J. & Sallfors, G. (1991) Experimental determination of soil properties. General Report to Session 1. *Proceedings of the 10th ECSMFE, Florence* **3**:915-956.
- Bahador, M. & Pak, A. (2012) Small-strain shear modulus of cement-admixed kaolinite. *Geotechnical and Geological Engineering* **30**:163-171.
- Baig, S., Picornell, M. & Nazarian, S. (1997) Low strain shear moduli of cemented sands. Journal of Geotechnical and Geoenvironmental Engineering 123(6):540-545.
- Bandyopadhyay, P. & Pillai, R. J. (2020) A Bounding Surface Model for Cement Stabilised Clay. In *Geotechnical Characterization and Modelling: Proceedings of IGC 2018*.) Springer, pp. 1005-1018.

- Bardet, J. (1986) Bounding surface plasticity model for sands. *Journal of engineering mechanics* **112(11)**:1198-1217.
- Baudet, B. & Stallebrass, S. (2004) A constitutive model for structured clays. *Geotechnique* **54(4)**:269-278.
- Bauer, E. & Wu, W. (1993) A hypoplastic model for granular soils under cyclic loading. *Modern* approaches to plasticity **247**.
- Becker, D. E. (1997) Eighteenth Canadian geotechnical colloquium: Limit states design for foundations. Part I. An overview of the foundation design process. *Canadian geotechnical journal* **33(6)**:956-983.
- Beckett, C. & Ciancio, D. (2014) Effects of compaction water content on the strength of cement-stabilised rammed earth materials. *Canadian geotechnical journal* **51(5)**:583-590.
- Been, K. & Jefferies, M. G. (1985) A state parameter for sands. *Geotechnique* **35(2)**:99-112.
- Bergado, D. & Lorenzo, G. (2005a) Economical mixing method for cement deep mixing. In *Innovations in grouting and soil improvement*.), pp. 1-10.
- Bergado, D. T. & Lorenzo, G. A. (2005b) A full-scale study on cement deep mixing in soft Bangkok clay. In *Elsevier Geo-Engineering Book series*.) Elsevier, vol. 3, pp. 305-325.
- Bi, J. & Chian, S. C. (2021) Modelling strength development of cement-stabilised clay and clay with sand impurity cured under varying temperatures. *Bulletin of engineering geology* and the environment **80(8)**:6275-6302.
- Bolton, M. (1987) Discussion: The strength and dilatancy of sands. *Geotechnique* **37(2)**:219-226.
- Bruce, D. A., Bruce, M. E. C. & Dimillio, A. F. (1998) Deep mixing method: A global perspective. *Geotechnical special publication*:1-26.
- Bullard, J. W., Jennings, H. M., Livingston, R. A., Nonat, A., Scherer, G. W., Schweitzer, J. S., Scrivener, K. L. & Thomas, J. J. (2011) Mechanisms of cement hydration. *Cement and concrete research* **41(12)**:1208-1223.
- Burland, J. B. (1990) On the compressibility and shear strength of natural clays. *Geotechnique* **40(3)**:329-378.
- Bushra, I. & Robinson, R. G. (2013) Effects of fly ash on cement admixture for a low plasticity marine soil. *Advances in Civil Engineering Materials* **2(1)**:608-621.
- Cai, G.-H., Zhang, C.-H., Zhou, Y.-F., Li, J.-S. & Poon, C. S. (2024) Mechanical behaviour and microstructure mechanism of artificially stabilised marine sediment under high water content. *Construction and Building Materials* **420**:135484.
- Cardoso, R., Ribeiro, D. & Néri, R. (2017) Bonding effect on the evolution with curing time

- of compressive and tensile strength of sand-cement mixtures. *Soils and Foundations* **57(4)**:655-668.
- Chai, J., Miura, N., Kirekawa, T. & Hino, T. (2010) Settlement prediction for soft ground improved by columns. *Proceedings of the Institution of Civil Engineers-Ground Improvement* **163(2)**:109-119.
- Chau, V. N., Nguyen, D. H., & Be, S. N. (2024). Effect of curing temperature on the mechanical characteristics of cement-treated soils: a review. *Journal of Science and Transport Technology*, 37-54.
- Chen, S., Guan, Y. & Dai, J. (2023) Behaviour of anchored sheet pile quay stabilised with deep cement mixing columns in soft soil: Centrifuge and numerical modelling. *Computers and Geotechnics* **160**:105504.
- Chen, S., Wu, A., Wang, Y. & Wang, W. (2021) Coupled effects of curing stress and curing temperature on mechanical and physical properties of cemented paste backfill. *Construction and Building Materials* **273**:121746.
- Cheung, H., Yan, C., Cheung, C. & Wong, A. (2022) Deep cement mixing—the experience in Tung Chung East reclamation and challenges ahead. *AIJR Proceedings*:348-360.
- Chew, S., Kamruzzaman, A. & Lee, F. (2004) Physicochemical and engineering behaviour of cement treated clays. *Journal of Geotechnical and Geoenvironmental Engineering* **130(7)**:696-706.
- Clayton, C. (2011) Stiffness at small strain: research and practice. Geotechnique 61(1):5-37.
- Clayton, C. & Heymann, G. (2001) Stiffness of geomaterials at very small strains. *Geotechnique* **51(3)**:245-255.
- Clough, G. W., Sitar, N., Bachus, R. C. & Rad, N. S. (1981) Cemented sands under static loading. *Journal of the Geotechnical Engineering Division* **107(6)**:799-817.
- Consoli, N., Cruz, R. C., Consoli, B. & Maghous, S. (2012a) Failure envelope of artificially cemented sand. *Geotechnique* **62(6)**:543-547.
- Consoli, N., Fonseca, A. D., Silva, S., Cruz, R. & Fonini, A. (2012b) Parameters controlling stiffness and strength of artificially cemented soils. *Geotechnique* **62(2)**:177-183.
- Consoli, N., Rotta, G. & Prietto, P. (2000) Influence of curing under stress on the triaxial response of cemented soils. *Geotechnique* **50(1)**:99-105.
- Consoli, N. C., Cruz, R. C., Floss, M. F. & Festugato, L. (2010) Parameters controlling tensile and compressive strength of artificially cemented sand. *Journal of Geotechnical and Geoenvironmental Engineering* **136(5)**:759-763.
- Consoli, N. C., Da Fonseca, A. V., Cruz, R. C. & Silva, S. R. (2011) Voids/cement ratio

- controlling tensile strength of cement-treated soils. *Journal of geotechnical and geoenvironmental engineering* **137(11)**:1126-1131.
- Consoli, N. C., Da Rocha, C. G. & Silvani, C. (2014) Devising dosages for soil–fly ash–lime blends based on tensile strength controlling equations. *Construction and Building Materials* **55**:238-245.
- Consoli, N. C., Festugato, L., Da Rocha, C. G. & Cruz, R. C. (2013) Key parameters for strength control of rammed sand–cement mixtures: Influence of types of portland cement. *Construction and Building Materials* **49**:591-597.
- Consoli, N. C., Foppa, D., Festugato, L. & Heineck, K. S. (2007) Key parameters for strength control of artificially cemented soils. *Journal of Geotechnical and Geoenvironmental Engineering* **133(2)**:197-205.
- Consoli, N. C., Quiñónez, R. A., González, L. E. & López, R. A. (2017) Influence of molding moisture content and porosity/cement index on stiffness, strength, and failure envelopes of artificially cemented fine-grained soils. *Journal of Materials in Civil Engineering* **29(5)**:04016277.
- Consoli, N. C., Rosa, F. D. & Fonini, A. (2009) Plate load tests on cemented soil layers overlaying weaker soil. *Journal of geotechnical and geoenvironmental engineering* **135(12)**:1846-1856.
- Consoli, N. C., Winter, D., Rilho, A. S., Festugato, L. & Dos Santos Teixeira, B. (2015) A testing procedure for predicting strength in artificially cemented soft soils. *Engineering geology* **195**:327-334.
- Cuccovillo, T. & Coop, M. (1999) On the mechanics of structured sands. *Geotechnique* **49(6)**:741-760.
- Cui, L. & Fall, M. (2016) Mechanical and thermal properties of cemented tailings materials at early ages: Influence of initial temperature, curing stress and drainage conditions. *Construction and Building Materials* **125**:553-563.
- Dafalias, Y. F. & Herrmann, L. R. (1986) Bounding surface plasticity. II: Application to isotropic cohesive soils. *Journal of engineering mechanics* **112(12)**:1263-1291.
- Dafalias, Y. F. & Manzari, M. T. (2004) Simple plasticity sand model accounting for fabric change effects. *Journal of engineering mechanics* **130(6)**:622-634.
- Dalla Rosa, F., Consoli, N. & Baudet, B. (2008) An experimental investigation of the behaviour of artificially cemented soil cured under stress. *Geotechnique* **58(8)**:675-679.
- Dang, L. C., Dang, C. C. & Khabbaz, H. (2020) Modelling of columns and fibre-reinforced load-transfer platform-supported embankments. *Proceedings of the Institution of Civil*

- Engineers-Ground Improvement 173(4):197-215.
- Dejong, J. T., Fritzges, M. B. & Nüsslein, K. (2006) Microbially induced cementation to control sand response to undrained shear. *Journal of Geotechnical and Geoenvironmental Engineering* **132(11)**:1381-1392.
- Delage, P. (2010) A microstructure approach to the sensitivity and compressibility of some Eastern Canada sensitive clays. *Geotechnique* **60(5)**:353-368.
- Dewitte, C., Bertron, A., Neji, M., Lacarrière, L. & Dauzères, A. (2022) Chemical and microstructural properties of designed cohesive MSH pastes. *Materials* **15(2)**:547.
- Diambra, A., Ibraim, E., Peccin, A., Consoli, N. & Festugato, L. (2017) Theoretical derivation of artificially cemented granular soil strength. *Journal of Geotechnical and Geoenvironmental Engineering* **143(5)**:04017003.
- Ding, H., Wang, X., Wen, D., Peng, H. & Liu, K. (2024) Stress stress-strain behaviour of hydraulic filled coral sand subjected to internal erosion. In *IOP Conference Series: Earth and Environmental Science*.) IOP Publishing, vol. 1337, pp. 012071.
- Do, H., Pham, V., Pham, A., Huynh, P. & Oh, E. (2021) An Investigation of the Elastic Modulus of Cement-Stabilised Soil by Wet Mixing Method for Sand Ground. *Geotechnical Engineering* (00465828) **52(1)**: 67-74.
- Doherty, J. P. & Wood, D. M. (2020) A bonding and damage constitutive model for lightly cemented granular material. *Computers and Geotechnics* **127**:103732.
- Du, C., Zhang, J., Yang, G. & Yang, Q. (2021) The influence of organic matter on the strength development of cement-stabilised marine soft clay. *Marine Georesources & Geotechnology* **39(8)**:983-993.
- El Kamash, W., Han, J. & Asce, F. (2014) Displacements of column-supported embankments over soft clay after widening considering soil consolidation and column layout: Numerical analysis. *Soils and Foundations* **54(6)**:1054-1069.
- Erarslan, N. & Williams, D. J. (2012) Experimental, numerical and analytical studies on tensile strength of rocks. *International Journal of Rock Mechanics and Mining Sciences* **49**:21-30.
- Fang, K. & Fall, M. (2018) Effects of curing temperature on shear behaviour of cemented paste backfill-rock interface. *International Journal of Rock Mechanics and Mining Sciences* **112**:184-192.
- Fang, Z. (2006) Physical and numerical modelling of the soft soil ground improved by deep cement mixing method.
- Fernandez, A. & Santamarina, J. (2001) Effects of cementation on the small-strain parameters

- of sands. Canadian geotechnical journal **38(1)**:191-199.
- Fhwa (2013) Federal highway administration design manual: Deep mixing for embankment and foundation support.
- Fhwa., F. H. A. (2013) Federal highway administration design manual: Deep mixing for embankment and foundation support.) United States. Federal Highway Administration. Offices of Research & Development.
- Fiskvik Bache, B. K., Wiersholm, P., Paniagua, P. & Emdal, A. (2022) Effects of temperature on the strength of lime—cement stabilised Norwegian clays. *Journal of Geotechnical and Geoenvironmental Engineering* **148(3)**:04021198.
- Fu, Z., Chen, S., Zhong, Q. & Ji, E. (2022) A damage hypoplasticity constitutive model for cemented sand and gravel materials. *Acta Geotechnica* **17(1)**:1-18.
- Geo (2023) Test Method for Unconfined Compressive Strength of Cement Stabilised Soil Cores (GEO Report No. 365).
- Gu, J., Zeng, C., Lyu, H. & Yang, J. (2021) Effects of cement content and curing period on strength enhancement of cemented calcareous sand. *Marine Georesources & Geotechnology* **39(9)**:1083-1095.
- Guo, C. & Cui, Y. (2020) Pore structure characteristics of debris flow source material in the Wenchuan earthquake area. *Engineering Geology* **267**:105499.
- Haeri, S. & Hamidi, A. (2009) Constitutive modelling of cemented gravelly sands. Geomechanics and Geoengineering: An International Journal 4(2):123-139.
- Han, J., Wang, K., Shi, J. & Wang, Y. (2014) Influence of sodium aluminate on cement hydration and concrete properties. *Construction and Building Materials* **64**:342-349.
- Han, J. & Ye, S.-L. (2001) Simplified method for consolidation rate of stone column reinforced foundations. *Journal of Geotechnical and Geoenvironmental Engineering* **127(7)**:597-603.
- Hardin, B. O. & Black, W. L. (1968) Vibration modulus of normally consolidated clay. *Journal of the Soil Mechanics and Foundations Division* **94(2)**:353-369.
- Hardin, B. O. & Drnevich, V. P. (1972) Shear modulus and damping in soils: design equations and curves. *Journal of the Soil mechanics and Foundations Division* **98(7)**:667-692.
- He, X., Chen, Y., Tan, X., Wang, S. & Liu, L. (2020a) Determining the water content and void ratio of cement-treated dredged soil from the hydration degree of cement. *Engineering Geology* **279**:105892.
- He, X., Chen, Y., Wan, Y., Liu, L. & Xue, Q. (2020b) Effects of curing stress on compression behaviour of cement-treated dredged sediment. *International Journal of Geomechanics* **20(11)**:04020204.

- Hirai, H., Takahashi, M. & Yamada, M. (1989) An elastic-plastic constitutive model for the behaviour of improved sandy soils. *Soils and Foundations* **29(2)**:69-84.
- Ho, L. S., Nakarai, K., Duc, M., Le Kouby, A., Maachi, A. & Sasaki, T. (2018) Analysis of strength development in cement-treated soils under different curing conditions through microstructural and chemical investigations. *Construction and Building Materials* 166:634-646.
- Ho, T.-O., Chen, W.-B., Yin, J.-H., Wu, P.-C. & Tsang, D. C. (2021) Stress-strain behaviour of cement-stabilised Hong Kong marine deposits. *Construction and Building Materials* **274**:122103.
- Horpibulsuk, S., Liu, M. D., Liyanapathirana, D. S. & Suebsuk, J. (2010a) Behaviour of cemented clay simulated via the theoretical framework of the Structured Cam Clay model. *Computers and Geotechnics* **37(1-2)**:1-9.
- Horpibulsuk, S., Miura, N. & Bergado, D. (2004) Undrained shear behaviour of cement admixed clay at high water content. *Journal of Geotechnical and Geoenvironmental Engineering* **130(10)**:1096-1105.
- Horpibulsuk, S., Rachan, R., Chinkulkijniwat, A., Raksachon, Y. & Suddeepong, A. (2010b) Analysis of strength development in cement-stabilised silty clay from microstructural considerations. *Construction and Building Materials* **24(10)**:2011-2021.
- Horpibulsuk, S., Rachan, R. & Raksachon, Y. (2009) Role of fly ash on strength and microstructure development in blended cement stabilised silty clay. *Soils and Foundations* **49(1)**:85-98.
- Houlsby, G. T. (1991) How the dilatancy of soils affects their behaviour.
- Huang, J. & Han, J. (2009) 3D coupled mechanical and hydraulic modeling of a geosynthetic-reinforced deep mixed column-supported embankment. *Geotextiles and Geomembranes* **27(4)**:272-280.
- Huang, P.-T., Patel, M., Santagata, M. C. & Bobet, A. (2009) Classification of organic soils.
- Ishihara, K., Tatsuoka, F. & Yasuda, S. (1975) Undrained deformation and liquefaction of sand under cyclic stresses. *Soils and foundations* **15(1)**:29-44.
- Ismail, M. A., Joer, H. A., Sim, W. H. & Randolph, M. F. (2002) Effects of cement type on shear behaviour of cemented calcareous soil. *Journal of Geotechnical and Geoenvironmental Engineering* **128(6)**:520-529.
- Jamsawang, P., Voottipruex, P., Boathong, P., Mairaing, W. & Horpibulsuk, S. (2015) Three-dimensional numerical investigation on lateral movement and factor of safety of slopes stabilised with deep cement mixing column rows. *Engineering Geology* **188**:159-167.

- Jamsawang, P., Yoobanpot, N., Thanasisathit, N., Voottipruex, P. & Jongpradist, P. (2016) Three-dimensional numerical analysis of a DCM column-supported highway embankment. *Computers and Geotechnics* **72**:42-56.
- Jaritngam, S., Swasdi, S., Tonnayopas, D. & Thongchim, P. (2008) Improvement for subsoil by cement column-a case study in Thailand. In *Proceedings of the 13th international conference of Hong Kong society for transportation*.).
- JGJ 79. 2012. Technical code ground treatment of buildings. Edited by Ministry of Housing and Urban-Rural Development of the People's Republic of China. China Architecture & Building Press, Beijing.
- Jia, R., Lei, H. & Li, K. (2020) Compressibility and microstructure evolution of different reconstituted clays during 1D compression. *International Journal of Geomechanics* **20(10)**:04020181.
- Jiang, M., Yan, H., Zhu, H. & Utili, S. (2011) Modeling shear behaviour and strain localization in cemented sands by two-dimensional distinct element method analyses. *Computers and Geotechnics* **38(1)**:14-29.
- Jiao, K.-F. & Zhou, C. (2024) A Bounding Surface Model for Cemented Soil at Small and Large Strains. *Journal of Geotechnical and Geoenvironmental Engineering* **150(2)**:04023136.
- Jongpradist, P., Jumlongrach, N., Youwai, S. & Chucheepsakul, S. (2010) Influence of fly ash on unconfined compressive strength of cement-admixed clay at high water content. *Journal of Materials in Civil Engineering* **22(1)**:49-58.
- Juang, C. H. & Holtz, R. D. (1986) Fabric, pore size distribution, and permeability of sandy soils. *Journal of Geotechnical Engineering* **112(9)**:855-868.
- Kamruzzaman, A., Chew, S. & Lee, F. (2009) Structuration and destructuration behaviour of cement-treated Singapore marine clay. *Journal of Geotechnical and Geoenvironmental Engineering* **135(4)**:573-589.
- Kasama, K., Ochiai, H. & Yasufuku, N. (2000) On the stress-strain behaviour of lightly cemented clay based on an extended critical state concept. *Soils and Foundations* **40(5)**:37-47.
- Kasama, K., Zen, K. & Iwataki, K. (2006) Undrained shear strength of cement-treated soils. *Soils and Foundations* **46(2)**:221-232.
- Kavvadas, M. & Amorosi, A. (2000) A constitutive model for structured soils. *Geotechnique* **50(3)**:263-273.
- Kek, H. Y., Pan, Y., Ng, Y. C. H. & Lee, F. H. (2021) An approach for modelling spatial variability in permeability of cement-admixed soil. *Acta Geotechnica* **16**:4007-4026.
- Kenai, S., Bahar, R. & Benazzoug, M. (2006) Experimental analysis of the effects of some

- compaction methods on mechanical properties and durability of cement stabilised soil. *Journal of Materials Science* **41**:6956-6964.
- Kezdi, A. (2016) Stabilised earth roads. Elsevier.
- Khalili, N., Habte, M. & Valliappan, S. (2005) A bounding surface plasticity model for cyclic loading of granular soils. *International journal for numerical methods in engineering* **63(14)**:1939-1960.
- Khan, Q., Ng, Y. & Ku, T. (2019) Small Strain Stiffness of Artificially Cemented Soft Clay: Modelling the Effects of Structure Degradation. In *E3S Web of Conferences*.) EDP Sciences, vol. 92, pp. 11009.
- Kitazume, M. & Terashi, M. (2013) The deep mixing method. CRC press London.
- Kivelo, M. (1998) Stabilisation of embankments on soft soil with lime/cement columns. *Ph. D. Thesis, Royal Institute of Technology*.
- Klimov, D. M., Karev, V. I., Kovalenko, Y. F. & Ustinov, K. B. (2022) On the atypical strength anisotropy of weakly cemented sandstones. In *Doklady Mathematics*.) Springer, vol. 106, pp. 398-401.
- Kolymbas, D. (1987) A novel constitutive law for soils. In *Proc. Int. Conf. on Constitutive Laws.*) Tucson, pp. 319-323.
- Lee, K., Chan, D. & Lam, K. (2004) Constitutive model for cement treated clay in a critical state frame work. *Soils and Foundations* **44(3)**:69-77.
- Lemaire, K., Deneele, D., Bonnet, S. & Legret, M. (2013) Effects of lime and cement treatment on the physicochemical, microstructural and mechanical characteristics of a plastic silt. Engineering Geology 166:255-261.
- Li, D. & Wong, L. N. Y. (2013) The Brazilian disc test for rock mechanics applications: review and new insights. *Rock Mechanics and Rock Engineering* **46**:269-287.
- Li, W. & Kwok, C. Y. (2024) Engineering behaviour of in situ cored deep cement mixed marine deposits subjected to undrained and drained shearing. *Journal of Rock Mechanics and Geotechnical Engineering* **16(5)**:1749-1760.
- Li, W., Yi, Y. & Puppala, A. J. (2022) Comparing carbide sludge-ground granulated blastfurnace slag and ordinary Portland cement: Different findings from binder paste and stabilised clay slurry. *Construction and Building Materials* **321**:126382.
- Li, X. (2002) A sand model with state-dapendent dilatancy. Geotechnique 52(3):173-186.
- Li, X. & Zhang, L. (2009) Characterization of dual-structure pore-size distribution of soil. Canadian Geotechnical Journal 46(2):129-141.
- Li, X. S. & Dafalias, Y. F. (2002) Constitutive modeling of inherently anisotropic sand

- behaviour. Journal of geotechnical and geoenvironmental engineering 128(10):868-880.
- Liao, D., Yang, Z., Wang, S. & Wu, W. (2023) A hypoplastic model for cemented sand under monotonic and cyclic loading. *Canadian Geotechnical Journal* **61(5)**:915-930.
- Liu, B., Fan, H., Jiang, Y. & Ma, R. (2023) Linking pore structure characteristics to soil strength and their relationships with detachment rate of disturbed Mollisol by concentrated flow under freeze–thaw effects. *Journal of Hydrology* **617**:129052.
- Liu, L., Deng, T., Deng, Y., Zhan, L., Horpibulsuk, S. & Wang, Q. (2022) Stabilisation nature and unified strength characterization for cement-based stabilised soils. *Construction and Building Materials* **336**:127544.
- Liu, S.-Y., Du, Y.-J., Yi, Y.-L. & Puppala, A. J. (2012) Field investigations on performance of T-shaped deep mixed soil cement column–supported embankments over soft ground. *Journal of Geotechnical and Geoenvironmental Engineering* **138(6)**:718-727.
- Liu, Y., Lee, F.-H., Quek, S.-T., Chen, E. & Yi, J.-T. (2015) Effects of spatial variation of strength and modulus on the lateral compression response of cement-admixed clay slab. *Geotechnique* **65(10)**:851-865.
- Liyanapathirana, D. & Yapage, N. (2021) A spreadsheet based stability calculation for geosynthetic reinforced column-supported embankments. *Transportation Geotechnics* **29**:100575.
- Lo, K. Y. & Lee, C. F. (1973) Stress analysis and slope stability in strain-softening materials. *Geotechnique* **23(1)**:1-11.
- Lo, S., Lade, P. & Wardani, S. (2003) An experimental study of the mechanics of two weakly cemented soils. *Geotechnical Testing Journal* **26(3)**:328-341.
- Lo, S. & Wardani, S. P. (2002) Strength and dilatancy of a silt stabilised by a cement and fly ash mixture. *Canadian geotechnical journal* **39(1)**:77-89.
- Long, W. & Chong, S. S. (2024) Advance Modeling of Soil Cement Mixing for Deep Excavation Using Plaxis 2D Concrete Model. In *International Conference on Transportation Geotechnics*.) Springer, pp. 67-76.
- Luis, A., Deng, L., Shao, L. & Li, H. A. (2019) Triaxial behaviour and image analysis of Edmonton clay treated with cement and fly ash. *Construction and Building Materials* **197**:208-219.
- Ma, J., Chen, J., Chen, W., Liu, C. & Chen, W. (2022) A bounding surface plasticity model for expanded polystyrene-sand mixture. *Transportation Geotechnics* **32**:100702.
- Maeda, K. & Miura, K. (1999) Confining stress dependency of mechanical properties of sands. *Soils and Foundations* **39(1)**:53-67.

- Mallawarachchi, M., Ekanayake, E., Kodagoda, S. & Dias, A. V. (2014) Comparison of soil modulus E 50 of residual soil slope failures in two different rainfall zones. In *Landslide Science for a Safer Geoenvironment: Vol. 1: The International Programme on Landslides (IPL)*.) Springer, pp. 135-141.
- Maltais, Y. & Marchand, J. (1997) INFLUENCE OF CURING TEMPERATURE ON CEMENT HYDRATION AND MECHANICAL STRENGTH DEVELOPMENT OF FLY ASH MORTARS. *Cement & Concrete Research* **27(7)**:1009-1020.
- Mansour, M., Samieh, A. & Matter, H. (2015) Engineering properties of cement/lime-stabilised Egyptian soft clay. In *IOP Conference Series: Earth and Environmental Science*.) IOP Publishing, vol. 26, pp. 012041.
- Manzari, M. T. & Dafalias, Y. F. (1997) A critical state two-surface plasticity model for sands. *Geotechnique* **47(2)**:255-272.
- Marques, S. F. V., Festugato, L. & Consoli, N. C. (2021) Stiffness and strength of an artificially cemented sand cured under stress. *Granular Matter* **23**:1-16.
- Marri, A., Wanatowski, D. & Yu, H. (2012) Drained behaviour of cemented sand in high pressure triaxial compression tests. *Geomechanics and Geoengineering* **7(3)**:159-174.
- Martinez, B. C. & Dejong, J. T. (2009) Bio-mediated soil improvement: Load transfer mechanisms at the micro-and macro-scales. In *Advances in ground improvement: research to practice in the United States and China.*), pp. 242-251.
- Meepon, I., Voottipruex, P. & Jamsawang, P. (2016) Behaviours of soil cement columns and stiffened soil cement column wall in shallow excavation. *Lowland technology international: the official journal of the International Association of Lowland Technology (IALT)/Institute of Lowland Technology, Saga University* **18(3)**:197-208.
- Mehta, P. K. & Monteiro, P. (2006) Concrete: microstructure, properties, and materials. (No *Title*).
- Melentijevic, S., Arcos, J. & Oteo, C. (2013a) Application of cement deep mixing method for underpinning. In *Proc.*, 18th Int. Conf. on Soil Mechanics and Geotechnical Engineering.), pp. 2549-2552.
- Melentijevic, S., Arcos, J. & Oteo, C. (2013b) Application of cement deep mixing method for underpinning. In *Proceedings of the 18th International Conference on Soil Mechanics and Geotechnical Engineering*.), pp. 2549-2552.
- Meyerhof, G. (1984) Safety factors and limit states analysis in geotechnical engineering. Canadian geotechnical journal 21(1):1-7.
- Mitchell, J. K. & Soga, K. (2005) Fundamentals of soil behaviour. John Wiley & Sons Inc.

- Moghaddasi, H., Shahbodagh, B. & Khalili, N. (2021) A bounding surface plasticity model for unsaturated structured soils. *Computers and Geotechnics* **138**:104313.
- Mohsin, A. (2008) Automated Gmax measurement to explore degradation of artificially cemented carbonate sand.
- Montoya, B. & Dejong, J. (2015) Stress-strain behaviour of sands cemented by microbially induced calcite precipitation. *Journal of Geotechnical and Geoenvironmental Engineering* **141(6)**:04015019.
- Moore, R. K., Kennedy, T. W. & Hudson, W. R. (1970) Factors affecting the tensile strength of cement-treated materials. *Highway Research Record* **315**:64-80.
- Moreira, E. B., Baldovino, J. A., Rose, J. L. & Dos Santos Izzo, R. L. (2019) Effects of porosity, dry unit weight, cement content and void/cement ratio on unconfined compressive strength of roof tile waste-silty soil mixtures. *Journal of Rock Mechanics and Geotechnical Engineering* 11(2):369-378.
- Nagaraj, T., Pandian, N. & Narasimha Raju, P. (1998) Compressibility behaviour of soft cemented soils. *Geotechnique* **48(2)**:281-287.
- Namikawa, T. & Koseki, J. (2006) Experimental determination of softening relations for cement-treated sand. *Soils and foundations* **46(4)**:491-504.
- Namikawa, T. & Koseki, J. (2007) Evaluation of tensile strength of cement-treated sand based on several types of laboratory tests. *Soils and Foundations* **47(4)**:657-674.
- Namikawa, T. & Mihira, S. (2007) Elasto-plastic model for cement-treated sand. *International Journal for Numerical and Analytical Methods in Geomechanics* **31(1)**:71-107.
- Nawaz, S., Ahmad, M., Asif, S., Klemeš, J. J., Mubashir, M., Munir, M., Zafar, M., Bokhari, A., Mukhtar, A. & Saqib, S. (2022) Phyllosilicate derived catalysts for efficient conversion of lignocellulosic derived biomass to biodiesel: A review. *Bioresource Technology* 343:126068.
- Nguyen, L., Fatahi, B. & Khabbaz, H. (2017) Development of a constitutive model to predict the behaviour of cement-treated clay during cementation degradation: C3 model. International Journal of Geomechanics 17(7):04017010.
- Nguyen, L. D., Fatahi, B. & Khabbaz, H. (2014) A constitutive model for cemented clays capturing cementation degradation. *International Journal of Plasticity* **56**:1-18.
- Nguyen, M.-D., Le, A.-T., Nguyen, T.-A., Thach, N.-T. & Phan, T.-K. (2020) The Influence of Water Content and Compaction on the Unconfined Compression Strength of Cement Treated Clay. In 2020 5th International Conference on Green Technology and Sustainable Development (GTSD).) IEEE, pp. 175-179.

- Ni, P., Yi, Y. & Liu, S. (2019) Bearing capacity of composite ground with soil-cement columns under earth fills: Physical and numerical modeling. *Soils and Foundations* **59(6)**:2206-2219.
- Noble, D. F. & Plaster, R. W. (1970) Reactions in Portland cement-clay mixtures.
- Nweke, C. (2017) *Constitutive Modeling of Weakly Cemented Sands*. University of California, Berkeley.
- Onitsuka, K., Modmoltin, C., Kouno, M. & Negami, T. (2003) Effects of organic matter on lime and cement stabilised Ariake clays. *Doboku Gakkai Ronbunshu* **2003(729)**:1-13.
- Ouellet, S., Bussière, B., Aubertin, M. & Benzaazoua, M. (2007) Microstructural evolution of cemented paste backfill: Mercury intrusion porosimetry test results. *Cement and concrete research* **37(12)**:1654-1665.
- Oztoprak, S. & Bolton, M. (2013) Stiffness of sands through a laboratory test database. *Geotechnique* **63(1)**:54-70.
- Papadopoulou, A. & Tika, T. (2008) The effects of fines on critical state and liquefaction resistance characteristics of non-plastic silty sands. *Soils and Foundations* **48(5)**:713-725.
- Park, D. & Kutter, B. (2016) Sensitive bounding surface constitutive model for structured clay. International Journal for Numerical and Analytical Methods in Geomechanics 40(14):1968-1987.
- Pestana, J. M. & Salvati, L. A. (2006) Small-strain behaviour of granular soils. I: Model for cemented and uncemented sands and gravels. *Journal of Geotechnical and Geoenvironmental Engineering* **132(8)**:1071-1081.
- Phutthananon, C., Jongpradist, P., Jongpradist, P., Dias, D. & Baroth, J. (2020) Parametric analysis and optimization of T-shaped and conventional deep cement mixing column-supported embankments. *Computers and Geotechnics* **122**:103555.
- Phutthananon, C., Jongpradist, P., Wonglert, A., Kandavorawong, K., Sanboonsiri, S. & Jamsawang, P. (2022) Field and 3D Numerical Investigations of the Performances of Stiffened Deep Cement Mixing Column-Supported Embankments Built on Soft Soil. *Arabian Journal for Science and Engineering* **48(4)**:5139-5169.
- Phutthananon, C., Jongpradist, P., Wonglert, A., Kandavorawong, K., Sanboonsiri, S. & Jamsawang, P. (2023) Field and 3D numerical investigations of the performances of stiffened deep cement mixing column-supported embankments built on soft soil. *Arabian Journal for Science and Engineering* **48(4)**:5139-5169.
- Pongsivasathit, S., Petchgate, W., Horpibulsuk, S. & Piyaphipat, S. (2021) Composite contiguous pile wall and deep mixing column wall as a dam-Design, construction and

- performance. Case Studies in Construction Materials 15:e00771.
- Rahimi, M., Chan, D. & Nouri, A. (2016) Bounding surface constitutive model for cemented sand under monotonic loading. *International Journal of Geomechanics* **16(2)**:04015049.
- Raja, P. S. K. & Thyagaraj, T. (2021) Significance of compaction time delay on compaction and strength characteristics of sulfate resistant cement-treated expansive soil. *Journal of Rock Mechanics and Geotechnical Engineering* **13(5)**:1193-1202.
- Rao, Y., Zhang, X., Gao, Z., Xiang, R. & Zhang, L. (2023) Experimental Study on Pore Structure and Soil-Water Characteristic Curve of Ionic Rare Earth Ore under Seepage. *Minerals* 13(8):1035.
- Ravanbakhsh, E. & Hamidi, A. (2013) Development of a generalized plasticity constitutive model for cemented sands using critical state concepts. *International Journal of Geotechnical Engineering* **7(4)**:364-373.
- Reddy, B. V. & Gupta, A. (2008) Influence of sand grading on the characteristics of mortars and soil–cement block masonry. *Construction and Building Materials* **22(8)**:1614-1623.
- Ribeiro, D., Néri, R. & Cardoso, R. (2016) Influence of water content in the UCS of soil-cement mixtures for different cement dosages. *Procedia engineering* **143**:59-66.
- Richart, F. E., Hall, J. R. & Woods, R. D. (1970) Vibrations of soils and foundations.
- Rinaldi, V. & Santamarina, J. (2008) Cemented soils: small strain stiffness. *Deformational Characteristics of Geomaterials* **1(1)**:267-273.
- Rios, S., Cristelo, N., Viana Da Fonseca, A. & Ferreira, C. (2017) Stiffness behaviour of soil stabilised with alkali-activated fly ash from small to large strains. *International Journal of Geomechanics* **17(3)**:04016087.
- Rios, S., Viana Da Fonseca, A. & Baudet, B. A. (2012) Effects of the porosity/cement ratio on the compression of cemented soil. *Journal of Geotechnical and Geoenvironmental Engineering* **138(11)**:1422-1426.
- Rios, S., Viana Da Fonseca, A. & Baudet, B. A. (2014) On the shearing behaviour of an artificially cemented soil. *Acta Geotechnica* **9**:215-226.
- Rotta, G., Consoli, N., Prietto, P., Coop, M. & Graham, J. (2003) Isotropic yielding in an artificially cemented soil cured under stress. *Geotechnique* **53(5)**:493-501.
- Russell, A. (2011) A compression line for soils with evolving particle and pore size distributions due to particle crushing. *Géotechnique Letters* **1(1)**:5-9.
- Russell, A. & Khalili, N. (2006) A unified bounding surface plasticity model for unsaturated soils. *International Journal for Numerical and Analytical Methods in Geomechanics* **30(3)**:181-212.

- Sakr, M. A., Elsawwaf, M. A. & Rabah, A. K. (2022) Numerical study of soft clay reinforced with deep cement mixing technique. *Indian Geotechnical Journal* **52(6)**:1487-1504.
- Salvati, L. A. & Pestana, J. M. (2006) Small-strain behaviour of granular soils. II: seismic response analyses and model evaluation. *Journal of Geotechnical and Geoenvironmental Engineering* **132(8)**:1082-1090.
- Sargent, P., Rouainia, M., Diambra, A., Nash, D. & Hughes, P. (2020) Small to large strain mechanical behaviour of an alluvium stabilised with low carbon secondary minerals. *Construction and Building Materials* **232**:117174.
- Saxena, S. K., Avramidis, A. S. & Reddy, K. R. (1988) Dynamic moduli and damping ratios for cemented sands at low strains. *Canadian geotechnical journal* **25(2)**:353-368.
- Scdot (2022) Geotechnical Design Manual.
- Schnaid, F., Prietto, P. D. & Consoli, N. C. (2001) Characterization of cemented sand in triaxial compression. *Journal of Geotechnical and Geoenvironmental Engineering* **127(10)**:857-868.
- Scrivener, K., Snellings, R. & Lothenbach, B. (2018) A practical guide to microstructural analysis of cementitious materials. Crc Press.
- Sedighi Moghadam, M., Zad, A., Yazdi, M. & Jalali Moghadam, M. (2022) Performance of T-Shaped and conventional Cement-Soil deep mixing piles to stabilise soft base of High-Speed trains. *International Journal of Geotechnical Engineering* **16(10)**:1253-1267.
- Seed, H. B. (1970) Soil moduli and damping factors for dynamic response analyses. *Reoprt*:EERC 70-10.
- Sharma, M. R., Baxter, C. D., Hoffmann, W., Moran, K. & Vaziri, H. (2011) Characterization of weakly cemented sands using nonlinear failure envelopes. *International Journal of Rock Mechanics and Mining Sciences* **48(1)**:146-151.
- Shen, Z., Jiang, M. & Thornton, C. (2016) DEM simulation of bonded granular material. Part I: contact model and application to cemented sand. *Computers and Geotechnics* **75**:192-209.
- Shi, J., Xiao, Y., Carraro, J. a. H., Li, H., Liu, H. & Chu, J. (2023) Anisotropic small-strain stiffness of lightly biocemented sand considering grain morphology. *Géotechnique*:1-14.
- Shien, N. K., Ming, C. Y. & Sukri, N. (2019) Fracture behaviour of Cement Treated Sandy Clay. In *MATEC Web of Conferences*.) EDP Sciences, vol. 303, pp. 01001.
- Simms, P. & Yanful, E. (2004) A discussion of the application of mercury intrusion porosimetry for the investigation of soils, including an evaluation of its use to estimate volume change in compacted clayey soils. *Geotechnique* **54(6)**:421-426.

- Subramaniam, P. & Banerjee, S. (2020) Dynamic properties of cement-treated marine clay. *International Journal of Geomechanics* **20(6)**:04020065.
- Subramaniam, P., Banerjee, S. & Ku, T. (2019) Shear modulus and damping ratio model for cement treated clay. *International Journal of Geomechanics* **19(7)**:06019010.
- Subramanian, S., Khan, Q. & Ku, T. (2020) Effects of sand on the stiffness characteristics of cement-stabilised clay. *Construction and Building Materials* **264**:120192.
- Suebsuk, J., Horpibulsuk, S. & Liu, M. D. (2010) Modified Structured Cam Clay: A generalised critical state model for destructured, naturally structured and artificially structured clays. *Computers and Geotechnics* **37(7-8)**:956-968.
- Sun, Z., Chen, W.-B., Zhao, R.-D., Jin, Y.-F. & Yin, J.-H. (2023a) Solidification/stabilisation treatment of Hong Kong marine deposits slurry at high water content by ISSA and GGBS. *Construction and Building Materials* **372**:130817.
- Sun, Z., Chen, W.-B., Zhao, R.-D., Li, J.-S., Yin, Z.-Y., Yin, J.-H. & Chen, Y.-G. (2024) Physicochemical properties of clayey deposits slurry treated by lime-activated ISSA and GGBS considering seawater salinity effect. *Applied Clay Science* **248**:107237.
- Sun, Z., Chen, W.-B., Zhao, R.-D., Shen, P., Yin, J.-H. & Chen, Y.-G. (2023b) Effects of seawater on solidification/stabilisation treatment of marine soft soil slurry by limeactivated ISSA and GGBS. *Engineering Geology* **323**:107216.
- Suzuki, Y. (1982) Deep chemical mixing method using cement as hardening agent. In *Symposium on Recent Development in Ground Improvement Techniques*.).
- Swasdi, S., Jaritngam, S., Tonnayopas, D. & Thongchim, P. (2007) Soft Subgrade Stabilisation with Cement in Satun Province, Thailand. *MH* 1:0.15.
- Taiebat, M. & Dafalias, Y. F. (2008) SANISAND: Simple anisotropic sand plasticity model. International Journal for Numerical and Analytical Methods in Geomechanics 32(8):915-948.
- Taiebat, M. & Dafalias, Y. F. (2010) Simple yield surface expressions appropriate for soil plasticity. *International Journal of Geomechanics* **10(4)**:161-169.
- Talabi, A. O., Ademilua, O. L. & Akinola, O. O. (2012) Compositional features and industrial application of Ikere kaolinite Southwestern Nigeria. *Research Journal in Engineering and Applied Sciences* **1(5)**:327-333.
- Tang, G., Guo, L., Liu, G. & Yang, X. (2023) Determination of the relationship between direct tensile test and Brazilian splitting test of cemented tailings backfill. In Paste 2023: Proceedings of the 25th International Conference on Paste, Thickened and Filtered Tailings.) University of Alberta, Edmonton, and Australian Centre for Geomechanics,

- Perth, pp. 98-111.
- Testing, A. S. F. & Materials (2016) Standard test method for splitting tensile strength of intact rock core specimens. ASTM International.
- Tremblay, H., Duchesne, J., Locat, J. & Leroueil, S. (2002) Influence of the nature of organic compounds on fine soil stabilisation with cement. *Canadian geotechnical journal* **39(3)**:535-546.
- Trhlíková, J., Mašín, D. & Boháč, J. (2012) Small-strain behaviour of cemented soils. *Geotechnique* **62(10)**:943-947.
- Van Nguyen, S., Ho, L. S. & Nakarai, K. (2021) Experimental Investigation of Cement Type Effect on Hydration and Strength Development of Cement-Treated Soils. In CIGOS 2021, Emerging Technologies and Applications for Green Infrastructure: Proceedings of the 6th International Conference on Geotechnics, Civil Engineering and Structures.) Springer, pp. 1045-1053.
- Vardanega, P. J. & Bolton, M. D. (2013) Stiffness of Clays and Silts: Normalizing Shear Modulus and Shear Strain. *Journal of Geotechnical & Geoenvironmental Engineering* **139(9)**:1575-1589.
- Vatsala, A., Nova, R. & Murthy, B. S. (2001) Elastoplastic model for cemented soils. *Journal of Geotechnical and Geoenvironmental Engineering* **127(8)**:679-687.
- Venkatarama Reddy, B., Lal, R. & Nanjunda Rao, K. (2007) Optimum soil grading for the soil-cement blocks. *Journal of Materials in Civil Engineering* **19(2)**:139-148.
- Vermeer, P. A. & De Borst, R. (1984) Non-associated plasticity for soils, concrete and rock. *HERON*, 29 (3), 1984.
- Viggiani, G. & Atkinson, J. (1995) Interpretation of bender element tests. *Geotechnique* **45(1)**:149-154.
- Voottipruex, P., Jamsawang, P., Sukontasukkul, P., Jongpradist, P., Horpibulsuk, S. & Chindaprasirt, P. (2019) Performances of SDCM and DCM walls under deep excavation in soft clay: Field tests and 3D simulations. *Soils and Foundations* **59(6)**:1728-1739.
- Waichita, S., Jongpradist, P. & Schweiger, H. F. (2020) Numerical and experimental investigation of failure of a DCM-wall considering softening behaviour. *Computers and Geotechnics* **119**:103380.
- Wang, L., Li, X., Cheng, Y., Zhang, Y. & Bai, X. (2018) Effects of coal-bearing metakaolin on the compressive strength and permeability of cemented silty soil and mechanisms. *Construction and Building Materials* **186**:174-181.
- Wang, M. & Huston, M. T. (1972) Direct-tensile stress and strain of a cement-stabilised soil.

- Highway Research Record 379:19-24.
- Wang, Y. & Leung, S. (2008) Characterization of cemented sand by experimental and numerical investigations. *Journal of Geotechnical and Geoenvironmental Engineering* **134(7)**:992-1004.
- Wang, Y., Xie, G. & Dou, H. (2019a) Stabilisation of soft clay by deep cement mixing (DCM) method—a case study. *HKIE Transactions* **26(3)**:115-125.
- Wang, Y., Xie, G. & Dou, H. (2019b) Stabilisation of Soft Clay by Deep Cement Mixing (Dcm) Method–A Case Study.". *HKIE Transactions* **26(3)**:115-125.
- Wang, Z.-L., Dafalias, Y. F. & Shen, C.-K. (1990) Bounding surface hypoplasticity model for sand. *Journal of engineering mechanics* **116(5)**:983-1001.
- Wijerathna, M. & Liyanapathirana, D. (2019) Significance of spatial variability of deep cement mixed columns on reliability of column-supported embankments. *International Journal of Geomechanics* **19(8)**:04019087.
- Wijerathna, M. & Liyanapathirana, D. (2021) Simplified modelling approaches for DCM column-supported embankments. *International Journal of Geotechnical Engineering* **15(5)**:553-562.
- Wong, A. L., Chung, P. W., Chu, F. L., So, S. T. & Wong, L. N. (2022) Tensile properties of cement-stabilised clays and their contribution to seawall design. *Proceedings of the Institution of Civil Engineers-Ground Improvement* 177(2):88-102.
- Wonglert, A., Jongpradist, P., Jamsawang, P. & Larsson, S. (2018) Bearing capacity and failure behaviours of floating stiffened deep cement mixing columns under axial load. *Soils and Foundations* **58(2)**:446-461.
- Woo, S. (1971) Cement and lime stabilisation of selected lateritic soils.) Thesis.
- Wu, J., Deng, Z., Deng, Y., Zhou, A. & Zhang, Y. (2022) Interaction between cement clinker constituents and clay minerals and their influence on the strength of cement-based stabilised soft clay. *Canadian geotechnical journal* **59(6)**:889-900.
- Wu, P.-C., Feng, W.-Q. & Yin, J.-H. (2020) Numerical study of creep effects on settlements and load transfer mechanisms of soft soil improved by deep cement mixed soil columns under embankment load. *Geotextiles and Geomembranes* **48(3)**:331-348.
- Wu, S., Zhang, S., Guo, C. & Xiong, L. (2017) A generalized nonlinear failure criterion for frictional materials. *Acta Geotechnica* **12**:1353-1371.
- Wu, W. & Bauer, E. (1993) A hypoplastic model for barotropy and pyknotropy of granular soils. *Modern approaches to plasticity*:225-245.
- Wu, W., Bauer, E., Niemunis, A. & Herle, I. (1993) Visco-hypoplastic models for cohesive

- soils. *Modern approaches to plasticity* **5**:365-383.
- Wu, W. & Kolymbas, D. (1990) Numerical testing of the stability criterion for hypoplastic constitutive equations. *Mechanics of materials* **9(3)**:245-253.
- Wu, Z., Deng, Y., Liu, S., Liu, Q., Chen, Y. & Zha, F. (2016) Strength and micro-structure evolution of compacted soils modified by admixtures of cement and metakaolin. *Applied Clay Science* **127**:44-51.
- Wud, W. & Niemunis, A. (1994) Beyond invertibility surface in granular materials. In *International workshop on localisation and bifurcation theory for soils and rocks.*), pp. 113-126.
- Xiao, H., Lee, F. H. & Liu, Y. (2017) Bounding surface cam-clay model with cohesion for cement-admixed clay. *International Journal of Geomechanics* **17(1)**:04016026.
- Xu, M., Liu, L., Deng, Y., Zhou, A., Gu, S. & Ding, J. (2021) Influence of sand incorporation on unconfined compression strength of cement-based stabilised soft clay. *Soils and Foundations* **61(4)**:1132-1141.
- Yang, C., Cui, Y.-J., Pereira, J.-M. & Huang, M. (2008) A constitutive model for unsaturated cemented soils under cyclic loading. *Computers and Geotechnics* **35(6)**:853-859.
- Yang, L. (2008) Shear stiffness modeling of cemented sand and cemented clay.) University of Notre Dame.
- Yang, L. & Woods, R. D. (2015) Shear stiffness modeling of cemented clay. *Canadian geotechnical journal* **52(2)**:156-166.
- Yao, K. (2017) Small strain behaviour of cement treated Singapore marine clay. *National University of Singapore*.
- Yao, K., Chen, Q., Ho, J., Xiao, H. & Lee, F. H. (2018) Strain-dependent shear stiffness of cement-treated marine clay. *Journal of Materials in Civil Engineering* **30(10)**:04018255.
- Yao, K., Xiao, H., Chen, D.-H. & Liu, Y. (2019) A direct assessment for the stiffness development of artificially cemented clay. *Geotechnique* **69(8)**:741-747.
- Yapage, N. & Liyanapathirana, D. (2014) A parametric study of geosynthetic-reinforced column-supported embankments. *Geosynthetics International* **21(3)**:213-232.
- Yapage, N. & Liyanapathirana, D. (2019) A review of constitutive models for cement-treated clay. *International Journal of Geotechnical Engineering* **13(6)**:525-537.
- Yapage, N., Liyanapathirana, D., Kelly, R. B., Poulos, H. G. & Leo, C. J. (2014) Numerical modeling of an embankment over soft ground improved with deep cement mixed columns: case history. *Journal of Geotechnical and Geoenvironmental Engineering* **140(11)**:04014062.

- Yapage, N., Liyanapathirana, D., Poulos, H. G., Kelly, R. B. & Leo, C. J. (2015) Numerical modeling of geotextile-reinforced embankments over deep cement mixed columns incorporating strain-softening behaviour of columns. *International Journal of Geomechanics* **15(2)**:04014047.
- Ye, G., Cai, Y. & Zhang, Z. (2017) Numerical study on load transfer effects of Stiffened Deep Mixed column-supported embankment over soft soil. *KSCE Journal of Civil Engineering* **21**:703-714.
- Yerro, A., Alonso, E. & Pinyol, N. (2016) Run-out of landslides in brittle soils. *Computers and Geotechnics* **80**:427-439.
- Yi, Y., Liu, S. & Puppala, A. (2016) Laboratory modelling of T-shaped soil—cement column for soft ground treatment under embankment. *Geotechnique* **66(1)**:85-89.
- Yilmaz, Y. & Ozaydin, V. (2013) Compaction and shear strength characteristics of colemanite ore waste modified active belite cement stabilised high plasticity soils. *Engineering Geology* **155**:45-53.
- Yin, K., Xiao, T., Luo, H., Zou, H. & Zhang, L. (2023) Probabilistic modeling of offshore deep cement mixing improved ground. *Computers and Geotechnics* **156**:105266.
- Yin, K., Zhang, L., Zou, H., Luo, H. & Lu, W. (2022) Key Factors for Deep Cement Mixing Construction for Undredged Offshore Land Reclamation. *Journal of Geotechnical and Geoenvironmental Engineering* **148(8)**:04022063.
- Yoobanpot, N., Jamsawang, P., Poorahong, H., Jongpradist, P. & Likitlersuang, S. (2020) Multiscale laboratory investigation of the mechanical and microstructural properties of dredged sediments stabilised with cement and fly ash. *Engineering Geology* **267**:105491.
- Yu, C. Y., Chow, J. K. & Wang, Y.-H. (2016) Pore-size changes and responses of kaolinite with different structures subject to consolidation and shearing. *Engineering Geology* **202**:122-131.
- Yun, T. S. & Santamarina, J. C. (2005) Decementation, softening, and collapse: changes in small-strain shear stiffness in k 0 loading. *Journal of Geotechnical and Geoenvironmental Engineering* **131(3)**:350-358.
- Zeng, Q., Li, K., Fen-Chong, T. & Dangla, P. (2012) Pore structure characterization of cement pastes blended with high-volume fly-ash. *Cement and Concrete Research* **42(1)**:194-204.
- Zhang, A., Dafalias, Y. F. & Jiang, M. (2023a) A bounding surface plasticity model for cemented sand under monotonic and cyclic loading. *Geotechnique* **73(1)**:44-61.
- Zhang, A., Dafalias, Y. F. & Wang, D. (2023b) SANISAND-H: A sand bounding surface model for high pressures. *Computers and Geotechnics* **161**:105579.

- Zhang, R., Lu, Y., Tan, T., Phoon, K. & Santoso, A. (2014) Long-term effects of curing temperature on the strength behaviour of cement-stabilised clay. *Journal of Geotechnical and Geoenvironmental Engineering* **140(8)**:04014045.
- Zhang, Z., Rao, F.-R. & Ye, G.-B. (2020) Design method for calculating settlement of stiffened deep mixed column-supported embankment over soft clay. *Acta Geotechnica* **15**:795-814.
- Zhao, L., Chen, Y., Chen, W., Wang, J. & Ren, C. (2023) The performance of T-shaped deep mixed soil cement column-supported embankments on soft ground. *Construction and Building Materials* **369**:130578.
- Zhao, Y., Taheri, A., Karakus, M., Deng, A. & Guo, L. (2021) The effects of curing under applied stress on the mechanical performance of cement paste backfill. *Minerals* 11(10):1107.
- Zheng, G., Yang, X., Zhou, H. & Chai, J. (2019) Numerical modeling of progressive failure of rigid piles under embankment load. *Canadian Geotechnical Journal* **56(1)**:23-34.
- Zhou, C., Ng, C. W. W. & Chen, R. (2015) A bounding surface plasticity model for unsaturated soil at small strains. *International Journal for Numerical and Analytical Methods in Geomechanics* **39(11)**:1141-1164.
- Zhou, C., Tai, P. & Yin, J. H. (2020) A bounding surface model for saturated and unsaturated soil-structure interfaces. *International Journal for Numerical and Analytical Methods in Geomechanics* **44(18)**:2412-2429.
- Zhou, N., Ouyang, S., Cheng, Q. & Ju, F. (2019) Experimental Study on Mechanical Behaviour of a New Backfilling Material: Cement-Treated Marine Clay. *Advances in Materials Science and Engineering* **2019(1)**:1261694.